Moisture-Cure Polyurethane Wood Adhesives: Wood/Adhesive Interactions and Weather Durability

Dakai Ren

Dissertation submitted to the faculty of the

Virginia Polytechnic Institute and State University

in partial fulfillment of the requirements for the degree of

Doctor of Philosophy

In

Macromolecular Science and Engineering

Charles E. Frazier, Chair

Kevin J. Edgar

Timothy E. Long

Maren Roman

Garth Wilkes

November 18, 2010

Blacksburg, Virginia

Keywords: moisture-cure polyurethane, wood adhesion, wood/adhesive interaction, weather durability

Moisture-Cure Polyurethane Wood Adhesives: Wood/Adhesive Interactions and Weather Durability

Dakai Ren

Charles E Frazier, Chairman

ABSTRACT

This project addresses two main subjects of moisture-cure polyurethane (PUR) wood adhesives: wood/PUR interactions and structure-property behavior emphasizing on weather durability. For these purposes, one simplified model PUR (MPUR) and three more commercially significant PURs (CPURs) with different hard segment contents were prepared. Separately, an early side project involved the synthesis of a ^{13}C and ^{15}N double-labeled polymeric methylenebis(phenylisocyanate) (pMDI) resin; this was used for the solid-state NMR characterization of isocyanate cure chemistry in wood bondline.

MPUR and a CPUR were employed to investigate whether wood/adhesive interactions influence PUR properties. Wood interactions significantly altered PUR hard/soft domain size distribution (atomic force microscopy, AFM), thermal transition temperatures (dynamic mechanical analyses, DMA), and urethane/urea hydrogen bonds (Fourier transform infrared spectroscopy, FTIR).

The effects of hard segment content on properties of PUR prepolymers, and cured PURs (films and wood composites) were studied. Hard segment content largely influenced the PURs'

molecular weights, viscosity, penetration, thermal transitions, and hard segment hydrogen bonds, but only slightly altered the dry (unweathered) bondline toughness.

Three accelerated weathering procedures were developed to evaluate CPUR bondline weather durability through mode-I fracture testing. Both hard segment content and weathering conditions were found to significantly influence the bondline weather durability. Among these weathering procedures, only one (VPSS) was able to effectively distinguish weather durability of PUR adhesives, and therefore it was selected for detailed structure-weather durability studies. PUR weather durability was found to correlate with its moisture sensitivity and hard segment softening temperature; both were provided by water-submersion DMA. Much attention was directed to the investigation of weather-induced PUR molecular changes. FTIR studies provided evidences of post-cure, hydrolytic degradation, and variation of urethane/urea hydrogen bonds. DMA presented weathering effects on PUR thermal properties. Special efforts have been made to correlate these analytical results with PUR weather durability.

A ^{13}C and ^{15}N double-labeled pMDI resin was synthesized and used for solid-state NMR characterization of isocyanate cure chemistry in wood bondline, particularly to detect the evidence of urethane formation. Rotational echo double resonance (REDOR) NMR clearly revealed the formation of urethane linkages, but largely overestimated their content.

ACKNOWLEDGEMENTS

I want to take the opportunity to express my appreciation to the support, understanding, and guidance of my family, friends, coworkers, and advisory committee. Without each of you, this work could never have been accomplished.

First and the foremost, I want to express my deepest gratitude to my advisor Dr. Charles Frazier. His guidance, encourage, patience, and support have given me every opportunity to explore my potentials and excel. Not only unquestionably contributed to my scientific development, Dr. Frazier has served as a remarkable role model for me. His kindness, confidence, enthusiasm, and work ethics have set an outstanding example for me. I feel extremely honored and lucky to have the opportunity to work under such a wonderful advisor.

I am very grateful for my other committee members, in alphabetical order including Dr. Kevin J. Edgar, Dr. Timothy E. Long, Dr. Maren Roman, and Dr. Garth Wilkes. Thank you all for your great contributions during my study and your efforts to serve on my committee. I want to thank Stephen McCartney for his tremendous help on preparing AFM specimens. I also want to thank Dr. Audrey Zink-Sharp for teaching me microscope techniques. I am thankful to Dr. Sungsool Wi for helping me conduct solid-state NMR studies. I would like to thank the staff members in the Department of Wood Science and Engineering for their supports. Special thanks to my fellow colleagues in the wood adhesion group. You guys are awesome and we were such a great basketball team.

Last but not the least, I am very grateful for my wife, Caiyan Luo. Thank you from the bottom of heart for always being with me, encouraging and supporting me. Without her love and enormous sacrifices, I would never be able to finish this work.

This research was supported by Wood-Based Composites Center and Virginia Tech Graduate School.

TABLE OF CONTENTS

LIST OF FIGURES

LIST OF TABLES

Chapter 1 Project description

There are two main objectives of this project. The first is to investigate whether and how wood/adhesive interactions influence the properties of moisture-cure polyurethane (PUR) wood adhesives. The second is to study the structure/property relationships of PURs with special emphasis on the weather durability of the adhesive as determined using mode-I fracture testing. Furthermore, much of the structure/property work is devoted to the development of novel analytical methods for studying PURs that are either directly bonded to wood, or excised from bonded fracture specimens.

1.1 Objective 1: Influence of Wood/Adhesive Interactions on PUR Properties

PURs are segmental copolymers exhibiting microphase-separated morphologies. One phase is derived from a typically flexible (subambient glass transition temperature, T_g) polyol that is generally referred to as the "soft phase." Likewise the corresponding "hard phase" in this case is primarily born from a di- or polyisocyanate reaction with ambient water, producing a highly crosslinked material with T_g well above room temperature. The highly varied properties of polyurethanes arise from variations in the dual-phase morphology [1-6], and therefore the factors controlling morphology are of great interest. For PURs, the influence of the various chemical components has been the focus of many studies [7-12]. However, the effects of the adherend, wood, on PUR properties have been overlooked. If wood indeed affects PUR properties, the structure-property behavior that is normally studied in polymer neat films should be investigated in composite specimens that resemble actual bondlines. Therefore, it is important to investigate whether and how wood/adhesive interactions change the properties of PURs.

Wood factors that could impact PUR morphology are: 1) wood's influence on available moisture, and 2) primary and/or secondary intermolecular interactions between wood and the adhesive. These factors are discussed below.

1.1.1 Wood influence on available moisture

It has been reported that moisture considerably influences the properties and performance of various polyurethanes [13-16]. For PURs, it has been documented that moisture availability has significant effects on the curing process (e.g. the moisture diffusion rate, curing speed, possibility of side reactions, etc.) [17-18]. The cure of PUR follows two steps: firstly, the isocyanate reacts with moisture to create a primary amine terminus and carbon dioxide; secondly, reactions between the amine and isocyanate yields urea-linked hard segments. When the PUR is exposed to the air, the surface layer reacts quickly to form a skin. This skin slows moisture diffusion into the uncured bulk. In general, the chemical reactions occur at a much faster rate than moisture diffusion. Thus, the PUR cure is a moisture-diffusion dominated process. Consequently the environmental humidity affects this moisture diffusion rate and therefore the cure kinetics. As the chemical reactions proceed, free isocyanate content decreases and the average size of the hard phase increases, leading to a change of interaction parameter (e.g. solubility parameter) for soft and hard segments. As a result, the moisture availablity influences the kinetics of cure and also of phase evolution. When casting a polymer film under atmospheric conditions, moisture comes primarily from the air. However, in the wood bondline, moisture delivery is more complex. Aside from the diffused moisture from the air, the PUR achieves direct contact with wood and wood-adsorbed water. Consistent with this scenario is a report

from Beaud et al. that the PUR performance is indeed sensitive to the wood moisture content [19].

1.1.2 Primary and/or secondary intermolecular interactions between wood and adhesive

Wood is a complex composite of at least four structural polymers: cellulose, lignin, glucomannan, and xylan. Semicrystalline cellulose fibrils are oriented generally parallel to the tree stem, and are embedded within an amorphous matrix of lignin and xylan. Amorphous glucomannans are believed to encrust the fibril surfaces, perhaps influencing fibril/fibril and fibril/matrix interactions [20-22]. The monomer composition of all non-cellulosic polymers varies by species, and even within species as a function of tissue maturity and growth conditions [23]. All of the wood polymers are hydrophilic, each containing functional groups that promote water adsorption and that could react with isocyanates. For example, cellulose, glucomannan, and lignin contain primary and secondary hydroxyl groups; xylans and lignin may contain carboxylic acid groups; and lignin contains phenolic hydroxyls. Additional complexity is found in the non-structural secondary metabolites that may be removed from wood through solvent extraction; these wood "extractives" are highly varied in structure and ocurrence [23]. Aside from chemical structure, nature's "packaging" of the wood substance varies dramatically by anatomical features and by specfic gravity- this speaks to wood porosity and the potential for adhesive penetration on the micro- and nanometer scale of wood. In other words, the natural porosity of wood, and the polar and reactive nature of the wood components will create secondary and perhaps primary interactions that could alter the kintetics of hard and soft phase evolution. The properties of the adhesive layer will reflect these wood-induced effects.

1.2 Objective 2: Structure/Durability Studies

Wood is an ancient and still critical human resource. In North America, wood remains the preferred material with which most people construct their homes. Naturally, the adhesive bonding of wood is central to its utilization by millions of homeowners. Consequently, studies intended to understand and further improve wood/adhesive durability are of great practical significance. For this purpose, it is critical to learn the long-term performance of wood/adhesive bonding after years of exposure to different environmental conditions. Short-term accelerated weathering procedures can be used to simulate these conditions, and allow the investigation of long-term durability over a drastically shorter period. Although the structure-property behavior of PURs has been widely studied, the influence of chemical structure on weather durability has rarely been reported. In this research, we are interested in the structure/property relationships of PURs as related to weather durability, hereafter referred to as structure/durability studies. The structure/durability behavior of a series of PURs will be studied as a function of various accelerated weathering procedures.

The weather durability of wood adhesives is often evaluated by comparing the mechanical properties determined by shear or fracture tests before and after accelerated weathering [24]. The accelerated weathering is normally composed of multiple cycles of water saturation under vacuum/pressure followed by drying at an elevated temperature. These weathering cycles require a significant amount of time, ranging from a few days to several weeks. Therefore, a quick evaluation method for weather durability would be very desirable. For this purpose, a novel water-submersion dynamic mechanical analysis (DMA) method will be utilized in this project. In this method, the sample is pre-saturated and immersed in water during a temperature

ramp. Consequently, the results obtained from the water-submersion DMA reflect the thermomechanical properties of the sample in response to both water saturation and temperature change, the two main aspects of accelerated weathering. Aside from being a quick and effective test method, water-submersion DMA may potentially aid in understanding the effects of weathering at the molecular level, and whether and how the DMA response relates to the weather performance observed in mode-I fracture testing.

1.3 Approaches to Objective 1

The influence of wood/adhesive interactions is evaluated by contrasting the properties of neat PUR films against PUR/wood composites cured under the same conditions.

1.3.1 Preparation of PUR prepolymers

The PURs for this objective include a well-defined model PUR system (MPUR) and a commercially-relevant PUR system (CPUR).

1.3.1.1 Preparation of MPUR Prepolymers

MPUR prepolymers are prepared from poly(tetramethylene oxide) (PTMO) and 1, 4-phenylene diisocyanate (PPDI) with NCO/OH = 2/1, shown in Figure 1-1.

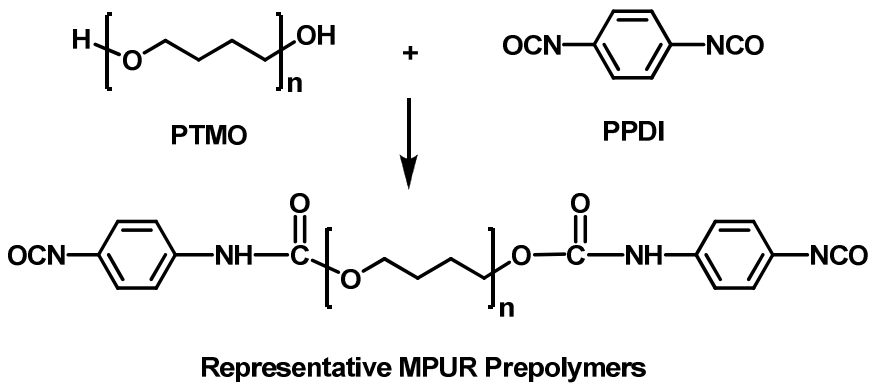

Figure 1-1 Preparation of CPUR prepolymers

1.3.1.2 Preparation of CPUR Prepolymers

The CPUR prepolymers are synthesized from poly (propylene glycol) (PPG) and polymeric methylenediphenyl diisocyanate (p-MDI) with NCO/OH = 5/1, shown in Figure 1-2.

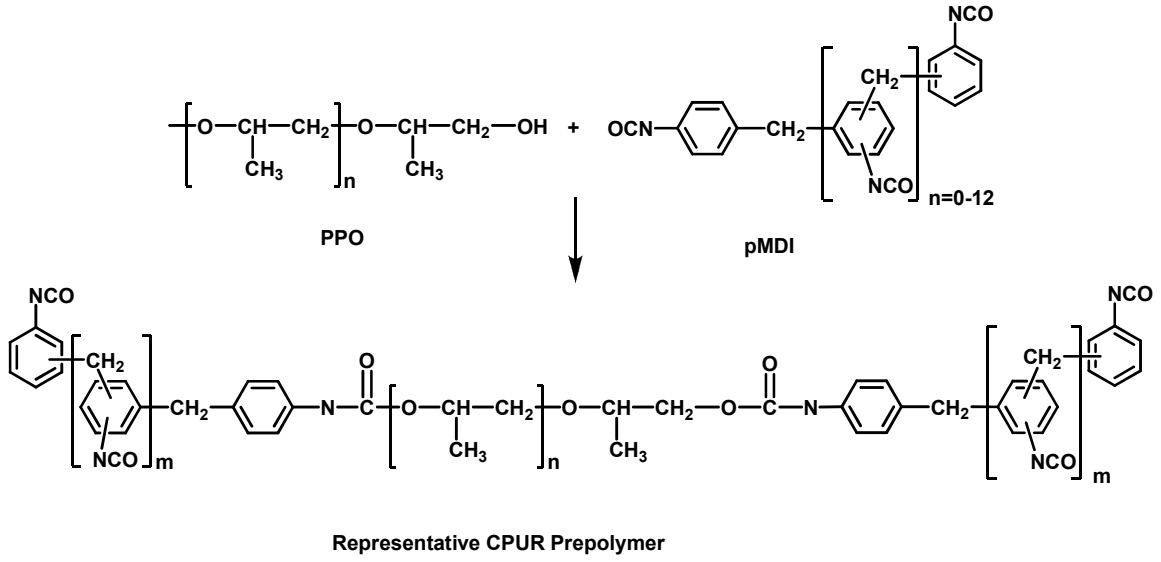

Figure 1-2 Preparation of CPUR prepolymers

1.3.2 Analytical Methods

1.3.2.1 PUR prepolymers

- ^{13}C nuclear magnetic resonance (NMR): chemical structure;
- Size exclusion chromatography (GPC): molecular weights and distribution;
- Rheometer: viscosity;
- Differential scanning calorimetry (DSC): thermal transitions;
- NCO content titration.

1.3.2.2 PUR neat films and PUR/wood composites

- Parallel-plate compression-torsion DMA: investigate thermomechanical properties at the molecular level (storage modulus, tan δ max temperature, and intensity);
- Tapping-mode AFM phase image: directly image the morphological features (e.g. hard domain shape and size distribution);
- Fourier transform infrared spectroscopy (FTIR): study changes of urethane and urea hydrogen bonds.

1.4 Approaches to Objective 2

1.4.1 Adhesives and Preparation

The influence of the soft segment composition on weather durability is of primary interest. A series of PUR prepolymers are synthesized from p-MDI and mixtures of PPG of M_n = 2000 or 400 g/mole with three different mass ratios (of high to low molar mass = 80/20, 50/50, 20/80). These PUR prepolymers are then used to prepare wood/PUR composites, respectively.

1.4.2 Structure-Weather Durability Studies

- Develop accelerated weathering procedures: water saturation conditions, drying temperature and time, number of cycles;
- Evaluate and compare the weather performance of each PUR-bonded composite by testing the mode-I fracture toughness before and after accelerated weathering;
- Examine the properties of each PUR-bonded composite at a molecular level using DMA and FTIR to evaluate weathering performance.

1.4.3 Develop water submersion-DMA for quick evaluation of weathering performance

- Investigate the change in thermomechanical properties of PURs in response to water saturation and temperature change;
- Determine whether and how this change in DMA behavior correlates to the change in weathering performance characterized by fracture toughness;
- Determine whether the water-submersion DMA can be used as a quick screening method for adhesive development.

References

1. Yilgor, I., E. Yilgor, I.G. Guler, T.C. Ward, and G.L. Wilkes, FTIR investigation of the influence of diisocyanate symmetry on the morphology development in model segmented polyurethanes. Polymer, 2006. 47(11): p. 4105-4114.

2. Yilgor, I. and E. Yilgor, Structure-morphology-property behavior of segmented thermoplastic polyurethanes and polyureas prepared without chain extenders. Polymer Reviews, 2007. 47(4): p. 487-510.

3. Petrovic, Z.S. and I. Javni, The Effect of Soft-Segment Length and Concentration on Phase-Separation in Segmented Polyurethanes. Journal of Polymer Science Part B-Polymer Physics, 1989. 27(3): p. 545-560.

4. J. Y. BAE, D.J.C., J. H. AN, Effects of the structure of chain extenders on the dynamic mechanical behaviour of polyurethane. Journal of Materials Science, 1999. 34: p. 2523-2527.

5. Sheth, J.P., D.B. Klinedinst, G.L. Wilkes, Y. Iskender, and I. Yilgor, Role of chain symmetry and hydrogen bonding in segmented copolymers with monodisperse hard segments. Polymer, 2005. 46(18): p. 7317-7322.

6. Yilgor, E., I. Yilgor, and E. Yurtsever, Hydrogen bonding and polyurethane morphology. I. Quantum mechanical calculations of hydrogen bond energies and vibrational spectroscopy of model compounds. Polymer, 2002. 43(24): p. 6551-6559.

7. DIPAK K. Chattopadhyay, B.S., Kothapalli V. S. N. Raju, Effect of chain extender on phase mixing and coating properties of polyurethane ureas. Ind. Eng. Chem. Res., 2005. 44: p. 1772-1779.

8. Richter, K., A. Pizzi, and A. Despres, Thermal stability of structural one-component polyurethane adhesives for wood - Structure-property relationship. Journal of Applied Polymer Science, 2006. 102(6): p. 5698-5707.

9. Sebenik, U. and M. Krajnc, Influence of the soft segment length and content on the synthesis and properties of isocyanate-terminated urethane prepolymers. International Journal of Adhesion and Adhesives, 2007. 27(7): p. 527-535.

10. X. Li, Z.G., J. Gu, F. Zhao, and X. Bai, Synthesis and characterisation of one-part ambient temperature curing polyurethane adhesives for wood bonding. Pigment & Resin Technology, 2004. 33(6): p. 345-351.

11. Martin-Martinez, M.S.S.-A.a.J.M., Structure, composition, and adhesion properties of thermoplastic polyurethane adhesives. Journal of Adhesion Science and Technology, 2000. 14(8): p. 1035-1055.

12. Chattopadhyay, D.K., B. Sreedhar, and K.V.S.N. Raju, Influence of varying hard segments on the properties of chemically crosslinked moisture-cured polyurethane-urea. Journal of Polymer Science Part B-Polymer Physics, 2006. 44(1): p. 102-118.

13. Yang, B., W.M. Huang, C. Li, and L. Li, Effects of moisture on the thermomechanical properties of a polyurethane shape memory polymer. Polymer, 2006. 47(4): p. 1348-1356.

14. Yang, B., W.M. Huang, C. Li, and J.H. Chor, Effects of moisture on the glass transition temperature of polyurethane shape memory polymer filled with nano-carbon powder. European Polymer Journal, 2005. 41(5): p. 1123-1128.

15. Yang, B., W.M. Huang, C. Li, C.M. Lee, and L. Li, On the enects of moisture in a polyurethane shape memory polymer. Smart Materials & Structures, 2004. 13(1): p. 191-195.

16. Abbott, S.G. and N. Brumpton, The Effect of Moisture on Polyurethane Adhesives. Journal of Adhesion, 1981. 13(1): p. 41-51.

17. Chattopadhyay, D.K., B. Sreedhar, and K.V.S.N. Raju, The phase mixing studies on moisture cured polyurethane-ureas during cure. Polymer, 2006. 47(11): p. 3814-3825.

18. Ni, H.F., C.K. Yap, and Y. Jin, Effect of curing moisture on the indentation force deflection of flexible polyurethane foam. Journal of Applied Polymer Science, 2007. 104(3): p. 1679-1682.

19. Beaud, F., P. Niemz, and A. Pizzi, Structure-property relationships in one-component polyurethane adhesives for wood: Sensitivity to low moisture content. Journal of Applied Polymer Science, 2006. 101(6): p. 4181-4192.

20. Fengel, D., Ideas on the ultrastructural organization of the cell wall components. Journal of Polymer Science Part c, 1971. 36: p. 383-392.

21. Salmen, L. and A.M. Olsson, Interaction between hemicelluloses, lignin and cellulose: Structure-property relationships. Journal of Pulp and Paper Science, 1998. 24(3): p. 99-103.

22. Akerholm, M. and L. Salmen, Interactions between wood polymers studied by dynamic FT-IR spectroscopy. Polymer, 2001. 42(3): p. 963-969.

23. Sjostrom, E., R. Alen, and E. Sjostrom, Analytical Methods in Wood Chemistry, Pulping and Papermaking 1999, New York: Springer Berlin Heidelberg.

24. ASTM, ASTM D2559 - 04, Standard Specification for Adhesives for Structural Laminated Wood Products for Use Under Exterior (Wet Use) Exposure Conditions. 2004.

Chapter 2 Literature Review

Polyurethanes were discovered by Otto Bayer and coworkers in 1930's at I. G. Farbenindustrie, Germany in response to the competitive challenge from polyamides at DuPont [1-3]. Since then, this material has benefited many industries, including plastics, coatings, synthetic fibers, adhesives, and synthetic rubbers. Polyurethanes could be found in coatings and adhesives by the mid-1950's [2]. Polyurethane adhesives are used in the assembly of a variety of products (e.g. shoes, wood composites, automotive interiors, and textile laminates), offering many advantages such as strong bonding and rapid development of "green strength" [4]. In addition, polyurethane chemistry is so versatile that adhesives with diverse chemical and physical properties can be manufactured.

2.1 Types of polyurethane Adhesives

Polyurethane adhesives mainly include two-component and one-component formulations. The one-component adhesives are also known as moisture-cure polyurethanes (PURs). Two-component adhesives utilize either a polyol / polyisocyanate combination or an isocyanate-terminated prepolymer with a low molar weight diol or triol or diamine curative [5]. PURs are NCO-terminated, therefore they will cure in the presence of moisture, generating a highly crosslinked network. Rath et al. [6] summarized the advantages of PURs: 1) They can be manufactured as one package and their application is easy; 2) Since the reactant is water, the formulations have less volatile organic compounds (VOCs) than two-component systems; 3)

They have good adhesion, abrasion resistance, thermal stability, hardness, chemical and solvent resistance compared to two-component polyurethanes.

2.2 Chemistry of PURs

PURs are normally synthesized from two primary chemical components: a long chain polyol, and a diisocyanate or polyisocyanate. A chain extender (CE) is an optional component and it has been included in many PUR systems to improve the performance. The versatility in the selection of these components provides polyurethanes with different properties and applications. The synthesis of chain-extended polyurethanes generally includes two steps (Figure 2-1). First, excess diisocyanate or polyisocyanate (e.g. methylene diphenyl diisocyanate, MDI) reacts with polyol (e.g. polypropylene oxide, PPO) to form an isocyanate end-capped product known as a prepolymer. Second, the prepolymer is then extended with a chain extender (e.g. 1, 4-butanediol, BD). For thermoplastic polyurethanes, the NCO/OH molar ratio is 1/1. However, for PURs, a stoichiometric excess of NCO is employed and environmental moisture completes the cure. The molar ratio of NCO/OH in PURs ranges from 2/1 to 8/1 [5, 7-8].

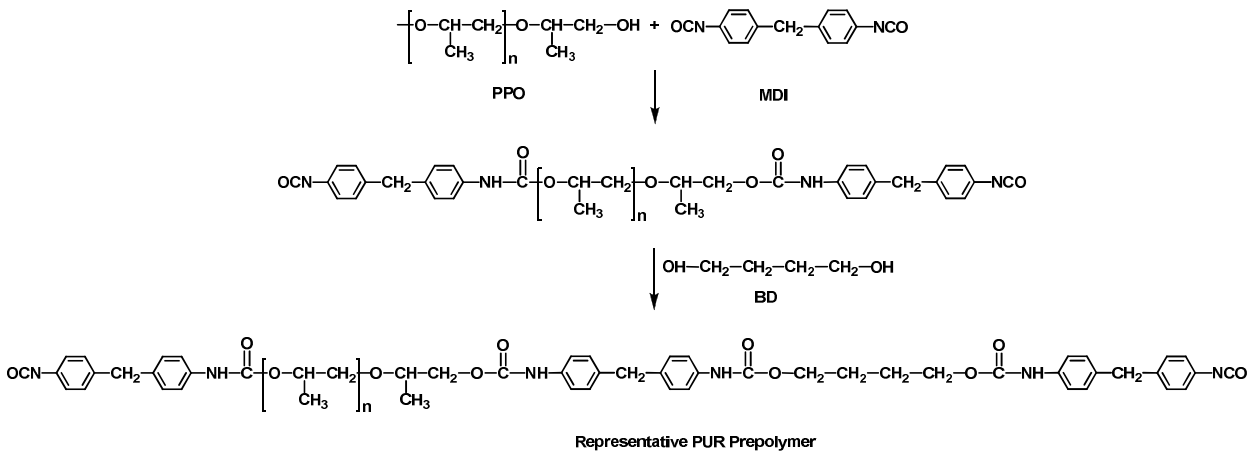

Figure 2-1 Synthetic scheme for a PUR prepolymer

2.2.1 Isocyanates

The difunctional or polyfunctional isocyanates used to prepare polyurethane adhesives can be aromatic, aliphatic, or cycloaliphatic isocyanates. Some common isocyanates include MDI, pMDI, toluene diisocyanate (TDI), 4, 4'-dicyclohexylmethane diisocyanate (HMDI). Aromatic isocyanates usually react faster than aliphatic isocyanates and provide more rigid polyurethanes, but their oxidative and ultraviolet stabilities are lower [1, 8].

Isocyanate is a highly reactive functional group, which is caused by the prominent positive character of the C atom in the N=C=O group. The positive character of the C atom is more pronounced if the NCO group is attached to an aromatic ring. There are mainly two types of reactions (Figure 2-2) for isocyanates: 1) react with nucleophiles, such as alcohols, amines, carboxylic acids; 2) self addition reactions.

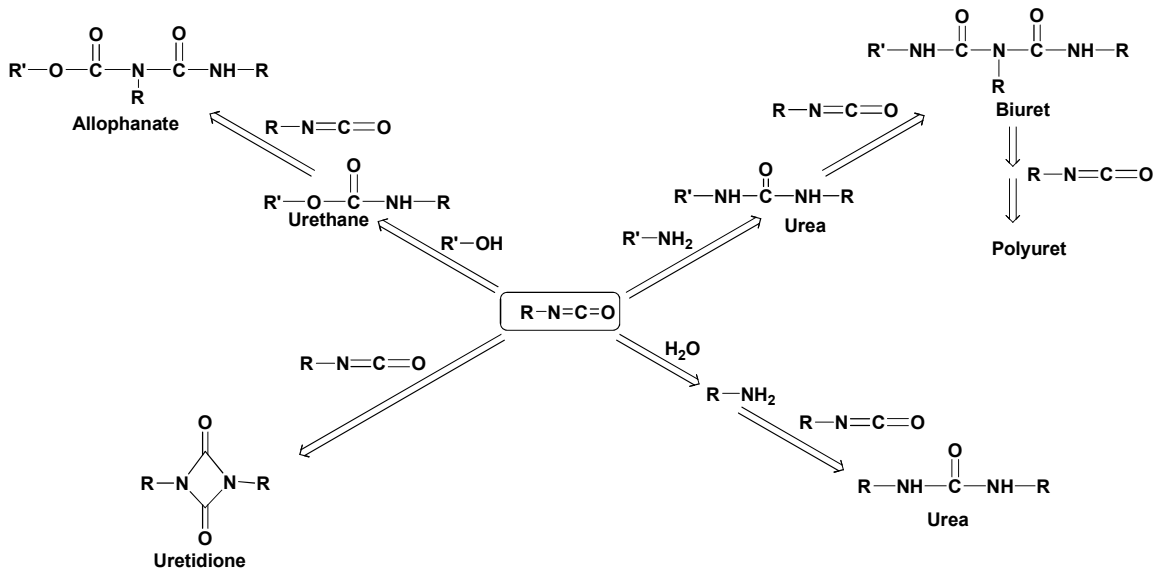

Figure 2-2 Chemical reactions of isocyanates

pMDI is a commonly used polyfunctional isocyanate component to prepare PURs. pMDI is a mixture of MDI monomers and the related methylene bridged dimmers, trimmers, and oligomers. Approximately one half of the mixture is diisocyanate monomer [9]. The chemical components of pMDI are shown in Figure 2-3. In general, pMDI has a number average molecular weight of 255-280 g/mol, a viscosity range from 175-250 mPa·s, and an isocyanate content of 31-32 % [9].

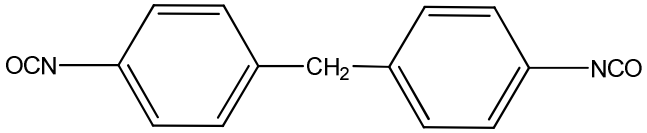

4,4'-MDI

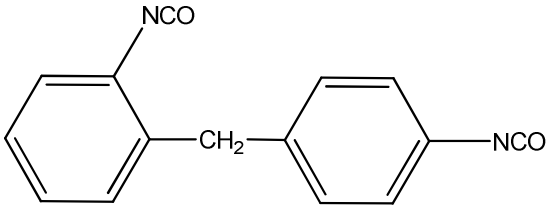

2,4'-MDI

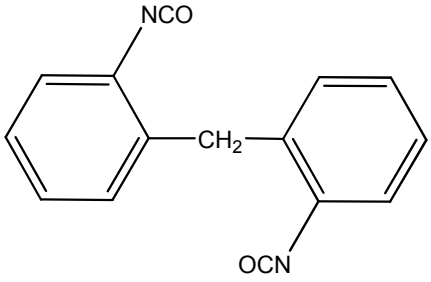

2,2'-MDI

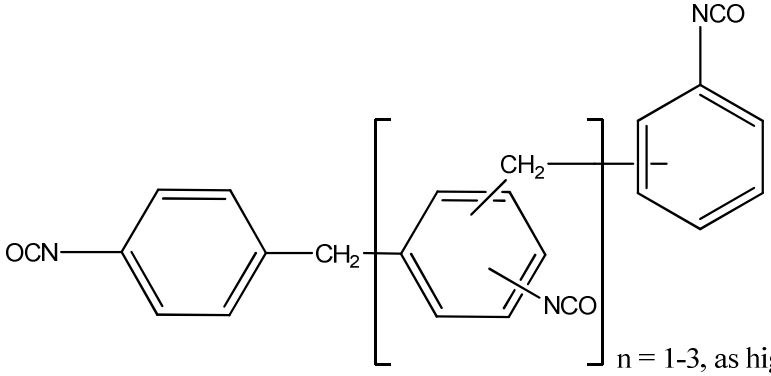

Isomeric mixture of methylene bridged polyisocyanates

Figure 2-3 Chemical components of pMDI

2.2.2 Polyol

There are wide varieties of polyols available for the preparation of polyurethanes, including aliphatic polyethers (e.g. PPO and PTMO), aliphatic polyesters (e.g. polycaprolactone), aliphatic polycarbonates (e.g. hexamethylene polycarbonate), hydrogenated polybutadiene, and polydimethylsiloxane (PDMS) [10-11]. Polyethers and PDMS can be hydroxyl- or primary amine-terminated, while polyesters, polycarbonates, and hydrogenated polybutadiene are generally hydroxyl-terminated [10].

Polyethers and polyesters are most commonly used for the production of PURs. Polyether polyols are formed by the addition of ethylene oxide or propylene oxide to a polyfunctional starter molecule, shown in Figure 2-4 [1, 12]. The typical starter molecules include alcohols (e.g. glycerol, ethylene glycol, propylene glycol, and trimethylolpropane) and amines (e.g. ethylenediamine) [12]. Polyester polyols are produced by a condensation reaction of difunctional carboxylic acids or anhydrides with difunctional alcohols (Figure 2-4). The polyester-based polyurethanes are vulnerable to the gradual hydrolysis taking place at the ester groups; the generated carboxylic acid in turn catalyzes further ester hydrolysis [1].

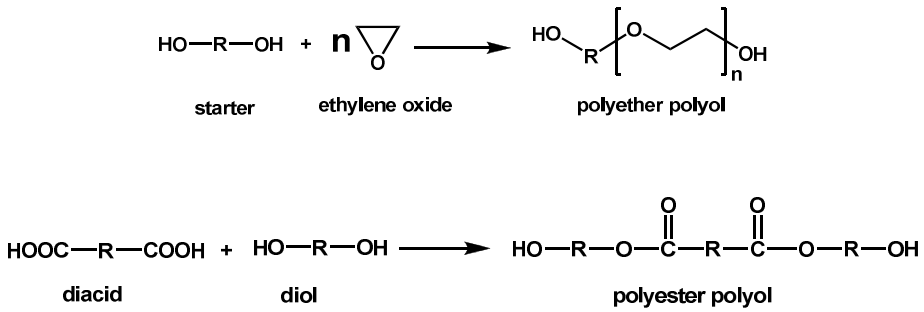

Figure 2-4 Synthesis of polyether and polyester polyols

2.2.3 Chain extender

Chain extenders (CE) are generally reactive, low molecular weight glycols or diamines. CEs react with diisocyanate to form urethane or urea linkages, resulting in an increase of hard segment molecular weight [13-15]. This facilitates the phase separation and influences the mechanical properties of polyurethanes. For example, by changing the ratio of polyol to CE, polyurethanes can change from a hard, brittle material to a rubbery elastomer [15].

Generally, aliphatic CEs yield softer materials than aromatic ones. Furthermore, amine functional extenders produce greater stiffness than hydroxyl functional ones [14]. The choice of CE depends on the targeted properties. In MDI-based prepolymers, a diol CE provides good properties and processing speed, and the most commonly used diol is 1,4-butanediol [16]. In TDI-based prepolymers, a diamine is the preferred CE, and the most commercially used ones are aromatic diamines [16].

2.3 Cure Chemistry of PUR

The PUR cures in several steps (Figure 2-5): 1) Moisture from the atmosphere diffuses into PUR and attacks the NCO-terminated prepolymer to form carbamic acid; 2) The carbamic acid is unstable and decomposes into a primary amine and CO_2; 3) The primary amine is very reactive towards NCO and produces a urea linkage; 4) Urea groups can further react with excess NCO to give biuret and polyuret structures [6]. As a result, the cured adhesive contains both urethane and urea segments, referred to as "poly(urethane urea)". The important parameters that affect the cure process are relative humidity, isocyanate content in the prepolymer, and catalyst type [6].

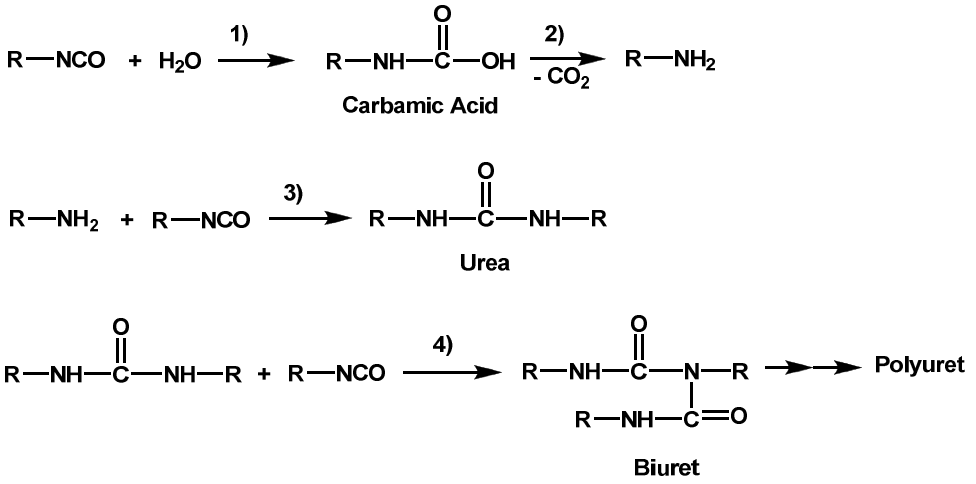

Figure 2-5 Cure chemistry of PURs

In addition, free isocyanate could react with hydroxyls present in the wood biopolymers to form urethane linkages [9] (Figure 2-6). Urethane groups can further react with excess NCO to form allophanates (Figure 2-6).

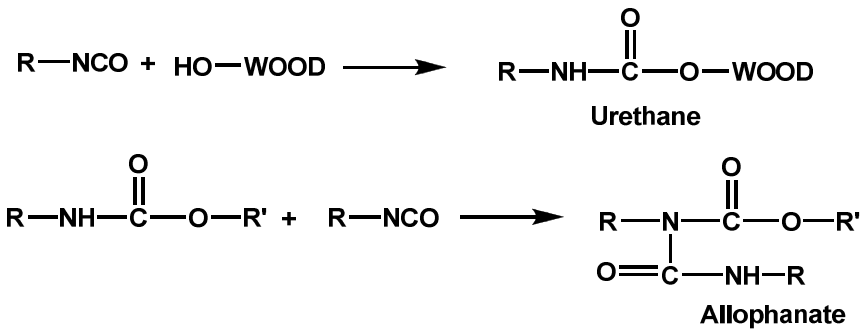

Figure 2-6 Formation of urethane and allophanate linkages

2.4 Morphology of Cured PUR

Polyurethanes or polyureas are segmented polymers containing long-chain polyols and shorter segments consisting of isocyanates and chain extenders. The long chain polyols have a T_g well below room temperature, and they are normally referred to as the "soft" segments; the segments built from isocyanates and chain extenders are called "hard" segments [17]. The chemical incompatibility between hard and soft segments promotes the formation of a phase-separated morphology [11, 18]. This dual-phase morphology largely determines properties and performance of polyurethanes /polyureas [10, 19-23]. Cured PURs [poly(urethane urea)s] contain both urethane and urea hard segments. The primary factors that influence the dual-phase morphology of both polyurethanes and polyureas will be included in the following discussion.

2.4.1 Hydrogen Bonding

Strong hydrogen bonding within the hard segments is believed to be the primary driving force to form the phase-separated morphology [19, 24-26]. Within the hard segments, the hydrogen in N-H groups forms hydrogen bonds with the oxygen in C=O of urethane or urea groups. Two primary types of hard segment hydrogen bonds are shown in Figure 2-7 [22, 27]. Meanwhile, the hydrogen in the N-H group can also form hydrogen bonds with ester carbonyl or ether oxygen in the polyol chains.

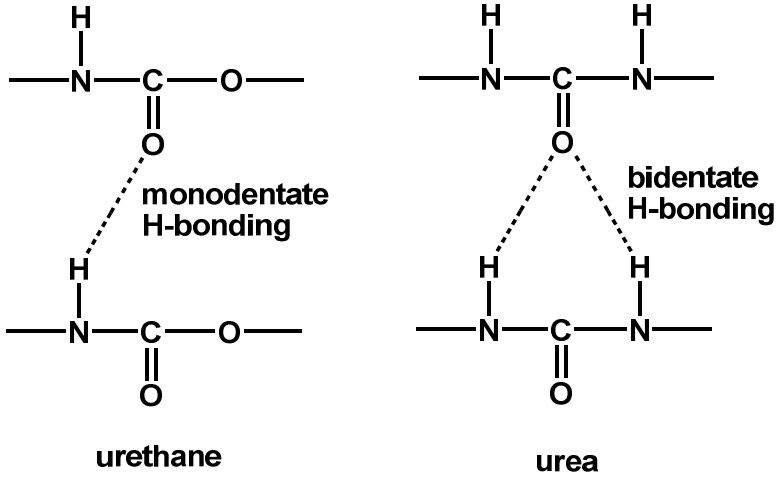

Figure 2-7 Typical types of hard segment hydrogen bonding for urethane and urea

Hydrogen bonding plays a very important role in determining the overall properties and performance of polyurethanes. Researchers have shown that the hydrogen-bonding capacities of the hard segments of polyurethanes and polyureas significantly affect the morphology and performance of these polymers [27-31]. For example, segmented poly(urethane urea)s show much higher tensile strength and modulus values when compared to polyurethanes of similar

composition. This is due to much stronger hydrogen bonding between ureas when compared to urethanes [30]. Furthermore, polyureas with bidentate hydrogen bonds show better microphase separation, improved mechanical properties, and broader service temperature window (STW) than corresponding polyurethanes with monodentate hydrogen bonds [28]. Scientists have made efforts to understand the significance of hydrogen bonding; some of the studies follow immediately.

Das et al. carefully studied the effects of hydrogen bonding on the hard domain connectivity and properties of polyureas by introducing a hydrogen-bond screening agent LiCl [28]. The effects of LiCl were observed using different techniques: 1) Tapping-mode AFM showed a decrease in the length of the thread-like hard segment and a loss in contrast between the hard domains and soft matrix; 2) ATR-FTIR spectra indicated that incorporation of LiCl led to a considerable decrease in the intensity of the bidentate C=O stretching, along with the increase in the intensity of monodentate C=O stretching; 3) Mechanical hysteresis measurements illustrated that the undoped polyurea from PPDI showed a small but distinct yield point in the stress-strain curves, while the yield point was absent in the LiCl-doped samples. These observations suggested that the long-range connectivity between hard domains significantly decreased with the addition of LiCl, which in turn affected the properties of these polyurea polymers: 1) Incorporation of LiCl resulted in a systematic decrease in the rubbery plateau modulus; 2) Addition of LiCl led to a systematic decrease in the breadth of the STW because of the easier hard-hard segments chain slippage.

Yilgor et al. compared the hydrogen bonding between PDMS- and polyether-based polyurethane/polyurea model copolymers [30]. They concluded that strong hydrogen bonding was formed within the hard segments in PDMS-based systems, and that there was negligible interaction between hard segments and siloxane soft segments, which led to a better phase separation. As a result, PDMS-based segmented polyurethanes had higher tensile strengths and tensile modulus values when compared to polyether-based polyurethanes of similar compositions [30, 32].

Luo et al. investigated the effects of thermal annealing on the hydrogen bonding of a poly (urethane urea) copolymer prepared from PPO, MDI, and 3,5-diethyltoluenediamine (DETDA) [29]. The paper suggested that thermal annealing increased free urethane content and ordered urea hydrogen bonds. The urethane hydrogen bonds disassociated during the thermal annealing process, but the disordered urea hydrogen bonds were strong enough that they did not disassociate below 130 °C.

2.4.2 Structure-Morphology Behavior

The structure-morphology behavior of polyurethanes/polyureas has been extensively studied [8, 10, 19-20, 22, 33-35]. Yilgor and et al. have summarized a series of important factors as the following [10, 19]:

1) Hard segments: chemical structure of the diisocyanate and the chain extender; crystallizability and symmetry of diisocyanate;
2) Soft segments: chemical structure, molecular weight, and crystallizability;

3) Competitive hydrogen bonding between hard-hard and hard-soft segments;
4) Inherent miscibility between hard and soft segments;
5) Polymerization procedure used to prepare polyurethanes;
6) The nature of the interfacial region between the soft and hard domains.

2.4.2.1 Effects of hard segments

Isocyanates are the primary components giving rise to the hard segments of polyurethanes/polyureas. The chemistry and structure of isocyanates dictate morphology and resulting properties. Yilgor et al. [19] studied the effects of diisocyanate symmetry on phase morphology. A series of polyurethanes were prepared from different diisocyanates, including MDI, PPDI, bis(4-isocyanatocyclohexyl)methane (HMDI), and trans-1,4-cyclohexyl diisocyanate (CHDI). After a heat treatment at 105 °C, the time-dependent morphological evolution upon cooling was monitored by transmission FTIR scans on thin films. It was found that hard segments prepared from symmetrical PPDI reformed strong hydrogen bonds and well-ordered structure within the first 600 min after room temperature storage. On the other hand, no change in the shape or position of the carbonyl peaks was detected for polyurethanes synthesized from kinked, asymmetric MDI and HMDI, after being stored at room temperature for up to 6 days.

Rath et al. prepared PURs by capping hydroxyl-terminated polybutadiene with isophorone diisocyanate (IPDI) [6]. IPDI contains a primary aliphatic and a less reactive secondary

cycloaliphatic isocyanate group. The primary isocyanate participated mainly in the capping reaction, while the secondary isocyanate principally formed urea linkages during cure. The secondary isocyanate allowed for a slower cure and provided ample time for the formation of more ordered hard segments [6].

2.4.2.2 Effects of soft segments

The phase-separated morphology forms due to the chemical incompatibility between the polar hard segments and non-polar soft segments. Therefore, the relative polarity of the soft segments significantly contributes to this dual-phase morphology. PDMS, as the soft segment, has gained the attention of many researchers due to its extreme incompatibility with the polar hard segments and a very low T_g (-123 to -130 °C) [10, 31, 36-38]. It is well known that symmetrical diisocyanates can improve the packing of hard segments and, as a result, the phase separation. Surprisingly, Yilgor et al. found that the symmetry of the diisocyanate did not influence the phase separation of silicone-urea copolymers [10]. In fact, complete phase separation was achieved even for nonsymmetrical diisocyanate due to the lack of interactions between the non-polar PDMS chains and polar hard segments [30]. While PDMS promotes good phase separation, it was found that PDMS-based polyurethanes and polyureas were limited for high deformation structural applications because of their poor ultimate tensile strength and elongation at break. Cooper et al. proposed that the extreme incompatibility between the hard segments and PDMS leads to reduced "interfacial adhesion" between hard and soft segments, which is responsible for their poor ultimate tensile properties[39]. Sheth et al. incorporated PPO as a co-soft segment with PDMS to improve the inter-segmental interactions (hydrogen bonding), giving

rise to a gradient interphase instead of a sharp one [38]. Distinct improvements in tensile strength and elongation at break were achieved by this approach. Gunatillake et al. showed similar results by incorporating poly (hexamethylene oxide) (PHMO) into PDMS soft segments [40]. The DSC results demonstrated that in cases where poor properties were observed, the corresponding polyurethanes were highly phase separated. The paper postulated that at low levels (~ 20 wt %), the PHMO-derived soft segments were concentrated mainly in the interfacial regions, strengthening the adhesion between hard and soft domains.

Das et al. studied the effects of soft segment molecular weight on the properties of non-chain extended polyureas with PTMO as the soft segment [11]. It was found that increasing PTMO molecular weight increased the formation of soft segment crystallites at low temperatures; this led to an enhanced tensile modulus at low temperatures but a shortened "service window." Petrovic et al. investigated the effects of PPG molecular weight (~1000, 2000, and 3000 g/mole) on the morphology of PPG-based polyurethanes [20]. It was shown that true phase mixing was only found in the PPG 1000 series at low soft segment concentration; no clear indication of phase mixing with PPG 2000- and PPG 3000-based polyurethanes was observed. It was suggested that raising the soft segment molar mass caused greater thermodynamic incompatibility between hard and soft segments [1].

The effects of polyester side chains on phase morphology have been studied using a series of polyurethanes prepared from 4, 4′-MDI and polyesters with varying mole ratios of -CH_3 side

chains[41]. This study revealed that the polyester $-CH_3$ side chain improved the hard segment ordering and phase separation.

2.4.2.3 Effects of Water

Pissis et al. studied the effects of water on polyurethanes prepared from polyethylene adipate, 4,4'-MDI, and BD [42]. The T_g of the soft segment was found to shift to a significantly lower temperature despite the relatively small amounts of water absorbed. A water weight fraction of 0.015 caused a T_g reduction of close to 10 °C. The paper suggested that the shift in T_g was in reasonable agreement with the Couchman-Karasz equation, indicating that polyurethane and water formed a homogeneous mixture, and water acted as a plasticizer. In addition, the paper revealed that the amount of water absorbed increased with the weight fraction of the soft segment.

Broos et al studied the endurance of polyurethane foams under different humidity conditions [43], and found that the amount of absorbed moisture was proportional to the weight fraction of soft segment. Moreover, FTIR spectroscopy pointed out that upon water absorption, the hydrogen-bonding states of the main fraction of carbonyls and N-H groups remained unchanged; only a slight decrease in hydrogen-bonded urea carbonyl was detected. In summary, all evidence led to the author's conclusion that the main carbonyl fraction was inaccessible to water.

Yang et al. reported that an ether-based polyurethane material can absorb about 5 mass percent water after soaking in DI water for 240 hours at room temperature [44]. DSC revealed that the T_g dropped up to 35 °C with the increase in immersion time. This large T_g decrease was because the absorbed water weakened the hydrogen bonding between N-H and C=O groups. Upon heating the samples, the absorbed water was fully removed and the T_g restored to its original value.

Ni et al. suggested that the absorbed moisture into polyurethane foam not only functioned as a plasticizer, but also promoted the formation of hydrogen bonds with the urea hard segments [45]. These hydrogen bonds strengthened the phase connectivity and provided the hard segments with additional resistance under compression [45]. Dounis et al. found that polyurethane foam compressive strain increased with water absorption [46]. The phenomenon was attributed to hydrophilic interactions between water and the hydrogen-bonded hard segments. These interactions were disrupted during testing, resulting in chain slippage and increased strain [46].

2.4.2.4 Effects of wood on morphology of PUR adhesives

2.4.2.4.1 Moisture in wood

In green wood, moisture is located within the cell wall and in the lumen. Water in the cell lumen is in the liquid state, and is referred to as "free" water. Water within the cell wall is called "bound" water; it is tightly held by adsorption to the wood polymers [47]. The moisture content at which the cell wall is saturated while the lumen is free from water is known as the fiber

saturation point (FSP) [47-48]. In other words, if the moisture content is above the FSP, both free water and bound water exist in wood; if the moisture content is below the FSP, water only exists as bound water within the cell wall in equilibrium with the water vapor in the cell lumen. The FSP is of importance in that wood mechanical properties only vary significantly when the moisture content is below FSP, not above it. For example, when moisture content falls below FSP, wood shrinkage occurs, strength increases, and electrical conductivity decreases with a loss of bound water [48].

2.4.2.4.2 Wood polymers

Wood is primarily composed of four biopolymers: cellulose, lignin, glucuronoxylan, and glucomannan (these last two are collectively referred to as hemicelluloses). Table 2-1 presents the major chemical compositions of some common wood species [49].

Cellulose contributes 40-45% to the dry mass of wood. It is composed of linear chains of D-glucose linked by ß-1,4-glycosidic bonds (Figure 2-8) with the degree of polymerization as large as 10,000 [47]. Each D-anhydroglucopyranose unit possesses hydroxyl groups at C2, C3, and C6 positions.

Table 2-1 Chemical compositions of some common wood species [60]

Constituent	**Scots Pine** (*Pinus sylvestris*)	**Spruce** (*Pecea abies*)	**Eucalyptus** *(Eucalyptus globulus)*	**Silver Birch** *(Betula verrucosa*)
Cellulose (%)	40.0	39.5	45.0	41.0
Hemicelluloses				
-Glucomannan (%)	16.0	17.2	3.1	2.3
-Glucuronoxylan (%)	8.9	10.4	14.1	27.5
-Other noncellulosic polysaccharides (%)	3.6	3.0	2.0	2.6
Lignin (%)	27.7	27.5	31.3	22.0
Total extractives (%)	3.5	2.1	2.8	3.0

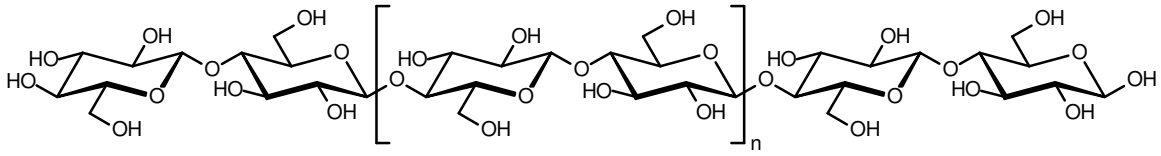

Figure 2-8 The structure of cellulose

Native wood cellulose is highly crystalline, approximately 50% [50]. Plant and animal celluloses are synthesized by a membrane-bound enzymatic complex that "extrudes" so-called "elementary fibrils," which in plants contain 36 parallel cellulose chains [51]. Elementary fibrils in higher plants are approximately 2.5 to 3.5 nanometers thick, roughly square in cross-section, and with a DP of 10,000 would be about 5,000 nanometers long [51-52]. As cellulose elementary fibrils are extruded from the plasma membrane, they associate into larger bundles.

These larger bundles achieve micrometer scale thicknesses and are commonly referred to as microfibrils [51-52]. The wood cell wall contains two layers, known as the primary and secondary layers; and the secondary layer has three sub-layers. Cellulose microfibrils are randomly organized within the primary layer (primary cell wall). Within the bulk of the secondary layer (secondary cell wall), the microfibrils are highly oriented, generally parallel with the plant stem.

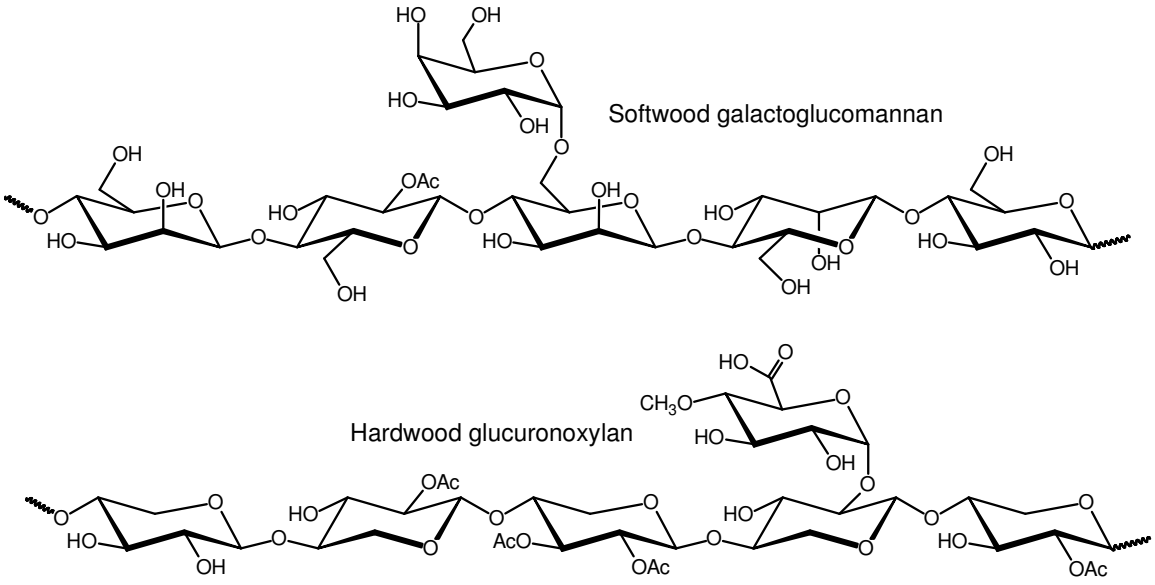

Figure 2-9 Representative chemical structures of hemicelluloses

Unlike cellulose, the hemicelluloses are branched-chain amorphous heterogeneous polymers with a much lower degree of polymerization on the order of hundreds [52-54]. Besides glucose, hemicelluloses are composed of other six-carbon (e.g. D-galactose, D-mannose) and five-carbon sugars (e.g. D-xylose, L-arabinose). The composition and structure of the hemicelluloses differ

between softwoods and hardwoods. The primary hemicelluloses in softwood are galactoglucomannans, while the primary hemicelluloses in hardwood are glucuronoxylans.

Galactoglucomannans: The backbone is built up of 1,4-linked β-D-glucopyranose and β-D-mannopyranose units; the α-D-galactopyranose residue is linked as a single-unit side chain to the backbone by 1,6-glycosidic bonds, shown in Figure 2-9. The C-2 and C-3 positions of mannose units are partially substituted by O-acetyl groups, on the average of one substituent per 3-4 hexose units [49]. Galactoglucomannans can be roughly divided into galactose-rich and galactose-poor fractions. The galactose-rich fraction has a galactose: glucose: mannose ratio of about 1:1:3 whereas the galactose-poor fraction has a corresponding ratio of 0.1:1:4 [49].

Glucuronoxylan: The backbone consists of 1,4-linked β-D-xylopyranose units. The xylose units carry 1,2-linked 4-O-methyl-α-D-glucuronic acid residues, on the average of one uronic acid per ten xylose units, as shown in Figure 2-9 [49]. In addition, xylose units are partially substituted by O-acetyl groups.

Different dynamic behaviors of the xylan and the glucomannan have been reported, indicating that the two hemicelluloses are organized differently in the wood fiber wall [55-56]. It is suggested that, in the fiber wall, xylan is associated with the lignin and glucomannan with the cellulose [55-57]. The cellulose fibrils are coated with a surface layer of glucomannan; xylan and lignin are interspaced between the cellulose aggregates in a 5 to 12 nm wide space, the larger space being in the radial direction of the fiber [56].

Ligin is a complex, high molecular weight polymer built upon the polymerization of three basic phenylpropane structural units, i.e. conifer alcohol, sinapyl alcohol, and *p*-coumaryl alcohol, shown in Figure 2-10. According to their structural elements, wood lignins can mainly be divided into guaiacyl lignin and guaiacyl-syringyl lignin. Guaiacyl lignin is a polymerization product of coniferyl alcohol. Guaiacyl-syringyl lignin is a copolymer of coniferyl and sinapyl alcohols with a ratio varying from 4:1 to 1:2 for the two monomeric units [54]. Guaiacyl lignin is the primary lignin present in softwoods, while the guaiacyl-syringyl lignin is the characteristic lignin in hardwoods [54, 58].

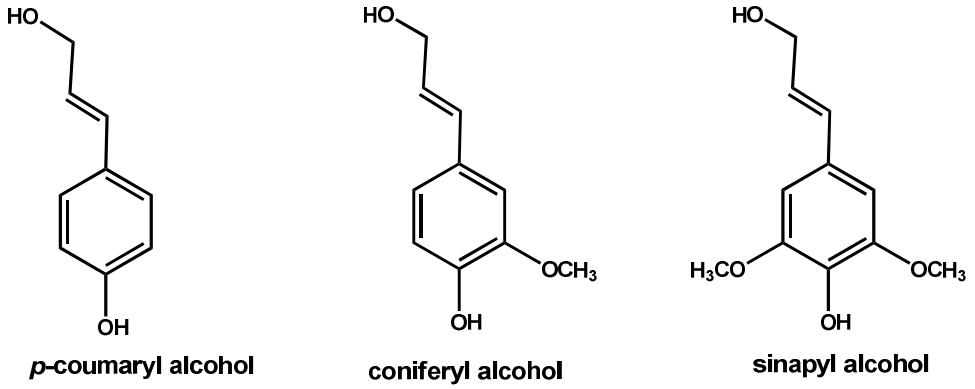

Figure 2-10 Lignin basic precursor phenylpropane units

Native lignin forms a complicated polymer network in which, even in larger sections, a schematic recurrence of combinations could not be detected [52]. As the lignification occurs after the deposition of the polysaccharides, the lignin precursors can only fill voids between the structure elements of the polysaccharides; by the condensation reaction, the polysaccharide elements become embedded in lignin. This very circumstance complicates or even prevents the formation of a schematic structure [52].

The lignin concentration in the middle lamella is much higher than that in the secondary cell wall. However, most lignin is located in the secondary cell wall because of its greater thickness [49]. It has been documented that lignin is not isotropically distributed in the fiber wall; the orientation of the phenyl ring is preferentially in the plane of the cell wall and along the cellulose fibrils [59-60].

Besides the methoxyl end groups from the basic phenylpropane units, lignin contains other terminal functional groups including phenolic hydroxyl, benzyl alcohol, and carbonyl groups, shown in table 2-2 [54].

Table 2-2 Terminal functional groups of lignin (per 100 C_6C_3 Units) [64]

Groups	Softwood lignin	Hardwood lignin
Methoxyl	92-97	139-158
Phenolic hydroxyl	15-30	10-15
Benzyl alcohol	30-40	40-50
Carbonyl	10-15	

2.4.2.4.3 Effects of wood on morphology of PURs

As described previously, it is reasonable to expect that wood moisture and wood/adhesive interactions could significantly affect the morphology and performance of PURs. However, the effects of wood on the in situ PUR properties have never been previously reported. Wood influence on PUR morphology and performance is a major focus of this study.

2.5 Weather Durability of PUR Wood Adhesives

2.5.1 Accelerated weathering procedure

Given that wood is the primary material used for North American residential construction, and that it often exists in adhesively bonded form, the long-term durability of wood-adhesive bonds has immense practical significance. Of course, much attention is devoted to short-term accelerated weathering procedures that simulate long-term weathering exposure. The American Society of Testing and Materials (ASTM) has published a series of standards to evaluate the properties of bonded wood joints and of wood-based composites. Three important standards are listed below, and perhaps most important among these is ASTM2559-04. Commonly referred to as the "delam" test, ASTM D2559 is an extremely rigorous durability test that all structural (exterior grade) wood adhesives must pass.

ASTM D4502 - 92(2004) *Standard Test Method for Heat and Moisture Resistance of Wood-Adhesive Joints*[61]. The purpose of this test method is to estimate the resistance of adhesive-bonded joints to thermal and hydrolytic degradation.

ASTM D3434 - 00(2006) *Standard Test Method for Multiple-Cycle Accelerated Aging Test (Automatic Boil Test) for Exterior Wet Use Wood Adhesives*[62]. The test method as described is for comparing potential long-term durability rather than for use as a quality control procedure. This makes it suitable for research, adhesive evaluation, process evaluation, and product design.

ASTM D2559 - 04 *Standard Specification for Adhesives for Structural Laminated Wood Products for Use Under Exterior (Wet Use) Exposure Conditions* [63]. The standard tests the performance of adhesives for resistance to delamination during accelerated aging exposure to

wetting and drying. This test aids in determining whether the adhesive is suitable for structural wet use or not [63]. The accelerated weathering procedure used in this standard includes the following steps: 1) Samples are soaked in water while exposed to a vacuum of at least 85 kPa for 5 minutes, and then a pressure of 517 +/- 14 kPa is applied for 1 hour. This vacuum-pressure cycle is repeated once. Samples are then dried in an oven at 65.5 +/- 2 °C for a period of 21 to 22 hours. 2) Samples are placed in a pressure vessel and steam is introduced at 100 °C for 1.5 hours, followed by soaking in water at 18 – 27 °C under a pressure of 517 +/- 14 kPa for 40 minutes. Samples are then dried in the oven at the same condition as in step 1. 3) Repeat step 1, resulting in a total test period of 3 days.

ASTM D2559 is an extremely severe delamination test procedure, and it is much harsher than actual environmental conditions. Researchers apply various modifications of this general weathering procedure.

Vacuum-atmospheric pressure water soak (VAS) [64-66]: 1) specimens are subjected to a vacuum while submerged in water for about 30-60 minutes; 2) specimens are soaked for an additional period (1-15 hours) after releasing the vacuum to atmospheric pressure; 3) specimens are dried; 4) repeat the above cycles several times as desired. Finally, the weathered specimens are tested while dry or wet.

Vacuum- pressure water soak (VPS) [65-66]: 1) specimens are subjected to a vacuum while submerged in water for 30 minutes; 2) specimens are soaked for an additional period under pressure (60 psi); 3) specimens are tested while wet.

Accelerated weathering methods determine the relative durability of materials. However, no accelerated weathering test can precisely mimic outdoor exposure, nor can it be expected to predict the exact performance throughout a product's actual service life [67].

2.5.2 Effects of Accelerated Weathering

As described in section 2.5.1, accelerated weathering is often composed of multiple cycles of vacuum/pressure water saturation followed by drying at elevated temperatures. The effects of accelerated weathering procedures or the effects of combined water and heat on polyurethanes have been studied and will be briefly reviewed here.

Vick and Okkonen [65] studied the durability of four commercial PUR adhesives against accelerated weathering procedures. They found that PUR adhesives showed significantly stronger dry shear strength than resorcinol-based ones (although they did not mention viscoelastic effects and that polyurethanes are much more compliant than the highly crosslinked resorcinol-based systems). However, a moderately severe delamination test indicated varying levels of water resistance among the polyurethanes, and a very severe cyclic delamination test (ASTM D2559) caused severe delamination of polyurethane bonds. Uysal and Ozcifci examined the durability behavior of polyurethane wood adhesives after being exposed to different water-resistance tests [68]. Oriental beech, oak, and scotch pine woods were bonded with a commercial polyurethane adhesive. The shear strengths of these samples were tested before and after water-resistance tests. After a severe weathering procedure, oak samples lost as much as

85.6% of their shear strength, while oriental beech and scotch pine samples lost 62.2% and 60.5% of their shear strength, respectively. This paper suggested that the extractive chemicals and high density of oak wood lead to a more severe decrease in bondline strength, and that polyurethane adhesives could not be recommended for the bonding of high-density woods. It was proposed that the poor chemical and physical interactions between wood surface and resin, as well as the dissimilar swelling between the two, were the most important mechanisms of bond failure. Chew and Zhou investigated the resistance of polyurethane sealants against prolonged exposure to water and heat [69]. It was found that the combination of water and heat had an enormous impact on the internal strength of PPG-based commercial polyurethane sealants. Three polyurethane sealants showed a loss of 15-25% of their tensile strength after soaking in 70 °C water for 28 days. The molecular relaxation phenomena during accelerated weathering of a polyurethane coating were carefully studied by Fernando et al.; a polyurethane coating was exposed to a weathering procedure that included a light cycle (55 °C) and a dark cycle (ambient temperature with water spray) [70]. This procedure introduced the effects of ultraviolet radiation, moisture absorption, and temperature variation. The stress relaxation studies showed that the nonexponentiality parameter β (β = 1-n, n is the coupling parameter in Kohlrausch - Williams - Watts equation) decreased with accelerated weathering exposure, which implied an increasingly broad distribution of relaxation times. With the chain scissions increased, the overall stress relaxation proceeded more quickly and a more diverse mixture of molecular chemistry was created that in turn broadened the relaxation time distribution. In addition, the paper disclosed that the molecular weight of cooperatively rearranging regions (CRRs) diminished while the molecular weight between crosslinks (M_c) increased after 8 weeks of weathering exposure. This explains the faster relaxation rate seen in stress relaxation as exposure time continued.

2.5.3 Progress in improving weather durability of PUR

Despite the importance of weather resistance, few articles discussed the structure-weather durability relationships. Vick and Okkonen reported that hydroxymethylated resorcinol (HMR) coupling agent can dramatically improve adhesion and weather performance of PUR wood adhesives [66]. After priming with HMR, performance of the PURs was equivalent to a highly durable RF structural adhesive. Chew and Zhou revealed that the resistance of PUR sealant against prolonged exposure to water and heat was largely enhanced by replacing the commonly used PPG polyol with a more hydrophobic polyether polyol [69].

In an effort to improve the weather durability of PURs, this research aims to investigate the structure-durability relationships and develop novel analytical methods for the quick assessment of PUR durability.

2.6 Analytical Methods

2.6.1 AC-mode (Tapping-mode) Atomic Force Microscopy (AFM)

2.6.1.1 Introduction

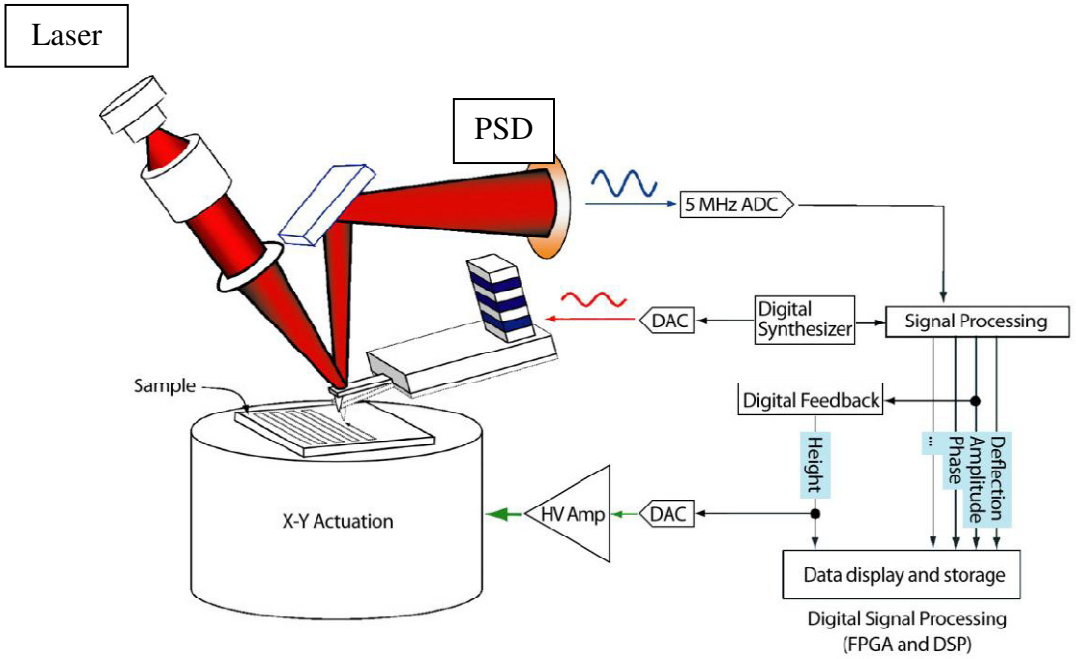

Figure 2-11 Basic Principle of AC mode AFM, adapted from Asylum Research Manual [71]

The basic principle of alternating current (AC) mode AFM is shown in Figure 2-11 [71]. In AC mode AFM, a cantilever is attached to a piezo actuator. The piezo actuator converts the voltage input to oscillatory motion and drives the cantilever to oscillate near or below its fundamental oscillation frequency. When the cantilever gets closer to the sample surface, the amplitude of oscillation normally decreases. In AC mode, the feedback loop always tries to keep a constant vibrating amplitude by adjusting the Z piezo position [71]. Today, most AFMs use a laser beam deflection system to detect the position of the cantilever. A laser beam is reflected from the back of the reflective AFM lever and onto a position-sensitive detector (PSD). The optical signal is then converted to digital signal by the analog to digital converter (ADC). These deflection values are used to measure the topographic variations of samples.

2.6.1.2 Phase imaging

Phase imaging is a powerful extension of AC mode AFM that provides nanometer-scale information about surface structure with no cost in speed or resolution. Phase images are principally constructed based on the phase shifts of the cantilever oscillation relative to the drive sine waves. In general, the response of the cantilever lags the drive. As a result, phase shift is also referred to as phase lag. Based on the fact that the average energy input to the system to maintain the cantilever oscillation must be equal to the average energy dissipated by the cantilever and the tip/sample interactions, a relationship between the phase lag and energy dissipation has been established [72-73].

$$\overline{P_{tip}} = \frac{1}{2}\frac{kA^2\omega_0}{Q}\left[\left(\frac{A_0}{A}\right)\sin\varphi - 1\right] \qquad \text{(Equation 2-1)}$$

In Equation 2-1, $\overline{P_{tip}}$ includes the dissipated energy of the tip/sample interactions; k is the spring constant of the cantilever; Q is the quality factor; ω_0 is the natural resonant frequency of cantilever; φ represents the phase lag angle; A_0 is the free amplitude of the cantilever; and A is the amplitude of the cantilever. When collecting phase images, the cantilever amplitude A is held constant by a feedback loop. Therefore, the phase contrast will be observed only when $\overline{P_{tip}}$ varies. In Equation 2-1, $\sin\varphi$ is proportional to the amount of energy dissipated by the tip.

2.6.1.3 AFM in Polyurethane/Polyurea Research

AFM phase imaging is an important technique to evaluate the viscoelastic properties of polymeric materials, especially for the morphological studies of multi-phase materials, e.g. polyurethanes and polyureas. Some examples are discussed here.

O'Sickey et al. studied the effects of low molecular weight polyol components on the properties of PPG/MD-based polyurethanes using AFM phase images [74]. Tri(propylene glycol) (TPG) was utilized as an artificial low molecular weight homolog to PPG, and was added to ultra-low monol content PPG to generate a series of polyol mixtures with different contents of the low molecular weight component. Although the mass percentage of isocyanate was the same, AFM phase images showed an increase of hard domain materials as the TPG content increased, which suggested that a significant portion of the TPG acted as a chain extending diol instead of soft segment.

Sheth et al. used AFM phase imaging to monitor the time-dependent morphological development in a segmented polyurethane at ambient temperature after cooling from the melt [75]. The AFM phase images clearly showed that a microphase-separated morphology started to form 30 minutes after the heat treatment. The morphology closely resembled the original solution-cast sample 19 hours after the heat treatment.

Song et al. applied AFM phase imaging to examine the change in morphology of polyurethane/clay nanocomposite as a function of clay content [76]. It was found that the size of the hard domain aggregates reduced slightly with the incorporation of clay; the size of clay tactoids grew as the clay content increased.

Das et al. employed AFM phase images to probe the change of urea hard domain connectivity after the addition of varying quantities of a hydrogen-bond screener, LiCl [28]. The breakdown of the urea hard domain connectivity was clearly observed in AFM images as the length of the thread-like hard segments decreased, and a loss in contrast between the hard domains and the soft matrix. Similarly, Sheth et al. used AFM to probe the hard segment phase connectivity in poly(urethane urea) copolymers by incorporating varying extents of hard segment branching [77].

Das et al. imaged the effect of deformation on polyurea morphology using AFM [11]. After the polyurea material was stretched uniaxially beyond its yield point, the hard segments were broken down and shown as distinctly smaller and less defined structures in the AFM phase image. If the deformed material was allowed to relax for 24 hours, randomly oriented thread-like hard segment crystals would be visible in the AFM phase image, similar to the initial material without stretching.

Korley et al. examined the effects of hard segment content on the morphology of polyurethanes using AFM phase images [78]. The phase images showed that the inter-domain spacings were reduced with the increase of hard segment content from 33% to 47%.

Garrett et al. utilized AFM to compare the morphological differences between the surface and bulk of poly(urethane urea) films [79]. The AFM phase images showed that the hard domains on

the surface were in the shape of cylinders, while the hard domains in the bulk were approximately spherical, and were aggregates of much smaller domains.

O'Sickey et al. used AFM phase images to investigate the structure-property relationship of poly(urethane urea)s [80]. The AFM images clearly showed higher amounts of light-colored regions with the increase of hard segment content, and larger spacing between the light-colored regions with the increase of polyol molecular weight.

2.6.2 Fourier Transform Infrared Spectroscopy (FTIR)

2.6.2.1 Introduction

Infrared spectroscopy (IR) is an important technique to identify the presence of certain functional groups in a molecule. It measures the intensity as a function of frequency (wavenumber) of infrared radiation. All molecules experience a wide variety of vibrational motions (e.g. stretching, bending), characteristic of their functional groups. When infrared light interacts with a molecule, the chemical functional groups tend to absorb infrared radiation in a specific wavenumber range that corresponds to their vibrational energies. Therefore, when infrared radiation is passed through a sample, some of the IR radiation is absorbed by the sample, and the rest is transmitted through it. As a result, the IR spectrum serves as a fingerprint of the molecular absorption of the sample.

2.6.2.2 FTIR Instrumentation

The main components of a FTIR instrument are shown in Figure 2-12. The polychromatic IR beam is divided into two optical beams by beam splitter. Approximately half of the light is reflected to the stationary mirror, while the other half goes to a moving mirror. The two beams are then reflected off of their respective mirrors and recombined when they meet back at the beam splitter. The motion of the moving mirror makes the total path length variable, which creates constructive and destructive interference between the two beams. The resulting signal is called an interferogram. When the interferogram passes through the sample, characteristic wavelengths of the interferogram are absorbed by the sample, and the rest reach the detector. Finally, the detected signal is digitized and sent to the computer where the Fourier transformation takes place, giving the final infrared spectrum.

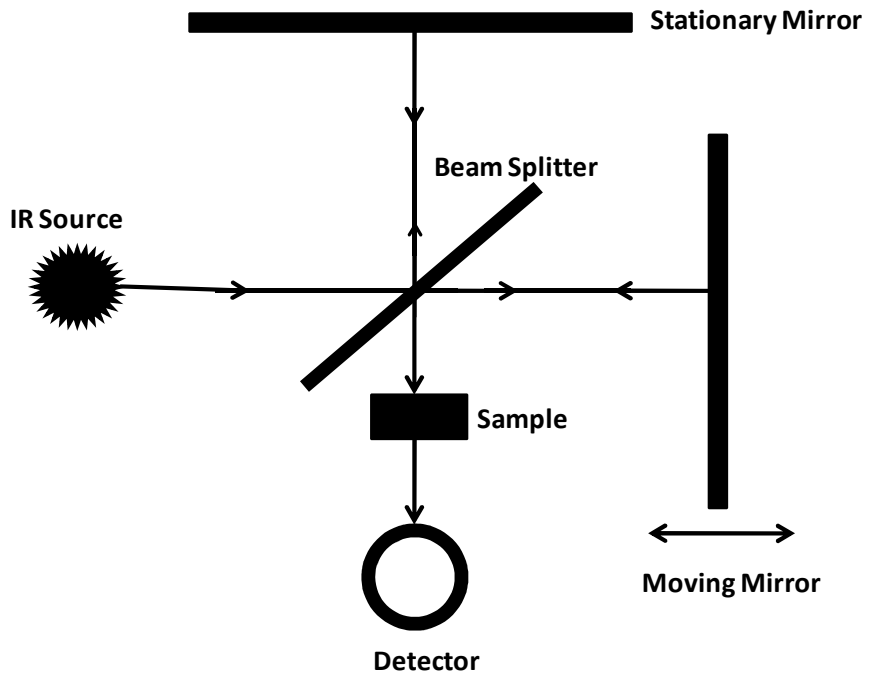

Figure 2-12 FTIR instrumentation

2.6.2.3 FTIR in Polyurethane/Polyurea Research

The shift of the FTIR absorbance for the carbonyl group to a lower frequency is evidence of the formation of hydrogen bonding [23, 27-29, 44, 81-82]. The magnitude of the shift is a measure of the strength of the hydrogen bonding, while the degree of bonding can be estimated by measuring the ratio of infrared band intensity of the bonded groups to that of the free groups [44].

The IR band assignments for polyurethanes are shown in Figure 2-13. For carbonyl groups, one would expect two bands. One is for the "free" and the other is for the hydrogen-bonded carbonyl groups. Hydrogen bonding is a cooperative phenomenon, hence the cooperativity influences the strength of the hydrogen bonds, and consequently the IR absorption frequency [27]. In polymer samples that crystallize, the chains are closer together and the hydrogen bonds are stronger. As a result, the hydrogen-bonded carbonyl band is sharper and observed at a lower frequency than the corresponding band observed in amorphous samples [27]. The bands for amorphous samples are normally referred to as "disordered hydrogen bonds," while bands for samples that have some degree of order or regularity are named "ordered hydrogen bonds" [10, 27, 30]. The same considerations and arguments apply to polyureas, but the IR band frequencies are naturally different from that of urethane. Each urea group has two N-H groups, leading to the formation of bidentate hydrogen bonding. The hydrogen bonds and IR assignments for urea carbonyls are depicted in Figure 2-14. As described previously, cured PURs are poly(urethane urea)s; the infrared stretching band assignments particularly for poly(urethane-urea) carbonyl groups are summarized in Table 2-3.

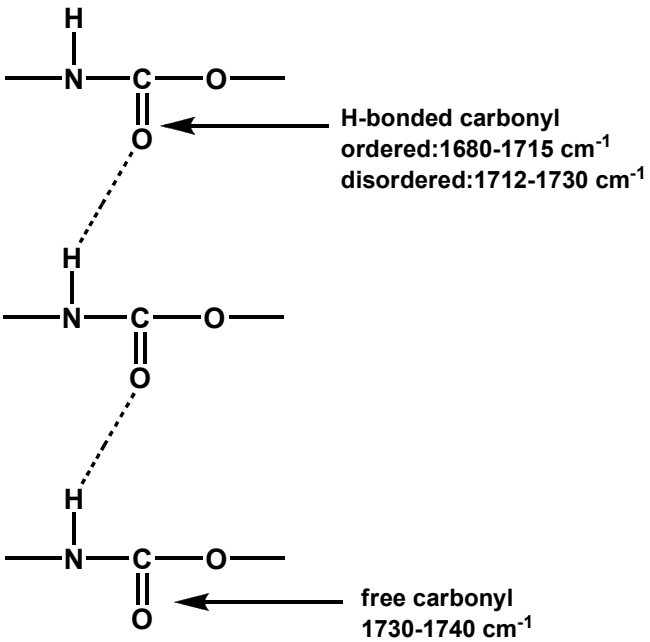

Figure 2-13 IR band assignments for the polyurethane carbonyl group [6, 10, 23, 27, 29, 83]

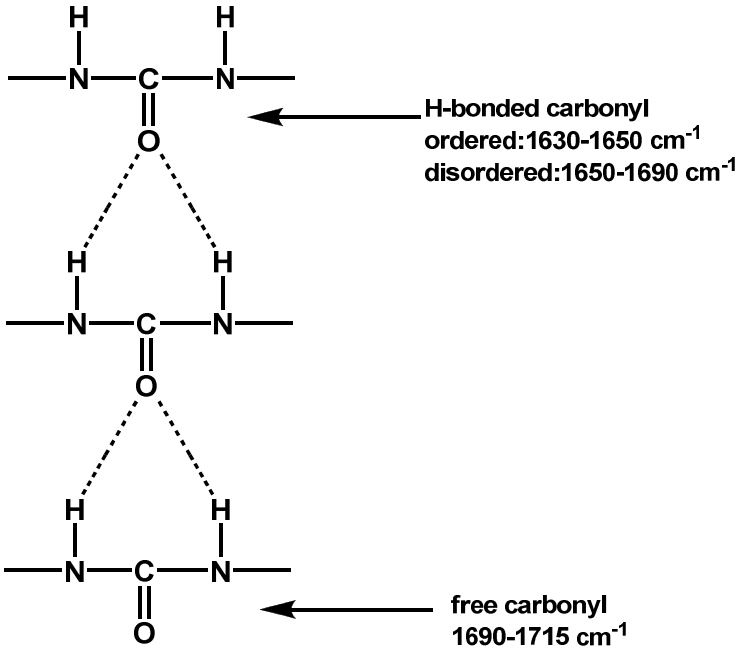

Figure 2-14 IR band assignments for the polyurea carbonyl group [6, 10, 23, 27-29, 83]

Table 2-3 Infrared band assignments of the carbonyl groups in poly(urethane urea)s [6, 29, 83]

Functional Group	Wavenumber (cm-1)	Band Assignment
C=O urethane	1740-1729	Free urethane
	1730-1725	H-bonded urethane (disordered)
	1715-1700	H-bonded urethane (ordered)
C=O urea	1700-1690	Free urea
	1690-1650	H-bonded urea (disordered)
	1650-1628	H-bonded urea (ordered)

2.6.3 Dynamic Mechanical Analysis (DMA)

2.6.3.1 Introduction

DMA is a one of the most common tools in a polymer analytical laboratory. It can be simply described as applying an oscillating force to a sample and analyzing the material's response to that force as a function of time, temperature, and frequency [84]. DMA applies an oscillatory force (or a sinusoidal stress σ) on the sample, and the sample exhibits a sinusoidal strain ε as a response (Figure 2-15). By measuring the deformation of the sample and the phase lag between the stress and strain, properties of polymers (e.g. modulus, viscosity, damping) can be derived. In addition, DMA allows a user to obtain the modulus and damping of a material from each oscillating cycle. This means the modulus and damping can be recorded at every second of the test if the DMA is running at a frequency of 1 Hz (1 cycle per second). This enables the acquisition of material properties at a wide range of temperatures or frequencies within a couple of hours through a temperature or frequency sweep.

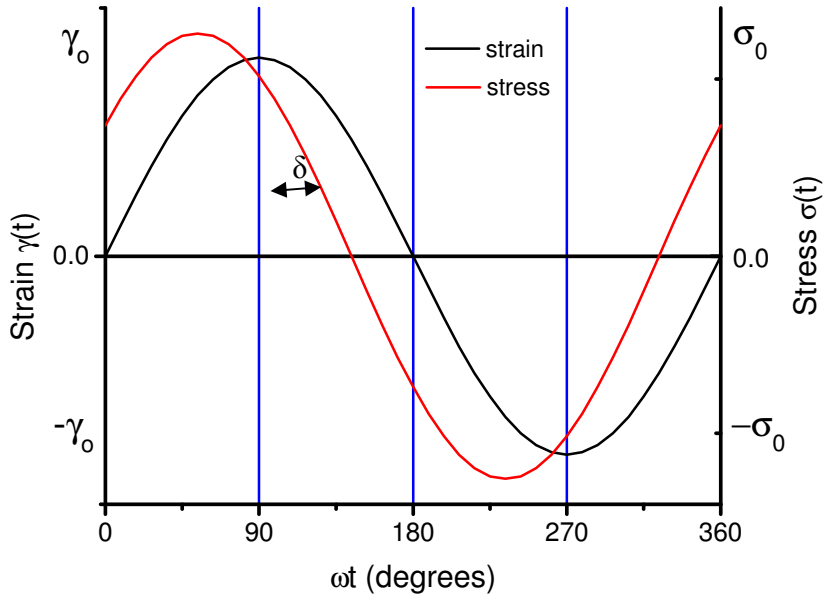

Figure 2-15 Relationship between applied stress, resultant strain, and phase lag in DMA

The applied sinusoidal stress is expressed as:

$$\sigma = \sigma_0 \sin \omega t \qquad \text{(Equation 2-2)}$$

Where σ is the stress at time t; σ_0 is the maximum stress; and ω is the frequency of oscillation. This cyclic stress will result in a sinusoidal deformation of the sample.

$$\varepsilon = \varepsilon_0 \sin(\omega t + \delta) \qquad \text{(Equation 2-3)}$$

The ε in Equation 2-3 represents the strain at time t, ε_0 is the strain at the maximum stress, ω is the frequency of oscillation, and δ is the phase lag. The phase lag between the strain response and the applied stress depends on the nature of the sample. For a perfectly elastic material, there is no phase lag (δ = 0°, in-phase response). In a purely viscous material, the phase lag is 90°

(out-of-phase response). Polymers are viscoelastic materials, therefore the phase lag δ is somewhere between 0° and 90°. Equation 2-3 is rewritten as:

$$\varepsilon(t) = \varepsilon_0[\sin(\omega t)\cos\delta + \cos(\omega t)\sin\delta] \quad \text{(Equation 2-4)}$$

The strain at time t can also be broken down into the in-phase (ε') and out-of-phase (ε'') strains:

$$\varepsilon' = \varepsilon_0 \sin\delta \quad \text{(Equation 2-5)}$$

$$\varepsilon'' = \varepsilon_0 \cos\delta \quad \text{(Equation 2-6)}$$

The sum of these two vectors gives the complex strain:

$$\varepsilon^* = \varepsilon' + i\varepsilon'' \quad \text{(Equation 2-7)}$$

As a result, the measured modulus by DMA is the complex modulus E*, which can be expressed as:

$$E^* = E' + iE'' \quad \text{(Equation 2-8)}$$

Where E' is the storage modulus, which is in-phase with E*; E" is the loss modulus, which is out-of-phase with E*. E' measures the elasticity of the material, and is related to the material's ability to store energy. E" is also called the imaginary modulus, and it measures the ability of the material to dissipate energy. The relationship among E*, E', and E" is shown in Figure 2-16.

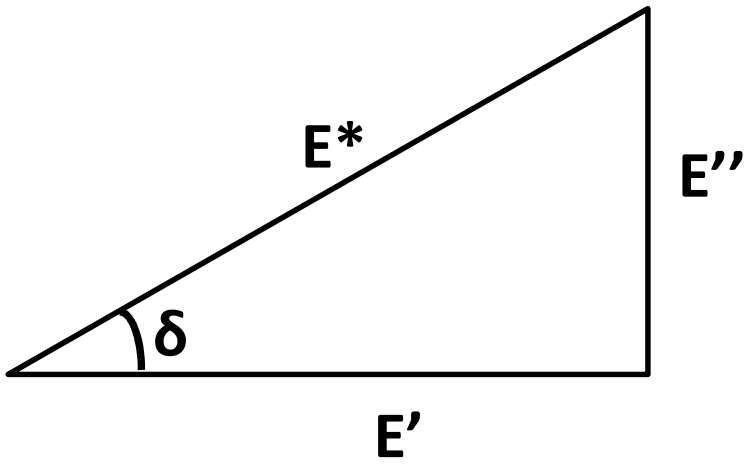

Figure 2-16 The relationship between E*, E′, and E′′

E' and E" are calculated by the following equations in DMA[84]:

$$E' = \left(\frac{f_0}{bk}\right)\cos\delta \qquad \text{(Equation 2-9)}$$

$$E'' = \left(\frac{f_0}{bk}\right)\sin\delta \qquad \text{(Equation 2-10)}$$

In which f_0 is the force applied at the peak of the sine wave; b is the sample geometry term; and k is the sample displacement at peak.

The tangent of the phase angle (tan δ) is called the damping, which is an indicator of how efficiently the material dissipates energy. Mathematically, tan δ is the ratio of E" to E'.

$$tan\delta = E''/E' \qquad \text{(Equation 2-11)}$$

Since it is the ratio of the loss to the storage modulus, tan δ is independent of geometry effects.

2.6.3.2 Applications of DMA

DMA is widely used for thermal analysis of polymeric materials. Compared to differential scanning calorimetry (DSC) and thermomechanical analysis (TMA), DMA is more sensitive, and can easily measure transitions not apparent in other thermal methods [84].

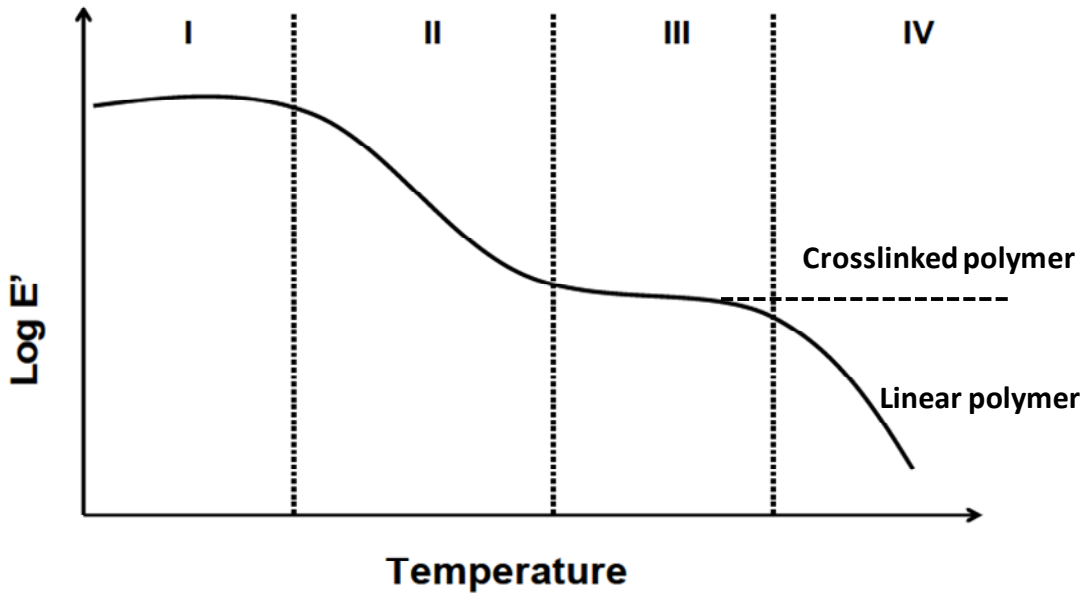

Figure 2-17 A typical modulus-temperature curve in DMA

Figure 2-17 shows the storage modulus as a function of temperature in a typical DMA temperature ramp. Region I is the glassy region. Polymers in this region exhibit a glassy and brittle behavior with high storage modulus on the order of 10^9 Pa. In this region only local motions can occur, such as localized bond movements (bending and stretching) and side chain movements, giving the β, γ, δ…transitions. These transitions are labeled by counting back from the melting temperature, so the glass transition is also named the α transition (T_α).

With a further increase in temperature, the polymer enters region II, the glass transition region. In this region, the free volume increases to the extent that the cooperative movements of large segments start to occur in the amorphous materials. The physical properties of amorphous materials change drastically as the material goes from a hard glassy state to a rubbery state, with a modulus drop of about 3 decades. The glass transition temperature (T_g) is the most important indicator for many polymers, depending on their end use. It is normally recognized as the upper temperature limit if the material is used where strength and stiffness are needed; it is also considered the lowest operating temperature for rubbers. Since the T_g only occurs in amorphous material, we would not see a T_g in a 100% crystalline material. The T_g is a function of molecular architecture, monomer units, presence of impurities or low molecular weight species, and the rate of temperature change. The T_g is very dependent on the degree of polymerization up to a value known as the critical T_g, or the critical molecular weight. Above this value, the T_g typically becomes independent of molecular weight [84]. There are multiple methods to determine the T_g in DMA: 1) the onset of E' drop; 2) the onset of E" peak; 3) the peak value of E"; 4) the onset of tan δ peak; 5) the peak value of tan δ.

Region III is the rubbery plateau, which is the region between the T_g and the melting point. In the rubbery plateau region, elastomers exhibit long-range rubber elasticity, which means they could be stretched perhaps several hundred percent and snap back to their original length upon being released [85-86]. The rubbery behavior in the plateau region is governed by the molecular weight, crosslinks, and entanglements of the polymer chains [85-87]. The modulus of the

plateau is proportional to either the number of crosslinks or the reciprocal of chain length between entanglements [87]. The modulus is often expressed as [87-88]:

$$G' \cong \rho RT/M_e \qquad \text{(Equation 2-12)}$$

In Equation 2-12, G' is the shear modulus; ρ is the polymer density; R is the gas constant; T is temperature; and M_e is the molecular weight between entanglements. In reality, the relative modulus at the plateau region shows the relative change in M_e, or the number of crosslinks compared to a standard material [89]. The plateau modulus is also related to the degree of crystallinity of a material [87].

Finally, when the temperature is further increased, linear polymers and crosslinked polymers behave very differently. For linear polymers, the polymer chains gain enough free volume so that large-scale chain slippage occurs, and the material begins to flow. For a crosslinked polymer, chemical bonds prevent the chains from slipping past one another [84, 90]. Thus, the modulus remains constant until the chemical degradation starts.

2.6.3.3 DMA in Polyurethane/Polyurea Research

DMA has been extensively used to study the structure-property behavior of polyurethanes/polyureas. Some examples are illustrated here.

DMA was utilized to study the effects of diisocyanate symmetry on properties of polyurethanes and polyureas [10, 22]. It was found that polyurethanes/polyureas prepared with unsymmetrical 1,3-phenylene diisocyanate (MPDI) displayed an extremely short rubbery plateau, with a low storage modulus. Polyurethanes/polyureas based on symmetrical PPDI showed a longer rubbery plateau with a higher storage modulus. This DMA behavior suggested that symmetrical PPDI resulted in more ordered hard segments, stronger intermolecular hard segment hydrogen bonding, and better phase-separated morphology.

Das et al. probed the urea hard domain connectivity by studying the effects of hydrogen-bond screening agent LiCl on the modulus of polyurea samples using DMA [28]. Incorporation of LiCl caused a systematic decrease in the rubbery plateau modulus and the breadth of the service temperature window, which was believed to be due to the loss of long-range connectivity between the urea hard domains.

Das et al. conducted DMA tests to investigate the effects of soft segment (PTMO) molecular weight (1k and 2k) on the properties of polyurethanes[11]. They found that 2k-polyurethanes had consistently higher storage modulus values than 1k polyurethanes in the glassy region. The authors believed this was because 2k-PTMO had a greater presence of crystallites. The melting of this partially crystalline PTMO was shown as a shoulder on the tan δ trace of 2k-polyurethane after the T_g peak of PTMO. Korley et al. observed similar results that the soft segment crystallinity enhanced the low-temperature storage modulus while it weakened the soft segment transition tan δ intensity. This suggested that crystalline regions of the soft domain contributed

to the mechanical integrity of the polyurethanes, but also retarded the soft segment molecular mobility [78].

O'Sickey et al. observed the effects of soft segment (PPG) molecular weight on poly(urethane urea)s using DMA[80]. It was found that a decrease in the molecular weight of the soft segment led to an increase of soft segment T_g, and a broadening of the tan δ peak. These DMA results implied greater restriction of the soft segment by the hard domain as soft segment molecular weight decreased.

Sheth et al. employed DMA tests to study the structure-property behavior of PDMS-based polyurea copolymers modified with PPO [38]. First, the plateau modulus was found to increase while the breadth of the plateau decreased with the incorporation of PPO into the PDMS soft segment. This behavior was related to the formation of an inter-segmental hydrogen bond network between the PPO and urea hard segments. The increased degree of phase mixing resulted in a more effective stress transfer from the soft matrix to the hard domains, but also lowered the temperature range over which the hard segments softened. In addition, the tan δ response suggested that the PDMS T_g peak intensity was reduced with the incorporation of PPO. This DMA behavior revealed that the molecular motion of PDMS soft segments was restricted not only by the hard segments, but also by the PPO segments.

Bae et al. studied the effects of the chain extender structures on polyurethanes utilizing DMA[21]. The authors compared the dynamic mechanical behaviors of polyurethanes composed of non-linear chain extenders with those containing linear chain extenders. It was found that the use of a linear chain extender (BD) resulted in a higher plateau modulus but a narrower rubbery plateau breadth (lower hard segment softening temperature) than those of non-linear chain-extended (1,4-pentanediol, 2,5-hexanediol, or 2,5-dimethyl-2,5-hexanediol) polyurethanes. In tan δ responses, non-linear chain extenders resulted in a higher soft segment T_g (30-40 °C higher) than BD chain-extended polyurethanes.

Meanwhile, Chattopadhyay et al. also utilized DMA to study the effects of chain extender on the properties of polyurethanes [91]. It was found that polyurethanes containing diamine or disulfide chain extenders exhibited a higher glassy storage modulus. This result indicated that these polyurethanes had a higher degree of phase separation because the polar sulfide and amine groups promoted more hydrogen bonding within the hard segments.

2.6.4 Mode-I Fracture Test

2.6.4.1 Introduction

Mode-I fracture toughness defines a material's resistance to crack propagation while under tensile forces normal to the crack surface[92]. Mode-I is regarded as more important than the in-plane shear mode (mode-II) and out-of-plane shear mode (mode-III) because the mode-I forces tend to cleave the joint, and the obtained fracture toughness is usually smaller than those of

mode-II and mode-III [93-94]. The crack is therefore more easily initiated and propagated under mode-I loading condition [93-94]. Mode-I fracture of materials is mostly evaluated using the double cantilever beam (DCB) specimen. The DCB specimen is a uniform thickness rectangular specimen with a crack starter at one end (Figure 2-18). The opening load is applied to the upper and lower cantilever via holes at the end of the DCB, shown in Figure 2-18. At critical load, the crack extends and the compliance of the specimen increases. The mode-I fracture toughness can be computed from [92, 95-96]:

$$G_{Ic} = \frac{P_c^2}{2b}\frac{dC}{da}$$

$$G_{Ia} = \frac{P_a^2}{2b}\frac{dC}{da} \qquad \text{(Equation 2-13)}$$

In Equation 2-13, G_{Ic} is the mode-I critical crack initiation energy; G_{Ia} is the crack arrest energy, the energy level at which the crack ceases to grow; P_c is the critical load required to extend the crack; dC/da is the change in compliance (C) with the change in crack length(a); b is the width of the DCB.

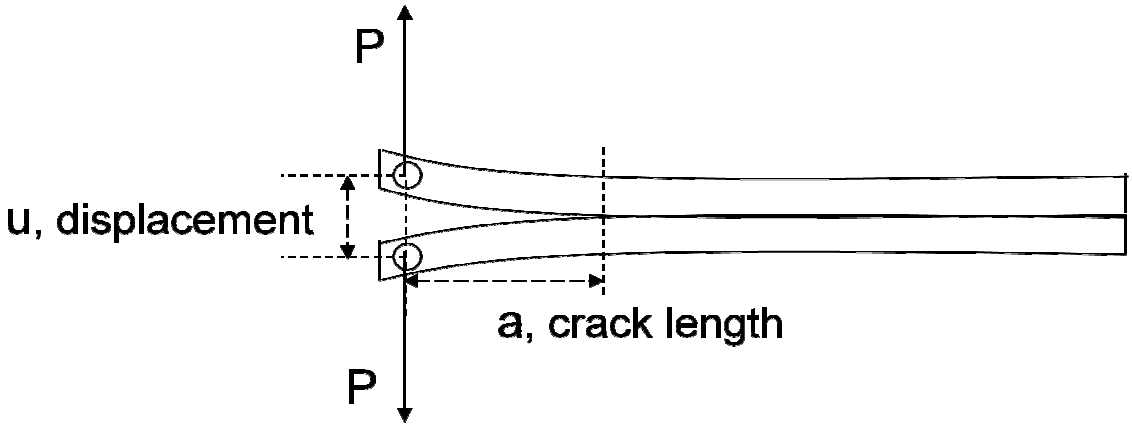

Figure 2-18 Mode-I fracture test and the specimen geometry

The compliance may be expressed using a load-deflection equation of the Euler-Bernoulli beam theory as [97]:

$$C = \frac{2a^3}{3EI} \quad \text{(Equation 2-14)}$$

The E in Equation 2-14 is the flexural modulus of the DCB arms, and the I is the cross-sectional moment of inertia of one of these arms. This equation may be rewritten as:

$$\frac{dC}{da} = \frac{2a^2}{EI} \quad \text{(Equation 2-15)}$$

Combining Equation 2-13 with Equation 2-15:

$$G_{Ic} = \frac{P_c^2}{b}\frac{a^2}{EI}$$

$$G_{Ia} = \frac{P_a^2}{b}\frac{a^2}{EI} \quad \text{(Equation 2-16)}$$

A shear corrected compliance method has been developed to correct the shear effects in adherends with a low shear modulus (e.g. wood) [96]. The shear corrected equation is as follows:

$$G_{Ic} = \frac{P_c^2}{b}\frac{(a+x)^2}{(EI)_{eff}}$$

$$G_{Ia} = \frac{P_a^2}{b}\frac{(a+x)^2}{(EI)_{eff}} \quad \text{(Equation 2-17)}$$

Where $(EI)_{eff}$ is the effective flexural rigidity of the DCB specimen; χ is the shear correction factor, or the crack length offset. $(EI)_{eff}$ and χ are derived from the slope (m) and the y-intercept (b) of the plot of the cube root of compliance versus crack length. An example plot is shown in Figure 2-19, in which m equals 0.2999 and b equals 0.0029.

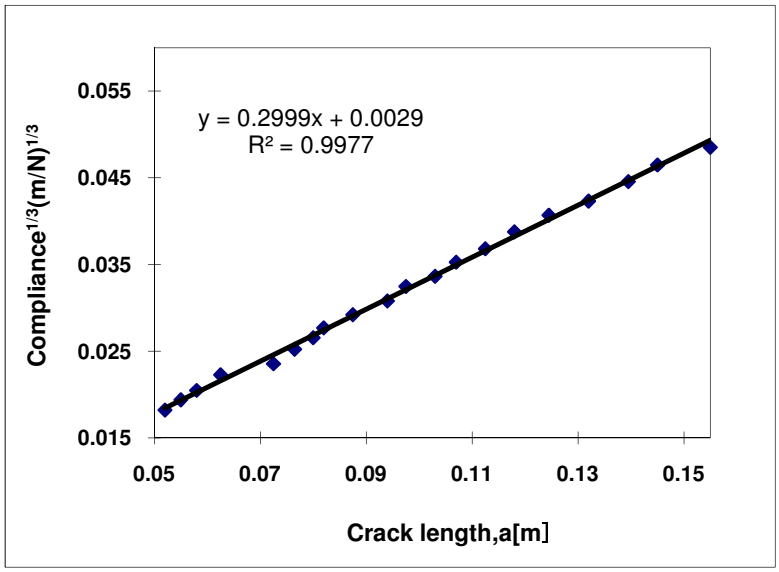

Figure 2-19 An example plot of the cube root of compliance versus crack length

$(EI)_{eff}$ is then computed using the following equation:

$$(EI)_{eff} = \frac{2}{3m^3}$$

The correction factor χ is the distance from the origin to the x-intercept of the line. It can be derived from the slope m and the y-intercept b:

$$x = \frac{b}{m}$$

2.6.4.2 Mode-I Fracture testing of wood-based products

Conventionally, most wood adhesion tests are conducted in shear-mode, similar to the lap-shear test. As such bondline rotation also occurs meaning that wood is stressed not only in shear parallel to grain, but also in tension perpendicular to grain. Shear parallel and tension perpendicular to grain are wood's weakest performance modes, and so it is not surprising that wood failure often dominated shear-mode wood adhesion tests. As a result, shear-mode wood adhesion tests typically obscure subtle aspects of adhesion. On the other hand, the mode-I fracture test was confirmed to be sensitive to intrinsic adhesive and adhesive bondline properties [96]. The fracture test characterizes the energy required for bondline crack propagation. In addition, fracture tests provide an impressive amount of data points. Each fracture specimen (bondline size 200 mm × 20 mm) can produce up to 20 fracture energy measurements, which provide a measure of uniformity along the adhesive bondline [98]. Large numbers of data points also make the statistic analysis more powerful and reliable.

Scientists have successfully utilized the mode-I fracture test to evaluate the bondline performance of wood-based products. In the 1970's and 80's, the fracture test was used to study the effects of different parameters on the performance of wood bonding. Some examples of these parameters are bondline thickness, resin cure time, resin constitution, wood surface roughness, and wood grain angle [96, 99-101]. In these studies, contoured or tapered DCB specimens had to be used to ensure a constant dC/da [96, 98, 102]. The significance of a constant dC/da is that only the fracture or crack initiation load is needed to calculate the fracture energy, and the crack length does not need to be measured at each crack tip position (Equation 2-13) [98]. Nevertheless, preparation of these test specimens is difficult and requires special

efforts for machining. Gagliano and Frazier simplified this method by conducting fracture tests using a simple flat wood DCB shown in Figure 2-18 [96]. However, in the flat DCB specimen, the dC/da is not constant, and the crack length "a" has to be measured at each crack tip position. Fortunately, with the modern digital techniques, this measurement is simple.

Fracture of wood/adhesive joints begins at a geometric or material discontinuity where displacement of the adherend creates the greatest stress concentration, and where either the adherend or the adhesive is the weakest [98]. The discontinuity in the wood/adhesive joint includes the interface between adhesive and wood, transition between earlywood to latewood bands, the grain angle variation, etc. Therefore, there is a strong tendency for the crack to deflect away from the center of the adhesive layer, into the adhesive/wood interphase and even into the wood layer. To avoid crack tip deviation, and to keep the fracture occurring within the adhesive bondline, the laminates were paired in a way that the grain converged to a "V" shape at the bondline, as shown in Figure 2-20 [94, 96, 98, 103].

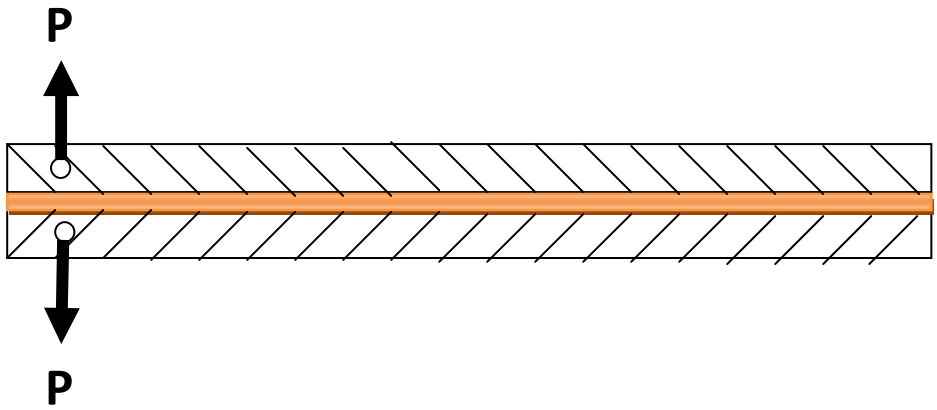

Figure 2-20 "V" shape grain converge in DCB fracture specimen

The combination of this "V"-shaped DCB specimen with the shear correct compliance method was successfully used to test the bonding properties of wood/adhesive joints. By using this combination, Gagliano and Frazier showed that the shear corrected compliance method reduced the variation of calculated fracture energy, and therefore provided more reliable calculations [96]. Scoville demonstrated that the fracture energy is a property of individual wood-based specimens, and is independent of crack length when using the shear corrected compliance method to account for variations in wood modulus [104]. Lopez-Suevos and Frazier used this combination to study the influence of phenolic additives on the weather durability of PVAc latex adhesives [64]. It was found that the system without phenolic additives exhibited great fracture toughness before weathering, but completely failed after weathering. On the other hand, the adhesive system with phenolic additives was found to retain some of its fracture toughness after weathering. These fracture results clearly revealed that phenolic additives could improve the weather resistance of PVAc latex adhesives.

This combination of a simple "V"-shaped DCB specimen with the shear corrected compliance method will be utilized to study the fracture toughness of PUR-bonded wood composite samples in this study.

References

1. Chattopadhyay, D.K. and K.V.S.N. Raju, Structural engineering of polyurethane coatings for high performance applications. Progress in Polymer Science, 2007. 32(3): p. 352-418.
2. Polyurethane History. Available from: http://www.polyurethane.org.
3. Meier-Westhues, U., Polyurethanes-Coatings, Adhesives and Sealants. 2007, Hannover: Vincentz Network.

4. Polyurethane Applications. Available from: http://www.americanchemistry.com.

5. Sebenik, U. and M. Krajnc, Influence of the soft segment length and content on the synthesis and properties of isocyanate-terminated urethane prepolymers. International Journal of Adhesion and Adhesives, 2007. 27(7): p. 527-535.

6. Rath, S.K., A.M. Ishack, U.G. Suryavansi, L. Chandrasekhar, and M. Patri, Phase morphology and surface properties of moisture cured polyurethane-urea (MCPU) coatings: Effect of catalysts. Progress in Organic Coatings, 2008. 62(4): p. 393-399.

7. Richter, K., A. Pizzi, and A. Despres, Thermal stability of structural one-component polyurethane adhesives for wood - Structure-property relationship. Journal of Applied Polymer Science, 2006. 102(6): p. 5698-5707.

8. X. Li, Z.G., J. Gu, F. Zhao, and X. Bai, Synthesis and characterisation of one-part ambient temperature curing polyurethane adhesives for wood bonding. Pigment & Resin Technology, 2004. 33(6): p. 345-351.

9. Frazier, C.E., Isocyanate Wood Binders, in Handbook of Adhesive Technology, K.L.M. A. Pizzi, Editor. 2003, Marcel Dekker: New York. p. 681-694.

10. Yilgor, I. and E. Yilgor, Structure-morphology-property behavior of segmented thermoplastic polyurethanes and polyureas prepared without chain extenders. Polymer Reviews, 2007. 47(4): p. 487-510.

11. Das, S., I. Yilgor, E. Yilgor, B. Inci, O. Tezgel, F.L. Beyer, and G.L. Wilkes, Structure-property relationships and melt rheology of segmented, non-chain extended polyureas: Effect of soft segment molecular weight. Polymer, 2007. 48(1): p. 290-301.

12. Meier-Westhues, U., Polyurethanes: coatings, adhesives and sealants 2007, Hannover: Vincentz Network.

13. Woods, G., The ICI Polyurethanes Book. 1990: ICI Polyurethanes.

14. Lamba, N.M.K., K.A. Woodhouse, and S.L. Cooper, Polyurethanes in Biomedical Applications 1997: CRC Press.

15. Shi, D., Introduction to Biomaterials 2006: Tsinghua University Press.

16. Clemitson, I., Castable Polyurethane Elastomers 2008: CRC Press.

17. Martin-Martinez, M.S.S.-A.a.J.M., Structure, composition, and adhesion properties of thermoplastic polyurethane adhesives. Journal of Adhesion Science and Technology, 2000. 14(8): p. 1035-1055.

18. Chattopadhyay, D.K., B. Sreedhar, and K.V.S.N. Raju, The phase mixing studies on moisture cured polyurethane-ureas during cure. Polymer, 2006. 47(11): p. 3814-3825.

19. Yilgor, I., E. Yilgor, I.G. Guler, T.C. Ward, and G.L. Wilkes, FTIR investigation of the influence of diisocyanate symmetry on the morphology development in model segmented polyurethanes. Polymer, 2006. 47(11): p. 4105-4114.

20. Petrovic, Z.S. and I. Javni, The Effect of Soft-Segment Length and Concentration on Phase-Separation in Segmented Polyurethanes. Journal of Polymer Science Part B-Polymer Physics, 1989. 27(3): p. 545-560.

21. Bae, J.Y., D.J. Chung, and J. H. An, Effects of the structure of chain extenders on the dynamic mechanical behaviour of polyurethane. Journal of Materials Science, 1999. 34: p. 2523-2527.

22. Sheth, J.P., D.B. Klinedinst, G.L. Wilkes, Y. Iskender, and I. Yilgor, Role of chain symmetry and hydrogen bonding in segmented copolymers with monodisperse hard segments. Polymer, 2005. 46(18): p. 7317-7322.

23. Yilgor, E., I. Yilgor, and E. Yurtsever, Hydrogen bonding and polyurethane morphology. I. Quantum mechanical calculations of hydrogen bond energies and vibrational spectroscopy of model compounds. Polymer, 2002. 43(24): p. 6551-6559.

24. Cooper, S.L. and A.V. Tobolsky, Viscoelastic Behavior of Segmented Elastomers. Textile Research Journal, 1966. 36: p. 800-803.

25. Schollenberger, C., Handbook of elastomers. 2001, New York: Marcel Dekker Inc.

26. Sun, H., Ab-Initio Characterizations of Molecular-Structures, Conformation Energies, and Hydrogen-Bonding Properties for Polyurethane Hard Segments. Macromolecules, 1993. 26(22): p. 5924-5936.

27. Mattia, J. and P. Painter, A comparison of hydrogen bonding and order in a polyurethane and poly(urethane-urea) and their blends with poly(ethylene glycol). Macromolecules, 2007. 40(5): p. 1546-1554.

28. Das, S., I. Yilgor, E. Yilgor, and G.L. Wilkes, Probing the urea hard domain connectivity in segmented, non-chain extended polyureas using hydrogen-bond screening agents. Polymer, 2008. 49(1): p. 174-179.

29. Luo, N., D.N. Wang, and S.K. Ying, Hydrogen-bonding properties of segmented polyether poly(urethane urea) copolymer. Macromolecules, 1997. 30(15): p. 4405-4409.

30. Yilgor, E., E. Burgaz, E. Yurtsever, and I. Yilgor, Comparison of hydrogen bonding in polydimethylsiloxane and polyether based urethane and urea copolymers. Polymer, 2000. 41(3): p. 849-857.

31. Yilgor, E. and I. Yilgor, Hydrogen bonding: a critical parameter in designing silicone copolymers. Polymer, 2001. 42(19): p. 7953-7959.

32. Yilgor, E. and I. Yilgor, High molecular weight, high strength silicone-urethane copolymers: preparation and properties Polymer Preprints, 1998. 39(1): p. 465-466.

33. Chen, K.S., T.L. Yu, and Y.H. Tseng, Effect of polyester zigzag structure on the phase segregation of polyester-based polyurethanes. Journal of Polymer Science Part a-Polymer Chemistry, 1999. 37(13): p. 2095-2104.

34. O'Sickey, M.J., B.D. Lawrey, and G.L. Wilkes, Structure-property relationships of poly(urethane-urea)s with mixed soft segments of ultra-low monol content poly(propylene glycol) and tri(propylene glycol). Abstracts of Papers of the American Chemical Society, 2001. 221: p. U345-U345.

35. Unal, S., I. Yilgor, E. Yilgor, J.P. Sheth, G.L. Wilkes, and T.E. Long, A new generation of highly branched polymers: hyperbranched, segmented poly(urethane urea) elastomers. Macromolecules, 2004. 37(19): p. 7081-7084.

36. Yilgor, I., A.K. Shaaban, W.P. Steckle, D. Tyagi, G.L. Wilkes, and J.E. Mcgrath, Segmented Organosiloxane Copolymers .1. Synthesis of Siloxane Urea Copolymers. Polymer, 1984. 25(12): p. 1800-1806.

37. Tyagi, D., I. Yilgor, J.E. Mcgrath, and G.L. Wilkes, Segmented Organosiloxane Copolymers .2. Thermal and Mechanical-Properties of Siloxane Urea Copolymers. Polymer, 1984. 25(12): p. 1807-1816.

38. Sheth, J.P., E. Yilgor, B. Erenturk, H. Ozhalici, I. Yilgor, and G.L. Wilkes, Structure-property behavior of poly(dimethylsiloxane) based segmented polyurea copolymers modified with poly(propylene oxide). Polymer, 2005. 46(19): p. 8185-8193.

39. Li, C., X. Yu, T.A. Speckhard, and S.L. Cooper, Synthesis and Properties of Polycyanoethylmethylsiloxane Polyurea Urethane Elastomers - a Study of Segmental Compatibility. Journal of Polymer Science Part B-Polymer Physics, 1988. 26(2): p. 315-337.

40. Gunatillake, P.A., G.F. Meijs, S.J. McCarthy, and R. Adhikari, Poly(dimethylsiloxane)/poly(hexamethylene oxide) mixed macrodiol based polyurethane elastomers. I. Synthesis and properties. Journal of Applied Polymer Science, 2000. 76(14): p. 2026-2040.

41. Chang, S.L., T.L. Yu, C.C. Huang, W.C. Chen, K. Linliu, and T.L. Lin, Effect of polyester side-chains on the phase segregation of polyurethanes using small-angle X-ray scattering. Polymer, 1998. 39(15): p. 3479-3489.

42. Pissis, P., L. Apekis, C. Christodoulides, M. Niaounakis, A. Kyritsis, and J. Nedbal, Water effects in polyurethane block copolymers. Journal of Polymer Science Part B-Polymer Physics, 1996. 34(9): p. 1529-1539.

43. Broos, R., R.M. Herrington, and F.M. Casati, Endurance of polyurethane automotive seating foams under varying temperature and humidity conditions. Cellular Polymers, 2000. 19(3): p. 169-204.

44. Yang, B., W.M. Huang, C. Li, and L. Li, Effects of moisture on the thermomechanical properties of a polyurethane shape memory polymer. Polymer, 2006. 47(4): p. 1348-1356.

45. Ni, H.F., C.K. Yap, and Y. Jin, Effect of curing moisture on the indentation force deflection of flexible polyurethane foam. Journal of Applied Polymer Science, 2007. 104(3): p. 1679-1682.

46. Dounis, D.V., J.C. Moreland, G.L. Wilkes, D.A. Dillard, and R.B. Turner, The Mechanosorptive Behavior of Flexible Water-Blown Polyurethane Foams. Journal of Applied Polymer Science, 1993. 50(2): p. 293-301.

47. Jim L. Bowyer, R.S., John G. Haygreen, Wood and Water, in Forest Products and Wood Science - An Introduction. 2003, Iowa State Press.

48. The Fiber Saturation Point of Wood. 1944, Forest Products Laboratory: Madison.

49. Sjostrom, E., Wood Chemistry - Fundamentals and Applications. 1993, San Diego: Academic Press.

50. Klemm, D., B. Philipp, Heinze, , H. T., U., , and W. Wagenknecht, Comprehensive cellulose chemistry. Fundamentals and analytical methods. Vol. 1. 1998, Weinhein, Germany: WILEY-VCH.

51. Ding, S.-Y. and M.E. Himmel, The maize primary cell wall microfibril: a new model derived from direct visualization. Journal of Agricultural and Food Chemistry, 2006. 54: p. 597-606.

52. Fengel, D., Ideas on the ultrastructural organization of the cell wall components. Journal of Polymer Science Part c, 1971. 36: p. 383-392.

53. Jim L. Bowyer, R.S., John G. Haygreen, Composition and Structure of Wood Cells, in Forest Products and Wood Science - An Introduction. 2003, Iowa State Press.

54. Sjostrom, E., Wood Chemistry: Fundamentals and Applications. 2nd ed. 1993, San Diego: Academic Press, Inc.

55. Akerholm, M. and L. Salmen, Interactions between wood polymers studied by dynamic FT-IR spectroscopy. Polymer, 2001. 42(3): p. 963-969.

56. Salmen, L. and M. Akerholm, Moisture controlled dynamic FT-IR spectroscopy for characterising the molecular rheology of wood fibers. Cellulose Chemistry and Technology, 2006. 40(1-2): p. 5-11.

57. Salmen, L. and A.M. Olsson, Interaction between hemicelluloses, lignin and cellulose: Structure-property relationships. Journal of Pulp and Paper Science, 1998. 24(3): p. 99-103.

58. Hon, D.N.-S. and N. Shiraishi, Wood and Cellulosic Chemistry. 2ND ed. 2001: Taylor & Francis, Inc.

59. Atalla, R.H. and U.P. Agarwal, Raman Microprobe Evidence for Lignin Orientation in the Cell-Walls of Native Woody Tissue. Science, 1985. 227(4687): p. 636-638.

60. Akerholm, M. and L. Salmen, The oriented structure of lignin and its viscoelastic properties studied by static and dynamic FT-IR spectroscopy. Holzforschung, 2003. 57(5): p. 459-465.

61. ASTM D4502 - 92(2004), Standard Test Method for Heat and Moisture Resistance of Wood-Adhesive Joints. 2004.

62. ASTM D3434-00 (2006), Standard Test Method for Multiple-Cycle Accelerated Aging Test (Automatic Boil Test) for Exterior Wet Use Wood Adhesives. 2006, American Society of Testing and Materials

63. ASTM, ASTM D2559 - 04, Standard Specification for Adhesives for Structural Laminated Wood Products for Use Under Exterior (Wet Use) Exposure Conditions. 2004.

64. Lopez-Suevos, F. and C.E. Frazie, Fracture cleavage analysis of PVAc latex adhesives: influence of phenolic additives. Holzforschung, 2006. 60: p. 313-317.

65. Vick, C.B. and E.A. Okkonen, Strength and durability of one-part polyurethane adhesive bonds to wood. Forest Products Journal, 1998. 48(11-12): p. 71-76.

66. Vick, C.B. and E.A. Okkonen, Durability of one-part polyurethane bonds to wood improved by HMR coupling agent. Forest Products Journal, 2000. 50(10): p. 69-75.

67. Clause Urban, T.M., Shogo Tomari, and Francois Adeleu, Formulating High Weathering Sealants: Possibilities and Challenges. Journal of ASTM International 2007. 4(1): p. 1-8.

68. Uysal, B. and A. Ozcifci, Bond strength and durabilty behavior of polyurethane-based Desmodur-VTKA adhesives used for building materials after being exposed to water-resistance test. Journal of Applied Polymer Science, 2006. 100(5): p. 3943-3947.

69. Chew, M.Y.L. and X. Zhou, Enhanced resistance of polyurethane sealants against cohesive failure under prolonged combination of water and heat. Polymer Testing, 2002. 21(2): p. 187-193.

70. Fernando, B.M.D., X. Shi, and S.G. Croll, Molecular relaxation phenomena during accelerated weathering of a polyurethane coating. Journal of Coatings Technology and Research, 2008. 5(1): p. 1-9.

71. Asylum Research AFM MFP-3D Manual. 2008.

72. Cleveland, J.P., B. Anczykowski, A.E. Schmid, and V.B. Elings, Energy dissipation in tapping-mode atomic force microscopy. Applied Physics Letters, 1998. 72(20): p. 2613-2615.

73. Anczykowski, B., B. Gotsmann, H. Fuchs, J.P. Cleveland, and V.B. Elings, How to measure energy dissipation in dynamic mode atomic force microscopy. Applied Surface Science, 1999. 140(3-4): p. 376-382.

74. O'Sickey, M.J., B.D. Lawrey, and G.L. Wilkes, Structure-property relationships of poly(urethane-urea)s with ultra-low monol content poly(propylene glycol) soft segments. Part II. Influence of low molecular weight polyol components. Polymer, 2002. 43(26): p. 7399-7408.

75. Sheth, J.P., D.B. Klinedinst, T.W. Pechar, G.L. Wilkes, E. Yilgor, and I. Yilgor, Time-dependent morphology development in a segmented polyurethane with monodisperse hard segments based on 1,4-phenylene diisocyanate. Macromolecules, 2005. 38(24): p. 10074-10079.

76. Song, M., H.S. Xia, K.J. Yao, and D.J. Hourston, A study on phase morphology and surface properties of polyurethane/organoclay nanocomposite. European Polymer Journal, 2005. 41(2): p. 259-266.

77. Sheth, J.P., G.L. Wilkes, A.R. Fornof, T.E. Long, and I. Yilgor, Probing the hard segment phase connectivity and percolation in model segmented poly(urethane urea) copolymers. Macromolecules, 2005. 38(13): p. 5681-5685.

78. Korley, L.T.J., B.D. Pate, E.L. Thomas, and P.T. Hammond, Effect of the degree of soft and hard segment ordering on the morphology and mechanical behavior of semicrystalline segmented polyurethanes. Polymer, 2006. 47(9): p. 3073-3082.

79. Garrett, J.T., C.A. Siedlecki, and J. Runt, Microdomain morphology of poly(urethane urea) multiblock copolymers. Macromolecules, 2001. 34(20): p. 7066-7070.

80. O'Sickey, M.J., B.D. Lawrey, and G.L. Wilkes, Structure-property relationships of poly(urethane urea)s with ultra-low monol content poly(propylene glycol) soft segments.

I. Influence of soft segment molecular weight and hard segment content. Journal of Applied Polymer Science, 2002. 84(2): p. 229-243.

81. Yilgor, E., E. Yurtsever, and I. Yilgor, Hydrogen bonding and polyurethane morphology. II. Spectroscopic, thermal and crystallization behavior of polyether blends with 1,3-dimethylurea and a model urethane compound. Polymer, 2002. 43(24): p. 6561-6568.

82. Yilgor, E., B. Metin, M. Gordeslioglu, and I. Yilgor, Studies on understanding the extent of hydrogen bonding between urethane, urea, and polyether segments: Comparison of experimental results and quantum mechanical calculations. Abstracts of Papers of the American Chemical Society, 2000. 219: p. U388-U388.

83. Daniel-da-Silva, A.L., J.C.M. Bordado, and J.M. Martin-Martinez, Moisture curing kinetics of isocyanate ended urethane quasi-prepolymers monitored by IR spectroscopy and DSC. Journal of Applied Polymer Science, 2008. 107: p. 700-709.

84. Menard, K.P., Dynamic mechanical analysis: a practical introduction 2nd ed. 2008, Boca Raton, FL: CRC Press.

85. Sperling, L.H., Introduction to Physical Polymer Science. 2005: Wiley, John & Sons, Incorporated.

86. Lakes, R., Viscoelastic Materials. 2009, New York: Cambridge University Press.

87. Wiley, Characterization and Analysis of Polymers 2008: John Wiley & Sons, Inc.

88. Rubinstein, M. and R.H. Colby, Polymer Physics. 2003, New York: Oxford University Press.

89. Lobo, H. and J.V. Bonilla, Handbook of Plastics Analysis 2003: CRC.

90. Shaw, M.T., Introduction To Polymer Viscoelasticity. 2005: Wiley, John & Sons, Incorporated.

91. DIPAK K. Chattopadhyay, B.S., Kothapalli V. S. N. Raju, Effect of chain extender on phase mixing and coating properties of polyurethane ureas. Ind. Eng. Chem. Res., 2005. 44: p. 1772-1779.

92. Raymond G. Boeman, D.E., Lynn Klett, and Ronny Lomax, A PRACTICAL TEST METHOD FOR MODE I FRACTURE TOUGHNESS OF ADHESIVE JOINTS WITH DISSIMILAR SUBSTRATES, in The Information Bridge: DOE Scientific and Technical Information. 1999.

93. Yoshihara, H. and T. Kawamura, Mode I fracture toughness estimation of wood by DCB test. Composites Part a-Applied Science and Manufacturing, 2006. 37(11): p. 2105-2113.

94. River, B.H., Fracture of adhesive-bonded wood joints, in Handbook of Adhesive Technology, A. Pizzi and K.L. Mittal, Editors. 1994, Marcel Dekker, Inc.: New York.

95. Davalos, J.F., S.S. Kodkani, and I. Ray, Fracture mechanics method for mode-iinterface evaluation of FRP bonded to concrete substrates. Journal of Materials in Civil Engineering, 2006. 18(5): p. 732-742.

96. Gagliano, J.M. and C.E. Frazier, Improvements in the fracture cleavage testing of adhesively-bonded wood. wood and fiber science, 2001. 33(3): p. 377-385.

97. Park, S. and D.A. Dillard, Development of a simple mixed-mode fracture test and the resulting fracture energy envelope for an adhesive bond. International Journal of Fracture, 2007. 148(3): p. 261-271.

98. River, B.H. and E.A. Okkonen, Contoured Wood Double Cantilever Beam Specimen for Adhesive Joint Fracture Tests. Journal of Testing and Evaluation, 1993. 21(1): p. 21-28.

99. Ebewele, R.O., B.H. River, and J.A. Koutsky, Tapered Double Cantilever Beam Fracture Tests of Phenolic-Wood Adhesive Joints .2. Effects of Surface-Roughness, the Nature of Surface-Roughness, and Surface Aging on Joint Fracture Energy. Wood and Fiber, 1980. 12(1): p. 40-65.

100. Ebewele, R., B. River, and J. Koutsky, Tapered Double Cantilever Beam Fracture Tests of Phenolic-Wood Adhesive Joints .1. Development of Specimen Geometry - Effects of Bondline Thickness, Wood Anisotropy and Cure Time on Fracture Energy. Wood and Fiber, 1979. 11(3): p. 197-213.

101. Mijovic, J.S. and J.A. Koutsky, Effect of Wood Grain Angle on Fracture Properties and Fracture Morphology of Wood-Epoxy Joints. Wood Science, 1979. 11(3): p. 164-168.

102. Blackman, B.R.K., H. Hadavinia, A.J. Kinloch, M. Paraschi, and J.G. Williams, The calculation of adhesive fracture energies in mode I: revisiting the tapered double cantilever beam (TDCB) test. Engineering Fracture Mechanics, 2003. 70(2): p. 233-248.

103. Scoville, C.R., Durability in Fracture Testing of Wood Composites - A Literature Review. 2001, Wood-based Composites Center: Blacksburg.

104. Scoville, C.R., Characterizing the Durability of PF and pMDI Adhesives Through Fracture Testing. 2001, Wood-Based Composites Center: Blacksburg.

Chapter 3 Wood/Adhesive Interactions and the Phase Morphology of Moisture-cure Polyurethane Wood Adhesives

Dakai Ren and Charles E. Frazier*

Macromolecules and Interfaces Institute

Wood-Based Composites Center

Department of Wood Science and Forest Products

Virginia Tech, Blacksburg, VA, 24061

* Corresponding author Tel: 540-231-8318 Email: cfrazier@vt.edu

Abstract

The purpose of this research is to determine whether wood/adhesive interactions influence the phase morphology and related properties of moisture-cure polyurethane adhesives (PURs). Two PUR systems were studied: a model (MPUR) prepared from a symmetrical diisocyanate that gave rise to a continuous soft phase, and a commercially relevant adhesive (CPUR) prepared from a less symmetrical polyisocyanate that resulted in a continuous hard phase. Atomic force microscopy revealed that the size and size distributions of the respective dispersed phases were altered by wood, as observed in localized specimen regions. Bulk effects were observed with dynamic mechanical analysis; both soft and hard phase MPUR relaxations were altered by wood (increased transition temperatures), whereas only the continuous CPUR hard phase revealed wood induced changes. Furthermore, infrared analysis showed that wood promoted the formation of hydrogen-bonded urea structures in CPUR bondlines. Significant wood/PUR interactions were detected, however it is difficult to determine whether the effects arise from

direct intermolecular associations, or from indirect effects arising from the mere presence of wood and how this impacts forces acting upon the liquid adhesive. Regardless, it is clear that PUR studies should be conducted under conditions that simulate real wood/PUR bondlines.

Keywords: Moisture-cure polyurethane, phase morphology, wood/adhesive interaction

3.1 Introduction

Moisture-cure polyurethanes (PURs) are isocyanate-terminated prepolymers that are formulated to cure with ambient water. Cured PURs are segmented copolymers (polyurethaneureas) exhibiting microphase-separated morphologies. One phase is derived from a typically flexible (subambient glass transition temperature, T_g) polyol that is generally referred to as the "soft phase." Likewise the corresponding "hard phase" is born from the di- or polyisocyanates that through water reaction produce a highly crosslinked material with softening temperature well above room temperature.

The highly varied properties of polyurethaneureas arise from variations in the dual-phase morphology, and therefore the structure-morphology behavior has been of great interest [1-8]. However, little is known about the phase morphology of PUR wood adhesives, specifically within the actual bondline. Wood effects on PUR morphology have not been specifically investigated. If wood does affect PUR properties, the classic structure-morphology relationships normally studied in neat-films may not be applicable to the wood bondline; these relationships would require investigation from within composite specimens that resemble actual bondlines. There are at least two important wood factors that could impact PUR morphology: 1) wood's

influence on available moisture, and 2) primary and/or secondary intermolecular interactions between wood and PURs.

While other details exist, PUR cure is dominated by the isocyanate reaction with water which releases carbon dioxide and produces an amine that subsequently forms urea-linked hard segments. When the liquid PUR is exposed to air, PUR surface molecules assume conformations only through their own cohesive forces because the adjacent gas phase is non-condensed and non-interactive. Water vapor difuses to the PUR/air interface where reactions produce a polymeric membrane or "skin" that slows moisture diffusion into the uncured bulk. In general, the chemical reactions occur at a much faster rate than moisture diffusion [8]. Thus, PUR cure is a moisture-diffusion dominated process. As isocyanate functionality is consumed, the urea content increases and the dual phase morphology evolves as urea segments associate and then demix (phase-separate) from the soft phase. Consequently, the moisture availablity not only influences the curing kinetics, but also the simutaneous biphasic morphology development. In the wood bondline, moisture delivery is quite different and more complex. The PUR achieves direct wood contact where water diffuses across a lower energy solid/liquid interface. Bondline cure is driven by adsorbed wood moisture, but water vapor is also trapped within the bondline and in nearby wood cell lumens. Consequently bondline cure reflects water diffusion across a solid/liquid interface and to a lesser degree also across a gas/liquid interface. Additionally, bond consolidation typically results in adhesive penetration into the cellular wood structure; the interfacial area increases, and a three dimensional interphase is created over a length scale ranging from hundreds of microns to tens of nanometers. Finaly, the wood moisture content will

play a role in this complex scenario, consistent with Beaud et al. [9] who report that pre-cure wood moisture content significantly impacts PUR performance.

Wood is a complex composite of at least four structural polymers: cellulose, lignin, glucomannan, and xylan. Semicrystalline cellulose fibrils are oriented generally parallel to the tree stem, and are embedded within an amorphous matrix of lignin and xylan. Amorphous glucomannans are believed to encrust the fibril surfaces, perhaps influencing fibril/fibril and fibril/matrix interactions [10-12]. The monomer composition of all non-cellulosic polymers varies by species, and even within species as a function of tissue maturity and growth conditions [13]. All of the wood polymers are hydrophilic, each containing functional groups that promote water adsorption and that could react with isocyanates. For example, cellulose, glucomannan, and lignin contain primary and secondary hydroxyl groups; xylans and lignin may contain carboxylic acid groups; and lignin contains phenolic hydroxyls. Additional complexity is found in the non-structural secondary metabolites that may be removed from wood through solvent extraction; these wood "extractives" are highly varied in structure, ocurrence, and reactivity [13]. Aside from chemical structure, nature's "packaging" of the wood substance varies dramatically by anatomical features and by specfic gravity- this speaks to wood porosity and the potential for micro- and nanometer scale adhesive penetration. In other words, the natural porosity of wood and the polar and reactive nature of the wood components will create secondary and perhaps primary interactions that could alter the kintetics of phase evolution. Naturally, the PUR bondline properties will reflect these wood-induced effects, as will the the greater performance of composite-structures manufactured from PURs. Consequently, this work is a first step towards the elucidation of whether (and perhaps how) wood/PUR interactions influence the PUR morphological structure

and properties. Within this context, wood/PUR interactions are defined not only as direct intermolecular interactions, but also as indirect effects that influence PUR cure because of the micro- and millimeter scale proximity of wood and liquid PUR. Because of the relative complexity of moisture-cure PUR wood adhesives, this work involved two different PUR systems, one which was simplified and perhaps not commercially relevant: linear poly(tetramethylene oxide) chains terminated with 1,4-phenylene diisocyanate. The second system was prepared from polypropylene glycol and polymeric methylenebis(phenylisocyanate); this is more typical of industrial practice and more complex regarding the relative symmetry and multifunctionality of the isocyanate.

3.2 Experimental

3.2.1 Materials

1,4-Phenylene diisocyanate (PPDI, NCO = 52.6%) and polymeric methylenebis(phenylisocyanate) (pMDI, NCO = 31%) were used as received respectively from Aldrich and Huntsman International LLC. Poly(tetramethylene oxide) diol (PTMO) (M_n = 978 g/mol, OH# = 114.7 mg KOH/g, Aldrich) and polypropylene glycol diols (PPG, M_n = 2000, 55.5 mg KOH/g; 400 g/mol, 263.6 mg KOH/g, Fluka Analytical) were dried under vacuum (0.5 mm Hg) at 80 °C overnight immediately prior to use. PTMO was terminated with primary hydroxyls, but the PPG termini were not specified; carbon NMR suggested an equal quantity of primary and secondary hydroxyls. The curing catalyst 4,4′-(oxydi-2,1-ethanediyl)bismorpholine (JEFFCAT® DMDEE, Huntsman International LLC) was used as received. The two-component epoxy resin (Epofix™, Electron Microscopy Science) was used as received. Southern yellow pine (*Pinus*

spp.) flakes (longitudinal × radial × tangential = 15 × 5 × 0.7 mm) and larger planks (longitudinal × tangential × radial = 250 × 150 × 10 mm) were equilibrated in a relative humidity (RH) 65% chamber at room temperature before use.

3.2.2 Synthesis of Model PUR (MPUR) Prepolymer

A 250-mL three-neck flask was oven dried, fixed with an overhead mechanical stirrer, rubber septum, and nitrogen inlet/outlet, and then flamed. PTMO (46.13 g, 0.0945 mol of OH) was transferred into the flask by syringe; PPDI flake (15.15 g, 0.189 mol of NCO) was added to the flask all at once with mechanical stirring; the mixture was heated to 80 °C in an oil bath, and allowed to react under nitrogen for 3 h. Every 30 min, 1-2 ml was sampled and immediately coated onto a KBr disc under nitrogen and tested by Fourier transform infrared spectroscopy (FTIR) in a dry environment. The completion of the reaction was determined when the isocyanate absorption (2270 cm^{-1}) became constant with reaction time. The final NCO content was measured as 6.43±0.05% (theoretical NCO = 6.48%). A cone and plate geometry was used to measure the prepolymer viscosity; the response was Newtonian with viscosity of 12,000 mPa•s over a shear rate range of 0.01 to 100 s^{-1}. The liquid prepolymer was stored under anhydrous N_2 until cure, not longer than 30 days. DMDEE (0.5%, 0.025 g) was mixed with the prepolymer (5 g) immediately prior to the preparation of each film or composite sample.

3.2.3 Synthesis of Commercially-relevant PUR (CPUR) Prepolymer

Following the same procedure described in section 3.2.2, a blend of PPG2000 and PPG400 (mass ratio of PPG2000/PPG400 = 80/20, 0.139 mol of OH) was reacted with pMDI (0.695 mol

of NCO) to provide the CPUR prepolymer. The final NCO content was measured as 13.35±0.04% (theoretical NCO = 13.28%). At 60,000 mPa•s, the viscosity was Newtonian over a shear rate range of 0.01 to 100 s^{-1}. The liquid prepolymer was stored under anhydrous N_2 until cure, not longer than 15 days. DMDEE (0.5%) was mixed with the prepolymer immediately prior to the preparation of film or composite samples.

3. 2.4 Preparation of Cured PUR Films

A polyethylene (PE) sheet was cleaned with acetone and dried under vacuum (0.5 mmHg) at room temperature for 30 min. The MPUR or CPUR prepolymer was cast onto the PE sheet under nitrogen using a film applicator (gap 152 µm, MPUR ~190 g/m^2, CPUR ~230 g/m^2), and then immediately placed into a dessicator that had been pre-conditioned to RH 65% using saturated ammonium nitrate salt. The film samples were allowed to cure at room temperature for two weeks; the resulting film thicknesses were ~150 µm and ~800 µm for MPUR and CPUR, respectively.

3.2.5 Preparation of MPUR/Wood Composite

PUR prepolymer was cast onto a PE sheet as described above. A southern yellow pine flake was then immediately placed on top of PUR with the radial face in contact with the adhesive. This composite sample was pressed (0.03 MPa, 4.3 psi) for 10 min at room conditions; pressure was removed and the composite was placed into a pre-conditioned desiccator (RH 65%) and allowed to cure for two weeks at room temperature. The PUR/Wood composite was obtained by peeling off the PE sheet. Fluorescence microscopy [14] was conducted to obtain a qualitative

assessment of MPUR wood penetration. The average penetration occurred to a depth of approximately 55 µm and the bulk MPUR-layer average thickness was about 100 µm. Consequently, the overall bondline thickness was about 155 µm, where about 35% of this dimension represented penetrated adhesive. In other words, the MPUR neat films and composite bondlines were of similar thickness.

3.2.6 Preparation of CPUR/Wood Composites

Immediately after being planed, the tangential surfaces of two southern yellow pine planks were bonded with the CPUR prepolymer (250 g/m^2). This composite was cured under pressure (0.69 MPa [100 psi], 24 h, room temp.). Subsequently, 20-mm wide dual cantilever beam (DCB) adhesion test specimens were cut from the composite sample and equilibrated (RH 65%, room temperature) for two weeks (DCB adhesion testing is not presented here, but note that debonded DCB specimens were used for infrared analysis, described below). Finally, the DCB bondlines were excised by trimming wood from both sides of the adhesive layer to achieve a thin composite (thickness ~600 µm). According to fluorescence microscopy, the bulk CPUR-layer average thickness was 57 µm with average wood penetration of 125 µm into both sides. Relative to the neat films (thickness ~800 µm), the CPUR bondline thickness was much thinner (300 µm) where about 80% of this dimension represented penetrated adhesive.

3.2.7 Atomic Force Microscopy (AFM)

Small PUR film specimens (14 x 3 mm) were placed in a standard flat rubber mold (dimensions of each depression: 14 x 5 x 3 mm), which was subsequently filled with epoxy resin and allowed

to cure for 2 days. A slice (3 x 5 x 3 mm thick) was removed from the cured resin block and mounted on the ultramicrotome (Powertome-PC, Boeckeler Instruments, Inc.) sample holder such that the PUR cross section was on the cutting surface (3 x 5 mm). A small square of the cutting surface (200 × 200 µm, containing PUR film cross section) was trimmed by removing the excess epoxy using a razor blade. After being equilibrated at -80 °C for 20 min, the trimmed surface was cut by a diamond knife to provide a final smooth surface. Without touching the surface, the length of this slice was further reduced to 0.5 mm. Finally, this cryo-ultramicrotomed sample was bonded to a glass slide. The composite AFM specimens were prepared following the same procedure, cutting on the wood cross-sectional surface. For all AFM specimens, the root-mean-square roughness of the surface was less than 3.5 nm.

Alternating Current (AC) mode AFM imaging of all specimens was performed on an Asylum Research MFP-3D BIO AFM system at ambient conditions. Images were captured at a set-point ratio of 0.7-0.8. AC160TS standard Si cantilever (spring constant of 42 N/m, resonance frequency 300 kHz) was used for imaging MPUR specimens; while AC240TS standard Si cantilever (spring constant of 2 N/m, resonance frequency 70 kHz) was chosen for CPUR specimens. Six representative phase images (two from each specimen) of film or composite specimens were analyzed to quantify hard or soft domain size and size distribution using the Igor Pro version 6.1.0.9 software (WaveMetrics, Portland, OR, U.S.A.).

3.2.8 Dynamic Mechanical Analysis (DMA)

Disk DMA specimens (dia. = 8 mm) were punched from PUR films, PUR/wood composites, and wood flakes. Specimens were vacuum dried (0.5 mmHg, room temperature, 48 h) and then stored over P_2O_5 and dry N_2 prior to analysis.

All DMA tests were conducted on a TA Instruments AR2000 rheometer using 8 mm dia stainless steel parallel-plate geometry. Neat-films (3 stacked discs) or single wood, or CPUR/wood composite specimens were held between the plates under a normal force of 10 N, 30 N and 15N, respectively. In the case of MPUR/wood composite specimens, two specimen disks were placed between the plates (normal force = 10 N) such that the two adhesive layers were in contact with the upper and lower plates. All specimens were equilibrated at -100 °C for 5 min, and then heated to 180 °C (3 °C/min, 1 Hz.); strain levels were all within the linear response (0.06%, 0.03%, and 0.05% for neat-film, pure wood, and composite specimens, respectively). For each sample group, at least three separate observations were used to generate an average DMA response using the "*Average Multiple Curves*" function in OriginPro software version 8.0.63 (OriginLab, Northampton, MA, U.S.A.)

3.2.9 Differential Scanning Calorimetry (DSC)

PPG2000 (2 g) and 60 mesh southern yellow pine wood powder (2 g) were mixed in a 10-mL flask. This PPG/wood mixture and PPG2000 (2 g) were vacuum dried (0.5 mmHg, room temperature, 72 h) and then stored over P_2O_5 and dry N_2 prior to analysis. All tests were conducted on a TA instruments Q100 DSC using hermetic aluminum pans under N_2 flow (50

mL/min). The specimen (~20 mg) was cooled to -90 °C at 5 °C/min. After being equilibrated at -90 °C for 5 min, the specimen was subsequently subjected to a heating scan at 10 °C/min to 50 °C. Separate PPG/wood mixtures and neat PPG2000 specimens were analyzed in this fashion.

3.2.10 Fourier Transform Infrared Spectroscopy (FTIR)

All FTIR spectra were recorded on a MIDAC M2004 spectrometer using an attenuated total reflection accessory (ATR, Durascope^{TM}, SensIR Technologies). A small piece of CPUR film (2×2 mm) was cut through its thickness, and the newly created surface was scanned to provide a bulk specimen response. As described above, CPUR/wood composite specimens were derived from bonded DCB specimens. DCB adhesion testing was conducted in mode-I cleavage (neither described nor reported here) such that the last 50-100 mm of the bondlines remained intact. The partially debonded DCB specimens were transported to the infrared analysis lab, whereafter the DCB specimens were completely debonded through manual cleavage. The freshly exposed failure surfaces were immediately analyzed in reflectance mode; and care was taken to sample the adhesive layer which was visible on the failure surface. Failure surfaces that were all or mostly wood were not sampled, or they were excluded from consideration when the corresponding spectra revealed a wood-dominated signal. All spectra were collected using 128 scans with a resolution of 4 cm^{-1}. Six film spectra (from three specimens) and eighteen composite spectra (from three specimens) were collected and used to generate the average spectra (same method described in Section 3.2.8).

3.3 Results and Discussion

3.3.1 Model Polyurethane System

Figure 3-1 shows the representative AC-mode AFM phase images of MPUR in neat-films and composites (more images are included in Appendix 3-1); white areas correspond to the hard segments, dark areas to soft segments. The theoretical MPUR hard segment content was 24.7% (PPDI mass divided by total liquid adhesive mass). For film specimens, images were collected from the specimen center, well removed from the film surfaces. Regarding the composite specimens, the images were obtained for MPUR that had penetrated the wood cellular structure, within a single wood cell lumen. Since it is in close proximity to the wood, MPUR that has penetrated cell lumens is perhaps not representative of a "bulk bondline" behavior. In the bulk MPUR neat-films (image A), hard segments appear as aggregates of smaller domains, consistent with the observations by Garrett et al [15]. Whereas in the MPUR composite specimens (image B), the hard segments appear larger and more evenly distributed.

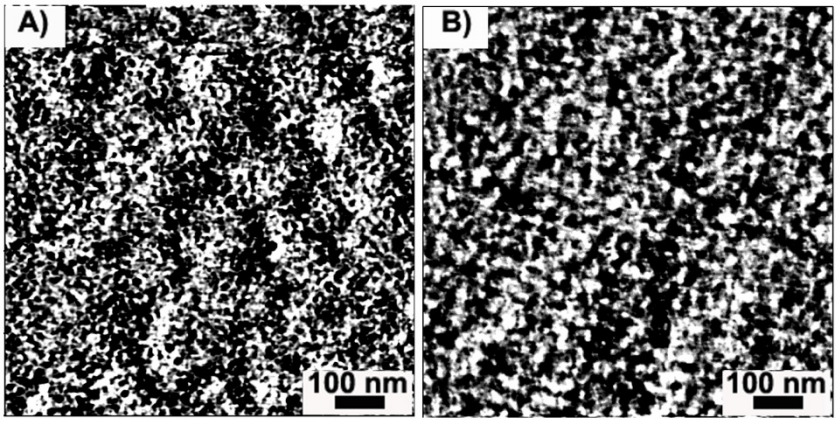

Figure 3-1 Representative AC-mode AFM phase images. A) MPUR bulk neat-film; B) MPUR in composite wood lumen

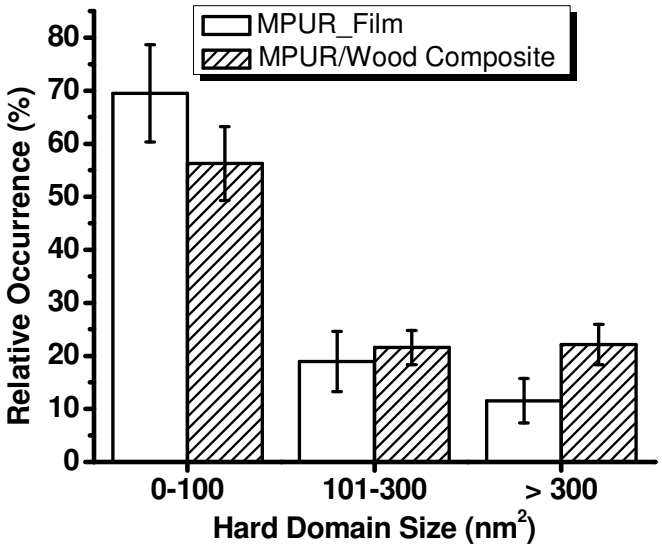

Figure 3-2 Average MPUR hard domain size and size distribution in bulk neat-film and composites; error bars represent ± 1 standard deviation (n = 6 from 3 specimens)

Hard domain size distributions are summarized in Figure 3-2. Compared to neat-films, composite specimens contain a significantly lower fraction of small domains, a similar fraction of intermediate domains, and a higher fraction of large domains. Six representative phase images (obtained from three separate specimens) were utilized to calculate the number average (A_n) and weight average (A_w) domain sizes of each sample group. Consistent with Figure 3-2, the bulk neat-film tends toward lower average domain sizes (A_n = 97.7 nm^2, A_w = 290.1 nm^2), whereas the composite specimens exhibit larger average domain sizes (A_n = 205.9 nm^2, A_w = 816.1 nm^2). These differences suggest that wood-induced effects may have altered the MPUR phase morphology; but keep in mind that the respective imaging loci differed in the relative distance from the moisture source, near the bulk center of the neat film and within the interphase

of the composite. The DMA data discussed below will consider the bulk response of both sample types.

Figure 3-3 shows the DMA first heating scans of MPUR neat-films, composites, and wood. It is seen that neat, dry wood exhibits no significant transitions in this temperature range; whereas the neat-film and composite specimens both exhibit two transitions. Therefore, the composite specimen transitions are attributed to MPUR. Both neat-film and composite specimens behave as glassy solids below -80 °C. The soft segment T_g (tan δ maximum) occurs near -55 °C. When compared to the neat-films, the soft segment T_g is about 5 °C higher in the composite specimens, reflecting a reduced flexibility that likely correlates to a finer scale of phase separation in the composite [16]. The higher soft segment T_g in composite specimens therefore suggests that the bulk MPUR phase morphology has been changed by wood effects. Following the soft segment T_g is a broad rubbery plateau. The slightly higher rubbery modulus of the composites may simply be due to wood reinforcement, and/or strong wood/adhesive interactions increasing the effective crosslinking density. Finally, MPUR neat-film hard segments start to soften near 135 °C; the composite hard segments begin to soften at an average of 5 °C higher.

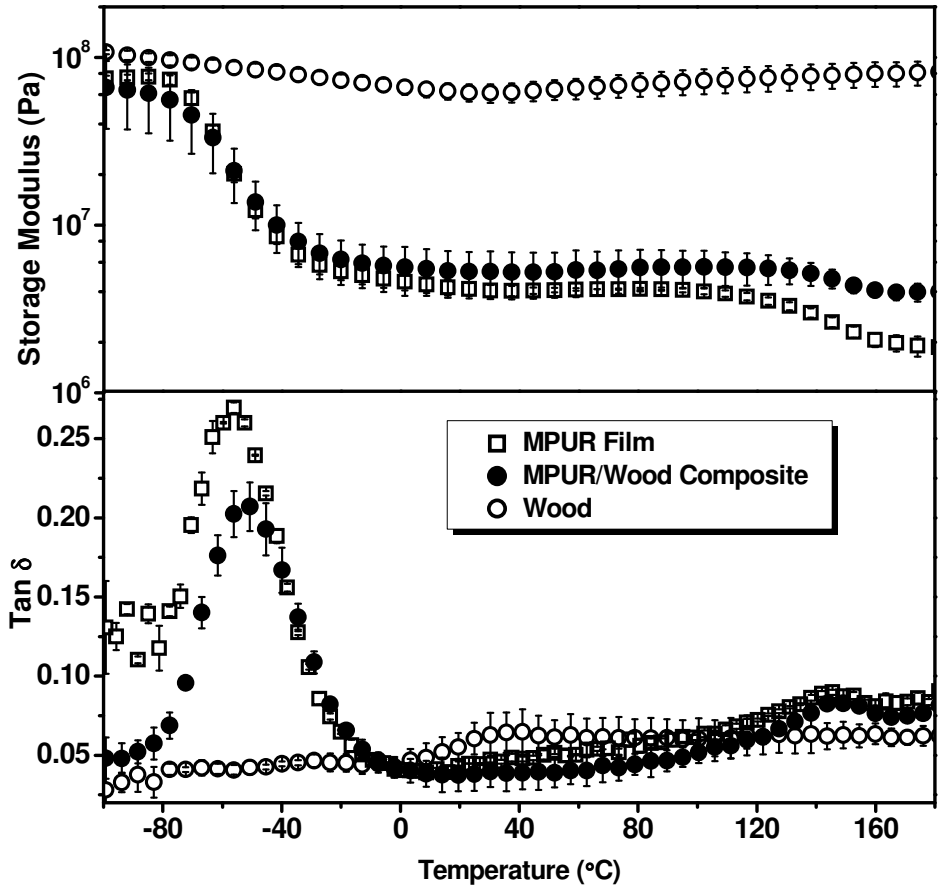

Figure 3-3 Average DMA 1st heating scans of cured MPUR neat-films, composites, and wood flakes (3 °C/min, 1 Hz.); error bars represent ± 1 standard deviation (n = 4)

The DMA response reflects bulk specimen properties; and our experience suggests that PUR relaxation within composite specimens is mostly born from the bulk adhesive layer, not from the interphase region. On the other hand, recall that the MPUR AFM imaging loci were localized, and at different distances from the moisture source. Considered together, the DMA data (bulk response) is consistent with the AFM results (localized); where, as expected, it appears that wood/MPUR interactions have significantly altered the MPUR phase morphology.

3.3.2 Commercially-relevant Polyurethane System

While MPUR was significantly affected by wood, it is practically important to investigate wood/adhesive interactions using a more commercially-relevant system. Unlike the MPUR system, CPUR neat-films and composite bondlines possess much different thicknesses, ~800 µm and ~300 µm, respectively. Cast with a film applicator (152 µm gap), the CPUR neat film thickness expanded by more than 500% due to CO_2 foaming; whereas the CPUR composite was cured while compressed (0.69 MPa, 100 psi) between two cellular substrates. This film/bondline thickness difference is an example of an indirect wood/PUR interaction that is separate from, and perhaps no less significant than, direct intermolecular association.

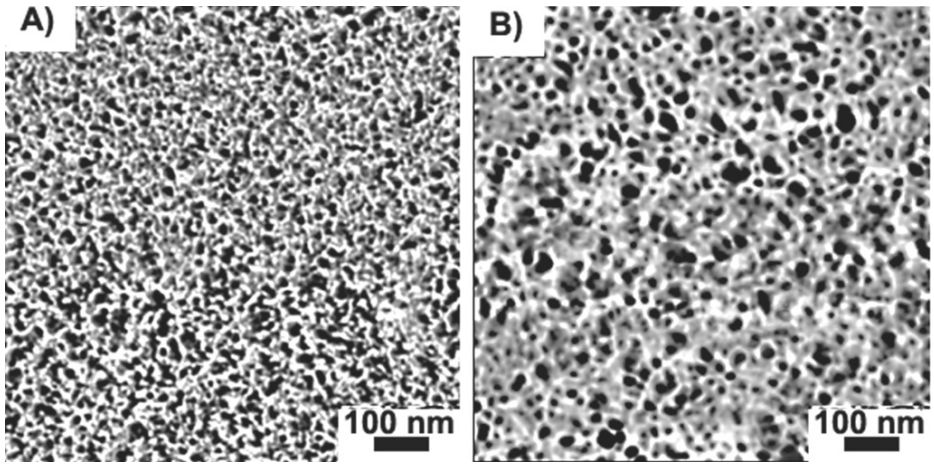

Figure 3-4 Representative AC-mode AFM phase images; A) CPUR bulk neat-film; B) CPUR in composite wood lumen

Figure 3-4 shows the representative AC-mode AFM phase images of CPUR in neat-films and composites (more images are included in Appendix 3-1). These phase images appear dramatically different from those of MPUR because MPUR has a lower hard segment content

(24.7%) which forms the discontinuous phase. CPUR on the contrary contains much higher hard segment (53.5%), resulting in a continuous hard phase (having an average width of 8 nm and 10 nm for neat-film and composite specimens respectively). Whereas the MPUR was examined in terms of the hard phase size distribution, the CPUR AFM images are instead considered through the size and size distribution of the soft phase regions, Figure 3-5. Compared to neat-films, the composite specimens exhibit a different size distribution and greater average domain size (A_n = 287.5 nm^2, A_w = 561.3 nm^2) than is seen in the neat-films (A_n = 191.1 nm^2, A_w = 455.8 nm^2). As before, it seems that wood interactions have impacted the localized phase morphologies observed with AFM. Possible bulk effects are considered by DMA, below.

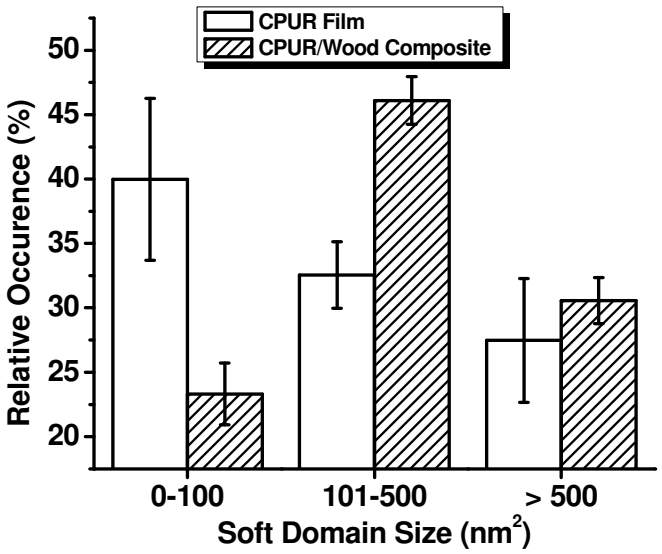

Figure 3-5 Average CPUR soft domain size and size distribution in bulk neat-film and composites; error bars represent ± 1 standard deviation (n = 4 from 2 specimens)

Figure 3-6 shows the DMA first heating scans of CPUR neat-films and composites. First considering the neat-films, the initial storage modulus decline, 0-40 °C, is a continuation of a broad but minor softening starting near -80 °C (not shown). The liquid CPUR soft segment T_g is about -38 °C (DSC, not shown), thus the portion of the softening ranging from about -30 to 40˚C is probably related to the soft segment glass transition. From -30 to 20˚C, the softening is accompanied by very little dissipation because no corresponding tan δ transition is observed. This suggests that the dispersed soft phase chains are highly restricted and perhaps extended to a degree that precludes significant relaxation. Following the initial softening, there is a slight stiffening (40 – 80 °C) which could be related to residual cure, or to reorganization near soft segment boundaries (perhaps the later is more probable considering the low temperature and that the specimen is clamped under a densifying compressive force). Regarding the composite specimens, a similar initial storage modulus decline is also observed, but with much greater variability noted by the error bars. Unlike the neat films, there is a corresponding tan δ transition; but this could be related to a wood-polymer relaxation (refer back to the minor wood relaxation observed in Figure 3-3). Since the neat film DMA indicates that the soft chains are highly restricted by the continuous hard phase, it seems unlikely that a wood/soft phase interaction could be detected, and none is seen in the composite specimens. Furthermore, wood apparently has little affinity for PPG chains; DSC revealed that a 50/50 mixture of pine powder and PPG2000 exhibited a T_g (-68.3 ˚C ±0.3) that was essentially identical to that for neat PPG2000 (-68.1 ˚C ±0.1) Consequently, PUR/wood interactions are likely driven by the hard phase. In both the film and composite specimens, Figure 3-6 shows a storage modulus decline starting near 80 ˚C. This is attributed to hard phase softening that, because of pMDI asymmetry, occurs at a much lower temperature than is observed in the MPUR. Perhaps also because of symmetry

effects, the CPUR hard phase softening exhibits a tan δ transition of much greater intensity than in the MPUR. The CPUR/hard phase tan δ transition is naturally weaker in composite specimens than in neat films. Furthermore, the tan δ maximum temperature is about 10 ˚C higher in the composite specimen, and from 40-170 ˚C, the respective shapes of the tan δ traces are different. Both exhibit a low temperature shoulder, but the relative intensity and temperature are lower in composite specimens. Finally, the breadth of the hard phase tan δ transition might be greater in the composite specimens; but this is uncertain due to the possible wood relaxation occurring near 40 ˚C. As with MPUR, DMA reveals that the bulk CPUR response is significantly altered by wood interactions. While MPUR exhibited wood interactions through the soft and hard phases, the continuity of the CPUR hard phase seems to dominate the soft chain configuration such that no wood/soft phase interactions are noticeable.

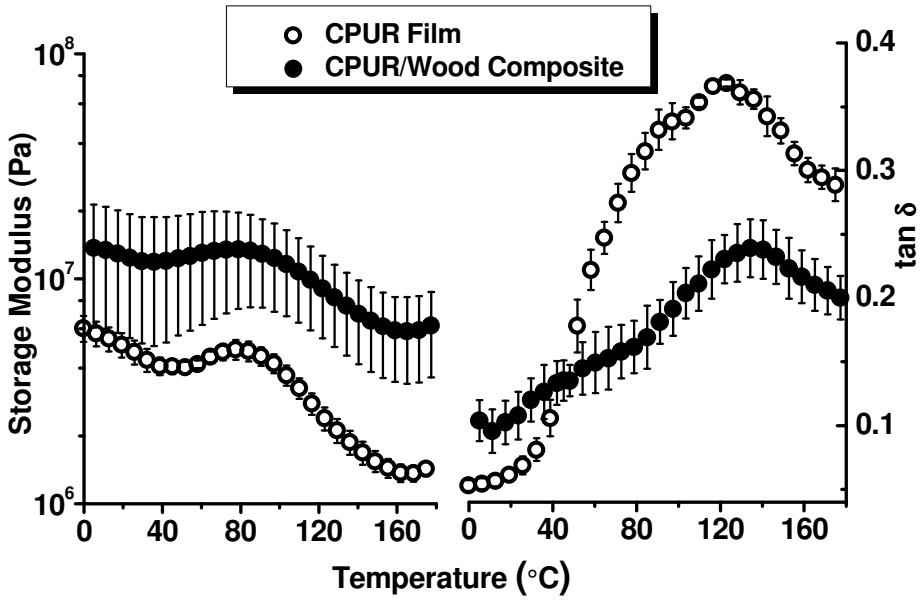

Figure 3-6 Average DMA 1st heating scans of cured CPUR neat-films and composites (3 °C/min, 1 Hz.); error bars represent ± 1 standard deviation (n = 3)

Figure 3-7 shows the carbonyl IR absorbance for CPUR in films and composites. The shift of the carbonyl absorbance to a lower frequency is evidence of hydrogen bond formation; the magnitude of the shift is a measure of the hydrogen bonding strength. Isolated or "free" urethane carbonyl groups exhibit stretching bands at 1729-1740 cm^{-1}, and free urea carbonyls stretch at 1690-1700 cm^{-1} [3, 17-18]. Hydrogen bonding shifts urethane carbonyl stretching to 1700-1715 cm^{-1} (urethane-urethane) and 1725-1730 cm^{-1} (urethane-soft segment ether). Whereas hydrogen bonding shifts urea carbonyls to 1650-1690 cm^{-1} (monodentate H-bonded) and 1628-1650 cm^{-1} (bidentate H-bonded). According to these assignments, significant differences exist between neat-film and composite specimens, Figure 3-7.

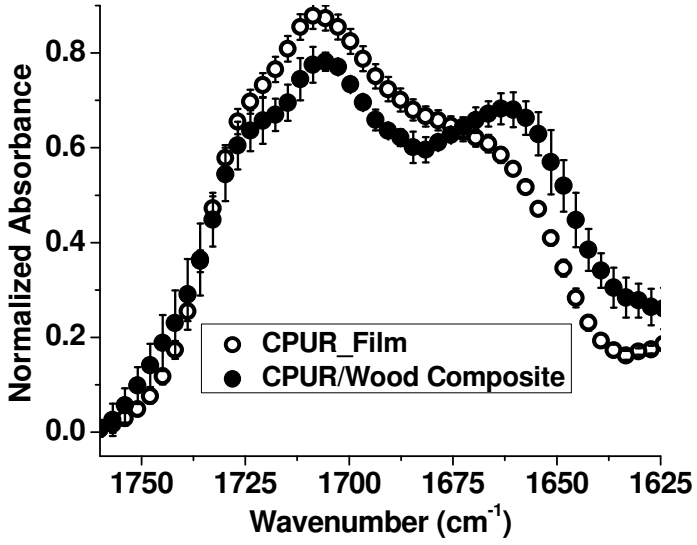

Figure 3-7 Average FTIR spectra of carbonyl region for cured CPUR neat-films (n=6) and composites (n=18); error bars represent ± 1 standard deviation; spectra normalized by the aromatic phenylene signal 1594 cm^{-1} (not shown) with intensities of 1.

For example, there is less urethane-urethane hydrogen bonding (1700-1715 cm^{-1}) and also less free urea (1690-1700 cm^{-1}) in the composite specimens. This difference appears to be balanced by a significantly greater content of hydrogen-bonded urea (1650-1690 cm^{-1}, monodentate; 1628-1650 cm^{-1}, bidentate) in the composite specimens (integrated total carbonyl peak areas were the same within experimental error). Wood/PUR interactions promote the formation of more hydrogen-bonded urea structures, and this is consistent with the higher hard phase softening temperature observed in composite specimen DMA. Finally, the wood induced effects seen with DMA and FTIR are also consistent with AFM observations, where composite specimens exhibited larger soft domains dispersed within the continuous hard phase.

3.4 Conclusions

The effects of direct and indirect wood/adhesive interactions on PUR phase morphology have been investigated employing a model (MPUR) and a commercially-relevant (CPUR) adhesive. The two systems differed in that the MPUR employed a symmetric diisocyanate that gave rise to a soft continuous phase, whereas the CPUR was prepared from a less symmetric polyisocyanate that produced a hard continuous phase. As determined from AFM, the size and size distribution of their respective dispersed phases (hard for MPUR and soft for CPUR) were significantly altered by wood interactions. While these AFM observations were localized to regions having varied distances to the moisture source, average bulk effects were also observed with DMA. For MPUR, DMA revealed that both phases, soft and hard, were affected by wood interactions. Whereas, the continuous CPUR hard phase appeared to restrict soft chain mobility to a degree that prevented the DMA detection of wood/soft phase interactions. Instead, DMA revealed that the CPUR hard phase relaxation was clearly altered by wood; the softening temperature was

significantly increased, and the shape and perhaps the breadth of the relaxation were altered. Additionally infrared analysis revealed that wood induced higher proportions of hydrogen-bonded urea structures in the CPUR. Consequently, it was found that wood altered the CPUR cure chemistry, mechanical relaxation, and the dual-phase morphology in a consistent fashion. While significant wood/PUR interactions have been uncovered, none could be clearly associated with direct intermolecular effects, or with indirect effects caused by the simple presence of wood and how this impacts forces acting upon the liquid adhesive. It is likely that wood/PUR interactions are a complex combination of direct and indirect effects. Regardless, the observations presented here suggest that PUR adhesives should be studied under conditions that simulate a functional wood/PUR bondline.

References

1. Sheth, J.P., G.L. Wilkes, A.R. Fornof, T.E. Long, and I. Yilgor, Probing the hard segment phase connectivity and percolation in model segmented poly(urethane urea) copolymers. Macromolecules, 2005. 38(13): p. 5681-5685.

2. Sheth, J.P., S. Unal, E. Yilgor, I. Yilgor, F.L. Beyer, T.E. Long, and G.L. Wilkes, A comparative study of the structure-property behavior of highly branched segmented poly(urethane urea) copolymers and their linear analogs. Polymer, 2005. 46(23): p. 10180-10190.

3. Rath, S.K., A.M. Ishack, U.G. Suryavansi, L. Chandrasekhar, and M. Patri, Phase morphology and surface properties of moisture cured polyurethane-urea (MCPU) coatings: Effect of catalysts. Progress in Organic Coatings, 2008. 62(4): p. 393-399.

4. O'Sickey, M.J., B.D. Lawrey, and G.L. Wilkes, Structure-property relationships of poly(urethane-urea)s with ultralow monol content poly(propylene glycol) soft segments.

III. Influence of mixed soft segments of ultralow monol poly(propylene glycol), poly(tetramethylene ether glycol), and tri(propylene glycol). Journal of Applied Polymer Science, 2003. 89(13): p. 3520-3529.

5. O'Sickey, M.J., B.D. Lawrey, and G.L. Wilkes, Structure-property relationships of poly(urethane urea)s with ultra-low monol content poly(propylene glycol) soft segments. I. Influence of soft segment molecular weight and hard segment content. Journal of Applied Polymer Science, 2002. 84(2): p. 229-243.

6. O'Sickey, M.J., B.D. Lawrey, and G.L. Wilkes, Structure-property relationships of poly(urethane-urea)s with ultra-low monol content poly(propylene glycol) soft segments. Part II. Influence of low molecular weight polyol components. Polymer, 2002. 43(26): p. 7399-7408.

7. Chattopadhyay, D.K., B. Sreedhar, and K.V.S.N. Raju, Effect of chain extender on phase mixing and coating properties of polyurethane ureas. Ind. Eng. Chem. Res., 2005. 44: p. 1772-1779.

8. Chattopadhyay, D.K., B. Sreedhar, and K.V.S.N. Raju, The phase mixing studies on moisture cured polyurethane-ureas during cure. Polymer, 2006. 47(11): p. 3814-3825.

9. Beaud, F., P. Niemz, and A. Pizzi, Structure-property relationships in one-component polyurethane adhesives for wood: Sensitivity to low moisture content. Journal of Applied Polymer Science, 2006. 101(6): p. 4181-4192.

10. Fengel, D., Ideas on the ultrastructural organization of the cell wall components. Journal of Polymer Science Part c, 1971. 36: p. 383-392.

11. Salmen, L. and A.M. Olsson, Interaction between hemicelluloses, lignin and cellulose: Structure-property relationships. Journal of Pulp and Paper Science, 1998. 24(3): p. 99-103.

12. Akerholm, M. and L. Salmen, Interactions between wood polymers studied by dynamic FT-IR spectroscopy. Polymer, 2001. 42(3): p. 963-969.

13. Sjostrom, E., R. Alen, and E. Sjostrom, Analytical Methods in Wood Chemistry, Pulping and Papermaking 1999, New York: Springer Berlin Heidelberg.

14. Sernek, M., J. Resnik, and F.A. Kamke, Penetration of liquid urea-formaldehyde adhesive into beech wood. Wood and Fiber Science, 1999. 31(1): p. 41-48.

15. Garrett, J.T., C.A. Siedlecki, and J. Runt, Microdomain morphology of poly(urethane urea) multiblock copolymers. Macromolecules, 2001. 34(20): p. 7066-7070.

16. Lamba, N.M.K., K.A. Woodhouse, and S.L. Cooper, Polyurethanes in Biomedical Applications. 1997: CRC Press.

17. Luo, N., D.N. Wang, and S.K. Ying, Hydrogen-bonding properties of segmented polyether poly(urethane urea) copolymer. Macromolecules, 1997. 30(15): p. 4405-4409.

18. Daniel-da-Silva, A.L., J.C.M. Bordado, and J.M. Martin-Martinez, Moisture curing kinetics of isocyanate ended urethane quasi-prepolymers monitored by IR spectroscopy and DSC. Journal of Applied Polymer Science, 2008. 107: p. 700-709.

Chapter 4 Structure-Property Behavior of Moisture-Cure Polyurethane Wood Adhesives: Influence of Hard Segment Content

Dakai Ren and Charles E. Frazier*

Macromolecules and Interfaces Institute

Wood-Based Composites Center

Department of Wood Science and Forest Products

Virginia Tech, Blacksburg, VA, 24061

* Corresponding author Tel: 540-231-8318 Email: cfrazier@vt.edu

Abstract

The primary objective of this research is to investigate how the properties of moisture-cure polyurethane (PUR) wood adhesives are affected by compositional variation. Three PUR adhesives were prepared from polymeric methylenebis(phenylisocyanate) and also poly(propylene glycol) (PPG) such that the PPG component was a variable mixture of two different chain lengths (Mn = 2000 or 400 g/mole). Since the NCO/OH ratio was fixed (5.0), the percentage hard phase increased as the soft segment composition favored shorter PPG chains. Liquid PUR properties were a strong function of the hard phase content; with increasing percentage hard phase, the liquid viscosity increased, the soft phase T_g increased, and the average molecular weight decreased. When cured as neat films, greater hard phase content was related to higher hard phase softening temperatures, and to greater quantities of hydrogen-bonded urea structures. When bonded to form wooden dual cantilever beams, adhesive penetration and bondline thickness varied, but not in a fashion simply related to liquid PUR viscosity. Similarly, mode-I fracture toughness did not sensibly relate to adhesive penetration

and bondline thickness. Toughness was highest at the lowest percentage hard phase, and this was correlated to greater mechanical damping in the -50 to 45 ˚C temperature range, perhaps facilitated by the greater proportion of PPG2000 chains.

Keywords: Moisture-cure polyurethane, wood adhesion, structure-property behavior, hard segment content

4.1 Introduction

Polyurethanes are segmented copolymers containing alternating soft and hard segments. The soft segments may be chosen from a wide variety of polyols, including polyethers, polyesters, and polycarbonates. Likewise, the hard segments may be derived from aliphatic, cycloalphatic, or aromatic isocyanates with the posible inclusion of numerous diol or diamine chain extenders. Polyurethane chemistry is therefore extremely versatile because a wide variety of properties may be tailored for many applications.

Moisture-cure polyurethanes (PURs) are NCO-terminated prepolymers that are widely used in adhesive, sealant, coating, and foam industries. PURs are formulated through reaction of a stoichiometric excess of a poly- or diisocyanate with a polyol. They cure in the presence of moisture, generating urea linkages with evolution of carbon dioxide. As isocyanate functionality is consumed, a dual phase morphology evolves because urea segments associate into inflexible, hard domains that phase separate from the softer domains that arise from the typically flexible polyol.

Many factors influencing PUR properties have been systematically studied. These include chemical structure [1-4], molecular weight [2, 5] and hard/soft phase ratio[2, 5-6], chain extender [1, 4, 7], catalyst [8], solvent [2], and curing conditions [9-10]. However, few articles have been devoted to the structure-property behavior of PUR wood adhesives, specifically within the actual bondline. Moreover, wood/PUR bondline performance is commonly evaluated by strength-based tests conducted in shear mode [2, 5, 11]. Such tests often impose a complex mixture of shear and tensile forces that respectively act parallel and perpendicular to the wood grain. Since wood is weakest in these two stress modes, wood failure is often easily achieved and subtle aspects of wood adhesion are obscured. An alternative (and often more sensitive) wood adhesion test is conducted in mode-I (cleavage) fracture, as described in Gagliano and Frazier [12]. This test avoids bulk wood failure, and is therefore more sensitive to bondline (adhesive and adhesive interphase) performance.

This chapter involves the structure/property analysis of three moisture-cure PUR wood adhesives. Considered are the properties of the liquid prepolymers, the properties of the cured PURs (neat films and PUR/wood composite specimens), and also the dry (unweathered) adhesion to wood as determined through mode-I fracture. The PUR adhesives were prepared from polymeric methylenebis(phenylisocyanate) and also poly(propylene glycol) (PPG) such that the PPG component was a variable mixture of two distinctly different chain lengths. Consequently, as the soft segment composition was changed, so did the hard and soft segment mass ratios simultaneously change. Note that this work follows that of Šebenik and Crank [5] who conducted a similar study that employed strength-based performance evaluation in shear mode.

4.2. Experimental

4.2.1 Materials

Polymeric methylene(bisphenylisocyanate) (pMDI, NCO = 31%, Huntsman International LLC) was used as received. Polypropylene glycol diols (PPG, M_n = 2000, OH# = 55.5 mg KOH/g; 400 g/mol, 263.6 mg KOH/g, Fluka Analytical) were dried under vacuum (0.5 mm Hg) at 80 °C overnight immediately prior to use. PPG termini were not specified; carbon NMR suggested an equal quantity of primary and secondary hydroxyls. The curing catalyst 4,4′-(Oxydi-2,1-ethanediyl)bismorpholine (JEFFCAT® DMDEE, Huntsman International LLC) was used as received. Southern yellow pine planks (longitudinal × tangential × radial = 250 × 150 × 10 mm) were equilibrated in a relative humidity (RH) 65% chamber at room temperature before use.

4.2.2 Synthesis of PUR Prepolymers

The PUR prepolymers were prepared by reacting a mixture of PPG400 and PPG2000 with pMDI; prepolymer compositions are shown in Table 4-1. A 250-mL three-neck flask was oven dried, fixed with an overhead mechanical stirrer, rubber septum, and nitrogen inlet/outlet, and then flamed. The PPG mixture was introduced into the flask followed by pMDI (NCO/OH = 5) using syringe transfer. This mixture was allowed to react under nitrogen for 3 h at 80 °C. Every 30 min, 1-2 ml was sampled and immediately coated onto a KBr disc under nitrogen and tested by Fourier transform infrared spectroscopy in a dry environment. The completion of the reaction was determined when the isocyanate absorption (2270 cm^{-1}) became constant with reaction time. The ^{13}C-NMR prepolymer spectra were collected on a Varian NMR 400 MHz spectrometer

using $CDCl_3$ solvent; the formation of urethane linkage (δ = 153 ppm) was clearly observed (Appendix 4-1). The final NCO contents in these prepolymers were determined using ASTM standard D5155-07, method C [13]; the values shown in Table 1 are the average of three separate measurements. The hard segment content (Table 4-1) was calculated as the mass of pMDI divided by the total liquid adhesive mass. The liquid prepolymers were stored under anhydrous N_2 over P_2O_5 until cure, not longer than 15 days. The cure catalyst DMDEE (0.5%) was mechanically mixed with the prepolymer under N_2 immediately prior to the preparation of film or composite samples.

Table 4-1 The composition and characteristics of PUR prepolymers

PUR Prepolymer	PPG2000/PPG400 mass ratio	Hard segment content (%)	Theoretical NCO (%)	Measured NCO (%)
PU8020	80/20	53.5	13.28	13.35 ± 0.04
PU5050	50/50	65.4	16.23	16.10 ± 0.02
PU2080	20/80	72.5	17.97	17.85 ± 0.09

4.2.3 Characterization of PUR Prepolymers

The number average (Mn) and weight average (Mw) molecular weights of PUR prepolymers were determined using a gel permeation chromatography system (GPC, TDA 302, Viscotek) with tetrahydrofuran (THF, containing 0.025% butylated hydroxytoluene inhibitor) as the mobile phase. Separation was achieved using Waters HR1 and HR3 columns connected in series, and the signal was detected by an inline refractive index detector (RI) and a differential viscometer. A universal column calibration curve was established using polystyrene standards. Prior to the measurement, the prepolymers (50 mg) were converted to their corresponding urea derivatives by reacting with excess diethylamine (1 mL) in anhydrous chloroform at room temperature for

30 min. Chloroform and the residual diethylamine were removed using a rotary evaporator under reduced pressure (5 mmHg, 35 °C). The resulting urea derivatives were dissolved in THF (~ 2 mg/mL) and tested at a flow rate of 1 mL/min at 30 °C.

The prepolymer viscosity was measured using a 25 mm dia disposable parallel-plate geometry (gap = 400 μm) on a TA Instruments AR1000 rheometer. All tests were conducted under anhydrous N2. Steady-state flow curves were measured over a shear rate range of 1 to 1000 s-1.

Prepolymer thermal properties were characterized with a differential scanning calorimeter (DSC). All tests were conducted using a TA instruments Q100 DSC with hermetic aluminum pans under N2 flow (50 mL/min). The specimen (~20 mg) was equilibrated (-90 °C, 5 min), and subsequently heated (10 °C/min) to 20 °C.

4.2.4 Preparation of PUR/Wood Composites and Mode-I Fracture Test

Approximately flat sawn southern yellow pine planks were prepared such that a ~3-5° angle was achieved between the tangential bonding surface and the longitudinal axis (Gagliano and Frazier [12]). The planks were equilibrated in a RH 65% environment at room temperature, and the tangential (bonding) surfaces were planed immediately prior to use. A PUR prepolymer (250 g/m^2) was applied onto the surface of one plank, and then immediately bonded with another, as per Gagliano and Frazier [12]; Appendix 4-2 is a simplified pictorial illustration of the assembled composite. The bonded composite samples were cured under a pressure of 0.69 MPa (100 psi) for 24 h at room temperature. Subsequently, five double cantilever beams (DCBs, 20-mm wide)

were ripped from each composite specimen and equilibrated (RH 65%, room temp., two weeks). For each adhesive, two separate PUR batches were synthesized to prepare 40 DCBs (20 from each batch). For each adhesive, the two separate batches provided the same fracture performance (Appendix 4-3); therefore, DCB specimens within an adhesive grouping were combined and six DCBs were randomly selected for mode-I fracture testing.

A cyclic mode-I fracture testing method was employed to obtain the crack initiation (G_c) and arrest (G_a) energies of the DCB specimens. All tests were conducted on a screw-driven MTS Systems (Model GL-10) in displacement control mode, using the TestWorks 4 software for data acquisition and system control. Prior to testing, a 10 N pre-load was applied, whereupon the displacement was zeroed. Fracture testing was conducted in a fashion similar to that described by Gagliano and Frazier [12]. Cleavage loading was started; once the load/displacement curve became nonlinear, the test frame crosshead displacement was halted for a 45 second arrest period; thereafter the crosshead was returned to the origin, and the process was repeated in cyclic fashion. The displacement rate was 1 mm/min in the first cycle; thereafter each cycle's displacement rate was increased such that crack initiation occurred on the order of 1 minute (displacement rate = opening displacement (mm) from previous arrest cycle divided by 1 min). Valid data was considered to occur at crack lengths greater than 50 mm (as measured from the loading pins) but not within 50 mm of the end of the DCB specimen.

A corrected beam theory method was used for data analysis to obtain G_c and G_a, as described by Gagliano and Frazier [12].

$$G_c = \frac{P_c^2}{B}\frac{(a+x)^2}{(EI)_{eff}}$$

$$G_a = \frac{P_a^2}{B}\frac{(a+x)^2}{(EI)_{eff}}$$

Where P_c and P_a are the crack initiation and arrest loads, respectively; a is the crack length; χ is the correction factor, or the crack length offset; B is the DCB width; $(EI)_{eff}$ is the DCB effective flexural rigidity. $(EI)_{eff}$ and χ are derived from the plot of the cube root of compliance versus crack length (Chapter 2, Figure 2-19), described in the literature [12].

4.2.5 Dynamic Mechanical Analysis (DMA)

A PUR prepolymer was cast onto a dry polyethylene sheet under nitrogen using a film applicator (gap 152 µm), and then immediately moved into a dessicator that had been pre-conditioned to RH 65% using saturated ammonium nitrate. The film was allowed to cure at room temperature for two weeks; the resulting film thickness was ~ 800 µm. Two individual films were prepared for each adhesive. Subsequently, disk DMA specimens (dia. = 8 mm) were directly punched from PUR films; these DMA specimens were vacuum dried (0.5 mmHg, room temp., 48 h) and stored over P_2O_5 and dry N_2 prior to analysis.

DMA tests were conducted on a TA Instruments AR1000 rheometer using an 8 mm dia stainless steel parallel-plate geometry. A single PUR film specimen was placed between the plates under a 10 N normal force. The specimen was equilibrated at -80 °C for 5 min, and then heated to 180 °C (3 °C/min, 1 Hz.); the strain level was within the linear response (0.1%). For each

sample group, at least three separate observations were used to generate an average DMA response using the "*Average Multiple Curves*" function in OriginPro software version 8.0.63 (OriginLab, Northampton, MA, U.S.A.).

4.2.6 Fourier Transform Infrared Spectroscopy (FTIR)

All FTIR spectra were recorded on a MIDAC M2004 spectrometer using an attenuated total reflection accessory (ATR, Durascope^{TM}, SensIR Technologies). A small piece of PUR film (2×2 mm) was cut in half through its thickness, and the newly created surface (representing the bulk film) was studied. All spectra were collected using 128 scans with a resolution of 4 cm^{-1}. For each sample group, six observations on three separate specimens were used to generate an average FTIR spectrum (same method described in Section 4.2.5).

4.2.7 Fluorescence Light Microscopy

Two small composite cubes (~ 10 × 10 × 10 mm, long × rad × tan) were randomly excised from the middle section (at least 50 mm away from either end) of a DCB specimen, with the adhesive layer centered at the cross section. The cubes were immersed in distilled water under vacuum (5 mmHg, 20 min), and then at room conditions for 24 h. A cross-sectional slice (thickness ~30 µm) was cut using a sledge microtome "G.S.L. 1" (Schenkung Dapples, Zürich, Switzerland) from both ends of each cube. This thin section was placed on a glass slide, straightened, stained using 0.5% Safranin O solution, and then covered with a cover slip. Subsequently, the slide was allowed to dry on a hot plate (~ 40 °C) for 30 min with a small weight on top of the cover slip, and then at room conditions for additional 24 h. Finally, the cover slip was permanently

mounted with cyanoacrylate adhesive at the four corners. For each adhesive, three DCB specimens were used to prepare 12 slides.

A Zeiss Axioskop microscope, a 100 W mercury lamp, and a Nikon DS-Fi1 digital camera were employed for fluorescence microscopy. The optical filter set consisted of a 360-nm excitation filter, a 400-nm dichromatic mirror, and a 420-nm emission filter. From each image, the adhesive effective penetration (EP) was measured and calculated using the method published by Kamke et al. [14] (Appendix 4-4 illustrates this method):

$$EP = \frac{\sum A}{b}$$

Where ∑A is the total adhesive penetrated area and b is the width of the image. Both ∑A and b were measured using the software NIS-Elements BR 3.10. Five images were taken for each slide, that is, 60 images were used to obtain the average EP for each adhesive.

4.3 Results and Discussion

Recall that the PURs in this study were prepared with the same NCO/OH ratio, and that the principle synthetic variable was the composition of the PPG (soft) phase; it contained a binary mixture of high and low molecular weight PPG (respectively 2000 and 400 number average g/mol). In other words, the soft phase composition involved a varied ratio of PPG2000/PPG400 (For simplicity, keep in mind that the sample names sequentially identify the HI & LOW molecular weight soft segments - for instance, the soft phase of PU8020 was prepared with 80% PPG2000 and 20% PPG400). Consequently, as the soft phase composition varies for samples

PU8020, PU5050, and PU2080, the hard phase mass percentage increases as 53.5%, to 65.4%, to 72.5%. In the following discussion, the effects of the varied soft phase composition (ranging from 80/20 to 20/80) are conveniently discussed in terms of increasing percentage of hard phase.

4.3.1 Properties of PUR Prepolymers

The RI size exclusion chromatographic traces of the starting materials (pMDI, PPG2000, and PPG400) and the corresponding PUR prepolymers are shown in Figure 4-1A and Figure 4-1B, respectively. Appearing in the prepolymers are the low molecular weight species (retention volume 16 - 18 mL) corresponding to pMDI monomers and oligomers. The signal appearing before the retention volume equal to 16 mL reveals the isocyanate end-capped PPG mixtures. Clearly, the highest-molecular-weight fraction (lowest retention volume, 11 - 14.5 mL) increases with the PPG2000 mass percentage; while the intermediate fraction (14.5 - 15.8 mL) rises with the PPG400 mass percentage. In other words, the average chain length decreases as the PPG composition tends towards shorter chains (as hard segment content increases). In all prepolymers, evidence of PPG chain coupling (block formation) is observed. M_n, M_w, and the polydispersity index (PDI) are summarized in Table 4-2.

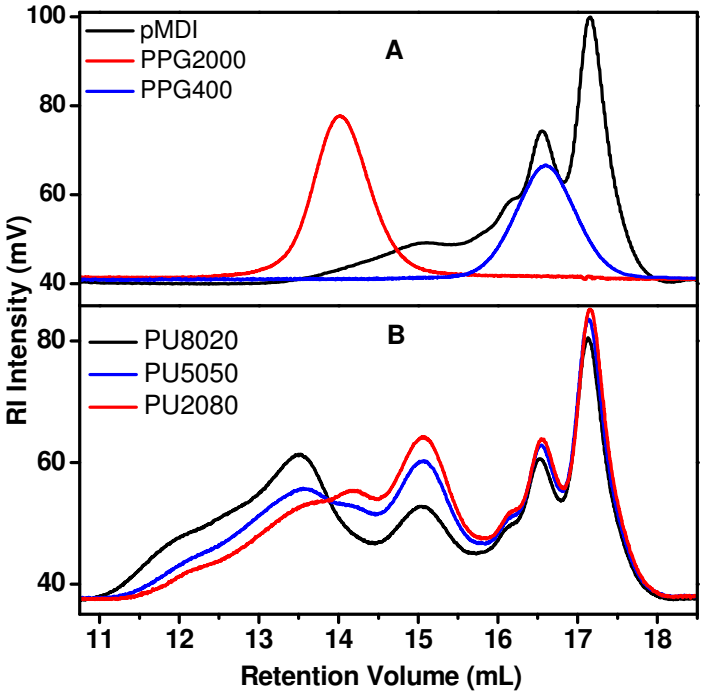

Figure 4-1 Refractive index (RI) chromatograms for A) pMDI, PPG2000, and PPG400; B) PUR prepolymers.

Table 4-2 Properties of PUR prepolymers

PUR Prepolymer	Mn (Da)	Mw (Da)	PDI	Soft Segment T_g (°C)	Viscosity (mPa•s, at 10 s^{-1})
PU8020	1010	2980	2.95	-37	38,000
PU5050	930	2350	2.53	-28	98,000
PU2080	910	2280	2.51	-21	160,000

Figure 4-2 reveals the effects of hard segment content on the prepolymer soft segment T_g. Compared to the pure PPGs, all PUR prepolymers show a dramatic T_g increase of at least 33 °C. The soft segment T_g increases as the PPG2000/PPG400 ratio decreases (as the percentage hard phase increases), consistent with the observations of Šebenik and Krajnc [5]. Recall that as the

PPG2000/PPG400 ratio decreases from 80/20 to 20/80, the hard segment content increases from 53.5% to 72.5%. The increasing hard segment content leads to greater intermolecular associations that restrict soft segment mobility. Consequently, while PU2080 has the lowest average molecular weight, its greater hard segment content results in the highest prepolymer soft segment T_g.

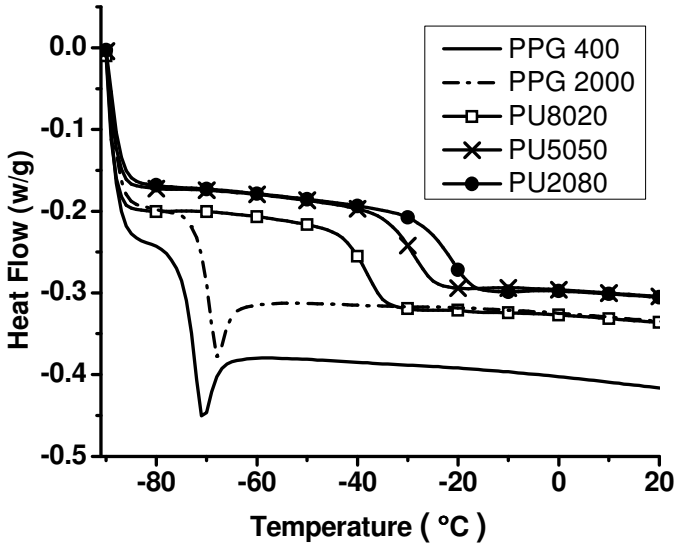

Figure 4-2 DSC thermograms showing the glass transition temperatures for pure PPGs and the PPG soft segments in PUR prepolymers

Figure 4-3 shows the steady-state flow curves for the PUR prepolymers. All PUR prepolymers show a similar response; up to about 100 s^{-1}, viscosities gradually decline as shear rate increases; thereafter an extreme shear-thinning occurs. As the prepolymer molecular weight increases, the extreme shear-thinning occurs at higher shear rates. Likewise, as hard segment content increases, so does the viscosity in the low shear region (Table 4-2), again because of increasing hard segment interaction.

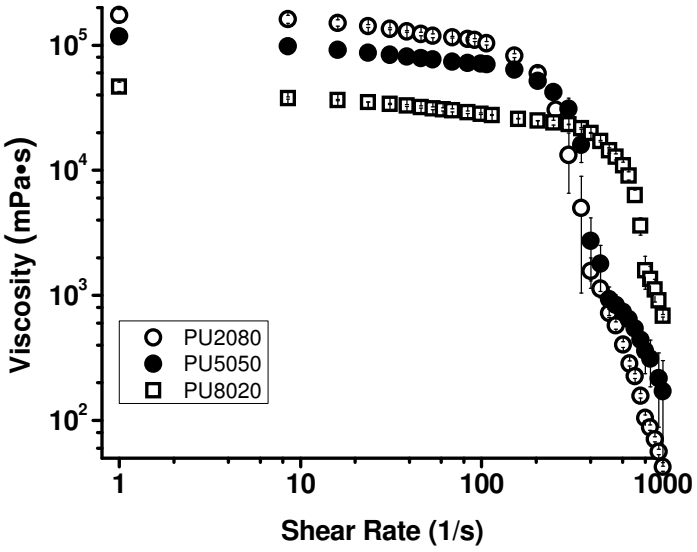

Figure 4-3 Steady-state flow curves of PUR prepolymers measured with parallel-plate geometry; errors bars represent ± 1 standard deviation (n = 3).

4.3.2 Properties of PUR Films

4.3.2.1 FTIR

As previously mentioned, the physical properties of PUR's are a strong function of the hard/soft phase morphology. One driving force behind the dual-phase morphology is the occurrence of hydrogen bonds between and among the urea, urethane and related structures (such as allophanates and biurets). Besides the synthetic versatility of PURs, another useful feature is that much can be learned about PUR solid-state structure/properties through the analysis of hydrogen bonding patterns. This is conveniently accomplished using infrared spectroscopy to observe subtle changes in the carbonyl stretching frequency. The shift of the FTIR absorbance for the carbonyl group to a lower frequency is evidence of hydrogen bond formation; the magnitude of the shift is a measure of the hydrogen bonding strength. Isolated or "free" carbonyl groups

exhibit stretching bands at 1729-1740 cm^{-1} and 1690-1700 cm^{-1} for urethane and urea, respectively[8, 15-16]. Hydrogen bonding shifts the urethane carbonyl stretching vibration to 1700-1715 cm^{-1} (urethane-urethane H-bonds) and 1725-1730 cm^{-1} (urethane-soft segment ether H-bonds), whereas the urea carbonyl shifts to 1650-1690 cm^{-1} (monodentate H-bonded) and 1628-1650 cm^{-1} (bidentate H-bonded).

Figure 4-4 shows the average FTIR spectra in the carbonyl region for cured PUR neat-films. According to the different forms of hydrogen bonding discussed previously, each spectrum contains multiple (at least five) carbonyl types, as highlighted by the dashed lines in Figure 4-4 (Note that the region labeled as "H-bonded Urethane" has been ascribed to two different interactions [8, 15-16]: urethane-ether interaction at 1725-1730 cm^{-1}, and urethane-urethane interaction at 1700-1715 cm^{-1}). Despite this complexity, effects of PPG composition on PUR properties are observed. With increasing percentage of hard phase (from PU8020 to PU2080): 1) the overall carbonyl intensity rises as expected; 2) the free urethane intensities are all similar, and minor differences are seen in the hydrogen-bonded urethane region which could perhaps reflect minor differences in urethane-ether and urethane-urethane interactions; 3) but most notably, relative to free urea the hydrogen-bonded urea signal increases significantly. So while minor differences in urethane associations might exist, the increasing percentage hard phase apparently has greatest impact on urea formation and association, as would be expected in a moisture-curing system.

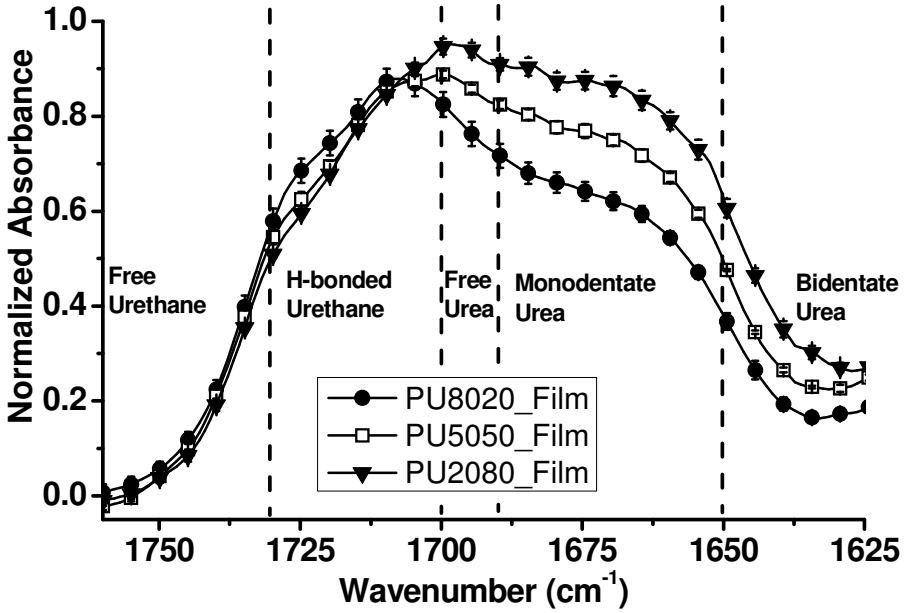

Figure 4-4 Average FTIR spectra in the carbonyl region for cured PUR neat-films; error bars represent ± 1 standard deviation (n=6); dashed lines divide the spectra to five carbonyl sub-regions; spectra normalized by the phenylene signal 1594 cm^{-1} (not shown) with intensities of 1.0, 1.22, and 1.36 based upon the hard phase contents of PU8020, PU5050, and PU2080, respectively.

4.3.2.2 DMA

As indicated previously, the hard segment content significantly alters the hydrogen bonding and thus PUR phase morphology and its thermal properties. Extensive DMA has been conducted on polyurethane materials [17-22]. In this research, parallel-plate, torsional DMA was employed to reveal the effects of hard segment content (PPG composition).

Figure 4-5 shows the DMA first heating scans of PUR films. Recall that PUR films (thickness ~ 800 µm) expanded more than 500% (film applicator gap 152 µm) during cure and formed a foam;

as a result, all adhesives show a low modulus (-80 °C) compared to a monolithic polymer (~ 10^9 Pa glassy modulus). Focusing on storage modulus, all samples show a gradual modulus decrease over a broad temperature range (-80 to 40 °C); this range is expanded in Figure 4-5B. None of the cured PURs exhibits a clearly defined soft phase relaxation. Since the prepolymer T_gs ranged from -21 to -37 ˚C, the cured soft chains are restricted, and this restriction prevents significant damping as indicated by the weak tan δ signals in this region. Distinct from the other specimens, PU8020 exhibits an additional softening as the modulus declines more dramatically between -10 and 40 °C. Perhaps this minor softening (-10 - 40 °C) in PU8020 is the only remnant of prepolymer relaxation, as might be expected with a higher proportion of long PPG chains. Whereas PU5050 and PU2080 possess more of the shorter PPG chains - perhaps these chains are substantially elongated and incapable of additional softening. The relative moduli (-80 °C) do not support this hypothesis, but the foam structure in these films likely causes erroneous modulus values. Alternatively, all soft phase relaxations may be substantially hidden at higher temperatures. However, while clear soft segment relaxation is absent for all specimens, it is notable that cured PU8020 exhibits greater dampening (tan δ intensity) from -50 to 40 ˚C. In other words, the changing PPG2000/PPG400 mass ratio leads to a greater hard phase content that dominates softening, but perhaps the soft phase composition also exerts a minor effect on PUR properties.

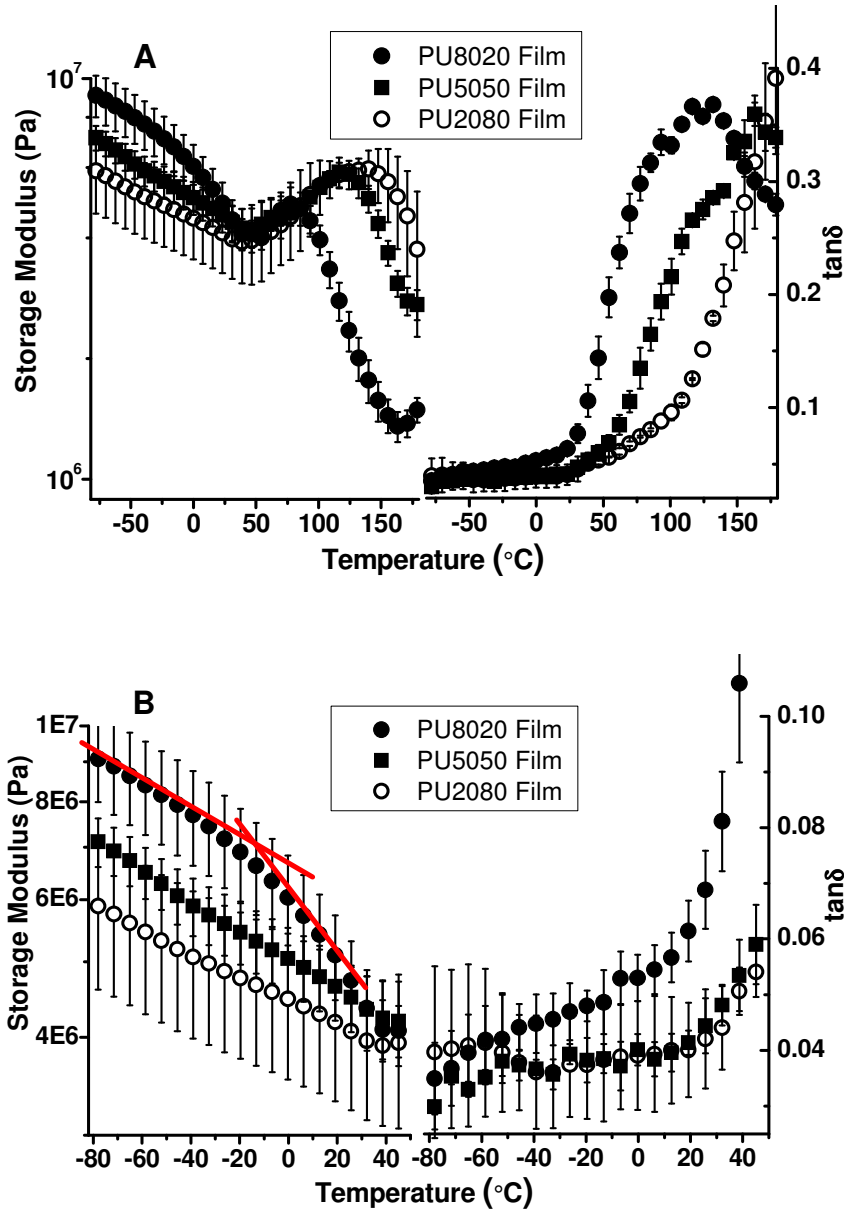

Figure 4-5 Average DMA 1st heating scans of cured PUR films (3 °C/min, 1 Hz.); error bars represent ± 1 standard deviation (n = 3); A) full thermograms; B) expanded view in the soft segment softening region; tangent red lines showing the onset of a possible PU8020 soft phase transition.

The initial softening is followed by slight stiffening (Figure 4-5A), which could be related to residual cure, or to reorganization near soft segment boundaries (perhaps the later is more

probable considering the low temperature and that the specimen is clamped under a densifying compressive force). Subsequently, hard segment softening occurs, corresponding to the extreme storage modulus decrease and the broad and strong tan δ peak. Clearly, the increasing percentage hard phase has greatly influenced the hard segment packing, reflected as increasing softening temperatures (tan δ maximum), which are 135, 167, and > 180 °C for PU8020, PU5050, and PU2080, respectively.

4.3.3 Properties of Wood/PUR Composites

4.3.3.1 Adhesive Penetration

Adhesive penetration is generally believed to have a strong influence on bondline mechanical performance. Adequate penetration provides a substantial interphase that promotes interaction, perhaps reaction, and also mechanical interlocking. On the other hand, excessive penetration could lead to a "starved" bondline having poor performance [14, 23]. Recall that hard segment content significantly affects PUR prepolymer viscosity (Figure 4-3), one of the most important factors controlling adhesive penetration. Fluorescence microscopy (Figure 4-6) revealed that increasing hard phase content (increasing prepolymer viscosity) resulted in thicker bondlines and less wood penetration, Figure 4-7.

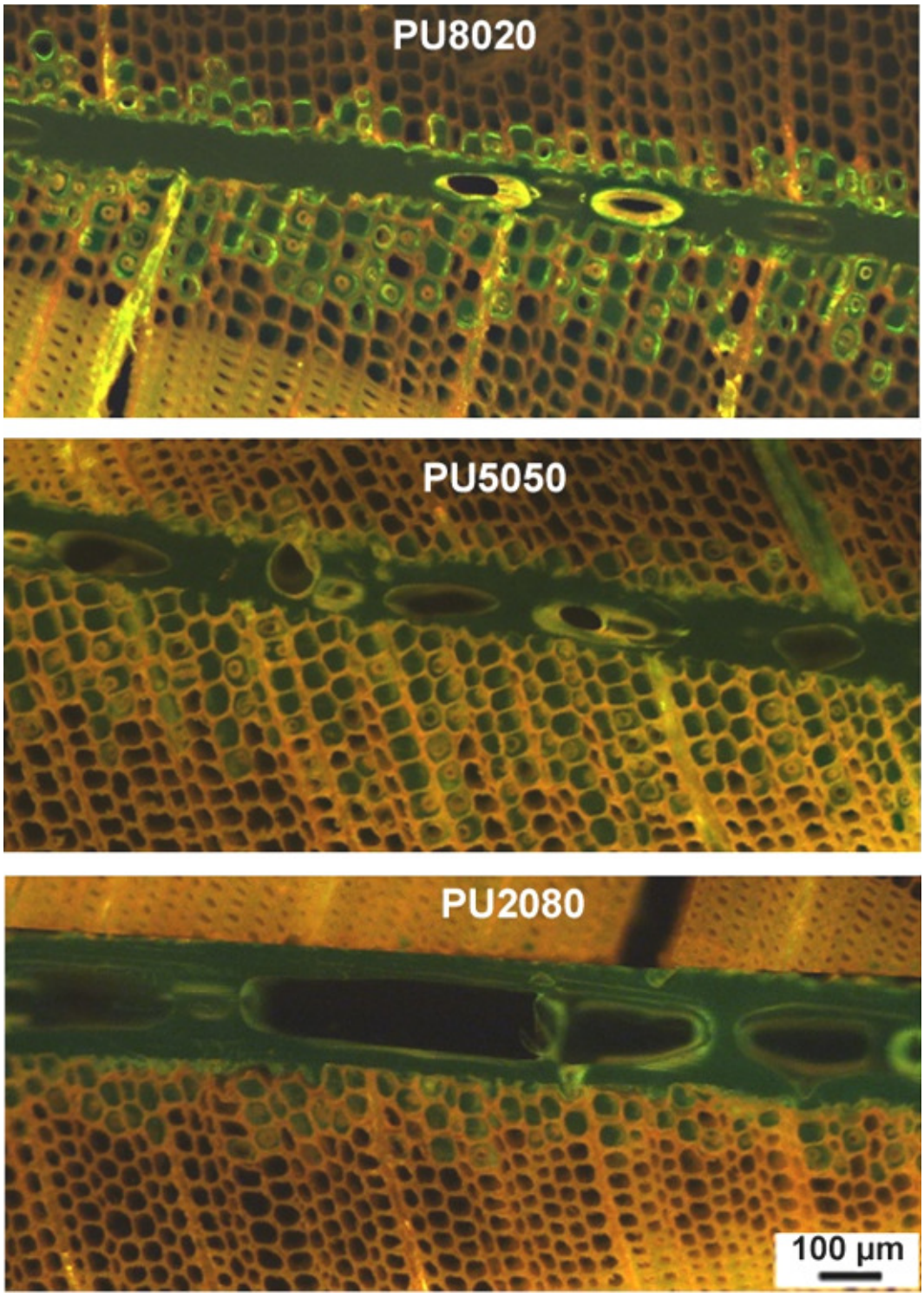

Figure 4-6 Representative fluorescence microscopy images of PUR wood bondlines in DCB specimens

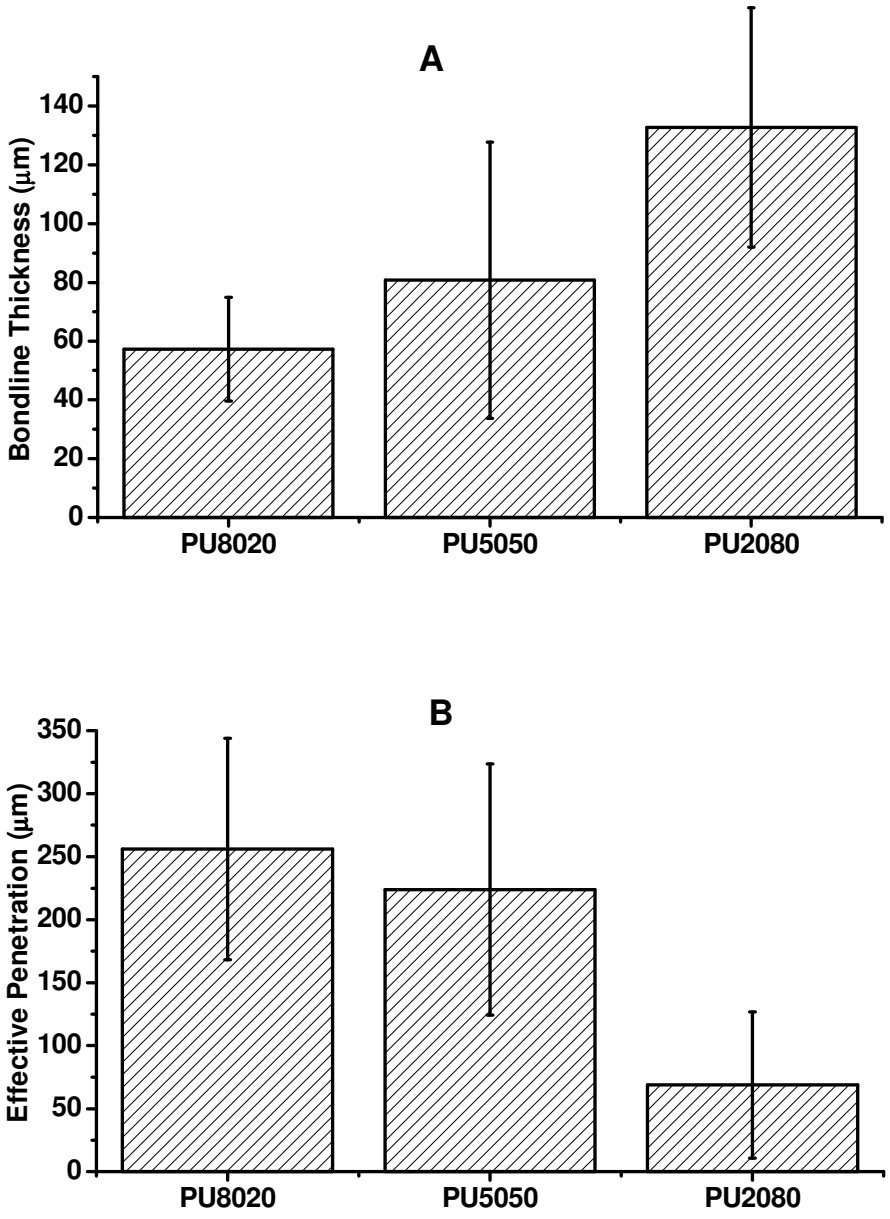

Figure 4-7 Bondline thickness (A) and Effective Penetration (B) of PURs in bonded-wood DCB specimens; errors bars represent ± 1 standard deviation (n = 60).

The effective penetration (Figure 4-7B) measured for PU8020 and PU5050 were not significantly different ($p = 0.21$); but both were significantly deeper than for PU2080. This is consistent with PUR bondline thickness (Figure 4-7 A); penetration depth is inversely proportional to the bondline thickness. The relation between prepolymer viscosity (FIGURE 4-3) and effective penetration (Figure 4-7B) is complex. Under low shear rates (< 100 s^{-1}), PU2080 has the highest viscosity, which seems to correlate to the low wood penetration observed; but PU8020 and PU5050 exhibit the same penetration while having distinctly different low shear viscosities. However, considering southern pine anatomy and the cold-press closure time employed in this work (2-3 seconds), the penetrating adhesive should experience a shear rate of from 230 to 350 s^{-1} [24]. Again however, the measured adhesive penetrations still do not sensibly relate to viscosities in the range of 230 to 350 s^{-1}. Besides adhesive viscosity, other factors such as wood permeability, wood surface energy, adhesive surface tension, and bondline consolidation parameters are known to influence wood adhesive penetration [25]. In this work, adhesive penetration is not simply related to prepolymer viscosity, and so other effects are apparently active.

4.3.3.2 Mode-I Fracture Testing

As mentioned earlier, wood adhesive performance is commonly evaluated by strength-based tests conducted in shear mode [2, 5, 11], in which wood failure often dominates and thus obscures subtle aspects of adhesion. Šebenik and Crank [5] conducted a similar study where the soft phase composition was varied just as in this work; however they employed a lower NCO/OH ratio (3.0) and they used the monomer 4,4'-methylenebis(phenylisocyanate) (not pMDI as in this work). Šebenik and Crank [5] found that hard segment content exerted an

increasing and then decreasing impact on PUR/wood bondline shear strength; maximum strength was achieved when the PPG2000/PPG400 ratio was 1:1 (the same as in PU5050 [5]. In this research, the effects of hard segment content were studied in terms of bondline fracture toughness.

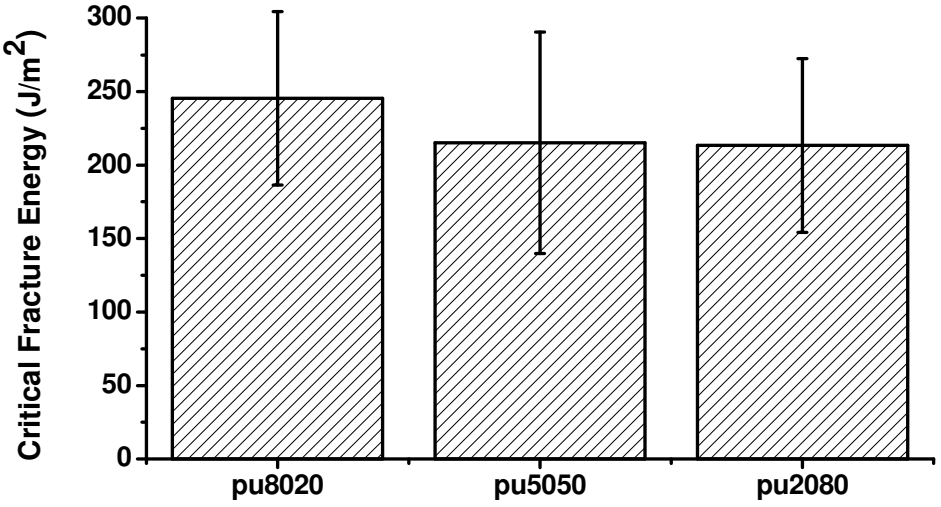

Figure 4-8 Average mode-I critical fracture energy of PUR/wood composites; error bars represent ± 1 standard deviation (n = 90-110).

Figure 4-8 demonstrates the effects of hard segment content on the fracture toughness of PUR bondlines. The data scatter depicted in Figure 4-8 is typical and this variation is postulated to arise from flexural modulus variation along the DCB length and the corresponding mixture of mode I and mode II effects [12]. On the other hand, fracture testing of bonded-wood DCB's generates many fracture events in a few specimens, therefore providing a desirable level of statistical power. Observed from Figure 4-8, PU8020 shows slightly but significantly higher fracture toughness than the other two adhesives; PU5050 and PU2080 exhibit similar

performance. The fracture results found here do not simply relate to the shear strength results obtained by Šebenik and Krajnc, where shear strength was clearly maximized at an equal mixture of PPG2000 and PPG400 [5].

The higher toughness of PU8020 is not simply explained; neither bondline thickness nor effective penetration is correlated with higher toughness since PU5050 is less tough but with comparable bond thickness and effective penetration (Figure 4-7). Likewise, PU2080 exhibits the thickest bondlines and lowest effective penetration, but its toughness is the same as for PU5050 (Figure 4-8). Aside from bond thickness and adhesive penetration, it seems that the measured fracture toughnesses could reflect compositional variations within the adhesives. In this regard, it could be that the greater average PPG chain length in PU8020 causes greater fracture toughness. If this is the case, then perhaps the greater fracture toughness of PU8020 is related to its greater damping (tan δ intensity) in the -50 to 45 ˚C temperature range as seen in Figure 4-5.

Correlations between toughness and damping intensity have been documented; a material appears to be tougher if the strength of its molecular relaxation increases near the mechanical testing temperature [26-28]. For example, a linear correlation was found between the Charpy notched impact toughness of isotactic polypropylene at room temperature and the strength of its β transition at about 0 °C [26]. Therefore, PU8020's higher damping between -50 and 45 °C (Figure 4-5) perhaps correlates with its higher bondline toughness (Figure 4-8).

4.4 Conclusions

Three PUR wood adhesives were prepared from pMDI and varied mixtures of PPG2000 and PPG400, all at constant NCO/OH. Thus as the soft phase composition favored shorter chains, the average hard phase content increased, and this significantly affected the liquid prepolymer properties. The liquid prepolymer viscosity and soft segment T_g increased with hard phase content (decreasing PPG2000/PPG400 mass ratio). Regarding cured films, the increasing hard phase content resulted in higher hard phase softening temperatures; and this correlated to greater percentages of hydrogen-bonded urea structures observed with infrared spectroscopy. For PUR/wood composite specimens, adhesive penetration and bondline thickness did not simply correlate with liquid PUR viscosity. Similarly, bondline fracture toughness was not sensibly related to bondline thickness or adhesive penetration. It was postulated that the greater PU8020 fracture toughness might be related to greater damping observed in the DMA response between -50 and 45 °C.

References

1. Chattopadhyay, D.K., B. Sreedhar, and K.V.S.N. Raju, Thermal stability of chemically crosslinked moisture-cured polyurethane coatings. Journal of Applied Polymer Science, 2005. 95(6): p. 1509-1518.

2. X. Li, Z.G., J. Gu, F. Zhao, and X. Bai, Synthesis and characterisation of one-part ambient temperature curing polyurethane adhesives for wood bonding. Pigment & Resin Technology, 2004. 33(6): p. 345-351.

3. Chattopadhyay, D.K., B. Sreedhar, and K.V.S.N. Raju, The phase mixing studies on moisture cured polyurethane-ureas during cure. Polymer, 2006. 47(11): p. 3814-3825.

4. Chattopadhyay, D.K., B. Sreedhar, and K.V.S.N. Raju, Influence of varying hard segments on the properties of chemically crosslinked moisture-cured polyurethane-urea. Journal of Polymer Science Part B-Polymer Physics, 2006. 44(1): p. 102-118.

5. Sebenik, U. and M. Krajnc, Influence of the soft segment length and content on the synthesis and properties of isocyanate-terminated urethane prepolymers. International Journal of Adhesion and Adhesives, 2007. 27(7): p. 527-535.

6. Richter, K., A. Pizzi, and A. Despres, Thermal stability of structural one-component polyurethane adhesives for wood - Structure-property relationship. Journal of Applied Polymer Science, 2006. 102(6): p. 5698-5707.

7. Chattopadhyay, D.K., B. Sreedhar, and K.V.S.N. Raju, Effect of chain extender on phase mixing and coating properties of polyurethane ureas. Ind. Eng. Chem. Res., 2005. 44: p. 1772-1779.

8. Rath, S.K., A.M. Ishack, U.G. Suryavansi, L. Chandrasekhar, and M. Patri, Phase morphology and surface properties of moisture cured polyurethane-urea (MCPU) coatings: Effect of catalysts. Progress in Organic Coatings, 2008. 62(4): p. 393-399.

9. Ni, H.F., C.K. Yap, and Y. Jin, Effect of curing moisture on the indentation force deflection of flexible polyurethane foam. Journal of Applied Polymer Science, 2007. 104(3): p. 1679-1682.

10. Li, S.Y., R. Vatanparast, E. Vuorimaa, and H. Lemmetyinen, Curing kinetics and glass-transition temperature of hexamethylene diisocyanate-based polyurethane. Journal of Polymer Science Part B-Polymer Physics, 2000. 38(17): p. 2213-2220.

11. Beaud, F., P. Niemz, and A. Pizzi, Structure-property relationships in one-component polyurethane adhesives for wood: Sensitivity to low moisture content. Journal of Applied Polymer Science, 2006. 101(6): p. 4181-4192.

12. Gagliano, J.M. and C.E. Frazier, Improvements in the fracture cleavage testing of adhesively-bonded wood. wood and fiber science, 2001. 33(3): p. 377-385.

13. ASTM, ASTM D5155-07, Standard Test Methods for Polyurethane Raw Materials Determination of the Isocyanate Content of Aromatic Isocyanates. 2007.

14. Sernek, M., J. Resnik, and F.A. Kamke, Penetration of liquid urea-formaldehyde adhesive into beech wood. Wood and Fiber Science, 1999. 31(1): p. 41-48.

15. Luo, N., D.N. Wang, and S.K. Ying, Hydrogen-bonding properties of segmented polyether poly(urethane urea) copolymer. Macromolecules, 1997. 30(15): p. 4405-4409.

16. Daniel-da-Silva, A.L., J.C.M. Bordado, and J.M. Martin-Martinez, Moisture curing kinetics of isocyanate ended urethane quasi-prepolymers monitored by IR spectroscopy and DSC. Journal of Applied Polymer Science, 2008. 107: p. 700-709.

17. Sheth, J.P., D.B. Klinedinst, G.L. Wilkes, Y. Iskender, and I. Yilgor, Role of chain symmetry and hydrogen bonding in segmented copolymers with monodisperse hard segments. Polymer, 2005. 46(18): p. 7317-7322.

18. Yilgor, I. and E. Yilgor, Structure-morphology-property behavior of segmented thermoplastic polyurethanes and polyureas prepared without chain extenders. Polymer Reviews, 2007. 47(4): p. 487-510.

19. Das, S., I. Yilgor, E. Yilgor, and G.L. Wilkes, Probing the urea hard domain connectivity in segmented, non-chain extended polyureas using hydrogen-bond screening agents. Polymer, 2008. 49(1): p. 174-179.

20. Das, S., I. Yilgor, E. Yilgor, B. Inci, O. Tezgel, F.L. Beyer, and G.L. Wilkes, Structure-property relationships and melt rheology of segmented, non-chain extended polyureas: Effect of soft segment molecular weight. Polymer, 2007. 48(1): p. 290-301.

21. O'Sickey, M.J., B.D. Lawrey, and G.L. Wilkes, Structure-property relationships of poly(urethane urea)s with ultra-low monol content poly(propylene glycol) soft segments. I. Influence of soft segment molecular weight and hard segment content. Journal of Applied Polymer Science, 2002. 84(2): p. 229-243.

22. J. Y. BAE, D.J.C., J. H. AN, Effects of the structure of chain extenders on the dynamic mechanical behaviour of polyurethane. Journal of Materials Science, 1999. 34: p. 2523-2527.

23. Johnson, S.E. and F.A. Kamke, Quantitative-Analysis of Gross Adhesive Penetration in Wood Using Fluorescence Microscopy. Journal of Adhesion, 1992. 40(1): p. 47-61.

24. Paris, J.L., Carboxymethylcellulose Acetate Butyrate Water-Dispersions as Renewable Wood Adhesives, in Wood Science and Forest Products. 2010, Virginia Polytechnic Institute and State University: Blacksburg.

25. Kamke, F.A. and J.N. Lee, Adhesive penetration in wood - a review. Wood and Fiber Science, 2007. 39(2): p. 205-220.

26. Grein, C., K. Bernreitner, and M. Gahleitner, Potential and limits of dynamic mechanical analysis as a tool for fracture resistance evaluation of isotactic polypropylenes and their polyolefin blends. Journal of Applied Polymer Science, 2004. 93(4): p. 1854-1867.

27. Kendall, K., Connection between Fracture Energy and Inelastic Behavior. Acta Metallurgica, 1979. 27(6): p. 1065-1073.

28. Kisbenyi, M., M.W. Birch, J.M. Hodgkinson, and J.G. Williams, Correlation of Impact Fracture-Toughness with Loss Peaks in Ptfe. Polymer, 1979. 20(10): p. 1289-1297.

Chapter 5 Weather Durability of Moisture-Cure Polyurethane Wood Adhesives: Identifying Accelerated Weathering Procedures

Dakai Ren and Charles E. Frazier*

Macromolecules and Interfaces Institute

Wood-Based Composites Center

Department of Wood Science and Forest Products

Virginia Tech, Blacksburg, VA, 24061

* Corresponding author Tel: 540-231-8318 Email: cfrazier@vt.edu

Abstract

This chapter focuses on two subjects regarding the weather durability of moisture-cure polyurethane (PUR) wood adhesives: the hard segment content effects and development of weathering procedures. For these purposes, three PUR adhesives with different hard segment contents were prepared from pMDI and varied mixtures of PPG2000 and PPG400, all at constant NCO/OH. Wood/PUR composites were subjected to three accelerated weathering procedures developed in this research, and then evaluated using mode-I fracture testing. Two relatively moderate procedures (VPS80C and VPS104C) could not effectively differentiate the weather durability of the three PURs. Treated specimens all showed enhanced bondline toughness, although PU8020 (lowest hard segment content) bondlines exhibited a survival ratio of only 50% after VPS104C weathering. On the other hand, VPSS procedure was able to well distinguish the weather durability of these PURs; treated-PU8020 specimens showed decreased toughness while the other two exhibited enhanced toughness. As a result, VPSS procedure was selected for further PUR structure-durability studies.

Keywords: Moisture-cure polyurethane, wood adhesion, accelerated weathering, weather durability

5.1 Introduction

Wood is the primary material used for North American residential construction, and it often exists in adhesively bonded form. Therefore, the long-term durability of wood-adhesive bonds has immense practical significance. The most demanding wood bonding performance criteria are in certification standards for structural applications such as laminated veneer lumber, plywood, and laminated timber (a.k.a. glulam timber). Of particular interest is the American Society of Testing and Materials (ASTM) standard D2559 which is commonly referred to as the delamination or "delam" test [1]. ASTM D2559 contains three parts, a creep test, a shear strength test, and a rigorous simulated weathering followed by visual inspection of bondline delamination. However, it is believed that the simulated weathering imposed in ASTM D2559 is much harsher than actual environmental conditions, and variations of this test have been investigated [2-4]. In this chapter, three accelerated weathering procedures were developed and evaluated, by mode-I fracture, for efficacy in distinguishing the performance of the three PURs prepared for this work.

5.2. Experimental

5.2.1 Materials

Polymeric methylene(bisphenylisocyanate) (pMDI, NCO = 31%, Huntsman International LLC) was used as received. Polypropylene glycol diols (PPG, M_n = 2000, OH# = 55.5 mg KOH/g; 400 g/mol, 263.6 mg KOH/g, Fluka Analytical) were dried under vacuum (0.5 mm Hg) at 80 °C overnight immediately prior to use. PPG termini were not specified; carbon NMR suggested an equal quantity of primary and secondary hydroxyls. The curing catalyst 4,4′-(Oxydi-2,1-ethanediyl)bismorpholine (JEFFCAT® DMDEE, Huntsman International LLC) was used as received. Southern yellow pine planks (longitudinal × tangential × radial = 250 × 150 × 10 mm) were equilibrated in a relative humidity (RH) 65% chamber at room temperature before use.

5.2.2 Synthesis of PUR Prepolymers

The PUR prepolymers were prepared by reacting a mixture of PPG400 and PPG2000 with pMDI; prepolymer compositions are shown in Table 5-1. A 250-mL three-neck flask was oven dried, fixed with an overhead mechanical stirrer, rubber septum, and nitrogen inlet/outlet, and then flamed. The PPG mixture was introduced into the flask followed by pMDI (NCO/OH = 5) using syringe transfer. This mixture was allowed to react under nitrogen for 3 h at 80 °C. Every 30 min, 1-2 ml was sampled and immediately coated onto a KBr disc under nitrogen and tested by Fourier transform infrared spectroscopy in a dry environment. The completion of the reaction was determined when the isocyanate absorption (2270 cm^{-1}) became constant with reaction time. The final NCO contents in these prepolymers were determined using ASTM standard D5155-07, method C [6]; the values shown in Table 5-1 are the average of three separate measurements.

The hard segment content (Table 5-1) was calculated as the mass of pMDI divided by the total liquid adhesive mass. The liquid prepolymers were stored under anhydrous N_2 over P_2O_5 until cure, not longer than 15 days. The cure catalyst DMDEE (0.5%) was mechanically mixed with the prepolymer under N_2 immediately prior to the preparation of film or composite samples.

Table 5-1 The compositions and characteristics of PUR prepolymers

PUR Prepolymer	PPG2000/PPG400 mass ratio	Hard segment content (%)	Theoretical NCO (%)	Measured NCO (%)
PU8020	80/20	53.5	13.28	13.35 ± 0.04
PU5050	50/50	65.4	16.23	16.10 ± 0.02
PU2080	20/80	72.5	17.97	17.85 ± 0.09

5.2.3 Preparation of Fracture Specimens

Approximately flat sawn southern yellow pine planks were prepared such that a ~3-5° angle was achieved between the tangential bonding surface and the longitudinal axis (Gagliano and Frazier [7]). The planks were equilibrated in a RH 65% environment at room temperature, and the tangential (bonding) surfaces were planed immediately prior to use. A PUR prepolymer (250 g/m^2) was applied onto the surface of one plank, and then immediately bonded with another, as per Gagliano and Frazier [7]; Appendix 4-2 is a simplified pictorial illustration of the assembled composite. The bonded composite samples were cured under a pressure of 0.69 MPa (100 psi) for 24 h at room temperature. Subsequently, five double cantilever beams (DCBs, 20-mm wide) were ripped from each composite specimen and equilibrated (RH 65%, room temperature) for two weeks. For each adhesive, two separate PUR batches were synthesized to prepare 40 DCBs (20 from each batch). For each adhesive, the two separate batches provided the same fracture

performance (Appendix 4-3); therefore, DCB specimens within an adhesive grouping were combined for weather durability studies. Four groups of DCBs (six in each group) were randomly selected; one was the control (unweathered) group and the other three were subjected to three different accelerated weathering procedures, respectively.

5.2.4 Accelerated Weathering Procedures

Three accelerated weathering procedures were developed in this study, namely two vacuum-pressure-soak procedures (VPS80C and VPS104C) and one vacuum-pressure-soak-steam (VPSS) procedure. VPS80C and VPS104C weathering treatments were conducted on specimens cyclically following these steps: 1) water soak under vacuum (10 mmHg, 1 h); 2) water soak after releasing vacuum (1 atm, 1 h); 3) oven dry to complete one cycle (VPS80C: 3 mmHg, 80 °C, 7 h; VPS104C: 1 atm, 104 °C, 24 h). This cycle was repeated seven more times in VPS80C and once in VPS104C. VPSS follows similar steps, except that a vigorous steaming step (105 °C, 1.2 bar, 2 h in an autoclave) was inserted between the first and second cycle, and that the specimens were dried at 65 °C for 22 h. The differences among these weathering procedures are summarized in Table 5-2. After being equilibrated in a chamber (RH 65%, room temp., two weeks), the treated specimens were evaluated using mode-I fracture testing.

Table 5-2 Differences among VPS80C, VPS104C, and VPSS weathering procedures

Procedure	Drying Conditions	Number of cycles	Steaming Step
VPS80C	80 °C, 3 mmHg, 7 h	8	No
VPS104C	104 °C, 1 atm, 24 h	2	No
VPSS	65 °C, 1 atm, 22 h	3	Between cycle 1 and 2

5.2.5 Mode-I Fracture Testing

A cyclic mode-I fracture testing method was employed to obtain the crack initiation (G_c) and arrest (G_a) energies of the DCB specimens. All tests were conducted on a screw-driven MTS Systems (Model GL-10) in displacement control mode, using the TestWorks 4 software for data acquisition and system control. Prior to testing, a 10 N pre-load was applied, whereupon the displacement was zeroed. Fracture testing was conducted in a fashion similar to that described by Gagliano and Frazier [7]. Cleavage loading was started; once the load/displacement curve became nonlinear, the test frame crosshead displacement was halted for a 45 second arrest period; thereafter the crosshead was returned to the origin, and the process was repeated in cyclic fashion. The displacement rate was 1 mm/min in the first cycle; thereafter each cycle's displacement rate was increased such that crack initiation occurred on the order of 1 minute (displacement rate = opening displacement (mm) from previous arrest cycle divided by 1 min). Valid data was considered to occur at crack lengths greater than 50 mm (as measured from the loading pins) but not within 50 mm of the end of the DCB specimen.

A corrected beam theory method was used for data analysis to obtain G_c and G_a, as described by Gagliano and Frazier [7].

$$G_c = \frac{P_c^2}{B}\frac{(a+x)^2}{(EI)_{eff}}$$

$$G_a = \frac{P_a^2}{B}\frac{(a+x)^2}{(EI)_{eff}}$$

Where P_c and P_a are the crack initiation and arrest loads, respectively; a is the crack length; χ is the correction factor, or the crack length offset; B is the DCB width; $(EI)_{eff}$ is the DCB effective flexural rigidity. $(EI)_{eff}$ and χ are derived from the plot of the cube root of compliance versus crack length (Chapter 2, Figure 2-19), described in the literature [7].

5.3. Results and Discussion

As discussed in Chapter 4 (section 4.3), PURs in this study were prepared from pMDI and PPG mixtures with varied ratios of PPG2000/PPG400 (for simplicity, keep in mind that the sample names sequentially identify the HI & LOW molecular weight soft segments - for instance, the soft phase of PU8020 was prepared with 80% PPG2000 and 20% PPG400). At a constant NCO/OH ratio, as the soft phase composition varies for samples PU8020, PU5050, and PU2080, the hard phase mass percentage increases as 53.5%, to 65.4%, to 72.5%. In the following discussion, the effects of the varied soft phase composition (ranging from 80/20 to 20/80) are conveniently discussed in terms of increasing percentage of hard phase.

Cyclic mode-I fracture testing was used to evaluate the control and weathered DCB specimens; one G_c and one G_a value were obtained from each cycle. A control DCB specimen generally produced 15-20 cleavage cycles while weathered specimens provided 5-22 cycles. As described

earlier, six DCB specimens were included in each treatment group, resulting in a large number of G_c and G_a values that were averaged. Appendix 5-1 shows the influence of weathering treatments on PUR G_c and G_a values. The same weathering effects are reflected in G_c and G_a plots; thus the following discussion will only focus on G_c values.

Figure 5-1 shows the average G_c of PU8020-bonded DCB specimens as a function of weathering treatments. The numbers shown on the bars are the specimen "survival ratios", the percentage of DCB specimens that survived weathering such that fracture testing could be conducted; survival ratio is defined as:

$$\frac{(total\ \#\ \ specimens - \#\ completely\ weather\ failed\ specimens)}{total\ \#of\ specimens} \times 100$$

Although VPS80C and VPS104C procedures impose a very different number of weathering cycles (eight for VPS80C and two for VPS104C), PU8020 specimens show a similar but slight increase of bondline toughness after both procedures (Figure 5-1). Note that the VPS104C-treated bondline toughness is misleading because PU8020 specimens exhibited a 50% survival ratio. So while VPS80C imposed eight weathering cycles, the two cycles in VPS104C pose a greater bonding challenge due to the higher drying temperature. In contrast, VPSS-treated PU8020 specimens show reduced fracture toughness; however, in this case note that survival was 100%, in spite of the steaming treatment. In other words, it appears to be contradictory that

VPS104C-treated specimens show enhanced toughness but only 50% survival ratio; whereas VPSS-treated specimens exhibit reduced toughness but with 100% survival ratio.

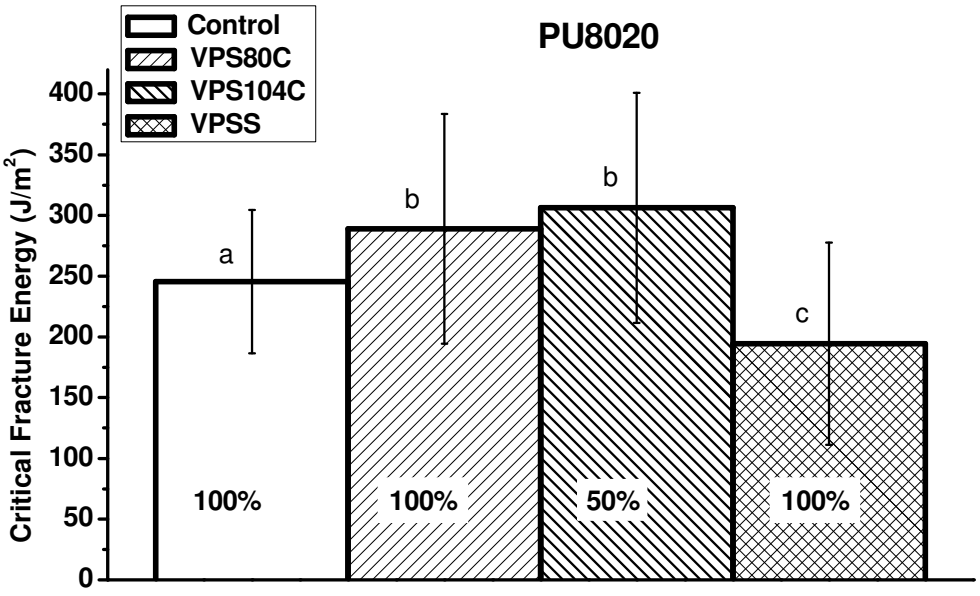

Figure 5-1 Average critical fracture energy (G_c) of PU8020-bonded DCB specimens as a function of weathering treatments; error bars represent ± 1 standard deviation; one-way ANOVA: letters indicate statistically significant groupings for each adhesive (Scheffe's test, $\alpha = 0.05$); numbers on the bars represent the specimen survival ratios.

PU5050 DCB specimens behave differently towards the weathering treatments, Figure 5-2. All three weathering procedures lead to improved relative bondline performance with similar fracture toughness. Furthermore, all PU5050 DCB specimens were in good condition (100% survival ratio) for fracture testing after all weathering treatments. Regarding PU2080 DCB specimens, Figure 5-3, the non-steam weathering procedures caused no change, whereas VPSS caused increased toughness.

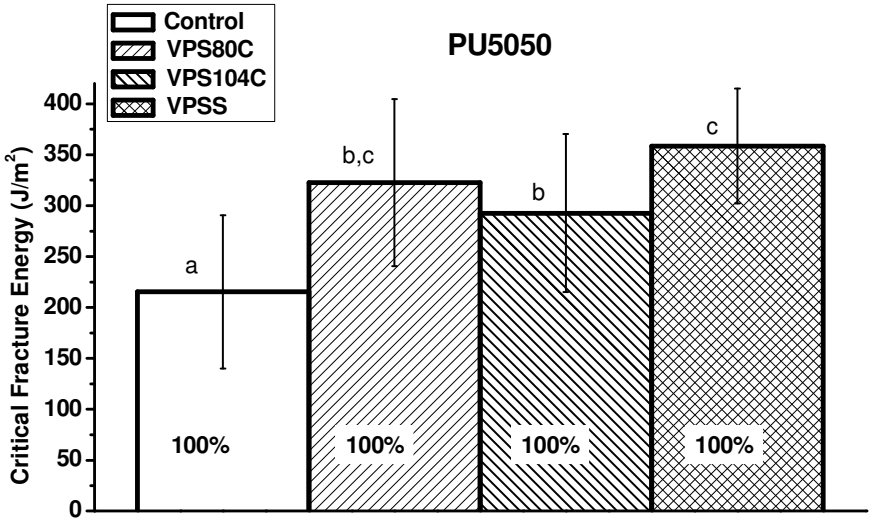

Figure 5-2 Average critical fracture energy (G_c) of PU5050-bonded DCB specimens as a function of weathering treatments; error bars represent ± 1 standard deviation; one-way ANOVA: letters indicate statistically significant groupings for each adhesive (Scheffe's test, $\alpha = 0.05$); numbers on the bars represent the specimen survival ratios.

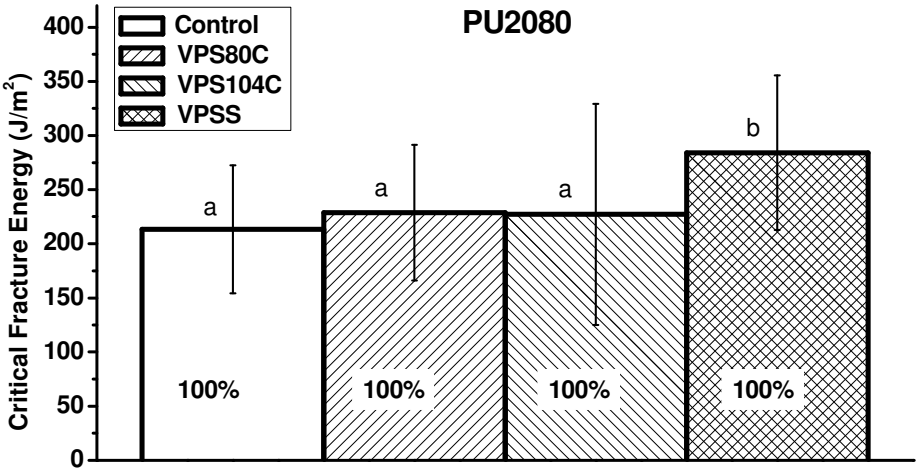

Figure 5-3 Average critical fracture energy (G_c) of PU2080-bonded DCB specimens as a function of weathering treatments; error bars represent ± 1 standard deviation; one-way ANOVA: letters indicate statistically significant groupings for each adhesive (Scheffe's test, $\alpha = 0.05$); numbers on the bars represent the specimen survival ratios.

An appropriate accelerated weathering procedure must be identified in order to devise PUR structure/durability studies. For this purpose, the fracture toughness results are re-plotted as a function of weathering procedure, Figure 5-4. Clearly, specimens show similar bondline toughness after VPS80C (Figure 5-4A) and VPS104C (Figure 5-4B) treatments. They all exhibit either increased or unchanged bondline toughness, again noting that PU8020 specimens exhibit 50% survival ratio under VPS104C treatment. Ideally, the survival ratio should be very high so that durability evaluation could be more simply related to changes in bondline toughness. From Figure 5-4C, VPSS-treated PU8020 bondline shows significantly reduced toughness while the other two adhesives exhibit enhanced performance. In other words, VPSS successfully distinguished the weather durability of these three PUR adhesives; in addition, the same survival ratio (100%) for each adhesive simplifies the durability comparison across adhesives. On the other hand, VPS80C and VPS104C are not able to effectively differentiate the durability of these PURs. Consequently, PUR weather durability against VPSS treatment will be the focus of our following discussions in this and the next chapters.

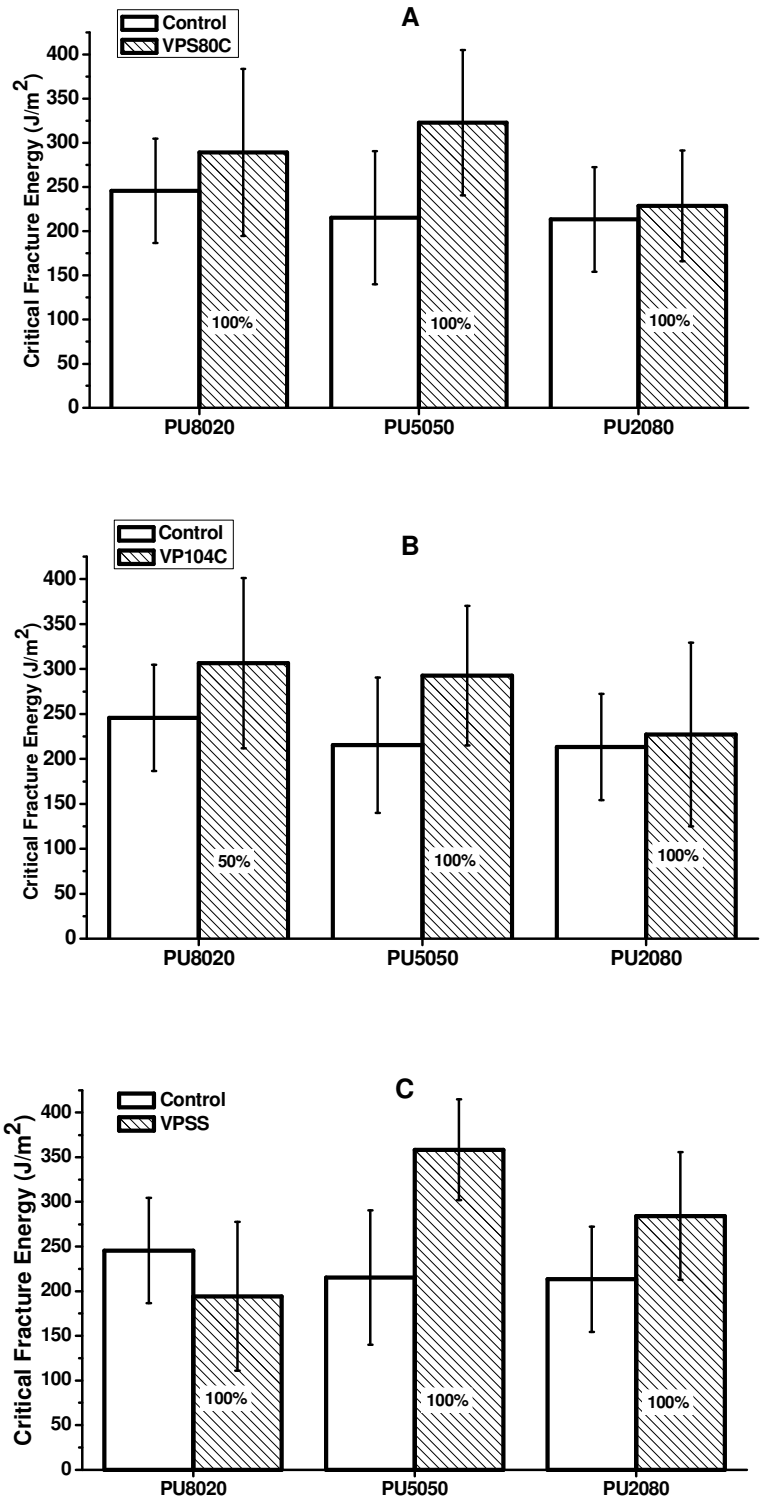

Figure 5-4 Average critical fracture energy of control (unweathered) and weathered DCB specimens; error bars represent ± 1 standard deviation (n = 33-110); numbers on the bars represent the weathering survival ratios; A) VPS80C; B)VPS104C; C) VPSS

As discussed previously, PU5050 and PU2080 bondlines show enhanced fracture toughness after VPSS treatment and PU5050 demonstrates the best weather durability (Figure 5-4C). The weathering-induced fracture toughness enhancement is not uncommon; this behavior has been reported [8-11]. However, the explanation for this behavior has not been well documented; several possible causes are proposed here. First of all, water-plasticized specimens are treated at high temperatures (80 – 105 °C), which could further cure the remaining isocyanates. Second, the dual-phase morphology is critical to the performance of polyurethane/ureas, and hydrogen bonding within the hard segments is the primary driving force for phase separation [12-14]. High temperatures and water plasticizing could certainly affect the hydrogen bonding strength, thus the phase morphology of cured PURs. Third, the fracture toughness of polymers has been found to correlate with their molecular mobility [15-17], which could also be altered by weathering treatments. Furthermore, it is believed that the bondline stress relaxation during weathering significantly contributes to the improved wood bondline toughness [8, 11]. All these weathering-induced effects will be discussed in the next chapter.

5.4. Conclusion

Three PUR wood adhesives with different hard segment contents were prepared by varying the mass ratio of PPG2000/PPG400 in the soft phase at a constant NCO/OH ratio. Three accelerated weathering procedures (VPS80C, VPS104C, and VPSS) were developed and used to study PUR/wood bondline weather durability evaluated by mode-I fracture testing. VPS80C and VPS104 weathering procedures were unable to differentiate the weather durability of the three PURs; the treated specimens all showed increased fracture toughness with a complication that VPS104C-treated PU8020 (lowest hard segment content) specimens only have a survival ratio of

50%. In contrast, VPSS procedure successfully distinguished the weather durability of the three PURs such that PU8020 showed decreased bondline toughness while the other two adhesives exhibited enhanced bondline toughness. Consequently, PUR structure-durability studies against VPSS weathering is the focus of our research, discussed in the next chapter.

References

1. ASTM, ASTM D2559 - 04, Standard Specification for Adhesives for Structural Laminated Wood Products for Use Under Exterior (Wet Use) Exposure Conditions. 2004.

2. Lopez-Suevos, F. and C.E. Frazie, Fracture cleavage analysis of PVAc latex adhesives: influence of phenolic additives. Holzforschung, 2006. 60: p. 313-317.

3. Vick, C.B. and E.A. Okkonen, Strength and durability of one-part polyurethane adhesive bonds to wood. Forest Products Journal, 1998. 48(11-12): p. 71-76.

4. Vick, C.B. and E.A. Okkonen, Durability of one-part polyurethane bonds to wood improved by HMR coupling agent. Forest Products Journal, 2000. 50(10): p. 69-75.

5. Uysal, B. and A. Ozcifci, Bond strength and durabilty behavior of polyurethane-based Desmodur-VTKA adhesives used for building materials after being exposed to water-resistance test. Journal of Applied Polymer Science, 2006. 100(5): p. 3943-3947.

6. ASTM, ASTM D5155-07, Standard Test Methods for Polyurethane Raw Materials Determination of the Isocyanate Content of Aromatic Isocyanates. 2007.

7. Gagliano, J.M. and C.E. Frazier, Improvements in the fracture cleavage testing of adhesively-bonded wood. wood and fiber science, 2001. 33(3): p. 377-385.

8. Scoville, C.R., Characterizing the Durability of PF and pMDI Adhesives Through Fracture Testing. 2001, Wood-Based Composites Center: Blacksburg.

9. Zheng, J., Studies of PF Resole / Isocyanate Hybride Adhesives, in Wood Science and Forest Products. 2002, Virginia Polytechnic Institute and State University: Blacksburg. p. 198.

10. Schmidt, R.G., Aspects of Wood Adhesion: Applications of 13C CP/MAS NMR and Fracture Testing, in Wood Science and Forest Products. 1998, Virginia Polytechnic Institute and State University: Blacksburg. p. 140.

11. Brown, N.R., Understanding the Role of N-Methyloacrylamide (NMA) Distribution in Poly(Vinyl Acetate) Latex Adhesives, in Wood Science and Forest Products. 2003, Virginia Polytechnic Institute and State University: Blacksburg. p. 331.

12. Yilgor, I., E. Yilgor, I.G. Guler, T.C. Ward, and G.L. Wilkes, FTIR investigation of the influence of diisocyanate symmetry on the morphology development in model segmented polyurethanes. Polymer, 2006. 47(11): p. 4105-4114.

13. schollenberger, C., Handbook of elastomers. 2001, New York: Marcel Dekker Inc.

14. Sun, H., Ab-Initio Characterizations of Molecular-Structures, Conformation Energies, and Hydrogen-Bonding Properties for Polyurethane Hard Segments. Macromolecules, 1993. 26(22): p. 5924-5936.

15. Grein, C., K. Bernreitner, and M. Gahleitner, Potential and limits of dynamic mechanical analysis as a tool for fracture resistance evaluation of isotactic polypropylenes and their polyolefin blends. Journal of Applied Polymer Science, 2004. 93(4): p. 1854-1867.

16. Kendall, K., Connection between Fracture Energy and Inelastic Behavior. Acta Metallurgica, 1979. 27(6): p. 1065-1073.

17. Kisbenyi, M., M.W. Birch, J.M. Hodgkinson, and J.G. Williams, Correlation of Impact Fracture-Toughness with Loss Peaks in Ptfe. Polymer, 1979. 20(10): p. 1289-1297.

Chapter 6 Investigate the Weather Durability of Moisture-Cure Polyurethane Wood Adhesives

Dakai Ren and Charles E. Frazier*

Macromolecules and Interfaces Institute

Wood-Based Composites Center

Department of Wood Science and Forest Products

Virginia Tech, Blacksburg, VA, 24061

* Corresponding author Tel: 540-231-8318 Email: cfrazier@vt.edu

Abstract

PUR water sensitivity was studied by water absorption experiments and water-submersion DMA. The hard segment softening temperatures of water-saturated specimens and the water plasticizing effects were detected using water-submersion DMA; both were found potentially to correlate with PUR weather durability evaluated by mode-I fracture testing. Both correlations suggest that the time efficient water-submersion DMA could be an excellent approach for quickly evaluating PUR weather durability. The weathering-induced molecular changes were investigated using attenuated total reflectance Fourier transform infrared spectroscopy (ATR-FTIR) and dynamic mechanical analyses (DMA). FTIR studies revealed that VPSS weathering resulted in post-cure, hydrolytic degradation, and urethane/urea hydrogen bonding changes; direct correlation between complex infrared data and weather durability was difficult. In DMA, VPSS-treated PUR films showed significant modulus reduction. In addition, a reduction of the hard segment softening damping intensity of PU8020 was observed in both weathered film and composite specimens;

this seems to correlate with its weakened bondline, but much is unknown about the nature of the damping intensity variation.

Keywords: Moisture-cure polyurethane, wood adhesion, weather durability, FTIR, DMA

6.1 Introduction

Moisture-cure polyurethane (PUR) adhesives are becoming more and more prevalent in the wood composites industry; nevertheless, there are few publications addressing their weather durability. Vick and Okkonen [3] found that a moderately severe weathering of PUR-bonded wood resulted in a low percentage of wood failure (poor performance), and that ASTM D2559 weathering/delamination testing resulted in severe delamination (up to 71.1%). Uysal and Ozcifci [5] found that PUR-bonded oak, oriental beech and scotch pine samples lost 85.6%, 62.2%, and 60.5% respectively of their shear strength after a severe weathering treatment. This same paper suggested that the extractive chemicals and the high density of oak wood were responsible for its more severe loss of bondline strength. These citations reveal that the wood bonding durability of PUR adhesives do not always meet structural certification criteria. These deficiencies can be overcome with adhesion primers. For instance, Vick and Okkonen [4] reported that hydroxymethylated resorcinol (HMR) priming agent will dramatically improve PUR/wood adhesion and durability. However, such primers are rarely if ever used during industrial practice. Consequently, PUR manufacturers are left with synthetic and formulation challenges as they balance cost and performance. This chapter addresses how variation of the PUR soft phase composition impacts adhesive durability against simulated weathering. As previously described, three PURs were prepared such that the soft segment composition varied as

a mixture of short and long poly(propylene glycol) (PPG) chains. As the PPG composition tends towards shorter chains, the percentage hard phase increases significantly; and this feature seems to dominate adhesive properties. Chapter 4 revealed that hard segment content significantly affected PUR molecular weight distribution, viscosity, wood penetration, and thermal properties. However, hard segment content had a minor influence on unweathered PUR bondline toughness. It is certainly of great interest to know how hard phase content affects weather durability as measured through mode-I toughness. As described in Chapter 5, accelerated weathering procedures were composed of multiple cycles of water soaking and heating (drying or steaming/drying steps). Therefore, the adhesive's water affinity, and water sensitivity (particularly at elevated temperatures) are fundamentals to understand adhesive weather durability. Generally, polyurethane water affinity depends on the weight fraction of the soft segments [1-2], and the absorbed water plasticizes the material thus reduces the thermal transition temperatures [1, 3]. As described in Chapter 5, the three moisture-cure polyurethane (PUR) wood adhesives used in durability studies contained different soft/hard phase fractions thus varying water affinity. In this research, their water absorption capacities were measured and the water plasticizing effects were studied using water-submersion dynamic mechanical analyses (DMA); subsequently, the relationship between these results and weather durability was explored.

In spite of the practical significance of PUR weather durability, little is known about the weathering-induced PUR molecular changes, especially within wood bondline. Fernando et al. [4] studied the molecular relaxation phenomena of a PUR coating during accelerated weathering, which introduced the effects of ultraviolet radiation, moisture absorption, and temperature variation. The stress relaxation studies showed an increasingly broad distribution of relaxation

times with increased chain scissions. In addition, this same paper disclosed that the effective crosslinking density decreased after 8 weeks of weathering exposure. Although this article does shed some light on this subject, but there are many differences between our systems - different PUR chemistry, substrates, and weathering procedures. In this study, the weathering-induced molecular changes to PUR wood adhesives were carefully investigated using FTIR and DMA methods. Importantly, FTIR and DMA specimens were directly excised from the double cantilever beam (DCB) fracture specimens; therefore, the correlation between analytical data and fracture results were conveniently studied concurrently.

6.2 Experimental

6.2.1 Materials

6.2.1.1 DCB Fracture Specimens

The same unweathered and weathered DCB fracture specimens used for weather durability studies (Chapter 5) were further investigated. These DCB specimens were bonded using three PURs with different hard phase contents; the properties of the PURs are shown in Table 6-1.

6.2.1.2 PUR Films

A PUR prepolymer was cast onto a dry polyethylene sheet under nitrogen using a film applicator, and then immediately moved into a dessicator that had been pre-conditioned to RH 65% using saturated ammonium nitrate. The film was allowed to cure at room temperature for two weeks;

the resulting film thickness was ~ 800 µm. Two separate film specimens were prepared for each adhesive.

Table 6-1 The compositions and characteristics of PUR prepolymers

PUR Prepolymer	PPG2000/PPG400 mass ratio	NCO/OH molar ratio	Hard segment content (%)	Measured NCO (%)
PU8020	80/20	5/1	53.5	13.35 ± 0.04
PU5050	50/50	5/1	65.4	16.10 ± 0.02
PU2080	20/80	5/1	72.5	17.85 ± 0.09

6.2.2 Dynamic Mechanical Analyses (DMA)

6.2.2.1 Preparation of DMA Film Specimens

Disk DMA film specimens (dia. = 8 mm) were directly punched from PUR films and divided into three groups. The first group was the control (untreated). The second was treated using the VPSS weathering procedure (refer to Chapter 5 for details). Subsequently, the first and second groups were vacuum dried (0.5 mmHg, room temp., 48 h) and then stored over P_2O_5 and dry N_2 prior to analysis. The third group was immersed in distilled water under vacuum (5 mmHg, 20 min), and then at room conditions (2 d) to reach water saturation. The first and second groups were tested in a dry environment (dry-DMA), while the third was evaluated in water-submersion DMA.

6.2.2.2 Preparation of DMA Composite Specimens

A small block (40-mm long) was removed from the end of each DCB specimen (control and weathered). Then the bondline was excised by trimming wood from both sides of the adhesive layer to achieve a thin composite (thickness ~650 μm). Table 6-2 shows the average composition of DMA composite specimens, measured using fluorescence microscopy. Disk DMA specimens (dia. = 8 mm) were punched from this thin composite; these DMA specimens were vacuum dried (0.5 mmHg, room temp., 48 h) and stored over P_2O_5 and dry N_2 prior to analysis.

Table 6-2 Average composition of DMA composite specimens

Adhesive	Adhesive layer thickness (μm)	Penetration to each side (μm)	Adhesive layer fraction (v %)	Penetration fraction (v%)	Total bondline fraction (v%)
PU8020	57	128	9	20	29
PU5050	81	112	12	19	31
PU2080	133	34	20	5	25

6.2.2.3 DMA Methods

Dry-DMA tests were conducted on a TA Instruments AR1000 rheometer using 8 mm dia stainless steel parallel-plate geometry. A single specimen was placed between the plates under a normal force (films 10 N; composites 15 N). The specimen was equilibrated at 5 °C for 5 min, and then heated to 180 °C (3 °C/min, 1 Hz); all tests were conducted within the linear response region. For water-submersion DMA, the same geometry was used except that the bottom plate was positioned at the center bottom of a steel water cup; therefore the specimen was immersed in

water throughout the test. A single water-saturated film specimen was held (normal force 2 N) between the plates under water and heated from 25 °C to 95 °C (3 °C/min, 1 Hz). For each sample group, at least three separate observations were used to generate an average DMA response using the "*Average Multiple Curves*" function in OriginPro software version 8.0.63 (OriginLab, Northampton, MA, U.S.A.).

6.2.3 Water Absorption of PUR Films

A 10-mL glass vial was filled with distilled water (3 mL) and closed using a rubber septum with a copper wire passing through its center. A small piece of PUR film (~ 10 × 10 mm) was hooked on the end of the wire and hung in the water-saturated air space without contacting the liquid water. The room temperature specimen weight gain was recorded over time. For each adhesive, five separate measurements were collected to obtain the average water absorption.

6.2.4 Fourier Transform Infrared Spectroscopy (FTIR)

Recall, DCB adhesion testing was conducted in mode-I cleavage such that the last 50 mm of the bondlines remained intact (refer to Chapter 4 and Chapter 5). The partially debonded DCB specimens were transported to the infrared analysis lab, whereafter the DCB specimens were completely debonded through manual cleavage. The freshly exposed failure surfaces were immediately analyzed in reflectance mode; and care was taken to sample the adhesive layer which was visible on the failure surface. Failure surfaces that were all or mostly wood were not sampled, or they were excluded from consideration when the corresponding spectra revealed a wood-dominated signal (sampling strategy is illustrated in Appendix 6-1).

FTIR spectra were recorded on a MIDAC M2004 spectrometer using an attenuated total reflection accessory (ATR, Durascope^{TM}, SensIR Technologies). All spectra were collected using 128 scans with a resolution of 4 cm^{-1}. Eighteen spectra for each sample group (three random DCBs and six spectra from each DCB) were collected and used to generate an average spectrum (same method described in Section 6.2.2.3).

6.3 Results and Discussion

As discussed in Chapter 5, VPSS was selected for PUR structure - weather durability studies because it effectively distinguished the weather durability of PUR adhesives (Figure 6-1). All with 100% survival ratio, PU8020 shows decreased bondline toughness while PU5050 and PU2080 exhibit increased bondline toughness after VPSS weathering. The following discussions will focus on discovering the fundamental properties of PURs that are associated with their distinct weathering performance, and revealing VPSS weathering-induced bondline molecular changes.

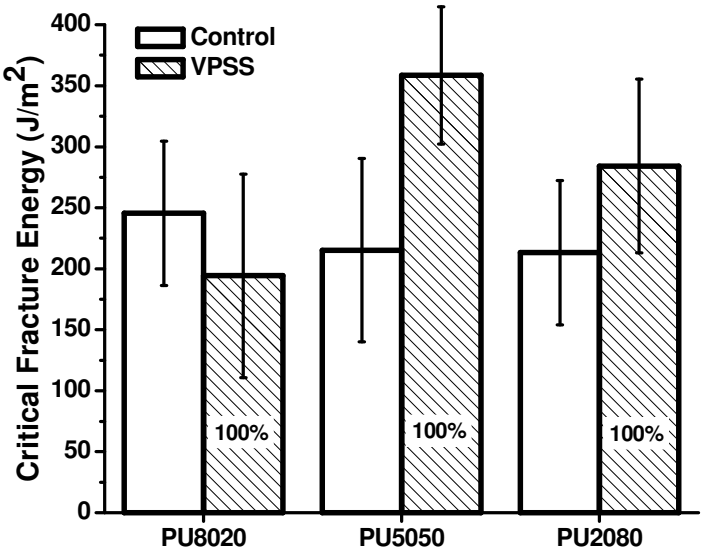

Figure 6-1 Average critical fracture energy of control (unweathered) and VPSS-weathered DCB specimens; error bars represent one standard deviation (n = 33-110); numbers on the bars represent the weathering survival ratios.

6.3.1 PUR Water Sensitivity

6.3.1.1 Water Absorption

PUR cures with moisture and simultaneously releases CO_2, thus forming a foam. To avoid capillary water uptake during the water absorption experiments, the PUR film specimen was equilibrated with moisture-saturated air without contacting liquid water.

As seen in Figure 6-2, all PUR films show initially rapid moisture absorption and take up the same amount of moisture after a 2-day period. With time, the absorption rates for PU5050 and PU2080 dramatically decrease and reach equilibrium after 8 days. Regarding PU8020, although the absorption slows down with time, the films have not reached equilibrium even after 21 days.

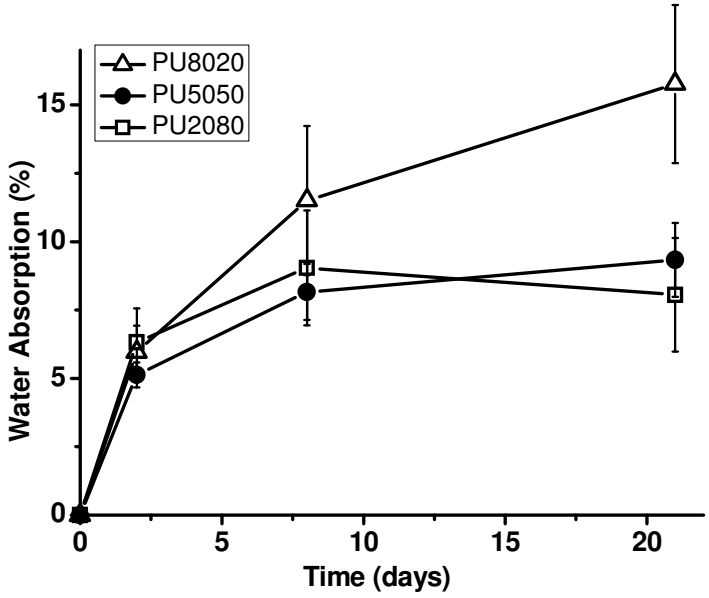

Figure 6-2 Average room temperature water absorption over time when PUR films equilibrated in saturated air; error bars represent one standard deviation (n = 5).

Gas permeation into a polymer film is a function of the penetrant solubility and its diffusive movement in the polymer matrix [8]. For water vapor permeation, the solubility of water molecule is related to the polymer hydrophilicity, whereas the diffusivity of the water molecule is mostly attributed to the polymer free volume [9-10]. Consequently, the water vapor permeability is controlled by not only hydrophilicity but also free volume of the polymer. Regarding polyurethane materials, the soft segments are generally flexible at room temperature (subambient T_g), containing higher free volume and thus greater diffusive coefficient [9-10]. Consequently, polyurethane water absorption is proportional to the weight fraction of the soft segments [4, 11-12]. Consistent with this scenario, PU8020 shows higher moisture uptake than the other two adhesives (Figure 6-2). However, PU5050 absorbs the same amount of moisture as

PU2080 although PU5050 contains higher soft segment content, which implies the hard segment effects. PUR hard segments are closely associated to a rigid structure by covalent and hydrogen bonding in cured films, reducing free volume in the hard segments and thus the diffusive coefficient. Moreover, strongly connected hard segments could largely restrict the soft segment mobility. For PU5050 and PU2080 films, high percentage of hard segment content dominates the systems such that no visible subambient soft segment T_g is observed (Figure 4-5); as a result, soft segment content does not significantly influence their free volume at room temperature. This may explain the similar water absorption behavior of PU5050 and PU2080 films (Figure 6-2). While the diffusivity is lower in hard domains, they are more hydrophilic in nature. The absorbed water could split the hard segment hydrogen bonds and plasticize the material [13], which will be discussed in the following Section 6.3.1.2.

6.3.1.2 Water-submersion DMA on PUR Films

In this method, specimens are water saturated prior to DMA tests and held immersed in water throughout the temperature ramp. That is, the specimens are subjected to both water saturation and heating treatments simultaneously. Recall that the DCB specimens were subjected to cyclic water soaking and heating (drying and steaming) during the accelerated weathering. In other words, water-submersion DMA simulates accelerated weathering conditions to some extent. Therefore, water-submersion DMA not only provides direct measurement of the water plasticizing effects, but also PUR thermal properties under simulated weathering conditions.

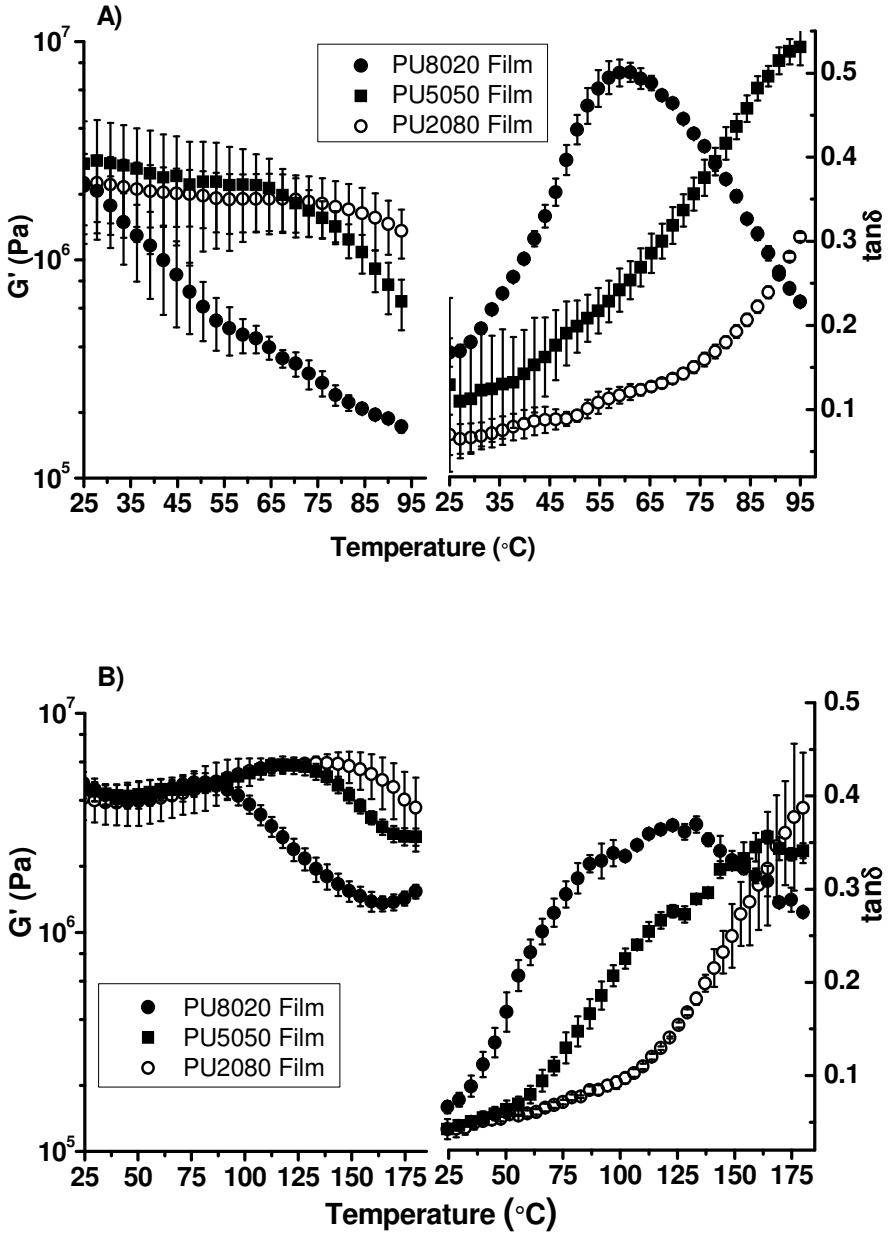

Figure 6-3 Average DMA 1st heating scans of cured PUR films showing the hard segment softening (3 °C/min, 1 Hz.); error bars represent ± 1 standard deviation (n = 3); A) Water-submersion DMA; B) Dry-DMA.

In this research, water-submersion DMA was conducted within 25 - 95 °C, corresponding to PUR hard segment softening (Figure 6-3A). Consistent with dry-DMA data (Figure 6-3B), the hard segment softening temperature (tan δ maximum, T_h) increases with the hard segment content. More importantly, water-submersion DMA thermograms clearly show evidences of water plasticizing effects when compared to dry-DMA: 1) lower storage modulus with greater reduction during transition; 2) narrower tan δ peaks with significantly higher damping intensities; 3) much lower T_h. The water-induced T_h reduction is estimated as the difference of storage modulus softening onset temperatures between the dry and water-submersion DMA (Figure 6-4). Note that PU8020 softening onsets even below room temperature; an additional water-submersion DMA experiment (Appendix 6-2) reveals the onset temperature at 13.3 °C.

Observed from Figure 6-4, PU8020 shows the largest water-induced T_h reduction, which is consistent with its highest water absorption (Figure 6-2) and poor weathering durability (Figure 6-1). It is interesting that PU5050 shows a significantly lower T_h reduction than PU2080, although they have similar water absorption (Figure 6-2); this seems to correlate with PU5050's better weather durability (Figure 6-1). Overall, the T_h reduction indicates water plasticizing strength, and the data (Figure 6-4) appears to correlate well with PUR weather durability; the smaller the T_h reduction, the better the weather durability.

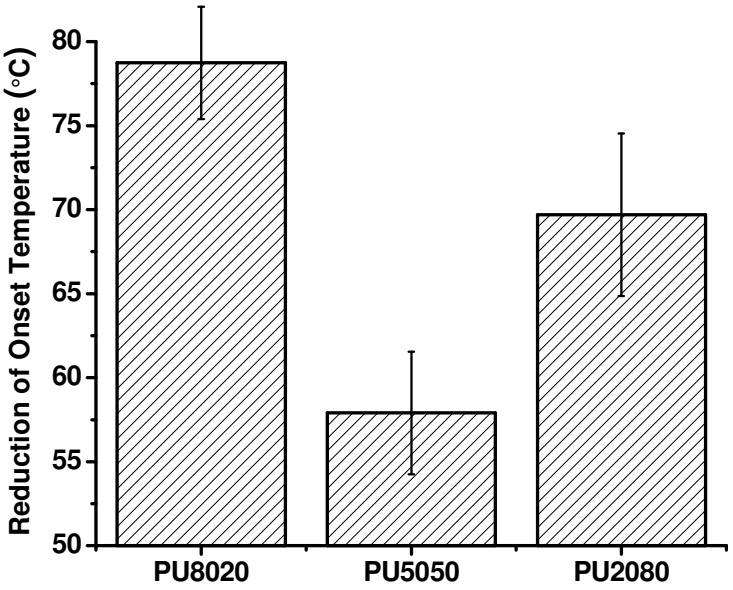

Figure 6-4 The reduction of PUR hard segment onset-softening temperature in water-submersion DMA compared to dry DMA; error bars represent ± 1 standard deviation (n = 3).

Recall that a vigorous steaming step (105 °C, 2 h) was included in the VPSS weathering procedure. Under water-saturated conditions, PU8020 shows a T_h of about 60 °C (Figure 6-3A), while the other two adhesives show T_hs more comparable to the steaming temperature. Combining results in Figure 6-1, the T_h in water-submersion DMA perhaps correlates with PUR weather durability; lower T_h (particularly much lower than the weathering temperature) correlates with inferior weather durability and higher T_h connects with better durability.

Water-submersion DMA provided the T_h of water-saturated specimens, and simultaneously the water plasticizing effects (T_h reduction, Figure 6-4), both were found to correlate with PUR weather durability in this study. Generally, it takes more than a month to measure wood bondline weather durability by accelerated weathering paired with mechanical testing. In

contrast, water-submersion DMA is very time efficient (about two days), which makes it an excellent candidate as a quick evaluation method for PUR weather durability. Obviously, the proposed preliminary correlations between water-submersion DMA data and weather durability are of practical significance, thus deserve further investigation.

6.3.2 Weathering-induced Molecular Changes

The following will focus on discussing PUR molecular changes caused by VPSS weathering, studied using FTIR and DMA methods. One strength of this research is that it directly analyzes the same control (unweathered) and weathered DCB specimens used for weather durability studies. This is essential for our efforts to correlate analytic data with PUR weather durability evaluated by mode-I fracture testing.

6.3.2.1 FTIR

As previously discussed in Chapter 3, PUR cure is a moisture-diffusion dominated process [6]. When the liquid PUR prepolymer is exposed to wood moisture, the surface layer reacts quickly to form a skin that slows moisture diffusion into the uncured bulk. As isocyanate functionality is consumed, the urea content increases and the dual phase morphology evolves as urea segments associate through strong hydrogen bonds and then phase-separate from the soft phase. The hydrogen-bonded hard segments in turn confine the mobility and water accessibility of remaining isocyanates, thus quench the cure reactions. During VPSS weathering, water saturation and steaming (105 °C and 1.2 bar) could provide sufficient chain mobility and moisture for complete cure; meanwhile, these treatments could also affect PUR hydrogen

bonding strength and thus the phase morphology. The weathering effects on PUR cure and hydrogen bonding are readily detected using infrared spectroscopy to observe changes in free isocyanate and carbonyl stretching frequencies.

Observed from Figure 6-5, all controls show a peak at 2280 cm^{-1}, indicating uncured free isocyanate. The amount of remaining isocyanate is estimated by comparing the isocyanate peak area to that of the corresponding uncured prepolymer; about 0.8%, 1.4%, and 1.1% isocyanate remains uncured in PU8020, PU5050, and PU2080 controls, respectively. A similar amount of uncured isocyanate (1.3%) was found in a cured polyurethane foam [7]. More importantly, weathering-induced cure is evident in Figure 6-5; free isocyanate peaks are absent in VPSS-treated specimens. Considering adhesive durability, Figure 6-1, the ocurrence of weathering-induced postcure is not simply correlated with durability; PU5050 and PU2080 exhibit enhanced toughness after weatheirng, but PU8020 suffers reduced bondline toughness.

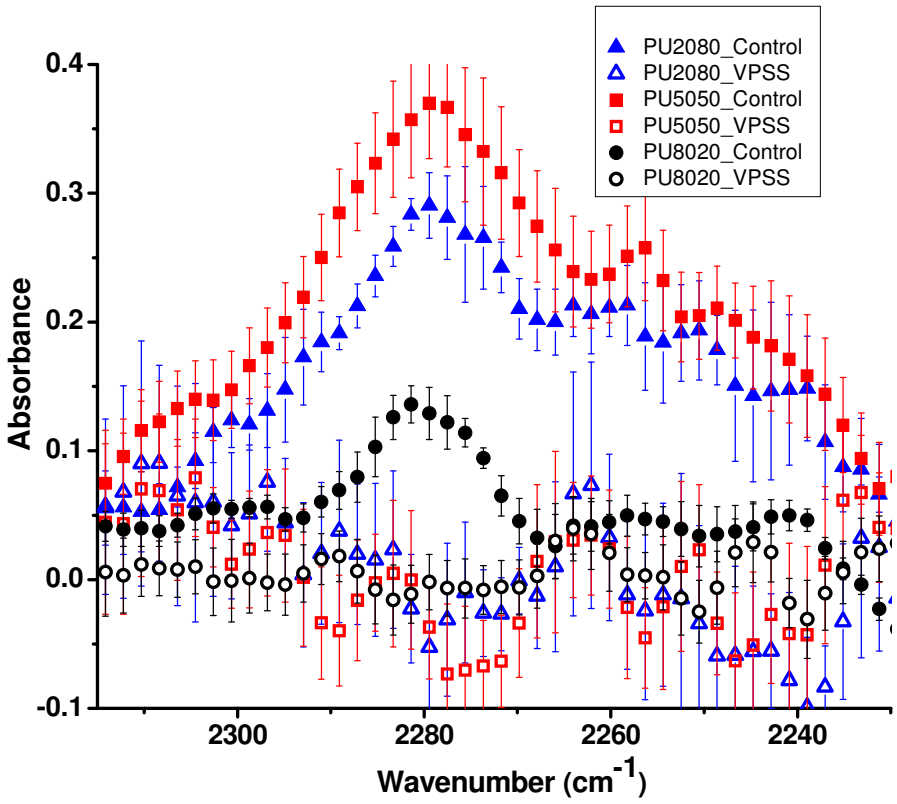

Figure 6-5 The average FTIR spectra showing the free isocyanate stretching region; bars represent ± 1 standard deviation (n = 18); spectra normalized by the phenylene signal 1594 cm^{-1} (not shown) with intensities of 1.0, 1.22, and 1.36 based upon the hard phase contents of PU8020, PU5050, and PU2080, respectively.

As shown in Figure 6-6, VPSS weathering significantly alters the IR carbonyl stretching absorbance. The shift of the FTIR absorbance for the carbonyl group to a lower frequency is evidence of hydrogen bond formation; the magnitude of the shift is a measure of the hydrogen bonding strength. Isolated or "free" carbonyl groups exhibit stretching bands at 1729-1740 cm^{-1} and 1690-1700 cm^{-1} for urethane and urea, respectively[8-10]. Hydrogen bonding shifts the urethane carbonyl stretching vibration to 1700-1715 cm^{-1} (urethane-urethane H-bonds) and 1725-

1730 cm^{-1} (urethane-soft segment H-bonds), whereas the urea carbonyl shifts to 1650-1690 cm^{-1} (monodentate H-bonded) and 1628-1650 cm^{-1} (bidentate H-bonded) [8-10].

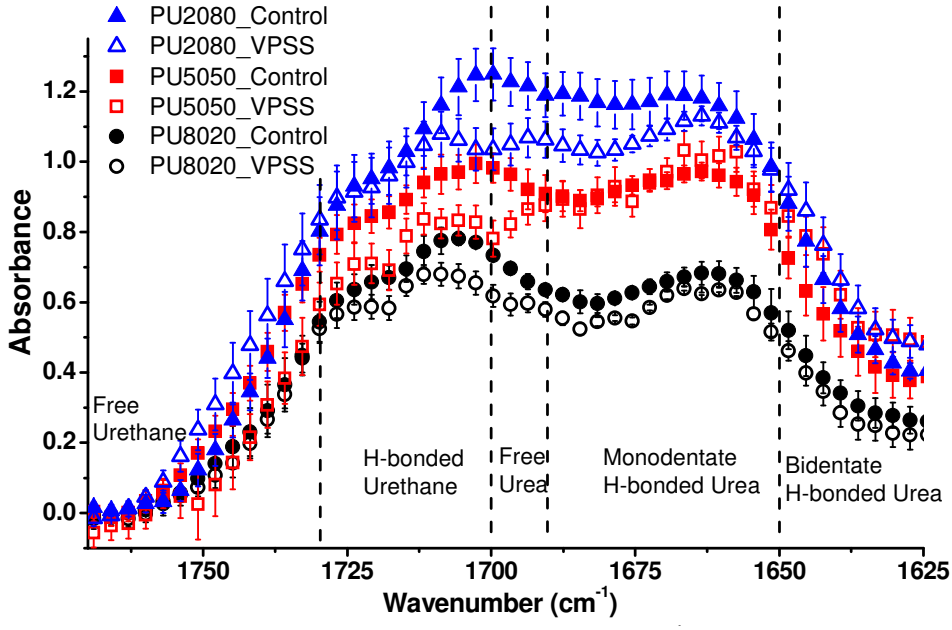

Figure 6-6 The average FTIR spectra showing the carbonyl stretching region; error bars represent ± 1 standard deviation (n = 18); spectra normalized by the phenylene signal 1594 cm^{-1} (not shown) with intensities of 1.0, 1.22, and 1.36 based upon the hard phase contents of PU8020, PU5050, and PU2080, respectively.

Observed in Figure 6-6, each adhesive exhibits common as well as different weathering effects. Fist focusing on similarities, all weathered bondlines show a reduction of overall carbonyl absorbance intensity (peak area); particularly in the urethane and free urea frequencies. In the mean time, all VPSS-treated specimens show increased amine infrared absorption (Appendix 6-3). As documented, amine is generated from hydrolysis of polyurethane/ureas [11-14]. Hence, the overall reduction of carbonyl intensity is attributed to urethane/urea hydrolysis. Besides the

similarities, each adhesive shows distinct weathering behavior as well. For instance, unlike PU5050, VPSS-treated PU8020 and PU2080 show decreased monodentate hydrogen-bonded urea content. For another, PU8020 is the only adhesive that shows reduced bidentate hydrogen-bonded urea content after VPSS treatment. These complex changes prevent direct correlations between infrared data and weather durability. For more quantitative analysis, the peak deconvolution of FTIR spectra has been attempted. As illustrated in Appendix 6-4, the deconvoluted data in general supports the weathering effects seen in Figure 6-6.

The same FTIR methodology was used to investigate VPS80C and VPS104C treated specimens; the results are included in Appendix 6-5. These two weathering procedures are relatively moderate comparing to VPSS, consequently only minor changes are observed. In both cases, it appears that only PU8020 shows an overall intensity reduction, particularly in the urethane region.

6.3.2.2 Dry-DMA

As described previously, composite DMA specimens were directly excised from the bondlines of control and weathered DCB specimens, and then investigated using parallel-plate torsional DMA to explore the changes of thermal and morphological properties. In other words, both mechanical (mode-I fracture toughness) and analytical results were obtained from the same specimens; the relations of these two were conveniently investigated. As mentioned, the purpose of this study is to reveal the weathering-induced changes, thus the following discussions will

focus on the differences between the control and weathered specimens; more detailed discussion on a single DMA thermogram can be found in Chapter 4.

Prior to DMA investigation of the complex PUR/wood bondline, VPSS-induced changes of thermal properties were first studied using neat-PUR films, Figure 6-7. All adhesives show a modulus reduction after VPSS treatment, particularly in the stiffening region prior to the hard segment softening, perhaps suggesting a decrease of effective crosslinking density. However, all adhesives have the same control modulus at this region, although their crosslinking densities are different (hard segment content effects, Chapter 4); their modulus values could have been complicated by the densifying normal force under compression DMA mode. In particular, PU8020 shows the largest modulus reduction, which is consistent with its overall decrease of hydrogen bonds, especially the strong bidentate urea hydrogen bonds (Figure 6-6). Regarding tan δ traces, PU8020 shows significantly reduced damping whereas PU5050 and PU2080 exhibits slightly enhanced damping.

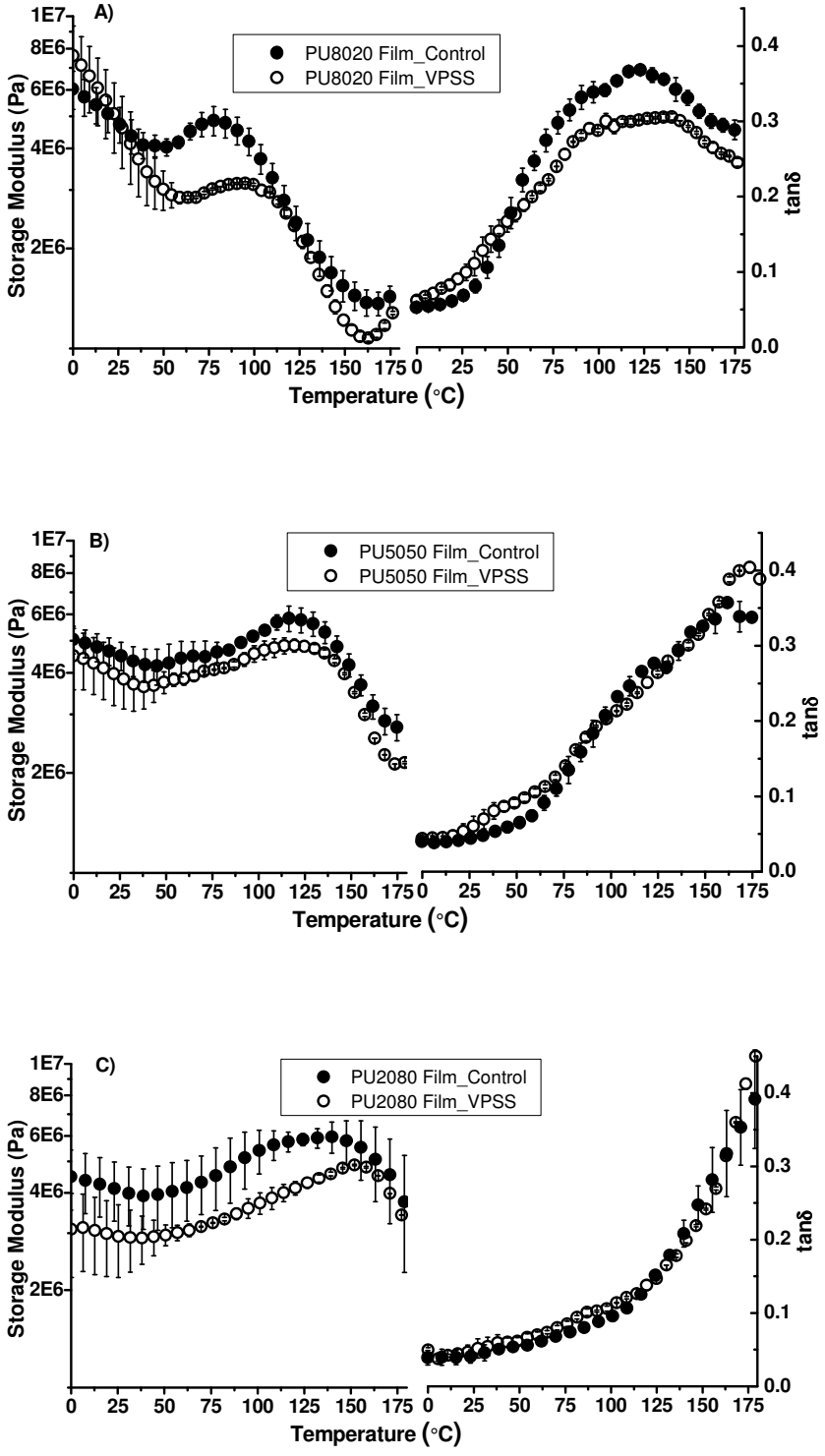

Figure 6-7 Average dry-DMA 1st heating scans of control and VPSS-treated PUR films (3 °C/min, 1 Hz.); error bars represent ± 1 standard deviation (n = 3); A) PU8020; B) PU5050; C) PU2080.

Figure 6-8 compares DMA first heating scans of control and VPSS-treated DCB specimens. First focusing on the storage modulus, all bondlines show either improved or unchanged modulus after weathering, but recall that all VPSS-treated adhesive films exhibit decreased storage modulus (Figure 6-7). This perhaps is simply due to increased wood modulus (dry wood DMA in Appendix 6-6) in composite specimens or enhanced wood/adhesive interactions during weathering. Observed from Figure 6-8 tan δ plots, a shoulder appears at around 45 °C for all control specimens and disappears for the weathered specimens. This shoulder corresponds to a weak wood transition at 45 °C, which is seen in the control wood but not in VPSS-treated wood (Appendix 6-6). Compared to Figure 6-7, all control DCBs softens at a higher temperature (ca. 5 -10 °C) than their respective PUR films, suggesting strong wood/PUR interactions; these interactions have been discussed in details in Chapter 3. Consistent with PUR films, PU5050 and PU2080 DCB specimens behave similarly that their hard segment softening tan δ intensities (simply referred to as "damping intensity" in the following discussion) increase after VPSS treatment; on the other hand, PU8020's damping intensity decreases after weathering. Recall that VPSS treatment only reduces PU8020 bondline toughness whereas increases PU5050 and PU2080 toughness (Figure 6-1). This appears to correlate with PUR damping intensity; reduced damping associates with decreased toughness after weathering. DMA studies on VPS80C (Appendix 6-7) and VPS104C-treated specimens (Appendix 6-8) in general supports this correlation. Unfortunately, the weathering-induced damping intensity variations are not understood, neither is the correlation between PUR weather durability and damping intensity. In addition, the water-submersion DMA was also used to investigate the weathering effects on water-plasticized PUR bondlines (Appendix 6-9). PU8020 bondline was found most sensitive to weathering treatments, consistent with its inferior weather durability.

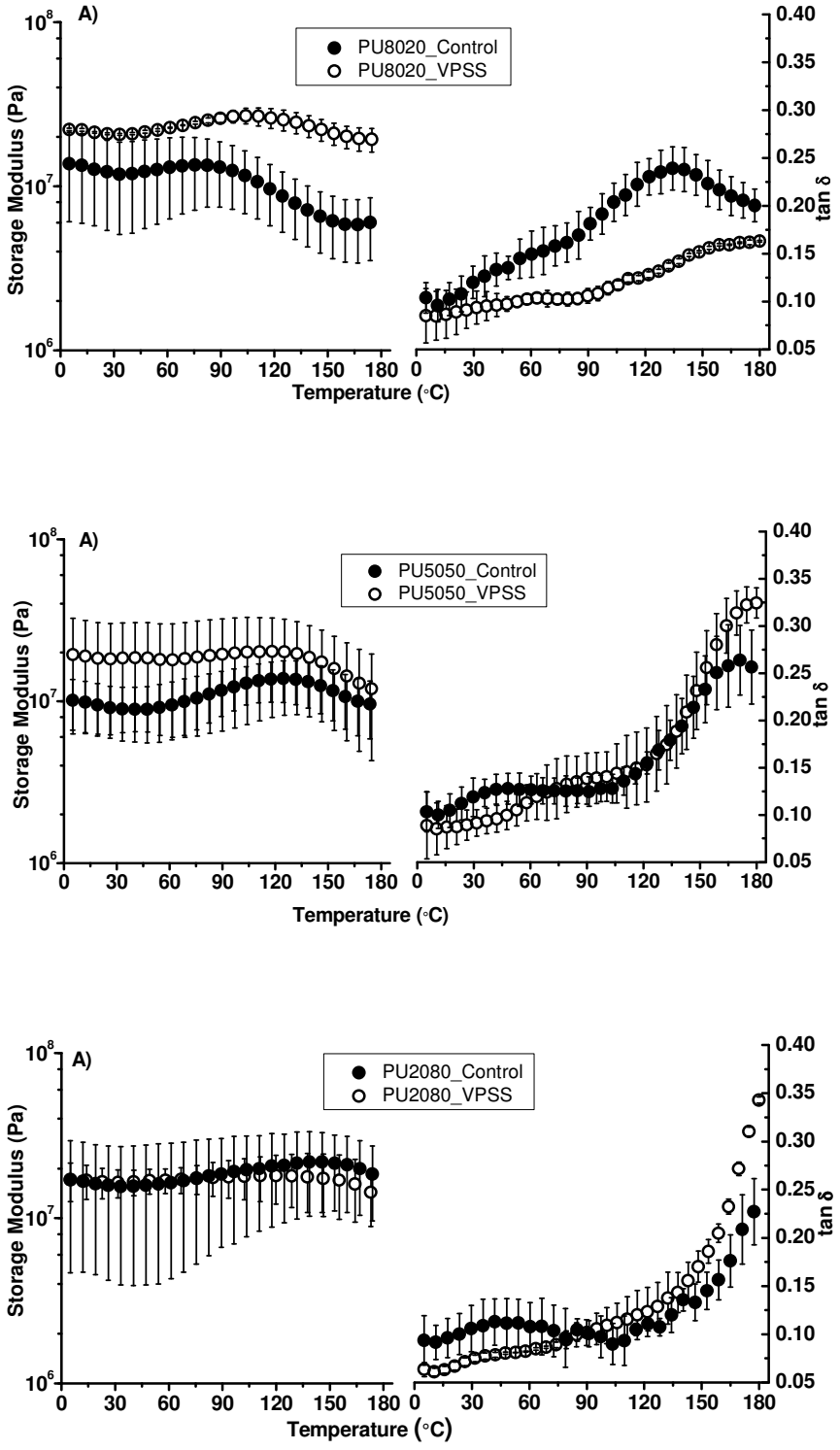

Figure 6-8 Average dry-DMA 1st heating scans of control and VPSS-treated DCB specimens (3 °C/min, 1 Hz.); error bars represent ± 1 standard deviation (n = 3); A) PU8020; B) PU5050; C) PU2080.

6.4 Conclusion

This study focused on the structure-durability studies of three PUR adhesives against VPSS weathering treatment. The PUR with lowest hard segment content showed the greatest water affinity and water plasticizing effects, which correlated to its inferior weather durability. Meanwhile, higher hard segment softening temperature in water-submersion DMA perhaps correlates with better weather durability. These correlations made the time efficient water-submersion DMA method an excellent candidate as a quick evaluation approach for PUR weather durability. FTIR and DMA methods were developed to study the weathering-induced molecular changes; correlations between analytical data and weather durability were explored concurrently. FTIR studies showed evidence of post-cure, hydrolytic degradation, and complex changes of hydrogen bonds, which prevented from establishing direct correlations with PUR weather durability. Regarding DMA thermograms, VPSS-treated PUR films showed significant modulus reduction, which was consistent with the urethane / urea hydrolytic degradation observed in FTIR. Being weathered, both PU8020 film and composite specimens showed a reduction of hard segment softening damping intensity, which appeared to correlate with its weakened wood/PUR bondline. However, neither the nature of the damping intensity variation nor this correlation was understood. As a whole, weathering-induced molecular changes were detected using FTIR and DMA methods; nevertheless, relationships between these changes and bondline durability still remain unclear.

References

1. Vick, C.B. and E.A. Okkonen, Strength and durability of one-part polyurethane adhesive bonds to wood. Forest Products Journal, 1998. 48(11-12): p. 71-76.

2. Uysal, B. and A. Ozcifci, Bond strength and durabilty behavior of polyurethane-based Desmodur-VTKA adhesives used for building materials after being exposed to water-resistance test. Journal of Applied Polymer Science, 2006. 100(5): p. 3943-3947.

3. Vick, C.B. and E.A. Okkonen, Durability of one-part polyurethane bonds to wood improved by HMR coupling agent. Forest Products Journal, 2000. 50(10): p. 69-75.

4. Pissis, P., L. Apekis, C. Christodoulides, M. Niaounakis, A. Kyritsis, and J. Nedbal, Water effects in polyurethane block copolymers. Journal of Polymer Science Part B-Polymer Physics, 1996. 34(9): p. 1529-1539.

5. Broos, R., R.M. Herrington, and F.M. Casati, Endurance of polyurethane automotive seating foams under varying temperature and humidity conditions. Cellular Polymers, 2000. 19(3): p. 169-204.

6. Yang, B., W.M. Huang, C. Li, and L. Li, Effects of moisture on the thermomechanical properties of a polyurethane shape memory polymer. Polymer, 2006. 47(4): p. 1348-1356.

7. Fernando, B.M.D., X. Shi, and S.G. Croll, Molecular relaxation phenomena during accelerated weathering of a polyurethane coating. Journal of Coatings Technology and Research, 2008. 5(1): p. 1-9.

8. Hu, J.L. and S. Mondal, Structural characterization and mass transfer properties of segmented polyurethane: influence of block length of hydrophilic segments. Polymer International, 2005. 54(5): p. 764-771.

9. Wang, Z.F., B. Wang, X.M. Ding, M. Zhang, L.M. Liu, N. Qi, and J.L. Hu, Effect of temperature and structure on the free volume and water vapor permeability in hydrophilic polyurethanes. Journal of Membrane Science, 2004. 241(2): p. 355-361.

10. Mondal, S., J.L. Hu, and Z. Yong, Free volume and water vapor permeability of dense segmented polyurethane membrane. Journal of Membrane Science, 2006. 280(1-2): p. 427-432.

11. Broos, R., R.M. Herrington, and F.M. Casati, Endurance of polyurethane automotive seating foams under varying temperature and humidity conditions. Cellular Polymers, 2000. 19(3): p. 169-204.

12. Dolmaire, N., E. Espuche, F. Mechin, and J.P. Pascault, Water transport properties of thermoplastic polyurethane films. Journal of Polymer Science Part B-Polymer Physics, 2004. 42(3): p. 473-492.

13. Shibaya, M., Y. Suzuki, M. Doro, H. Ishihara, N. Yoshihara, and M. Enomoto, Effect of soft segment component on moisture-permeable polyurethane films. Journal of Polymer Science Part B-Polymer Physics, 2006. 44(3): p. 573-583.

14. Chattopadhyay, D.K., B. Sreedhar, and K.V.S.N. Raju, The phase mixing studies on moisture cured polyurethane-ureas during cure. Polymer, 2006. 47(11): p. 3814-3825.

15. Cole, K.C., P. Vangheluwe, M.J. Hebrard, and J. Leroux, Flexible Polyurethane Foam .1. Ftir Analysis of Residual Isocyanate. Journal of Applied Polymer Science, 1987. 34(1): p. 395-407.

16. Luo, N., D.N. Wang, and S.K. Ying, Hydrogen-bonding properties of segmented polyether poly(urethane urea) copolymer. Macromolecules, 1997. 30(15): p. 4405-4409.

17. Daniel-da-Silva, A.L., J.C.M. Bordado, and J.M. Martin-Martinez, Moisture curing kinetics of isocyanate ended urethane quasi-prepolymers monitored by IR spectroscopy and DSC. Journal of Applied Polymer Science, 2008. 107: p. 700-709.

18. Rath, S.K., A.M. Ishack, U.G. Suryavansi, L. Chandrasekhar, and M. Patri, Phase morphology and surface properties of moisture cured polyurethane-urea (MCPU) coatings: Effect of catalysts. Progress in Organic Coatings, 2008. 62(4): p. 393-399.

19. Sendijarevic, V., A. Sendijarevic, I. Sendijarevic, R.E. Bailey, D. Pemberton, and K.A. Reimann, Hydrolytic stability of toluene diisocyanate and polymeric methylenediphenyl diisocyanate based polyureas under environmental conditions. Environmental Science & Technology, 2004. 38(4): p. 1066-1072.

20. MATUSZAK, M.L., K.C. FRISCH, and L. REEGENS, Hydrolysis of Linear Polyurethanes and Model Monocarbarnates. Journal of Polymer Science: Polymer Chemistry Edition, 1973. 11: p. 1683-1690.

21. Dickie, R.A., S.S. Labana, and R.S. Bauer, Cross-linked Polymers: Chemistry, Properties, and Applications. 1988: An American Chemical Society Publication.

22. Crawford, D.M., A.R. Teets, and D. Flanagan, Differential Scanning Calorimetry as a Method for indicatIng Hydrolysis of Urethane Elastomers. 1988: Fort Belvoir.

Chapter 7 Preparation of A Double-Labeled pMDI Resin for Solid-State NMR Characterization of pMDI Cure Chemistry

Dakai Ren[a,b,c,] Sungsool Wi[d], and Charles E. Frazier[a,b,c,*]

[a]Macromolecules and Interfaces Institute

[b]Wood-Based Composites Center

[c]Department of Wood Science and Forest Products

[d]Department of Chemistry

Virginia Tech, Blacksburg, VA, 24061

* Corresponding author Tel: 540-231-8318 Email: cfrazier@vt.edu

Abstract

A ^{13}C and ^{15}N double-labeled pMDI resin was prepared and used for solid-state NMR characterization of the pMDI/wood bondline. Previous NMR studies revealed the predominant formation of urea linkages, and provided only indirect evidence of urethane formation with wood because of the overlap of urethane and urea ^{13}C and ^{15}N signals. This research introduced rotational echo double resonance (REDOR) NMR technique as a new approach to quantitatively detect urethane formation independent of chemical shifts. REDOR NMR clearly revealed the formation of urethane linkages, but largely overestimated their content. This REDOR NMR method needs to be improved to be useful for quantitatively characterizing pMDI bondlines.

Keywords: Isocyanate, Wood Adhesives, Solid-state NMR, REDOR

7.1 Introduction

Polymeric methylenebis(phenylisocyanate) (pMDI) is an important wood bonding thermoset, primarily for bonding oriented strand board (OSB) and related strand products [1]. Commercial pMDI contains about 50% of the MDI monomer fraction and the higher order oligomeric polyisocyanates account for the remainder [1-2]. Initiated by a reaction with water to generate amine end groups, pMDI polymerizes to a polyurea network that subsequently adds additional isocyanate to form uret and polyuret structures. Meanwhile, pMDI could react with wood hydroxyl groups to form urethane linkages that should dramatically improve adhesive durability. It has been established that the essence of pMDI cure is the formation of poly(urea/uret) network; however, the significance of urethane formation is still uncertain and under debate [1]. There has been considerable interest in characterizing the cure chemistry of pMDI with wood; particularly in detecting the formation of urethane linkages. The known cure chemistry along with the putative urethane (and subsequent allophanate formation) is depicted in Scheme 5-1.

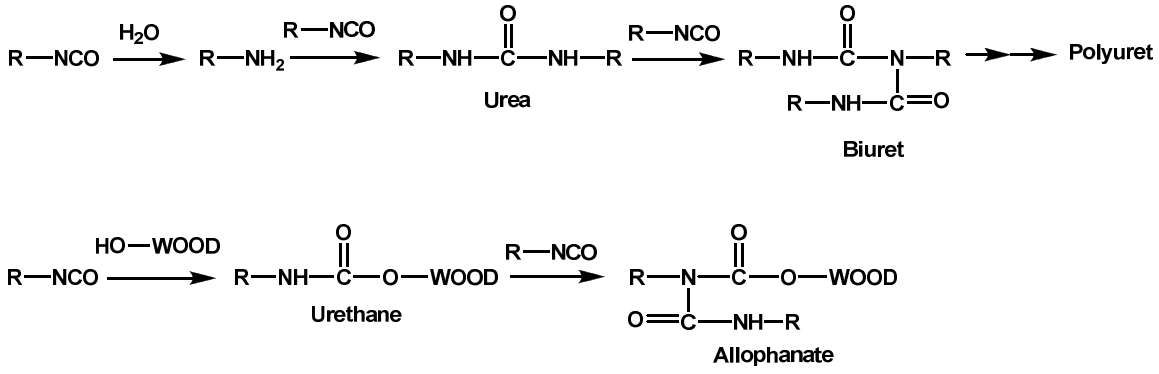

Scheme 7-1 Generalized cure chemistry of pMDI wood adhesives

It has been a long-term interest in Frazier's research group to reveal pMDI/wood cure chemistry using solid-state NMR methods [2-7]. The initial efforts utilized the ^{15}N isotopic labeling coupled with solid-state NMR to probe the bondlines [2-5]. This method revealed that urea, biuret, and polyuret structures were dominant in the bondline with or without urethane formation; the formation of these linkages were largely influenced by the cure temperature, cure time, pre-cure moisture content, structural isomerism, and pMDI molecular weight. Indirect evidence of urethane formation was detected through high-temperature urethane decomposition and relaxation measurements; unfortunately, this ^{15}N solid-state NMR method could not provide a definitive conclusion on this matter due to the signal overlap of urea and urethane. An improvement of this method was to doubly label the isocyanate group with ^{15}N and ^{13}C; the complimentary carbon and nitrogen NMR spectra assisted the spectral interpretation [6-7]. Zhou and Frazier demonstrated that ^{15}N isotope narrowed the ^{13}C signals and therefore aided the partial resolution of urethane and urea carbonyls [6]. This same paper revealed that the nitrogen peak shift from 102 to 104 ppm correlated with the carbon peak shift from 156 to 154 ppm with the increase of curing temperature, suggesting a thermal cleavage of urethane linkage at a temperature above 165 °C. This evidence of urethane decomposition provided an indirect measurement of urethane formation in the bondline. However, this double-labeled NMR method still could not resolve the signal overlap between urethane and urea; therefore, no quantitative measurement of urethane and urea was achieved. Recently, Das at el. employed spectral decomposition to quantify the urethane, urea, and biuret linkages in the bondline [7]. The ^{15}N NMR peak was fitted with three sub-regions: urethane, urea, and biuret; the results indicated that there was about 55% urethane in the bondline if cured at 100 °C while about 25% if cured at 200 °C. However, the spectral decomposition method showed several deficiencies [7]: 1) the

urethane quantities were overestimated because non-urethane linkages were found in the urethane region; 2) the nitrogen spectrum 85-125 ppm region was certainly more complex than suggested. Besides urethane, urea, and biuret linkages, allophanate and amide could also contribute to the peak; 3) the signal dispersion of urethane, urea, and biuret were unknown. To summarize, this paper provided a method to relatively assess the urethane linkages; however, an unambiguous and precise detection could not be achieved.

Rotational echo double resonance (REDOR) NMR is a popular tool for measuring heteronuclear dipolar couplings under magic angle spinning (MAS); the dipolar interactions that are averaged to zero by MAS are reintroduced by a train of rotor-synchronized π pulses [8-9]. An important feature of REDOR is that the dipolar couplings can be obtained independent of the chemical shifts; only the dipolar interaction is important in the evolution of the spin system [10]. Urethane and urea have distinct dipolar pairs; the carbonyl carbon is coupled with one nitrogen in urethane, while it is coupled with two nitrogens in urea.

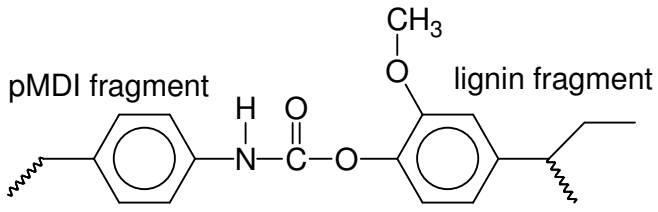

urethane linkage depicting one dipolar N-C pair

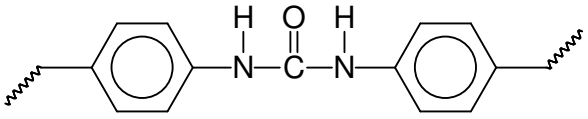

urea linkage depicting two dipolar N-C pairs

Therefore, urethane and urea linkages in the pMDI bondlines theoretically can be distinguished using REDOR NMR. Continuing on the efforts to elucidate the urethane linkages in the bondline, this research focuses on: 1) preparation of double-labeled pMDI (^{13}C-^{15}N-pMDI) through a safer approach; 2) quantitative detection of urea and urethane linkages in the wood/pMDI bondline using the REDOR NMR technique.

7.2 Experimental

7.2.1 Materials

^{15}N-aniline (98% ^{15}N, Cambridge Isotope Laboratories Inc.) was used as received. Paraformaldehyde (95%), ^{13}C3-dimethyl carbonate (99% ^{13}C), chlorine gas, chloroform, anhydrous CCl_4, anhydrous 1,2-dichlorobenzene (ODCB), anhydrous dioxane, dichloroethane, and phenylmercuric acetate catalyst were purchased from Aldrich and used as received.

7.2.2 Synthesis of ^{15}N-labeled Polyamine

^{15}N-labeled polyamine was synthesized by the acid catalyzed condensation of formaldehyde with ^{15}N-aniline; the molar ratios of ^{15}N-aniline : HCl and aniline-^{15}N : formaldehyde were chosen to be 1:1.5 and 4:1 respectively according to Ni and Frazier [2]. A 100-mL triple neck flask was fixed with a condenser and thermometer, and then submerged in an ice-water bath. 6 N HCl (40 mL, 0.24 mol) was first charged into the flask. Then, ^{15}N-aniline (14.5 mL, 0.16 mol) was added slowly under magnetic stirring followed by paraformaldehyde (1.26 g, 0.04 mol). This mixture was allowed to reflux at 103 °C for 8 hours. Being cooled down to room temperature, the

product was extracted using chloroform, washed with deionized water, and then concentrated on a rotational evaporator, as previous described by Ni and Frazier [2]. Finally, the residual ^{15}N-aniline was recovered by vacuum distillation (0.1 mmHg, 100 °C) and the polyamine product (7.28 g) was obtained. The yield was 91.0% assuming complete conversion of paraformaldehyde to methylenedianiline.

7.2.3 Synthesis of ^{13}C-labeled Triphosgene

^{13}C-labeled triphosgene was prepared using a modified literature method [11] where dimethylcarbonate is perchlorinated with Cl_2 under UV excitation. ^{13}C-dimethyl carbonate (3.0 g) and CCl_4 (35 mL) were placed in a Schlenk flask and subjected to five freeze-thaw degassing cycles. A reactor with an internal cooling system was built up according to Falb et al. [11] and then flamed under N_2 flow. The degassed ^{13}C-dimethyl carbonate / CCl_4 solution was transferred to the reactor, and irradiated with a Philips mercury lamp (400 W) for 5 minutes. Subsequently, chlorine gas was bubbled through the ^{13}C-dimethyl carbonate/ CCl_4 solution under magnetic stirring and continued irradiation, Figure 7-1. The gas flow was adjusted with reaction time so that no or only light green color appeared in the reaction solution. The temperature of the reaction solution was maintained between 5-10 °C. Meanwhile, HCl gas generated during the reaction was absorbed by saturated Na_2CO_3 (250 mL). Finally, the reaction was terminated when the green solution color would not disappear within one hour without introducing additional chlorine gas. Excess chlorine gas in the solution was removed by purging nitrogen gas into the solution; ^{13}C-labeled triphosgene (9.34 g, yield 96.5%) was obtained by removing CCl4 using rotational evaporation.

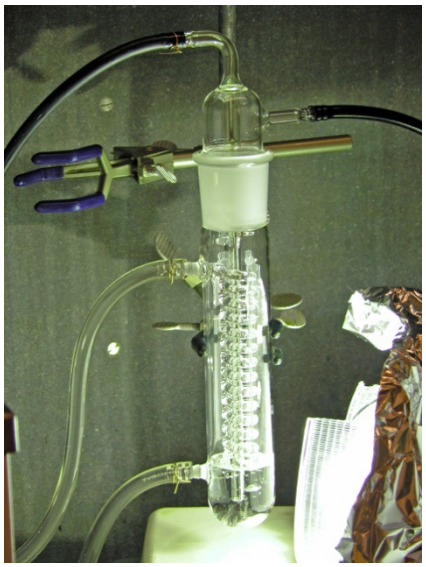

Figure 7-1 Chlorination apparatus showing the internal cooling coil, with Cl_2 gas flow under stirring, and with mercury lamp irradiation.

7.2.4 Synthesis of ^{13}C-^{15}N-pMDI

All glassware was dried and flamed under N_2 flow prior to use. In a 100-mL flask, the ^{15}N-polyamine (7.28 g) was vacuum dried (1 mm Hg, 50 °C) overnight, and then dissolved in anhydrous ODCB (61 mL). In another 100-mL flask, ^{13}C-triphosgene (8.37 g) was dissolved in anhydrous ODCB (71 mL); 15% excess of ^{13}C-triphosgene was used assuming ^{15}N-polyamine was completely in the form of ^{15}N-methylenedianiline. This ^{13}C-triphosgene solution was charged into a 250-mL three-neck flask fixed with a magnetic stirrer, thermometer, rubber septum, and nitrogen inlet/outlet; this flask was then submerged in an ice-water bath. ^{15}N-polyamine solution was then added drop wise into the three-neck flask through a 20-gauge cannula with vigorous stirring. Subsequently, the reaction mixture was heated to 170 °C in an oil bath and allowed to react for 30 min under N_2 flow. Being cooled to 150 °C, the reaction

solution was degassed with N_2 bubbling for 30 min; the phosgene gas was absorbed using a NaOH solution. The resulting solution was then vacuum distilled (0.1 mmHg, °100 C) to completely remove ODCB. Finally, the polyisocyanate product was heat treated at 200 °C for 10 min under N_2 purge to remove chlorine-containing impurities. After being quench-cooled in an ice-water bath, the product ^{13}C-^{15}N-pMDI (8.89 g) was obtained (yield 96.9 %).

Solution-state ^{13}C and ^{15}N NMR measurements of pMDI were obtained with a Varian Unity 400 MHz spectrometer in $CDCl_3$. The ^{13}C spectrum was referenced to tetramethylsilane at 0 ppm, and the ^{15}N spectrum was referenced to ^{15}N-glycine at 31 ppm. Because of the labeling and ^{15}N coupling, the isocyanate carbon signal is a strong doublet (δ 124.6) in the ^{13}C-NMR spectrum (Appendix 7-1). The ^{15}N NMR spectrum reveals two doublets for ^{15}N-labeled isocyanate nitrogen (Appendix 7-2); the strong doublet corresponds to the 4,4'-isomer of MDI, suggesting the resin contains mainly the 4,4' isomer. The ^{13}C-^{15}N-pMDI was converted to the urethane derivative by reaction with excess anhydrous methanol using a published procedure from Ni and Frazier [2]. The average molecular weights and molecular weight distribution of the urethane derivative were evaluated with Gel Permeation Chromatography (GPC) using tetrahydrofuran as the mobile phase. The number and weight average molecular weights were found to be 300 and 377 g/mol, respectively. The isocyanate content of ^{13}C-^{15}N-pMDI was determined according to the ASTM Standard D 5155-07 Test Method C [12] but at one fifth of the scale described in the method; the isocyanate content was found to be 32.5%.

7.2.5 Preparation of ^{13}C-^{15}N-pMDI /wood urethane model compound

The ^{13}C-^{15}N-pMDI /wood urethane model compound was prepared by a modified method from Zhou and Frazier [6]. A 100-mL triple neck flask was fixed with a thermometer, septum, and N_2 inlet/outlet, and then flamed. Southern yellow pine *(Pinus* spp.) wood powder (168 mg, 60 mesh) was vacuum dried (0.1 mmHg) in the flask at 80 °C for 3.5 h. After being cooled to 50 °C, anhydrous dioxane (35 mL) was charged and stirred to produce a suspension. A mixture of ^{13}C-^{15}N-pMDI (504 mg) and phenylmercuric acetate (25 mg) catalyst was dissolved in anhydrous dioxane (15 mL) and then transferred to the flask using a cannula under N_2. The mixture was allowed to react for 18.5 h at 50 °C under dry N_2 atmosphere. Finally, the wood powder was filtered and rinsed with excess acetone, and then vacuum dried (0.1 mmHg, room temperature) overnight to provide the urethane model compound (161 mg).

7.2.6 Preparation of ^{13}C-^{15}N-pMDI /aniline urea model compound

The ^{13}C-^{15}N-pMDI/aniline urea model compound was prepared using a literature procedure [6]. ^{15}N-aniline (0.5 mL) was dissolved in dichloroethane (2 mL) in a 10-mL flask. ^{13}C-^{15}N-pMDI (0.163 g) was dissolved in dichloroethane and then added into the aniline solution dropwise under magnetic stirring. The mixture was allowed to react for 3 h at room temperature. Finally, dichloroethane and the excess aniline were removed by vacuum distillation (0.1 mmHg, 100 °C) to provide the yellowish urea model compound (202 mg).

7.2.7 Preparation of ^{13}C-^{15}N-pMDI /Wood Composite Samples

Yellow poplar (*Liriodendren tulipifera*) flakes (longitudinal × radial × tangential = 25 × 25 × 0.7 mm) were dried (105 °C, 2 days), and then conditioned to achieve 5% and 20% moisture content over saturated potassium acetate and potassium nitrate solutions, respectively). ^{13}C-^{15}N-pMDI (281 mg) and a commercial pMDI (Huntsman, 1124 mg) was mixed, vacuum dried (0.1 mmHg, room temperature), and then heat treated at 200 °C. Being cooled to room temperature, the pMDI mixture (ca. 20% of the dry wood weight) was spread onto one surface of two yellow poplar flakes. After an open time of 9 minutes, the two flakes were bonded together and cured (no pressure, 200 °C, and 4 minutes). The composites prepared with 5% moisture content flakes (YPMC5) and 20% moisture content flakes (YPMC20) were studied by solid-state NMR.

7.2.8 NMR Spectroscopy

7.2.8.1 NMR Methods

The NMR experiments were performed on a Bruker Avance II-300 wide-bore NMR spectrometer (7.05 T) operating at Larmor frequencies of 30.41 MHz for ^{15}N, 75.47 MHz for ^{13}C, and 300.13 MHz for ^{1}H nuclei. All ^{15}N and ^{13}C solid-state NMR spectra were acquired by employing a ^{1}H-X (X = ^{13}C or ^{15}N) cross-polarization (CP) scheme for signal enhancement. Figure 7-2 shows solid-state NMR techniques for selectively observing ^{15}N-^{13}C-^{15}N signals out of ^{13}C-^{15}N moiety (Figure 7-2A) and for obtaining a two-dimensional (2D) ^{13}C-^{15}N heteronuclear correlation (HETCOR) spectrum (Figure 7-2B) under magic-angle spinning (MAS) condition. Directly bonded ^{13}C-^{15}N and ^{15}N-^{13}C-^{15}N molecular fragments are found in ^{13}C- and ^{15}N-labeled urethane and urea functional groups in our wood/pMDI composite samples. The selective detection of ^{15}N-^{13}C-^{15}N

signal in the presence of ^{15}N-^{13}C-^{15}N and ^{13}C-^{15}N molecular fragments simultaneously is achieved by utilizing a variant method [13] of the rotational echo double resonance (REDOR) scheme [14] that provides a separation of two signals from these molecular fragments. While observing high-resolution spectra via *S* channel (either ^{13}C or ^{15}N), irradiating the *I* channel by a series of 180 degree radio-frequency pulses (two 180 degree pulses per a rotor period), the REDOR pulse block reintroduces *I-S* and I_2S dipolar couplings (r (^{13}C-^{15}N) = 1.4 Å; d(^{13}C-^{15}N) = 800 Hz) that are initially averaged out by MAS (Figure 7-2A). The optimal duration for the REDOR mixing period can be adjusted by changing the *n* (*n* = 1, 2, 3, …), which is designated in Figure 7-2A. When *n* = 1, the REDOR mixing time is $4\tau_r$, where τ_r designates a rotor period. As the parameter *n* increases to 2, 3, …, the corresponding REDOR mixing period becomes $8\tau_r$, $12\tau_r$, …, etc. With the ^{13}C- and ^{15}N-labeled model compounds (^{13}C and ^{15}N labeled glycine-alanine-leucine and pMDI/aniline urea), we have tested *n* = 2, 4, and 6. Therefore the REDOR mixing time incorporated were 666.4, 1332.8, and 1999.2 μs, respectively, since the MAS spinning speed utilized was $\omega_r/2$ = 12 kHz. Optimal experimental results were obtained at *n* = 4 for both standard samples. The $90^{\circ}_{x}(S) - 45^{\circ}_{y}45^{\circ}_{\phi 1}(I)$ (ϕ_1 = y or –y) pulse component that is placed in the middle of REDOR mixing block provides leverage for separating the evolutions of ^{15}N-^{13}C-^{15}N and ^{13}C-^{15}N molecular fragments, as is described in the following section 7.2.8.2.

A 2D HETCOR scheme, utilizing a ^{15}N-^{13}C cross-polarization method [15], was used to obtain a ^{13}C-^{15}N 2D correlation spectrum. A ^{15}N- and ^{13}C-labeled polyurea sample, a standard sample we prepared for identifying our REDOR pulse scheme, provided unresolved, two peaks along both ^{13}C and ^{15}N dimensions, demonstrating two ^{15}N sites in urea functional group that are barely

separable in a NMR spectrum. A polyurethane standard sample we prepared, however, demonstrated a single peak along both frequency dimensions.

The NMR signal averaging was achieved by co-adding 4096 transients with a 5s acquisition delay time for REDOR. For obtaining a 2D ^{15}N-^{13}C HETCOR spectrum, co-addition of 64 transients was employed for direct t_2 acquisition with a 4s acquisition delay, with 128 t_1 slices. The sample temperature used in our NMR experiments was 22 ˚C. The temperature was regulated by an air flow, which was under the control of a BVT-3000 digital temperature control unit of a Bruker console and a BCU-X precooling and stabilization accessory. ^{1}H, ^{15}N, and ^{13}C $\pi/2$ pulse lengths were 4, 10, and 8 μs, respectively. The small phase incremental alternation sequence, with 64 steps (SPINAL-64) [16] was employed for proton decoupling during the ^{13}C or ^{15}N signal detection at 85 kHz power.

7.2.8.2 Selective detection of I_2S signal

A selective NMR detection scheme for an I_2-S spin pair can be achieved by employing the REDOR-based pulse sequence shown in Figure 7-2A. Here I and S stand for either ^{13}C or ^{15}N, and S designates the detection channel and I the irradiation channel. Our experiments consist of two separate measurements: 1) a control experiment, with ϕ_1 = -y that implements only $90^{\circ}_{x}(S)$ pulse, in the middle of the REDOR evolution period; 2) with ϕ_1 = y that implements a simultaneous $90^{\circ}_{x}(S) - 90^{\circ}_{y}(I)$ pulse (see Figure 7-2A). For analyzing the signal evolution patterns of both I-S and I_2-S spin pairs, we begin with S spin signal prepared by CP from ^{1}H channel which is S_x. The

signal evolutions of *IS* and I_2-*S* spin pairs during the first REDOR block before the simultaneous $90^\circ_x(S)-45^\circ_y 45^\circ_{\phi 1}(I)$ (ϕ_1= y or –y) pulse block are: [13]

$$S_x \xrightarrow{2\pi d_{CN}\tau\cdot I_z S_z} S_x c + 2I_z S_y s \tag{1}$$

for *I*-*S* and

$$S_x \xrightarrow{2\pi d_{CN}\tau\cdot I_{1z} S_z} S_x c + 2I_{1z} S_y s \xrightarrow{2\pi d_{CN}\tau\cdot I_{2z} S_z} S_x c^2 + 2I_{2z} S_y cs + 2I_{1z} S_y sc - 4I_{1z} I_{2z} S_x s^2 \tag{2}$$

for I_2-*S*, where *c* and *s* are $\cos[\pi\int_0^\tau d_{CN}dt]$ and $\sin[\pi\int_0^\tau d_{CN}dt]$, respectively, and d_{CN} is the dipolr coupling of ^{13}C-^{14}N. The action of a simultaneous $90^\circ_x(S)-90^\circ_y(I)$ pulse on the above signals is:

$$S_x c + 2I_z S_y s \xrightarrow{90^\circ_x(S)-90^\circ_y(I)} S_x c + 2I_x S_z s \tag{3}$$

and

$$S_x c^2 + 2I_{2z} S_y cs + 2I_{1z} S_y sc - 4I_{1z} I_{2z} S_x s^2 \xrightarrow{90^\circ_x(S)-90^\circ_y(I)} S_x c^2 + 2I_{2x} S_z cs + 2I_{1x} S_z sc - 4I_{1x} I_{2x} S_x s^2. \tag{4}$$

Whereas, the actions of $90^\circ_x(S)$ pulse on Eqs. (1) and (2) are:

$$S_x c + 2I_z S_y s \xrightarrow{90^\circ_x(S)} S_x c + 2I_z S_z s \tag{5}$$

and

$$S_x c^2 + 2I_{2z} S_y cs + 2I_{1z} S_y sc - 4I_{1z} I_{2z} S_x s^2 \xrightarrow{90^\circ_x(S)} S_x c^2 + 2I_{2z} S_z cs + 2I_{1z} S_z sc - 4I_{1z} I_{2z} S_x s^2. \tag{6}$$

Among coherence terms expressed in Eqs. (3)-(6), only S_x and $4I_{1z}I_{2z}S_x$ terms are directly detectable or can be converted to the detectable single-quantum *S*-spin signal. Other terms designate a single-quantum *I*-spin signal (e.g., $2I_{1x}S_z$), a multiple-quantum term ($4I_{1x}I_{2x}S_x$), or a Zeeman-order term (e.g., $2I_zS_z$) that are not detectable along the S channel. Then, keeping only the relevant terms, the actions of the second REDOR mixing block are:

$$S_x c \xrightarrow{2\pi d_{CN}\tau \cdot I_z S_z} S_x c^2 + \ldots \tag{7}$$

for *I*-*S* and

$$S_x c^2 \xrightarrow{2\pi d_{CN}\tau \cdot I_{1z} S_z} \xrightarrow{2\pi d_{CN}\tau \cdot I_{2z} S_z} S_x c^4 + \ldots \tag{8}$$

for I_2-*S*, from the first experiment, and

$$S_x c \xrightarrow{2\pi d_{CN}\tau \cdot I_z S_z} S_x c^2 + \ldots \tag{9}$$

for *I*-*S* and

$$S_x c^2 - 4I_{1z}I_{2z}S_x s^2 \xrightarrow{2\pi d_{CN}\tau \cdot I_{1z} S_z} \xrightarrow{2\pi d_{CN}\tau \cdot I_{2z} S_z} S_x c^4 + S_x s^4 + \ldots \tag{10}$$

for I_2-*S*, from the second experiment.

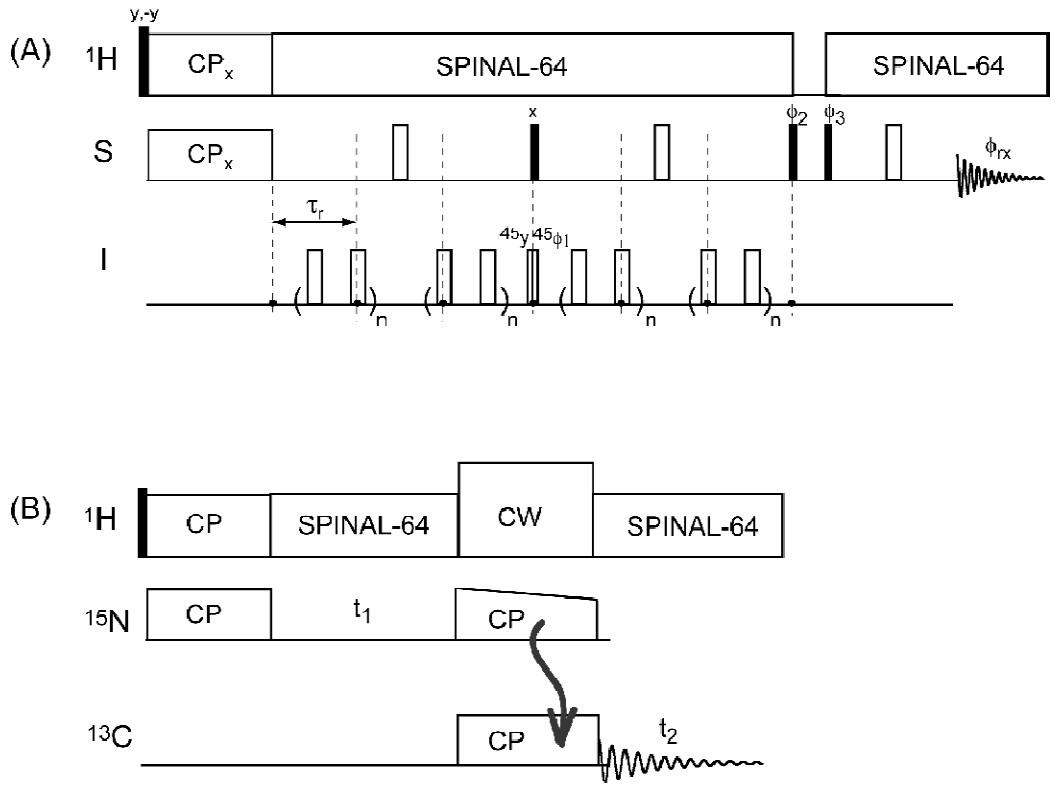

Figure 7-2 Pulse sequences used in our experiments: REDOR based SI_2 spin selection sequence (A); sequence for 2D ^{15}N-^{13}C HETCOR spectroscopy (B). ^{1}H magnetizations created by a 90 degree pulse are transferred to either ^{13}C or ^{15}N in a CP step for both experiments. The ^{1}H-X (X = ^{13}C or ^{15}N) CP mixing time used in both experiments is 1 ms. S-spin echo signal is detected while applying a train of π-pulses (open rectangles) along either S or I channel to recouple ^{13}C-^{15}N dipolar interactions under MAS (A). A pair of 90°_x (S)/$45^\circ_y 45^\circ_{\phi 1}$ (ϕ_1 = y or –y) pulses is applied in the middle of the dipolar recoupling block for obtaining ^{13}C (S)-$^{15}N_2$ (I) or ^{15}N (S)-$^{13}C_2$ (I) molecular segments. Basic pulse phases used are: ϕ_2 = -y –y x x y y –x –x; ϕ_3 = x x y y –x –x –y –y; ϕ_{rx} = x –x –x x y –y –y y. XY-8 or XY-16 phase cycles were used for π-pulse trains in REDOR recoupling block. The spectrum measured with ϕ_1 = y is subtracted by the spectrum measured by ϕ_1 = -y (control experiment) to produce SI_2 only signal. Nitrogen magnetizations prepared by ^{1}H-^{15}N CP is allowed to evolve under proton decoupling for t_1 is transferred to ^{13}C channel via ^{15}N-^{13}C DCP scheme for signal detection during t_2 (B). Unless specified explicitly, a filled bar represents a 90 degree pulse (4 μs) and an open bar a 180 degree pulse (8 μs) in both ^{1}H and ^{13}C channels. The MAS spinning speeds used are 12 kHz. The spin-lock rf pulse power along the carbon and proton channels for CP mixing was 50 kHz. An optimal ^{15}N-^{13}C CP condition was found by optimizing not only the ^{13}C and ^{15}N pulse power but the ^{1}H decoupling power. The ^{13}C/^{15}N CP mixing time used was 3 ms, with 25 kHz pulse power for both channels. The SPINAL-64 sequence with 85 kHz power was used for proton decoupling in each sequence.

When the signal obtained from the experiment 2 is subtracted from the signal obtained from the experiment 1, the signal remained for the *I*-*S* spin pair is $S_x c^2 - S_x c^2 = 0$, however, the signal remained from the subtraction for the I_2-*S* spin pair is $S_x c^4 + S_x s^4 - S_x c^4 = S_x s^4$. Therefore, we obtain only the signal coming from the I_2-*S* spin pair from the subtracted spectrum.

7.3 Results and Discussion

7.3.1 2D HETCOR NMR

^{13}C-^{15}N 2D HETCOR spectra for double-labeled urea and urethane model compounds are shown in Figure 7-3. The spectrum A is for the ^{13}C-^{15}N-pMDI/aniline urea model. The ^{15}N peak at 102 ppm is correlated with the ^{13}C peak at 156 ppm; while the ^{15}N shoulder at 109 ppm is correlated with the ^{13}C shoulder at 160 ppm. According to the literature [6-7], the peaks are the ^{15}N and ^{13}C chemical shifts for the urea group and the shoulders are for the biuret amide group. The chemical shifts are similar to the published values [6]. The spectrum B in Figure 7-3 is for the ^{13}C-^{15}N-pMDI/wood urethane model. A single ^{15}N peak (102 ppm) is associated with a single ^{13}C peak (153 ppm), which is attributed to the urethane nitrogen and urethane carbonyl, respectively [6]; the ^{15}N and ^{13}C chemical shifts of urethane model compound are similar to the published values [6]. The broad, however, single-peaks along both ^{13}C and ^{15}N dimensions indicate that the urethane model was synthesized successfully without introducing urea into the compound. Furthermore, Figure 7-3 demonstrates that the ^{15}N and ^{13}C signals from urethane and urea are not resolved; this is a common disappointment when one tries to quantify the relative amount of urethane and urea linkages in the pMDI bondline [2, 6-7].

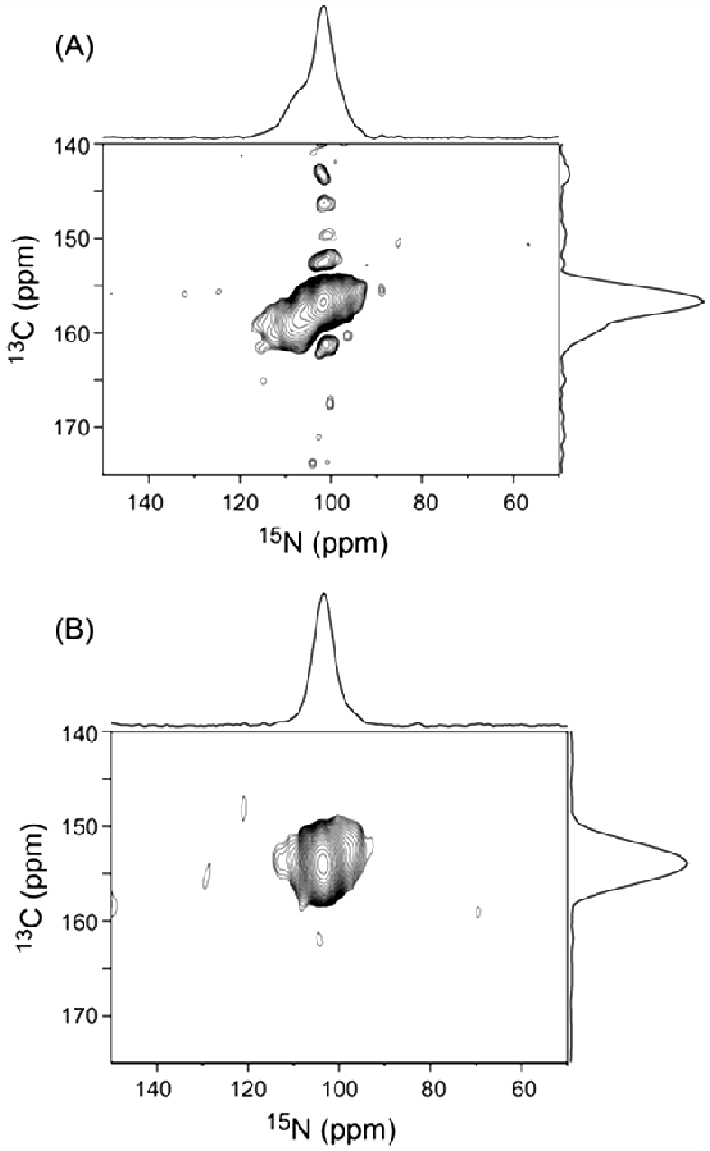

Figure 7-3 ^{13}C-^{15}N 2-D HETCOR spectra; A) ^{13}C-^{15}N-pMDI/Aniline Urea Model; B) ^{13}C-^{15}N-pMDI/Wood Urethane Model.

7.3.2 Selective Detection of Urethane and Urea in REDOR NMR

Figure 7-4A and 7-4B show the ^{13}C-{^{15}N} REDOR NMR spectra of the carbonyl region for ^{13}C and ^{15}N double-labeled urea and urethane model compounds, observing the ^{13}C signals without (spectrum 1) and with (spectrum 2) irradiating the ^{15}N channel. Spectrum 1 (signal intensity S_0)

and spectrum 2 (signal intensity S) are obtained separately from the experiment 1 and experiment 2 described in section 7.2.8.2. The difference spectrum is obtained by subtracting spectrum 2 from spectrum 1 as shown in Figure 7-4A to 7-4D; the remaining signal intensity $\Delta S = S_0 - S$. For the urea model, a significant amount of signal remains in the difference spectrum, with the relative signal intensity $\Delta S/S_0 = 0.49$. For urethane model, besides the carbonyl carbon peak, there are two other peaks at 135 and 173 ppm respectively in spectrum 1 and 2 even though they are not relevant to our REDOR analysis; these two peaks are also seen in the two pMDI/Wood composite samples (Figure 7-4C and 7-4D) and believed to be wood signals. More importantly for urethane model, no signal is visible in the difference spectrum. As described in section 7.2.8.2, the difference NMR spectrum is used to distinguish I-S and I_2-S spin pairs where S represents ^{13}C and I represents ^{15}N in this research; $\Delta S = 0$ for I-S pair and $\Delta S > 0$ for the I_2-S pair. In the urethane linkage, only the I-S spin pair (^{15}N-^{13}C) exists; whereas in the urea linkage, only I_2-S spin pair is present (^{15}N-^{13}C-^{15}N). Therefore, ΔS of the urethane model should be zero while ΔS of the urea model is larger than zero, according to the theory we have provided previously. This is consistent with our observation in Figure 7-4. Consequently, Figure 7-4A and 7-4B demonstrate that the REDOR NMR technique employed is able to selectively detect the urea linkage.

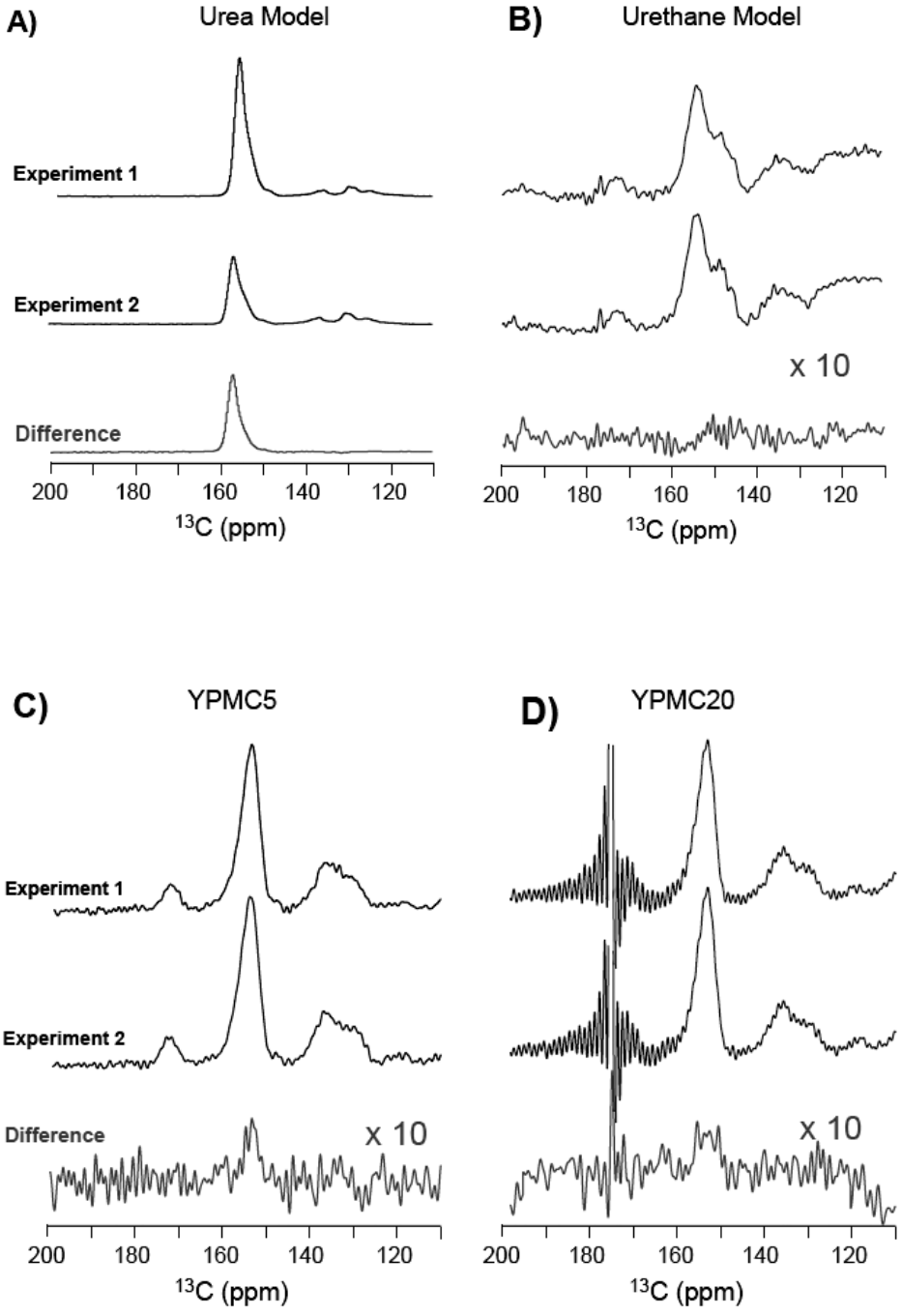

Figure 7-4 REDOR NMR spectra showing the selective NMR detection of urethane and urea linkages; A) ^{13}C-^{15}N-pMDI/Aniline urea model, B) ^{13}C-^{15}N-pMDI/Wood urethane model, C) YPMC5 ^{13}C-^{15}N-pMDI/wood composite, and D) YPMC20 ^{13}C-^{15}N-pMDI/wood composite.

Figure 7-4C and 7-4D show the REDOR NMR spectra of two pMDI/Wood composites: YPMC5 and YPMC20; they were bonded with yellow poplar wood flakes at moisture content of 5% and 20% respectively. A weak carbonyl peak is observed in the difference spectra for both samples, indicating the existence of urea linkages in the composites. The $\Delta S/S_0$ values of both spectral set (Figure 7-4C and 7-4D) are calculated and then compared to the $\Delta S/S_0$ obtained from the urea model compound to estimate the mass percentage of urea-type linkages in the bondline, shown in Table 7-1. In addition to urea and urethane bonds, biuret and allophanate could form in the bondline during cure. From Scheme 1, each biuret group contains two ^{15}N-^{13}C-^{15}N pairs and each allophanate group has one ^{15}N-^{13}C-^{15}N pair, thus both contribute to the urea-type linkage content shown in Table 7-1.

Table 7-1 Estimation of urethane and urea content in pMDI bondlines

Sample	$\Delta S/S_0$	Urea-type linkage (%)	Urethane linkage (%)
Urea Model	0.49	100%	0%
YPMC5	0.064	13%	87%
YPMC20	0.086	17%	83%

It has long been believed that the urea-type linkages (in urea, biuret, and polyuret) dominate the pMDI cure, with uncertain amounts of urethane present [1, 4-7]. In this research, the pMDI/Wood composites were cured at 200 °C; this high temperature could cleave urethane linkages and thus further reduce the urethane content in the bondline [4, 6-7]. Surprisingly, the data shown in Table 7-1 reveals that moisture content only has a minor effect on the cure chemistry, and that urethane linkages are predominant in the bondline (more than 80%); this is

completely contradictory to the published results. If urethanes were predominant in the bondline, this result would suggest that more than 80% of pMDI isocyanate groups achieved atomic proximity with wood hydroxyls and wood hydroxyls were much more reactive to isocyanate than water. In fact, however, water has a similar reactivity as primary hydroxyls towards isocyanates [17-18]. At the same time, water is able to penetrate into the adhesive bulk and react, whereas wood hydroxyls are restricted by the wood structure. Apparently, it is practically impossible for urethane linkage to dominate the bondline cure under the given preparation conditions for pMDI/Wood composites.

It seems that the REDOR NMR method used in this research works well with the model compounds. Unfortunately, the method appears to overestimates the urethane linkages when applied to the pMDI/Wood bondlines. The reason for this deficiency is not clear. Obviously, the bondline chemistry is much more complex than the model systems. In addition, the signal-to-noise ratio is low for the composite samples, which makes peak integration difficult. pMDI/Wood composites were prepared with a resin mixture containing 20% labeled and 80% unlabelled pMDI; increasing the labeled pMDI content in the mixture may be an approach to improve the signal-to-noise ratio. Furthermore, it is reported that radiofrequency (rf) fields at the end of the rf coil can be as low as 60% of that at the center of the coil [9]. The inhomogeneity of the rf fields can cause imperfections of the π pulses, particularly when a hundred or more π pulses are normally used in a REDOR experiment and the imperfections accumulate to a substantial effect [9]. To compensate for the pulse imperfections, samples are normally center-packed in the rotor. However, in this research, samples were filled in the whole rotor; the non-center packed samples could introduce significant pulse length missets into the experiments. The

pulse length misset causes a fraction of ^{15}N spins not to change their spin states and therefore their coupled ^{13}C spins do not dephase. As a result, pulse length missets will lead to smaller $\Delta S/S_0$ values [10]. In this research, smaller $\Delta S/S_0$ of a composite sample means a lower fraction of urea linkages, thus overestimating the urethane linkage content. Although the content of urethane linkages was likely overestimated, this method confirmed the formation of urethane linkages in the pMDI bondline, which corresponds to the findings of others [5-7]. Through improving the acquisition parameters, this REDOR NMR method will potentially be a useful tool to investigate pMDI cure chemistry in wood bondlines.

7.4 Conclusion

A ^{13}C and ^{15}N double-labeled pMDI resin was prepared by a safer approach; polyamine was phosgenated using solid triphosgene instead of phosgene gas that was previously employed in our group. ^{13}C-{^{15}N}EDOR NMR confirmed that exclusive urea and urethane linkages are present in the double-labeled urea and urethane model compounds, respectively. When extended this technique to real pMDI/Wood composites, the formation of urethane linkages between pMDI and wood was clearly detected; however, the content of urethane linkages was believed to be largely overestimated. This apparent deficiency of the method was not well understood; some possible reasons were proposed.

Reference

1. Frazier, C.E., Isocyanate Wood Binders, in Handbook of adhesive technology, K.L.M. Antonio Pizzi, Editor. 2003, CRC Press. p. 681-694.

2. Ni, J.W. and C.E. Frazier, N-15 CP/MAS NMR study of the isocyanate/wood adhesive bondline. Effects of structural isomerism. Journal of Adhesion, 1998. 66(1-4): p. 89-116.

3. Wendler, S.L. and C.E. Frazier, The N-15 CP/MAS NMR characterization of the isocyanate adhesive bondline for cellulosic substrates. Journal of Adhesion, 1995. 50(2-3): p. 135-153.

4. Wendler, S.L. and C.E. Frazier, The effects of cure temperature and time on the isocyanate-wood adhesive bondline by N-15 CP/MAS NMR. International Journal of Adhesion and Adhesives, 1996. 16(3): p. 179-186.

5. Wendler, S.L. and C.E. Frazier, Effect of moisture content on the isocyanate/wood adhesive bondline by N-15 CP/MAS NMR. Journal of Applied Polymer Science, 1996. 61(5): p. 775-782.

6. Zhou, X.B. and C.E. Frazier, Double labeled isocyanate resins for the solid-state NMR detection of urethane linkages to wood. International Journal of Adhesion and Adhesives, 2001. 21(3): p. 259-264.

7. Das, S., M.J. Malmberg, and C.E. Frazier, Cure chemistry of wood/polymeric isocyanate (PMDI) bonds: Effect of wood species. International Journal of Adhesion and Adhesives, 2007. 27(3): p. 250-257.

8. Weldeghiorghis, T.K. and J. Schaefer, Compensating for pulse imperfections in REDOR. Journal of Magnetic Resonance, 2003. 165(2): p. 230-236.

9. Sinha, N., K. Schmidt-Rohr, and M. Hong, Compensation for pulse imperfections in rotational-echo double-resonance NMR by composite pulses and EXORCYCLE. Journal of Magnetic Resonance, 2004. 168(2): p. 358-365.

10. Gullion, T., Introduction to rotational-echo, double-resonance NMR. Concepts in Magnetic Resonance, 1998. 10(5): p. 277-289.

11. Falb, E., A. Nudelman, and A. Hassner, A Convenient Synthesis of Chiral Oxazolidin-2-Ones and Thiazolidin-2-Ones and an Improved Preparation of Triphosgene. Synthetic Communications, 1993. 23(20): p. 2839-2844.

12. ASTM, ASTM D5155-07, Standard Test Methods for Polyurethane Raw Materials Determination of the Isocyanate Content of Aromatic Isocyanates. 2007.

13. Mao, J.D. and K. Schmidt-Rohr, Methylene spectral editing in solid-state C-13 NMR by three-spin coherence selection. Journal of Magnetic Resonance, 2005. 176(1): p. 1-6.

14. Gullion, T. and J. Schaefer, Rotational-Echo Double-Resonance Nmr. Journal of Magnetic Resonance, 1989. 81(1): p. 196-200.

15. Baldus, M., A.T. Petkova, J. Herzfeld, and R.G. Griffin, Cross polarization in the tilted frame: assignment and spectral simplification in heteronuclear spin systems. Molecular Physics, 1998. 95(6): p. 1197-1207.

16. Fung, B.M., A.K. Khitrin, and K. Ermolaev, An improved broadband decoupling sequence for liquid crystals and solids. Journal of Magnetic Resonance, 2000. 142(1): p. 97-101.

17. Aneja, A., Structure-Property Relationships of Flexible Polyurethane Foams, in Chemical Engineering. 2002, Virginia Polytechnic Institute and State University: Blacksburg.

18. Szycher, M., Szycher's Handbook of Polyurethanes. 1999: CRC Press.

Chapter 8 Conclusions

8.1 Wood/PUR Interactions

The effects of wood/adhesive interactions on PUR phase morphology have been investigated employing a model (MPUR) and a commercially-relevant (CPUR) adhesive. MPUR was prepared from linear PTMO terminated with difunctional PPDI while CPUR from PPG and multifunctional pMDI. AFM phase images suggested that wood interactions altered the hard (MPUR) or soft (CPUR) domain size distribution. DMA revealed that wood raised the transition temperatures of MPUR soft and hard phases, as well as CPUR hard phase. FTIR studies on CPUR indicated that wood promoted the formation of hydrogen-bonded urea structures. These results suggested significant wood effects on PURs, but could not distinguish direct and indirect wood effects.

8.2 PUR Structure-Property (Weather Durability) Studies

Three PUR wood adhesives were prepared from pMDI and mixtures of PPGs with varying PPG2000/PPG400 mass ratios (of 80/20, 50/50, 20/80, the adhesives were named PU8020, PU5050, and PU2080 accordingly). Since the NCO/OH ratio was fixed (5.0), the percentage hard phase increased as the soft segment composition favored shorter PPG chains. Higher hard segment content led to increased intermolecular interactions, thus raised the viscosity and soft segment T_g of the prepolymers. The hard segment softening temperatures of cured PURs (film and composite) rose with the hard phase content, corresponding with enhanced urethane/urea hydrogen bonds. PUR/wood bondline performance was evaluated through mode-I fracture testing. PU8020 (lowest hard segment content) bondline showed slightly higher fracture

toughness than other adhesives, which was not simply explained by adhesive penetration or bondline thickness data obtained using fluorescence microscopy. It was postulated that the greater PU8020 fracture toughness might be related to greater damping observed in the DMA response between -50 and 45 °C.

For PUR structure-durability studies, efforts were made to establish an appropriate accelerated weathering procedure. Three procedures were developed and used to evaluate the weather durability of the three PURs using mode-I fracture testing. Two relatively moderate procedures (VPS80C and VPS104C) could not effectively differentiate the weather durability of the three PURs. On the other hand, VPSS procedure was able to well distinguish the weather durability of PURs; treated-PU8020 specimens showed decreased toughness while the other two exhibited enhanced toughness. As a result, VPSS procedure was selected for further PUR structure-durability studies.

PUR water affinity was evaluated through water absorption experiments. Water-submersion DMA provided the thermal transition temperatures of the water-saturated specimens and the water plasticizing effects simultaneously. Both were found potentially to correlate with PUR weather durability; a greater plasticizing effects and a lower hard segment softening temperature in water-submersion DMA potentially correlated with inferior durability. Consequently, the time efficient water-submersion DMA could be an excellent approach for quickly evaluating PUR weather durability.

One strength of this research was to investigate the weathering-induce molecular changes by conducting FTIR and DMA experiments directly on the same DCB specimens that were used in weather durability studies. Thus, the relationship between analytical data and weather durability were conveniently explored concurrently. Focusing on VPSS weathering procedure, FTIR studies in the free isocyanate frequency provided evidence of post-cure for all adhesives. Infrared spectra in the carbonyl frequency suggested that VPSS weathering treatment caused hydrolytic degradation and changes of urethane/urea hydrogen bonding. However, the changes were too complex to establish direct visual correlation with PUR weathering performance. From DMA, VPSS-treated PUR films showed significant modulus reduction, which was consistent with the urethane hydrolytic degradation observed in FTIR. VPSS-treated PU8020 film and composite specimens showed reduced hard segment softening damping intensity, which appeared to correlate with its weakened wood/PUR bondline. However, neither the nature of the damping intensity variation nor this correlation was understood. To sum up, weathering-induced molecular changes were detected using FTIR and DMA methods; nevertheless, relations between these changes and bondline durability still remain unclear.

8.3 Solid-State NMR Characterization of pMDI Cure Chemistry

A ^{13}C and ^{15}N double-labeled pMDI resin was successfully prepared through a safer approach, using solid triphosgene instead of phosgene gas that was previously employed in our group. A model urethane and urea model compounds were prepared to establish and verify a ^{13}C-{^{15}N}REDOR NMR method for urethane and urea quantitative detection. This technique was then extended to real pMDI/Wood composites to study the effects of pre-cure wood moisture content on isocyanate cure chemistry. The formation of urethane linkages between pMDI and

wood was clearly detected with little influence of pre-cure wood moisture content. However, the urethane linkage content was believed to be largely overestimated. This deficiency of the method was not well understood; some possible reasons were proposed.

Chapter 9 Appendix

Appendix 3-1 AFM Phase & Height Images for MPUR and CPUR in Films and Composites

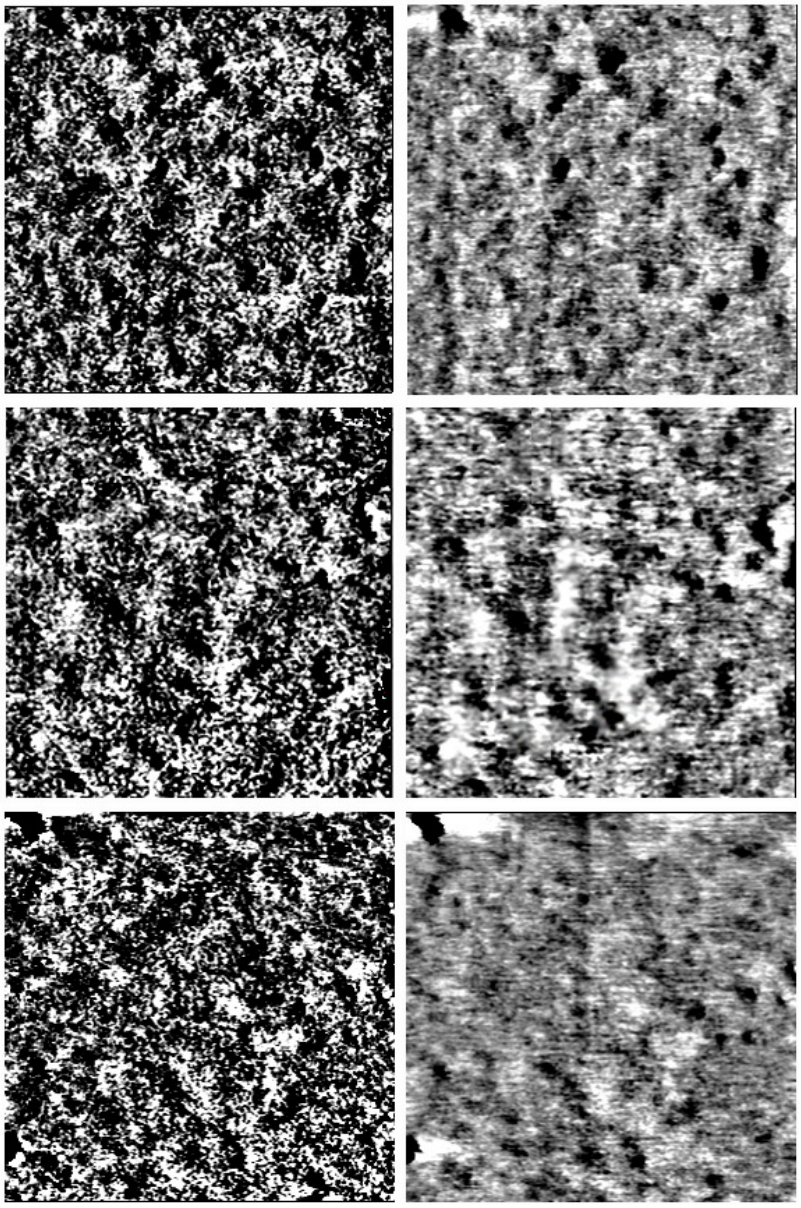

Figure A3.1 Phase (left) and Height (right) images of MPUR film; scan size: 1 μm × 1 μm; cantilever: AC106TS standard Si cantilever (spring constant 42 N/m); set-point ratio 0.7; the z-scales for the phase and height images are 6 degrees and 3 nm, respectively.

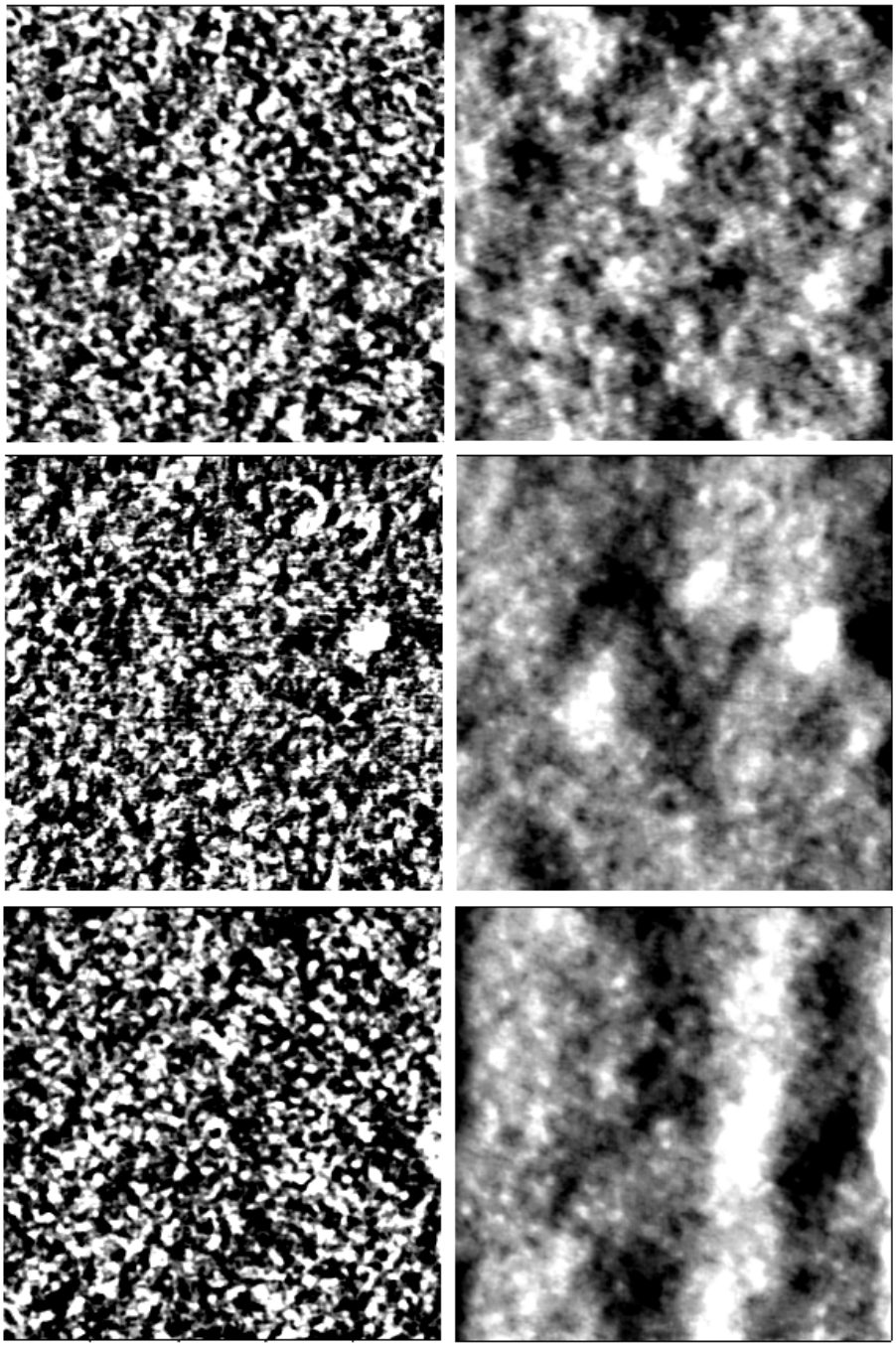

Figure A3.2 Phase (left) and Height (right) images of MPUR in wood lumen; scan size: 1 µm × 1 µm; cantilever: AC160TS standard Si cantilever (spring constant 42 N/m); set-point ratio 0.6-0.7; the z-scales for the phase and height images are 6 degrees and 6 nm, respectively.

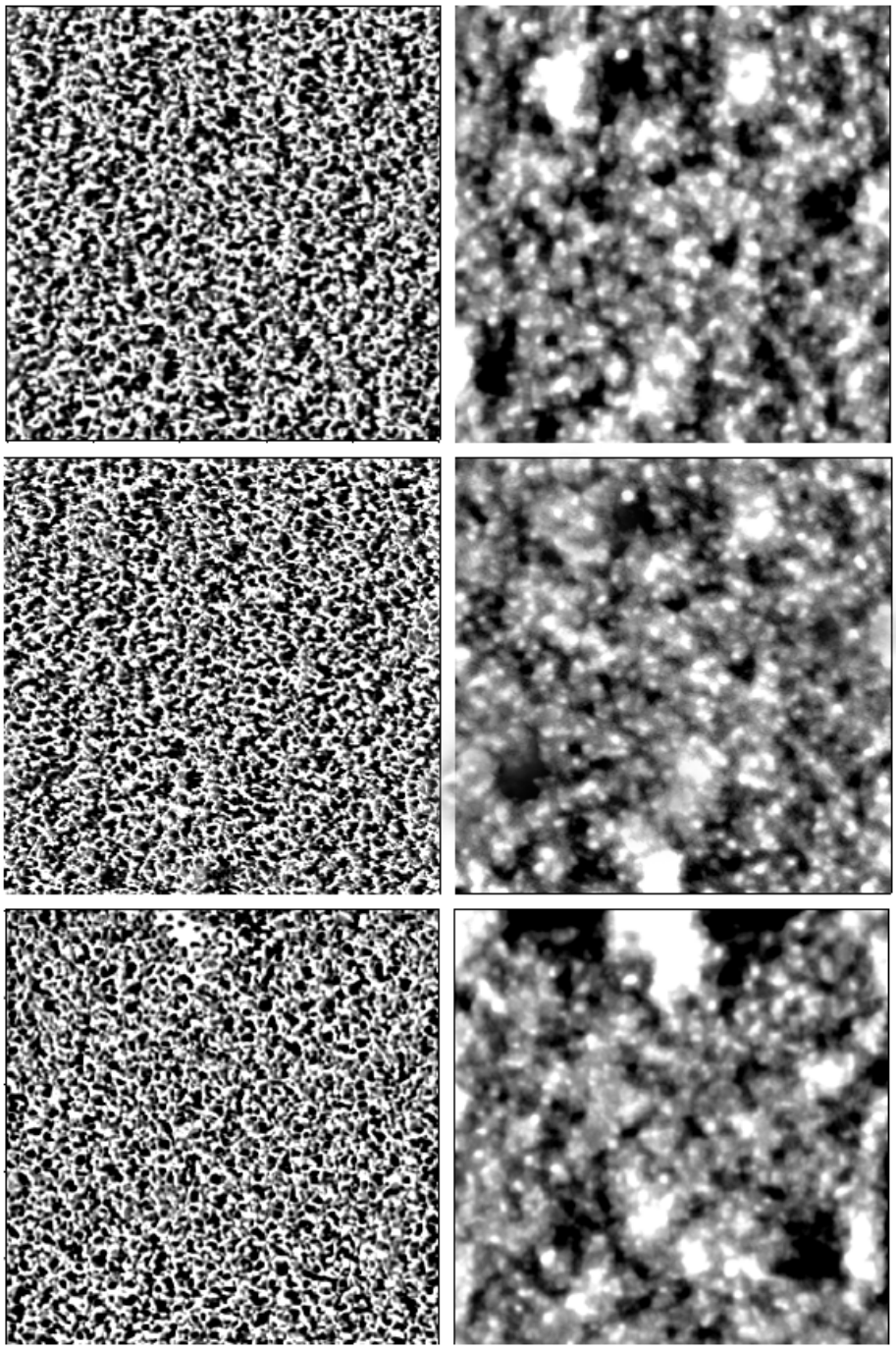

Figure A3.3 Phase (left) and Height (right) images of CPUR film; scan size: 1 μm × 1 μm; cantilever: AC240TS standard Si cantilever (spring constant 2 N/m); set-point ratio 0.7; the z-scales for the phase and height images are 25 degrees and 10 nm, respectively.

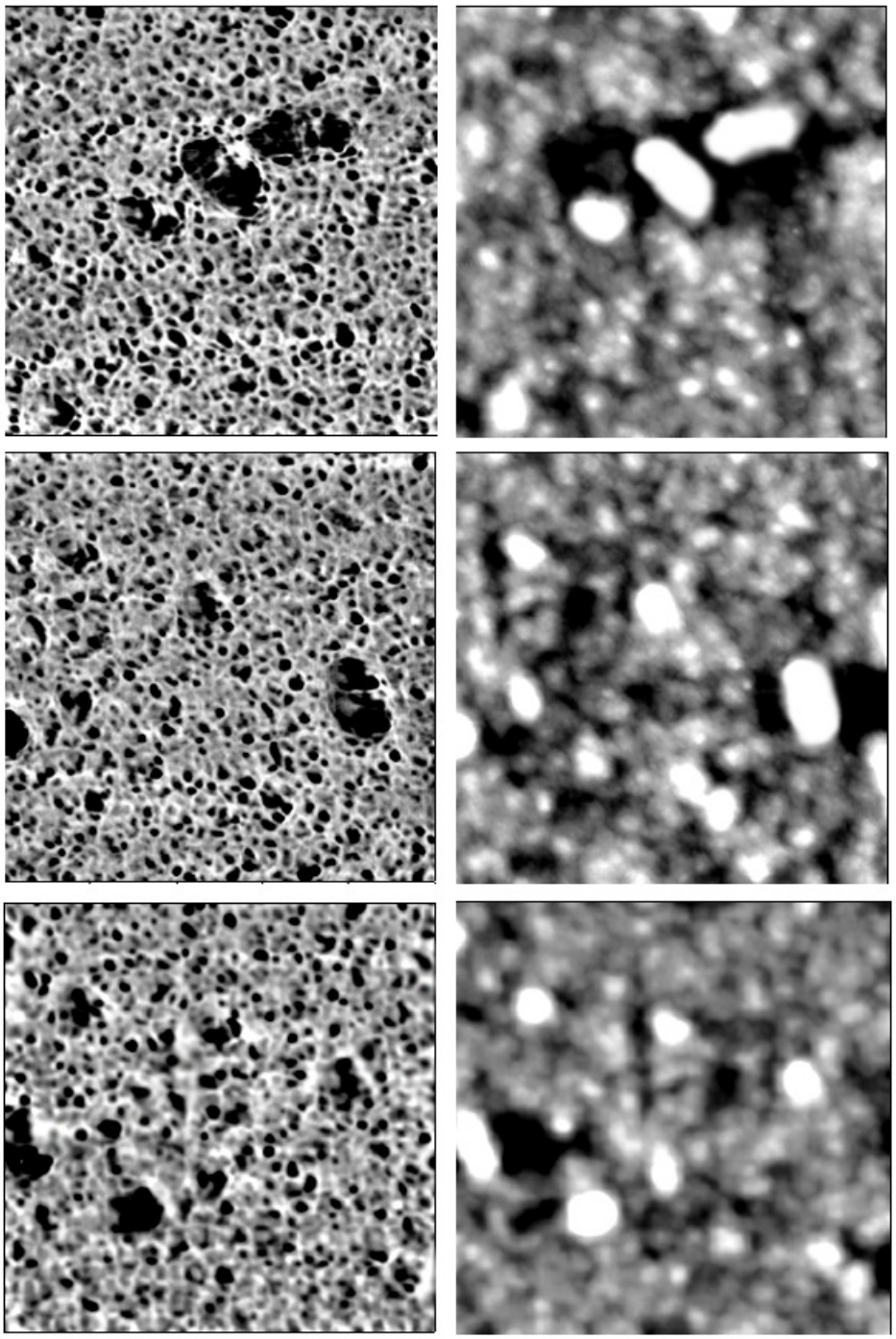

Figure A3.4 Phase (left) and Height (right) images of CPUR film; scan size: 1 μm × 1 μm; cantilever: AC240TS standard Si cantilever (spring constant 2 N/m); set-point ratio 0.7; the z-scales for the phase and height images are 25 degrees and 10 nm, respectively.

Appendix 4-1 Solution 13C-NMR of PPG400, pMDI, and PU2080 Prepolymer

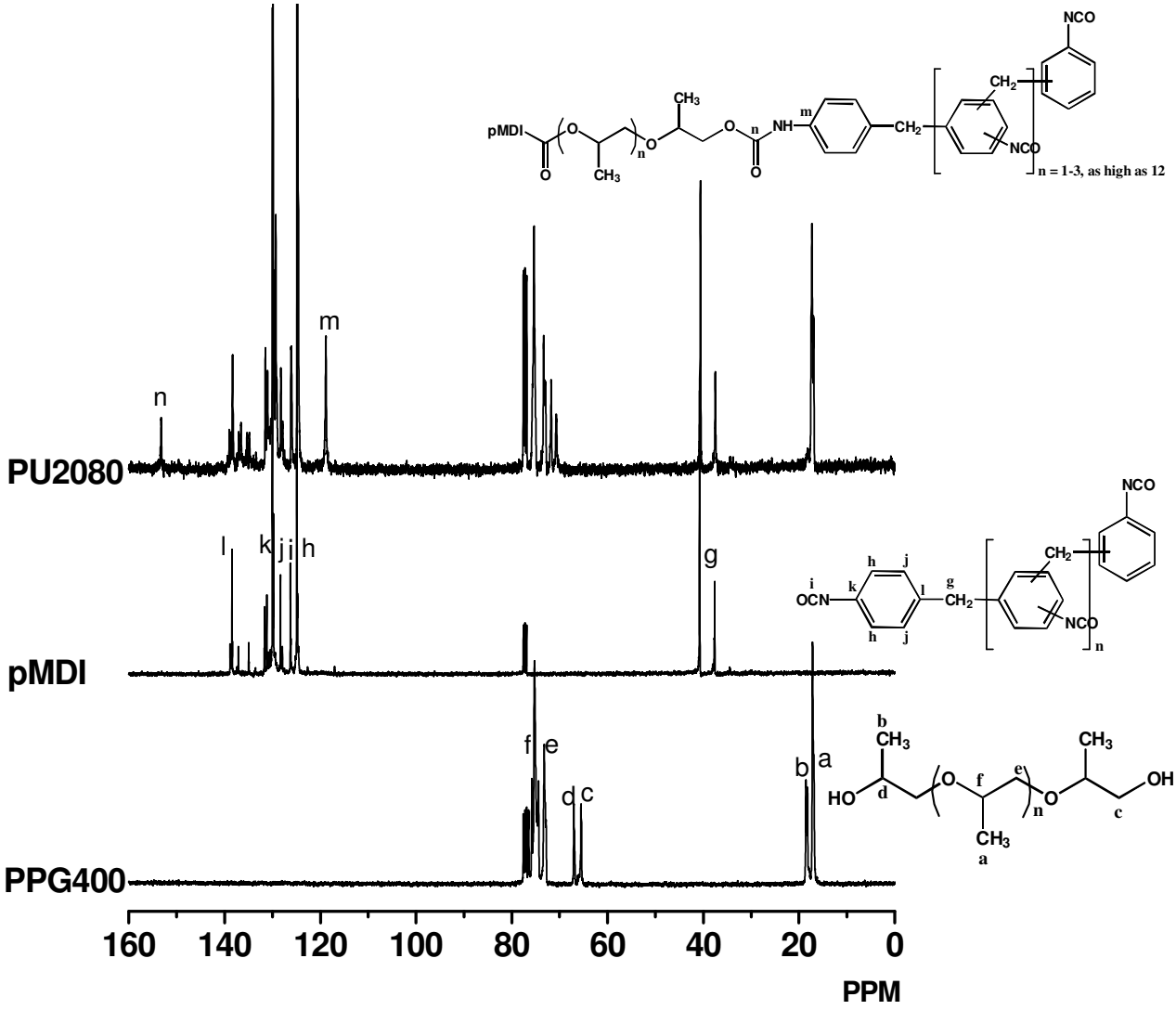

Figure A4.1 Solution 13C-NMR spectra for PPG400, Pmdi, and PU2080 prepolymer in CDCl3; peaks are assigned as labeled; formation of urethane linkage (δ = 153 ppm) is confirmed.

Appendix 4-2 Pictorial Illustration of the Assembled Wood/PUR Composite Specimens

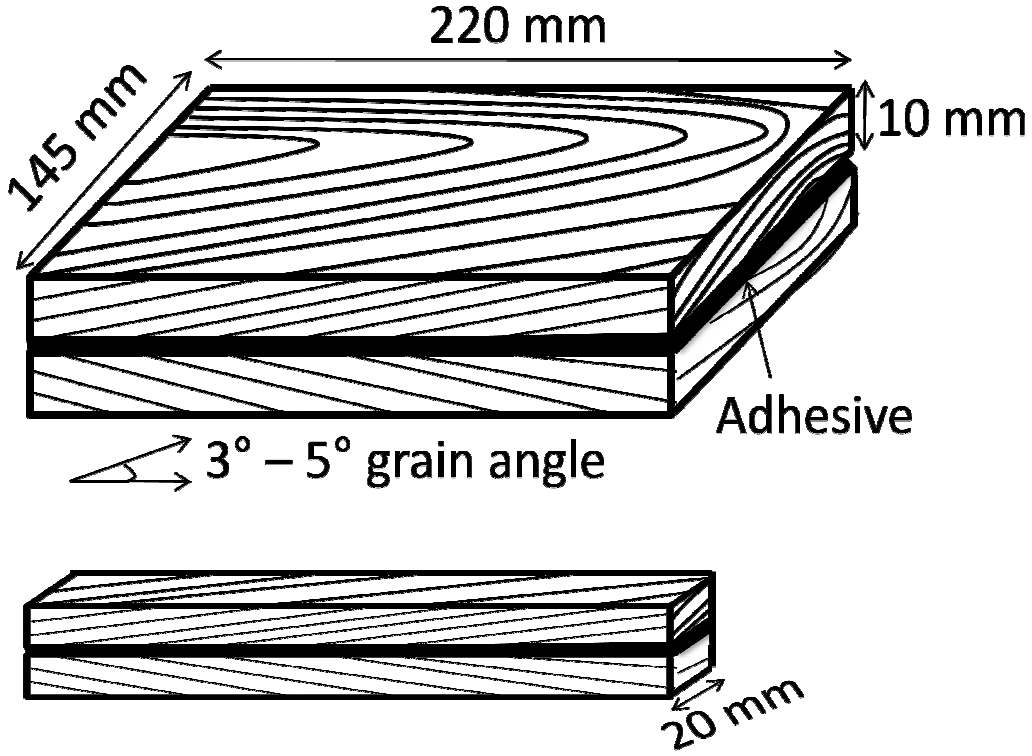

antilever Beam (DCB)

Figure A4.2 Pictorial illustration of the assembled wood/PUR composite and dual cantilever beam (DCB) fracture specimen

- PUR application rate = 250 g/ m^2;
- Controlled grain angle of 3-5° between the tangential bonding surface and the longitudinal axis;
- Consolidation conditions: room temperature, 100 psi, 24 hours;
- Each laminate provides five DCB specimens.

Appendix 4-3 Fracture Toughness of DCBs Bonded with Two Separate Batches of PURs.

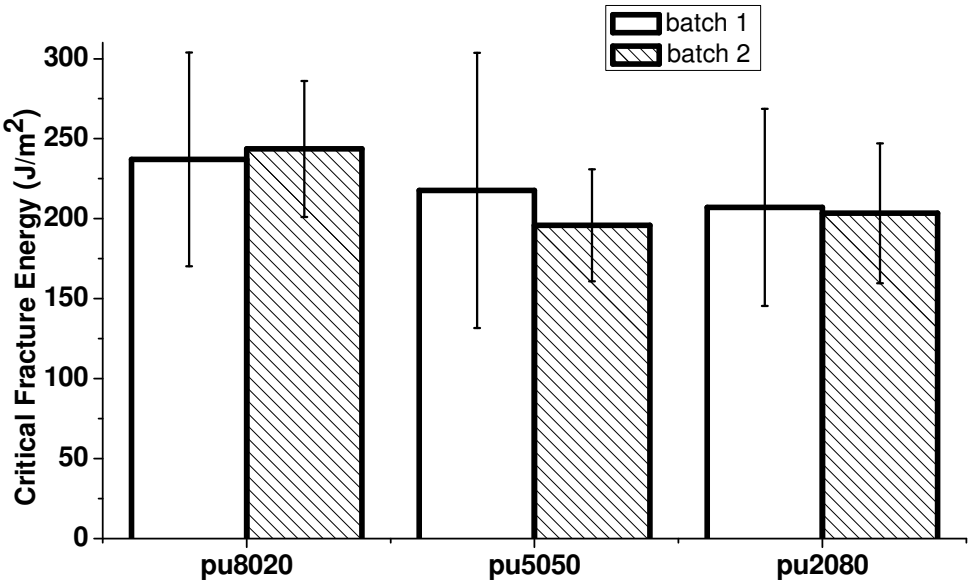

Figure A4.3 Average mode-I critical fracture energy of wood composites bonded with batch 1 and batch 2 PURs; error bars represent ± 1 standard deviation (n = 31-73).

- Adhesives: PU8020, PU5050, and PU2080; two separate batches (batch 1 and batch 2) were synthesized for each adhesive;
- Fracture specimens: 20 DCBs were prepared from each batch; at least three were randomly selected and then evaluated using mode-I fracture testing;
- Batch 1 and batch 2 PUR adhesives provide the same fracture toughness.

Appendix 4-4 Measurement of Adhesive Effective Penetration (EP)

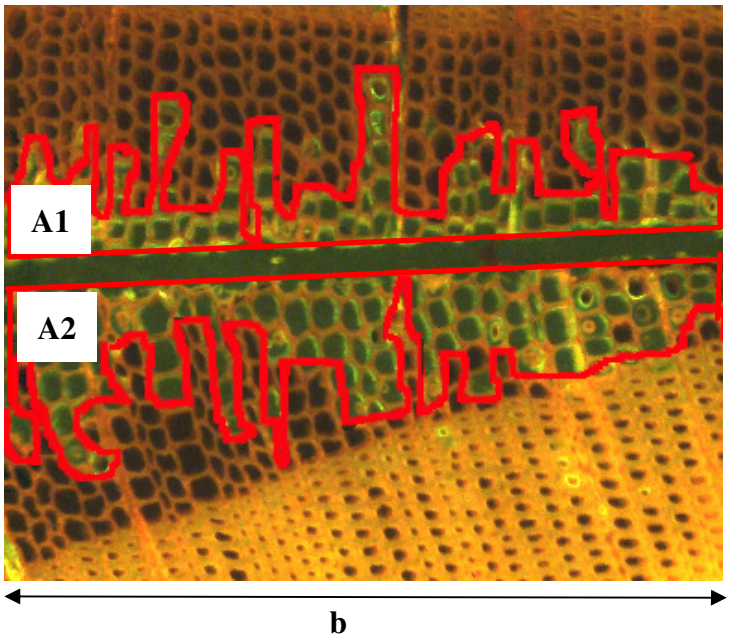

Figure A4.4 Pictorial illustration of adhesive effective penetration measurement

- Red lines highlight the penetrated regions with area A1 and A2;
- The image width b;
- Adhesive effective penetration is defined as:

$$EP = \frac{A_1 + A_2}{b}$$

- Average EP was obtained from 60 images for each adhesive.

Appendix 5-1 Comparison of Critical and Arrest Fracture Toughness

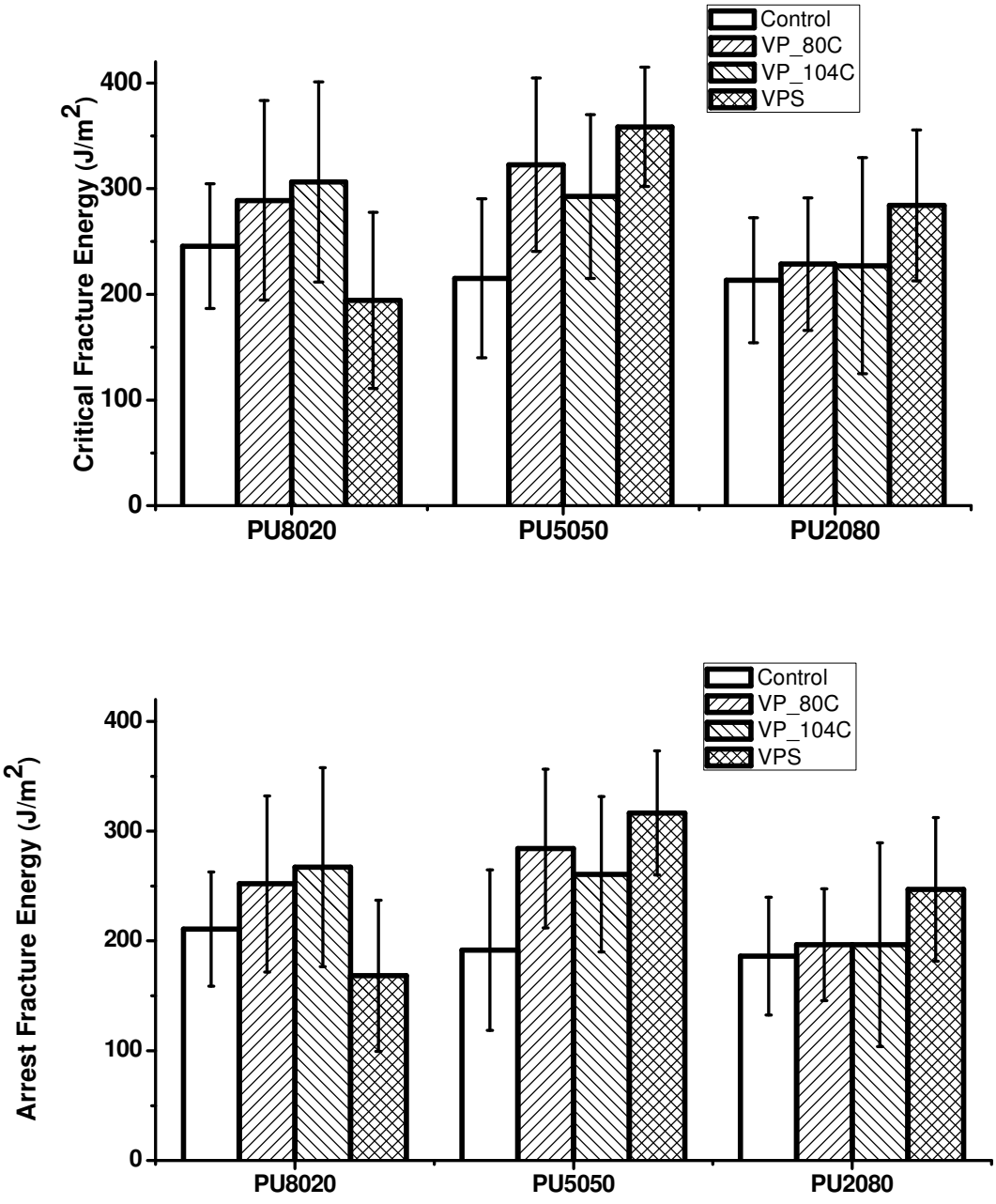

Figure A5.1 Average critical fracture energy and arrest fracture energy of PURs as a function of weathering treatments; error bars represent one standard deviation; both plots show the same trend of weathering effects.

Appendix 6-1. FTIR Sampling Strategy for DCB Failure Surfaces

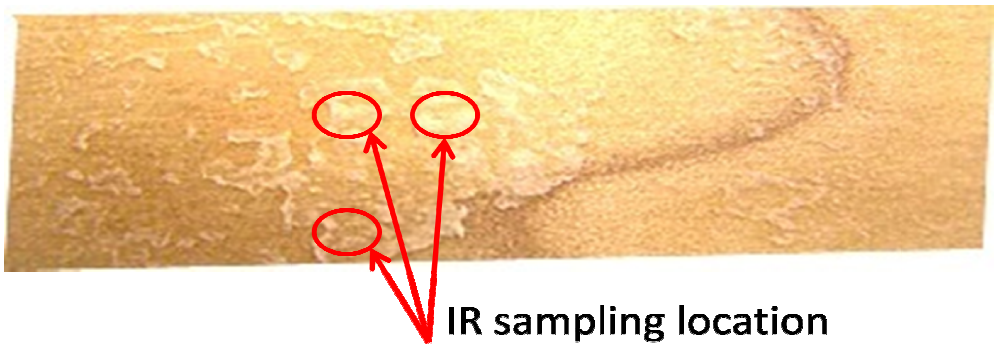

Figure A6.1 An example of DCB failure surface; the red circles highlight the sampling locations for FTIR studies.

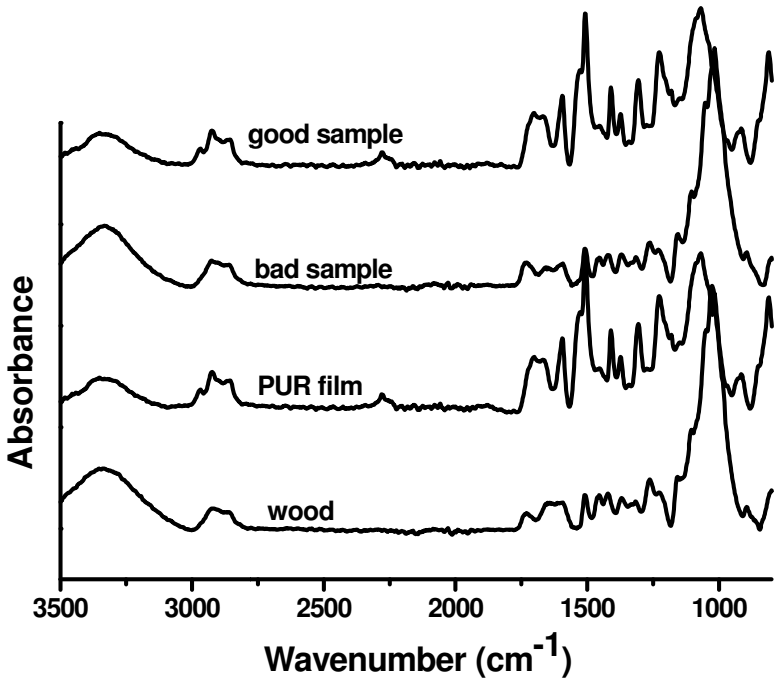

Figure A6.2 FTIR spectra showing the sampling strategy for DCB failure surfaces. A good sampling location gives a spectrum similar to the neat PUR film.

Appendix 6-2 Water-submersion DMA of PU8020 Film Specimens

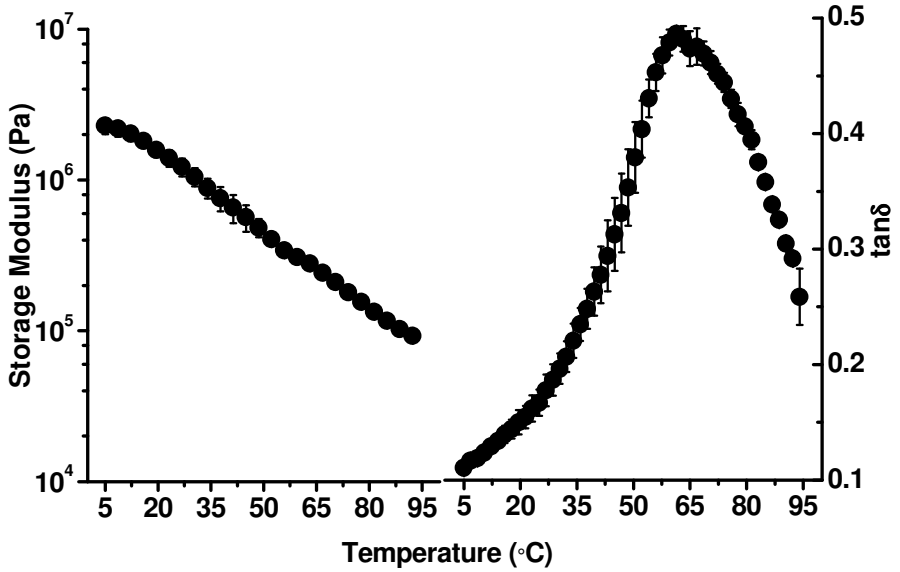

Figure A6.3 Average water-submersion DMA 1st heating scans of PU8020 film specimens (3 °C/min, 1 Hz.); error bars represent ± 1 standard deviation (n = 3); temperature ramp starts at 5 °C (instead of 25 °C normally) to show the onset of softening at 13.3 °C.

Appendix 6-3 VPSS Weathering Effects on PUR Amine Infrared Stretching

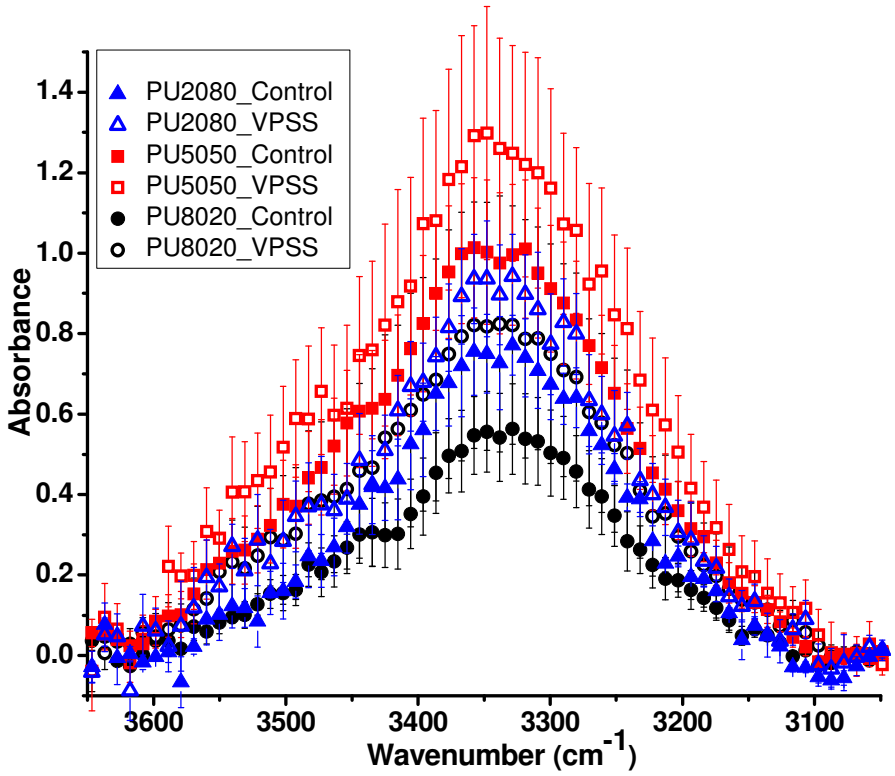

Figure A6.4 The average FTIR spectra showing the amine stretching region; error bars represent ± 1 standard deviation (n = 18); spectra normalized by the phenylene signal 1594 cm-1 (not shown) with intensities of 1.0, 1.22, and 1.36 based upon the hard phase contents of PU8020, PU5050, and PU2080, respectively; all adhesives show increased amine content after VPSS treatment.

Appendix 6-4 Deconvolution of FTIR Spectra

A6.4.1 Method

Each carbonyl IR absorbance curve was deconvoluted to five well-documented peaks, corresponding free urethane (1730 - 1740 cm^{-1}), hydrogen-bonded urethane (1700 - 1715 cm^{-1}), free urea (1690 - 1700 cm^{-1}), monodentate urea (1650 - 1690 cm^{-1}), and bidentate urea (1630 - 1650 cm^{-1}). The peak fitting was conducted using using the "*peak analyzer*" function in OriginPro software version 8.0.63 (OriginLab, Northampton, MA, U.S.A.). An example of peak deconvolution is shown in Figure A6.4.

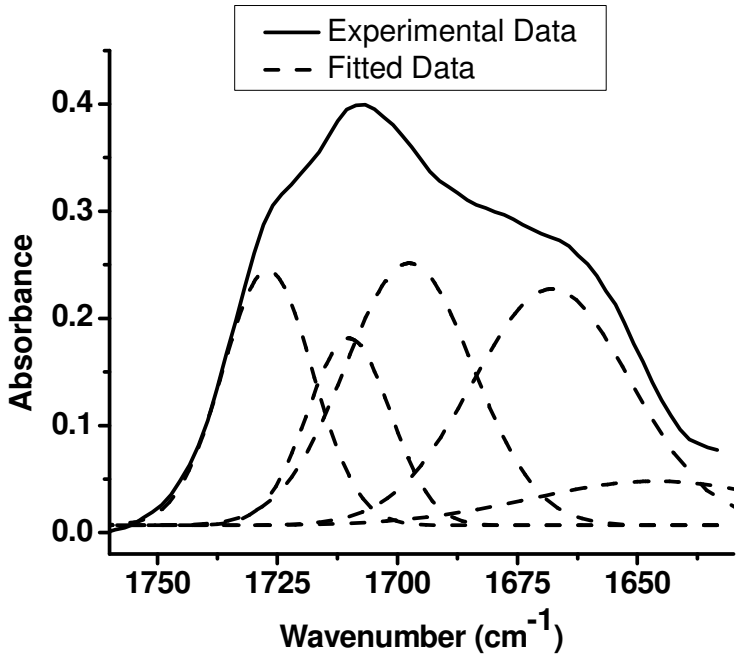

Figure A6.5 An example of FTIR spectrum deconvolution in the carbonyl stretching frequencies

A6.4.2 Results and Disscussion

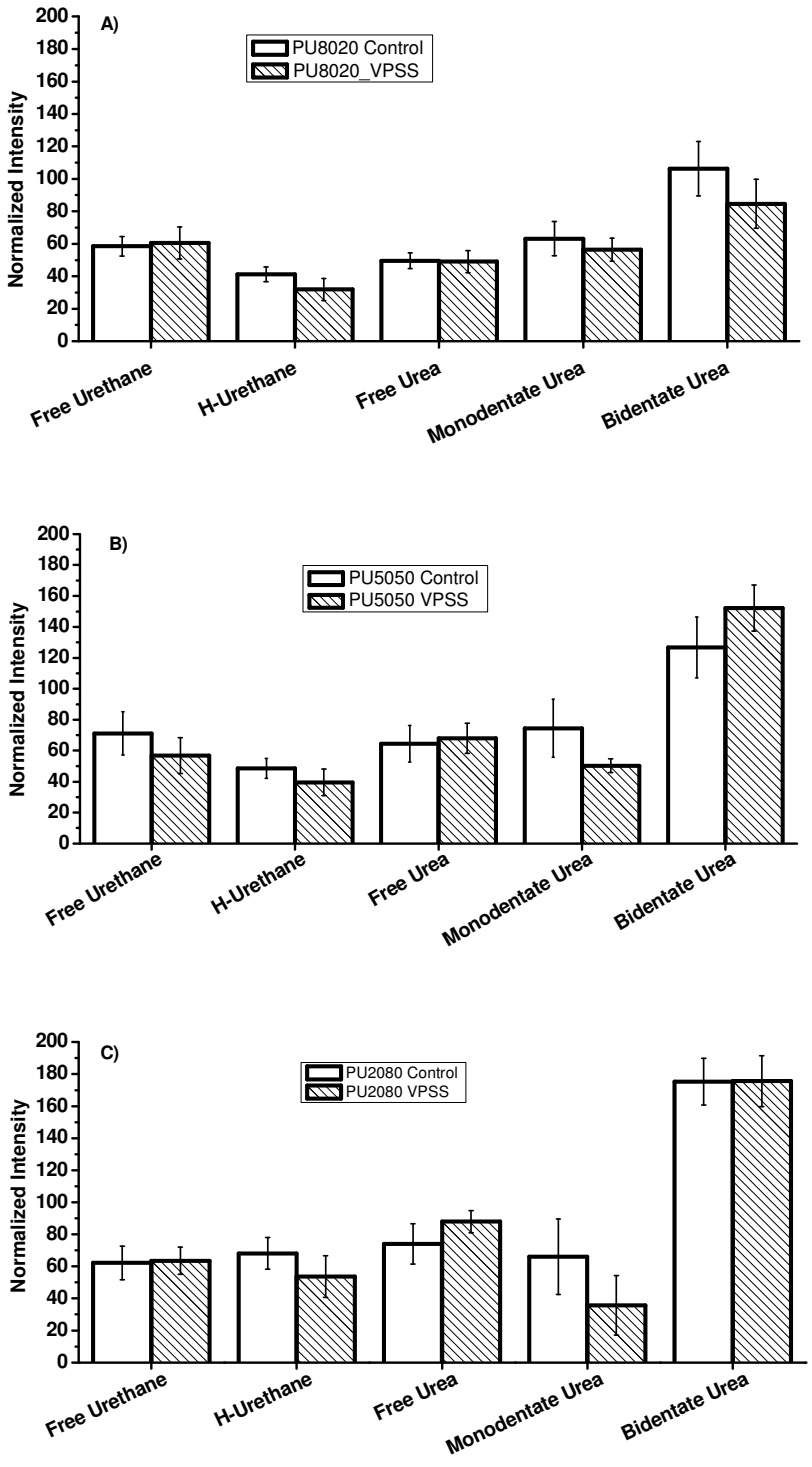

Figure A6.6 Normalized average infrared absorbance of deconvoluted carbonyl peaks for control and VPSS-treated bondlines; error bars represent ± 1 standard deviation (n = 18); A) PU8020; B) PU5050; C) PU2080.

The normalized intensity of the deconvoluted carbonyl peaks are shown in Figure A6.5. In general, the weathering effects are consistent with the observation in Figure 6-6: 1) the overall intensity is reduced for each adhesive; 2) the total urethane carbonyl intensity is decreased for each adhesive; 3) PU8020 is the only adhesive that shows a significant reduction of bidentate ureas; losing the strong bidentate hydrogen bonds may significantly contribute to its reduced fracture toughness. On the other hand, some features of the deconvoluted data seem inconsistent with Figure 6-6. For example, VPSS-treated PU5050 shows significant decrease of monodentate ureas, which is not seen in Figure 6-6. Keep in mind that the used deconvolution method simplified the infrared spectra based on major types of hydrogen bonds. The actual carbonyl infrared absorbance is extremely complex; various types of hydrogen bonds may be formed between two kinds of proton donators (urethane N-H and urea N-H) and three kinds of proton acceptors (urethane C=O, urea C=O, and PPG C-O-C). Even the same type of hydrogen bonds shift carbonyl vibration to different frequencies (e.g. “ordered” versus “disordered” H-bonded urethane carbonyls). Consequently, although peak deconvolution could provide useful information to analyze the weathering effects, a precise peak fitting is very challenging due to the extreme complexity of the system.

Appendix 6-5 Effects of VPS80C and VPS104C Weathering on PUR Hydrogen Bonding

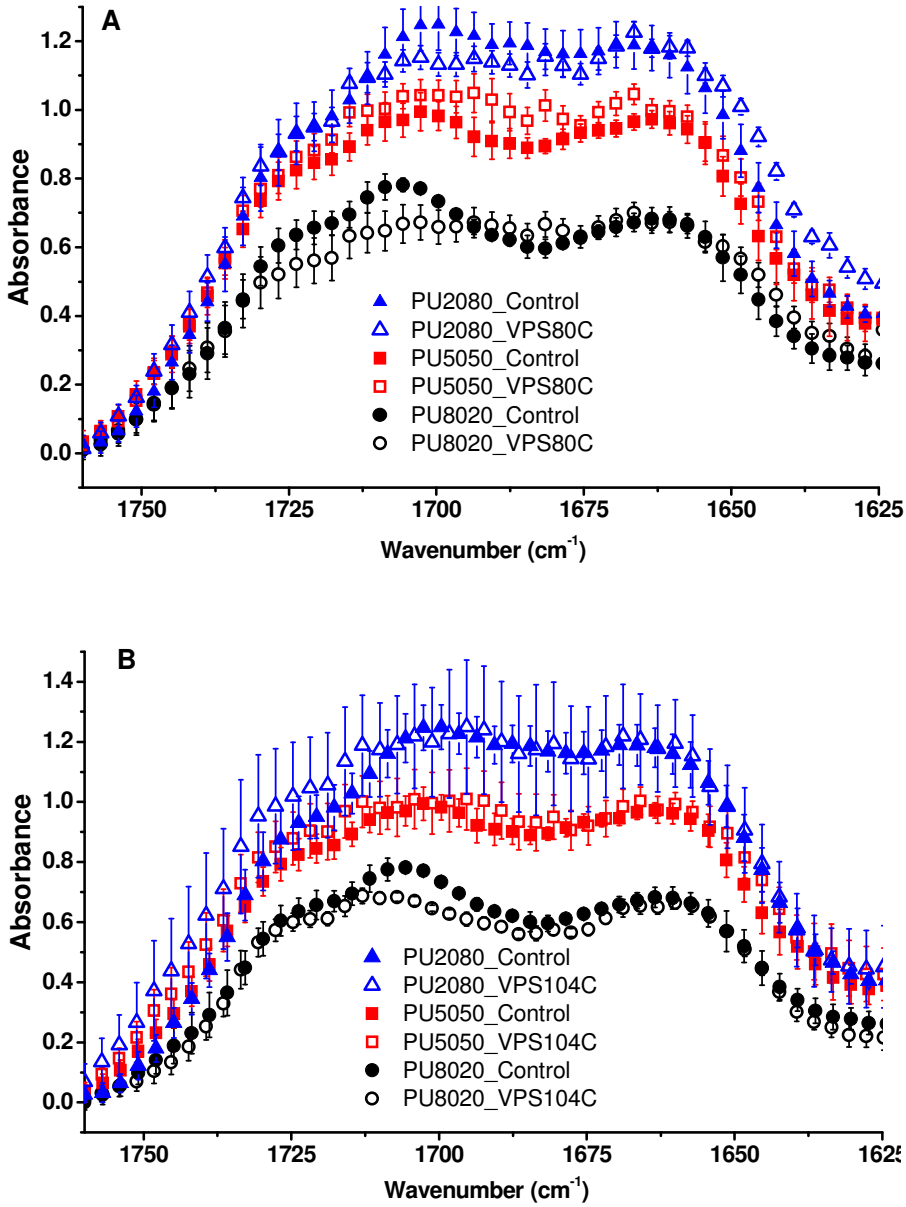

Figure A6.7 The average FTIR spectra showing the carbonyl stretching region of the controls and weathered specimens; error bars represent ± 1 standard deviation (n = 18); spectra normalized by the phenylene signal 1594 cm-1 (not shown) with intensities of 1.0, 1.22, and 1.36 based upon the hard phase contents of PU8020, PU5050, and PU2080, respectively; A) VPS80C weathering; B) VPS104C weathering.

Appendix 6-6 Effects of VPSS treatment on Wood Thermal Properties

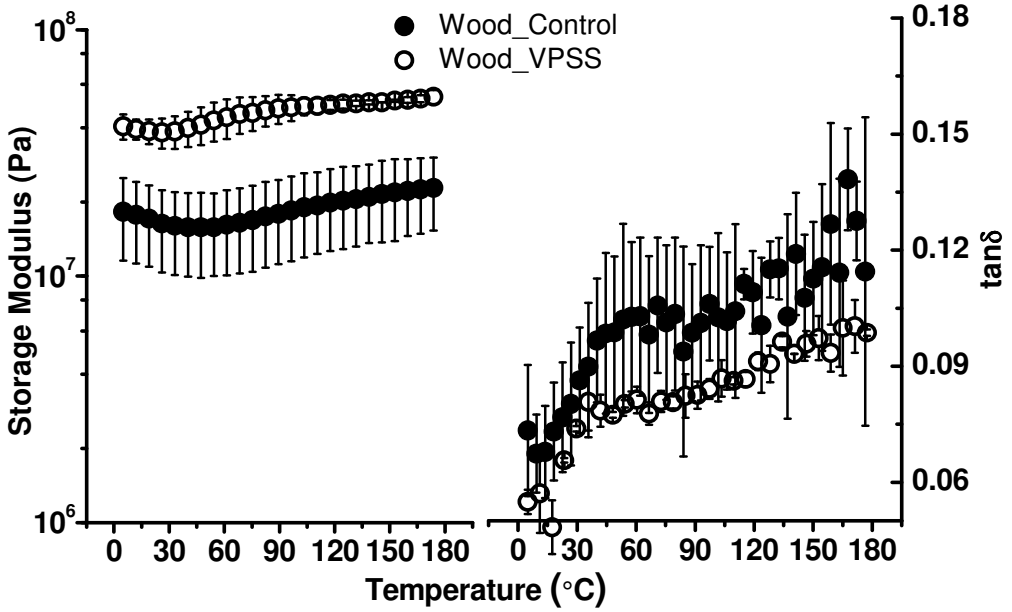

Figure A6.8 Average dry-DMA 1st heating scans of control and VPSS-treated wood specimens (3 °C/min, 1 Hz.); error bars represent ± 1 standard deviation (n = 3); wood specimens were excised from the same DCBs used for weather durability studies.

Appendix 6-7 Effects of VPS80C Weathering on Bondline Toughness and PUR Thermal Properties

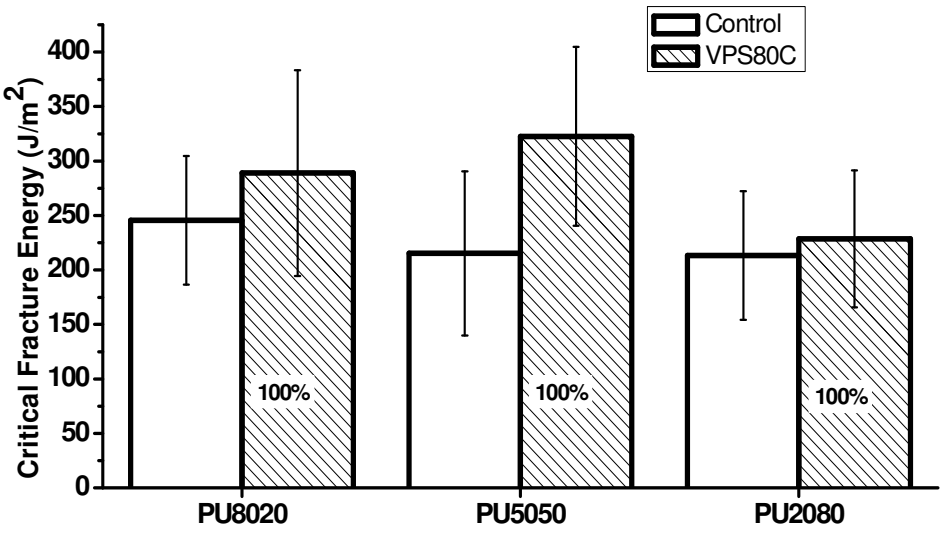

Figure A6.9 Average critical fracture energy of control and VPS80C-treated DCB specimens; error bars represent one standard deviation (n = 57-110); numbers on the bars represent the weathering survival rate.

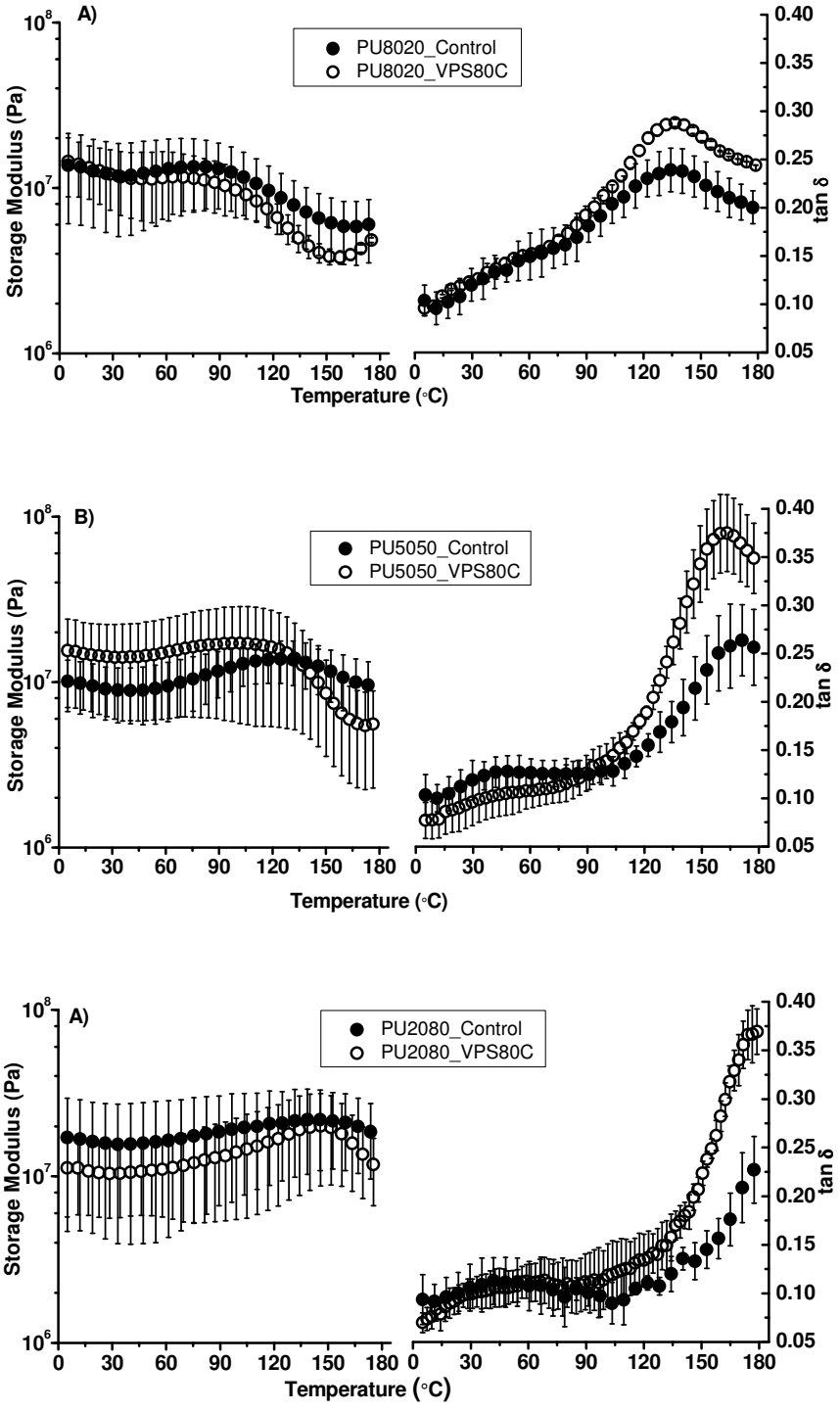

Figure A6.10 Average dry-DMA 1st heating scans of control and VPS80C-treated DCB specimens (3 °C/min, 1 Hz.); error bars represent ± 1 standard deviation (n = 3); A) PU8020; B) PU5050; C) PU2080.

Appendix 6-8 Effects of VPS104C Weathering on Bondline Toughness and PUR Thermal Properties

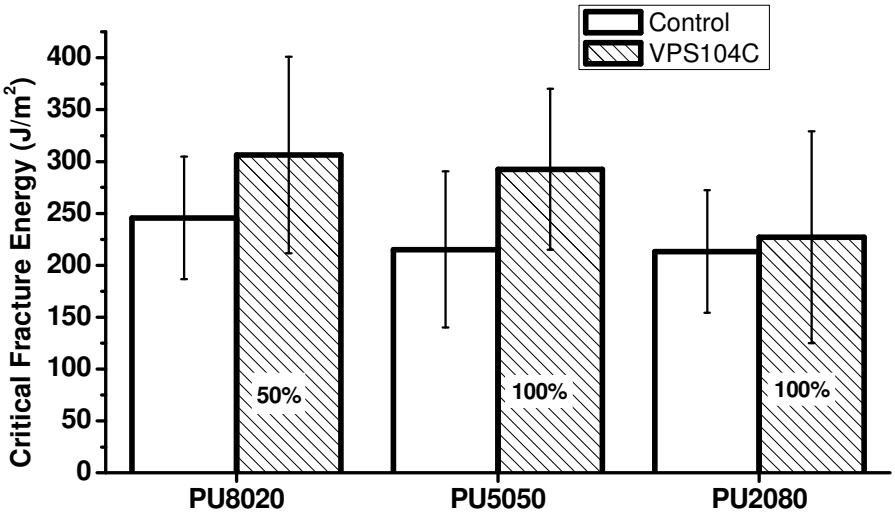

Figure A6.11 Average critical fracture energy of control and VPS104C-treated DCB specimens; error bars represent one standard deviation (n = 42-110); numbers on the bars represent the weathering survival rate.

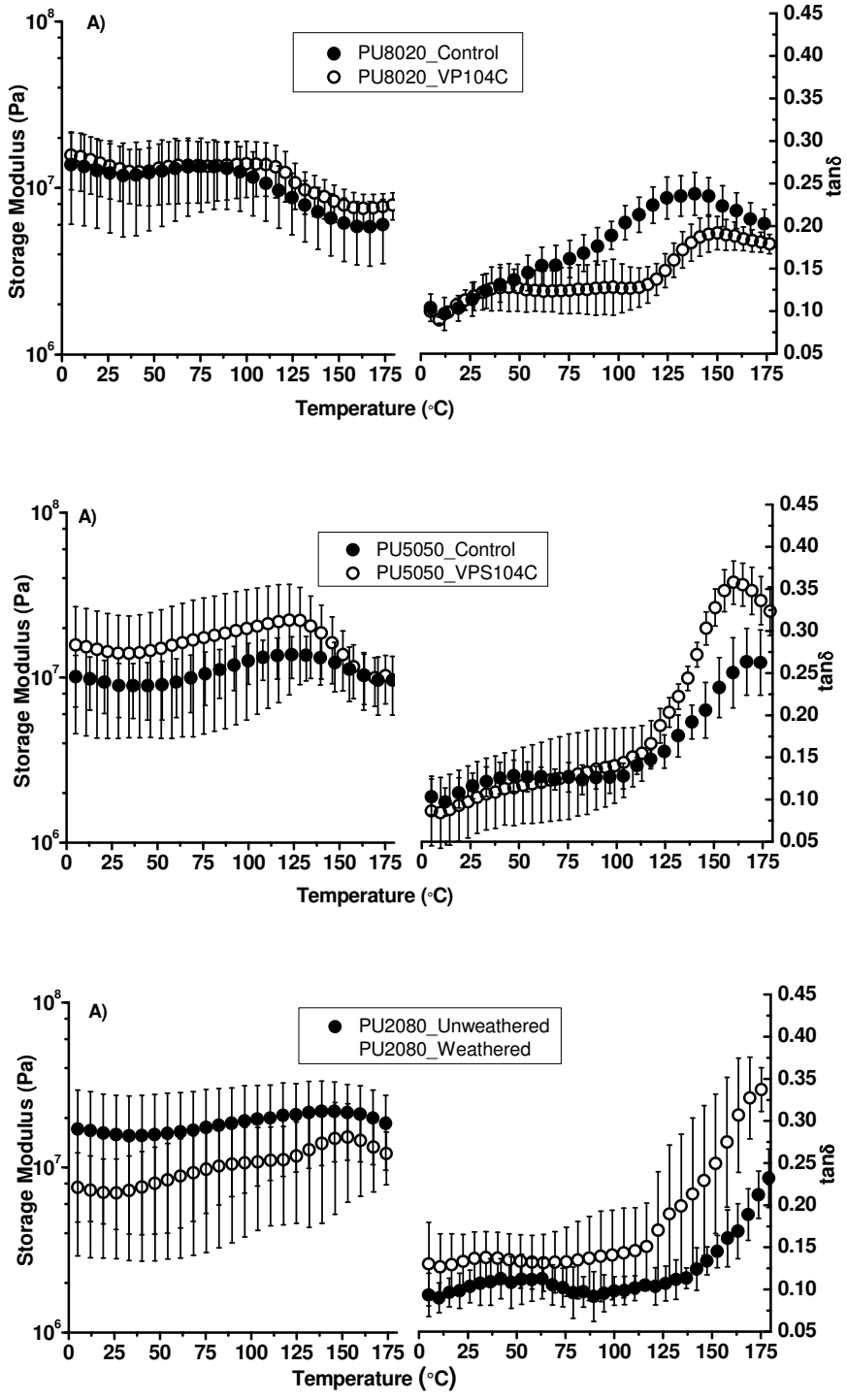

Figure A6.12 Average dry-DMA 1st heating scans of control and VPS104C-treated DCB specimens (3 °C/min, 1 Hz.); error bars represent ± 1 standard deviation (n = 3); A) PU8020; B) PU5050; C) PU2080.

Appendix 6-9 VPSS Weathering Effects on PUR Bondlines Studied by Water-submersion DMA

A6.8.1 Method

Disk DMA bondline specimens (control and VPSS-weathered) were immersed in distilled water under vacuum (5 mmHg, 20 min), and then at room conditions (2 d) to reach water saturation. Water-submersion DMA was conducted using parallel-plate compression-torsion DMA; the geometry was modified such that the bottom plate was positioned at the center bottom of a steel water cup. A single water-saturated composite specimen was held (normal force 10 N) between the plates under water and heated from 5 °C to 95 °C (3 °C/min, 1 Hz).

A6.8.2 Results

Observed from Figure A6.12, PU8020's storage modulus and damping intensity are significantly altered by each weathering procedure. PU5050 bondline shows no changes after VPS80C treatment while exhibits slightly increased damping after VPS104C and VPSS treatments. PU2080 seems unchanged after VPS80C and VPS104C treatments, and only shows a slight reduction of damping intensity after VPSS treatment. To summarize, PU8020 was most sensitive to weathering treatments, corresponding to its inferior weather durability.

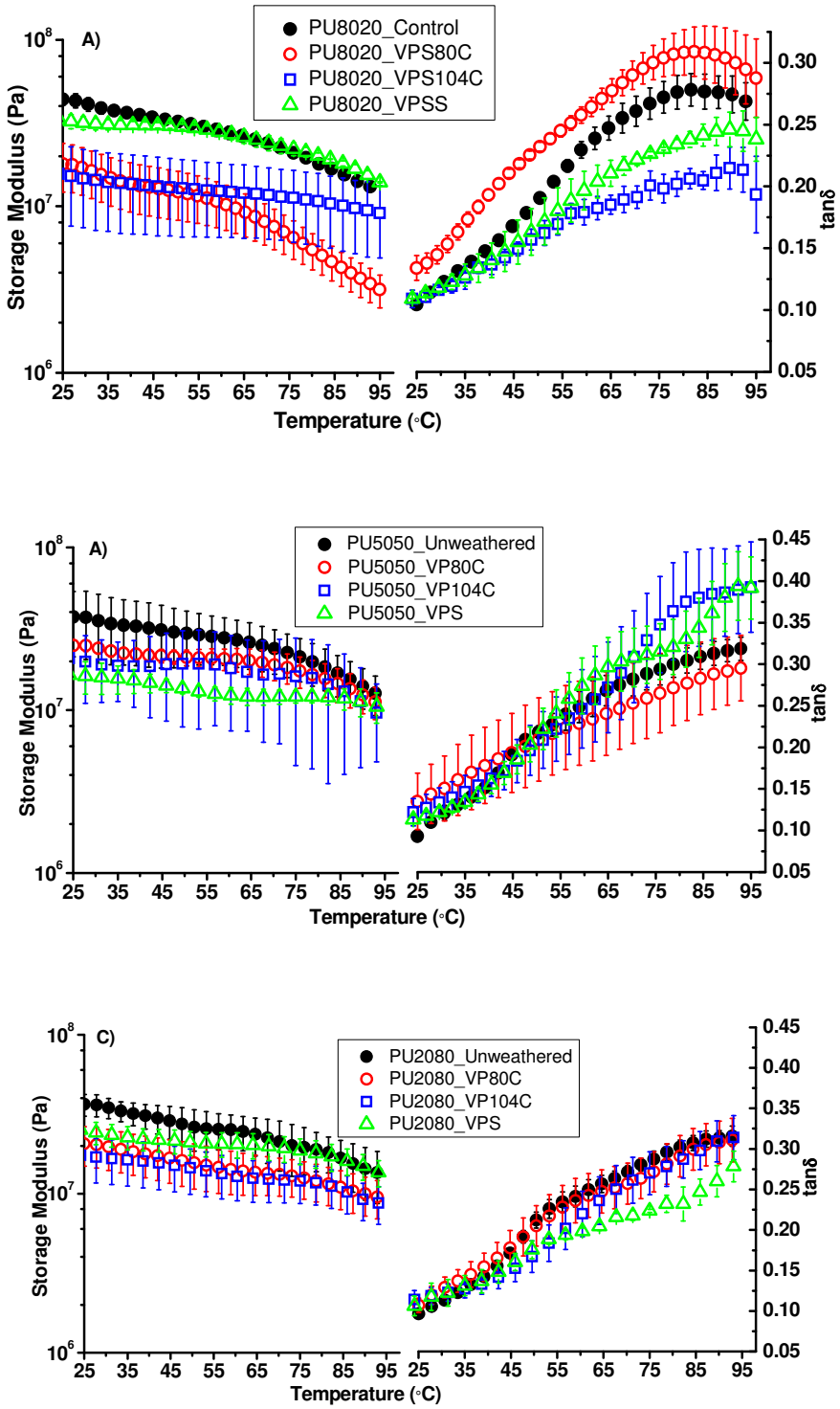

Figure A6.13 Average water-submersion DMA 1st heating scans of control and weathered DCB specimens (3 °C/min, 1 Hz.); error bars represent ± 1 standard deviation (n = 3); A) PU8020; B) PU5050; C) PU2080.

Appendix 7-1 Solution-state ^{13}C-NMR spectra of ^{13}C-^{15}N-pMDI

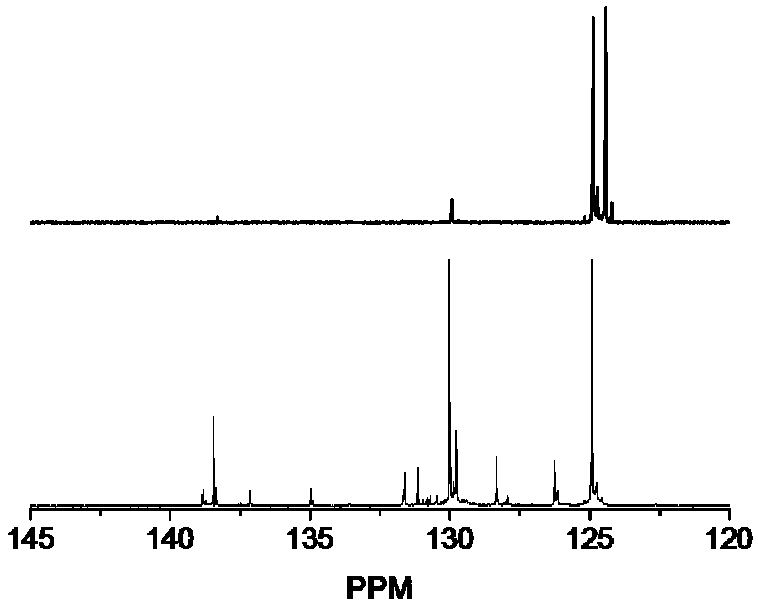

Figure A7.1 Solution-state ^{13}C-NMR spectra of ^{13}C-^{15}N-pMDI (top) and commercial pMDI (bottom) in $CDCl_3$; the isocyanate signal is shown up as a strong doublet (δ 124.6) as an evidence of ^{15}N coupling.

Appendix 7-2 Solution-state ^{15}N-NMR spectra of ^{13}C-^{15}N-pMDI

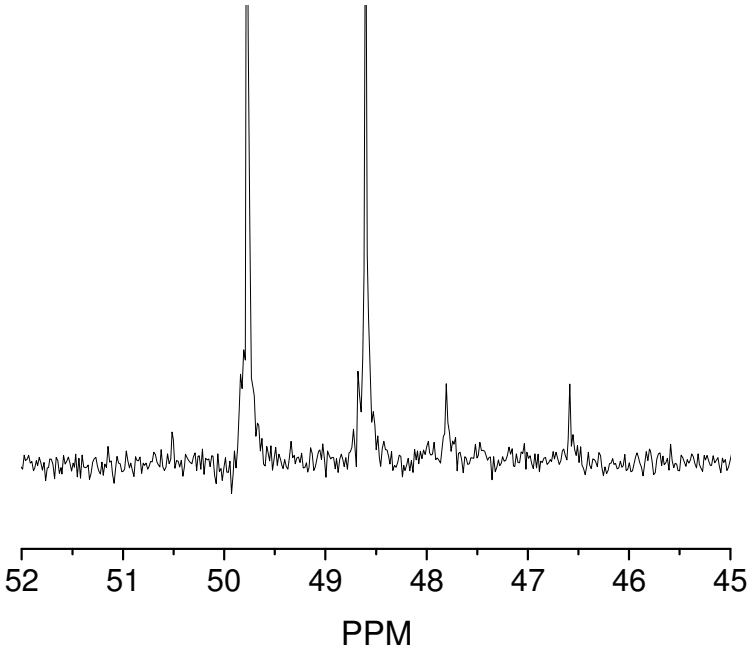

Figure A7.2 Solution-state 15N-NMR spectra of 13C-15N-pMDI in CDCl3; the isocyanate signals are shown up as two strong doublets as an evidence of 13C coupling; the strong doublet corresponds to the 4,4'-isomer of MDI, suggesting the resin contains mainly the 4,4' isomer.